PURDUE UNIVERSITY
GRADUATE SCHOOL
Thesis/Dissertation Acceptance

This is to certify that the thesis/dissertation prepared

By Rishikesh Venugopal

Entitled Numerical Simulations of Flame Dynamics in the Near-field of High-Reynolds Number Jets

For the degree of Doctor of Philosophy

Is approved by the final examining committee:

Professor John Abraham
_____
Chair

Professor Gregory A. Blaisdell

Professor Robert P. Lucht

Professor Jayathi Y. Murthy

To the best of my knowledge and as understood by the student in the *Research Integrity and Copyright Disclaimer (Graduate School Form 20)*, this thesis/dissertation adheres to the provisions of Purdue University's "Policy on Integrity in Research" and the use of copyrighted material.

Approved by Major Professor(s): Professor John Abraham

_____

Approved by: Professor Anil K. Bajaj   09/10/08
                      Head of the Graduate Program   Date

PURDUE UNIVERSITY
GRADUATE SCHOOL

Research Integrity and Copyright Disclaimer

Title of Thesis/Dissertation:

Numerical Simulations of Flame Dynamics in the Near-field of High-Reynolds Number Jets

For the degree of Doctor of Philosophy

I certify that in the preparation of this thesis, I have observed the provisions of *Purdue University Executive Memorandum No. C-22,* September 6, 1991, *Policy on Integrity in Research.**

Further, I certify that this work is free of plagiarism and all materials appearing in this thesis/dissertation have been properly quoted and attributed.

I certify that all copyrighted material incorporated into this thesis/dissertation is in compliance with the United States' copyright law and that I have received written permission from the copyright owners for my use of their work, which is beyond the scope of the law. I agree to indemnify and save harmless Purdue University from any and all claims that may be asserted or that may arise from any copyright violation.

Rishikesh Venugopal

Signature of Candidate

09/10/08

Date

*Located at http://www.purdue.edu/policies/pages/teach_res_outreach/c_22.html

NUMERICAL SIMULATIONS OF FLAME DYNAMICS IN THE NEAR-FIELD OF HIGH-REYNOLDS NUMBER JETS

A Dissertation

Submitted to the Faculty

of

Purdue University

by

Rishikesh Venugopal

In Partial Fulfillment of the

Requirements for the Degree

of

Doctor of Philosophy

December 2008

Purdue University

West Lafayette, Indiana

UMI Number: 3373255

INFORMATION TO USERS

The quality of this reproduction is dependent upon the quality of the copy
submitted. Broken or indistinct print, colored or poor quality illustrations and
photographs, print bleed-through, substandard margins, and improper
alignment can adversely affect reproduction.
In the unlikely event that the author did not send a complete manuscript
and there are missing pages, these will be noted. Also, if unauthorized
copyright material had to be removed, a note will indicate the deletion.

UMI®

To my beloved parents and elder brother, without whose constant support, understanding and encouragement, this doctoral thesis would not have materialized…

ACKNOWLEDGMENTS

TABLE OF CONTENTS

LIST OF TABLES

LIST OF FIGURES

NOMENCLATURE

Upper-Case Roman

AR amplitude ratio

C Smagorinsky model constant; curvature effect

C_B vortex ring perturbation model constant

D mass diffusivity

Da Damkőhler number

Da_i initial Damkőhler number

Da_v vortex Damkőhler number

D_k mass diffusivity of the kth species

D_{km} mixture-averaged diffusivity of kth species

D_{lam} laminar diffusivity

$\tilde{D}_{eff}$ Favre-filtered effective diffusivity

$\tilde{D}_t$ LES subgrid-scale turbulent diffusivity

E_a activation energy

L characteristic length

L_{11} longitudinal integral length-scale

Pr_t	turbulent Prandtl number
R	specific gas constant
Re	Reynolds number
Re_v	vortex Reynolds number
R_{11}	normalized longitudinal two-point correlation
R_u	universal gas constant
$\tilde{S}_{ij}$	strain rate tensor
$\left|\tilde{S}\right|$	strain rate magnitude
Sc_t	turbulent Schmidt number
T	temperature
TR	time-scale ratio
U	mean axial velocity; unsteady effect
U_{inj}	injection velocity of the jet
U_j	jet centerline velocity at the inlet
U_{cl}	jet centerline velocity
U_{xo}, U_{ro}	axial and radial components of vortex ring velocity
Y_i	mass fraction of the ith species
Z	mixture fraction
$\tilde{Z}$	instantaneous filtered mixture fraction
$\bar{Z}$	mean mixture fraction

$\overline{Z''^2}$	mixture fraction variance
Z_{cl}	jet centerline mixture fraction

Lower-Case Roman

a	characteristic strain rate
c_p	mixture specific heat
d	jet diameter
d_v	viscous diameter of the vortex
h	total enthalpy per unit mass; grid spacing
h_k	enthalpy of the kth species
$\overline{k}$	Reynolds-averaged turbulent kinetic energy
δ	diffusion thickness
l_r	length-scale ratio
m_1, m_2, m_3	momentum densities in Cartesian coordinate directions
n	soot number density
$p, \overline{p}$	total and filtered pressure
r	radial distance
$r_{1/2}$	jet half-width based on axial velocity
r_o	jet radius at the inlet
$rz_{1/2}$	jet half-width based on mixture fraction
t	time

u, v, w	Cartesian velocity components
u_1, u_2, u_3	velocity in Cartesian coordinate directions
$u_i, \langle u_i \rangle, u_i'$	total, mean and fluctuating velocity in the ith direction
u_e	internal energy
u_f	velocity-scale of the flame
u_{fv}	velocity-scale ratio
u_v	velocity-scale of the vortex
u_x, u_r	axial and radial velocities in region of vortex ring
$\dot{w}_i$	chemical production/destruction rate of species i
x_i	distance in the ith coordinate direction
x_1, x_2, x_3	Cartesian coordinate directions

Upper-Case Greek

$\Gamma(\ )$	Gamma function used in the beta PDF
Δ	spatial filter width; grid width
Δ_t	time step
$\Psi_1 \cdots \Psi_5$	characteristic wave amplitudes

Lower-Case Greek

α, β	beta PDF parameters
α, β	filter coefficients

δ	thickness of the hyperbolic tangent profile
δ_{ij}	Kronecker delta function
δ_θ	inlet jet momentum thickness
$\overline{\varepsilon}$	Reynolds-averaged turbulent dissipation rate
ε_n, φ_n	uniform random numbers
η	overall reaction order; Kolmogorov length-scale
κ	curvature of the mixture fraction isosurface
λ	thermal conductivity; Taylor micro-scale
$\lambda_1 \cdots \lambda_5$	characteristic wave velocities
$\tilde{\lambda}_{\text{eff}}$	Favre-filtered effective conductivity
μ_{lam}	laminar viscosity
$\tilde{\mu}_{\text{eff}}$	Favre-filtered effective viscosity
$\tilde{\mu}_{\text{T}}$	subgrid-scale turbulent viscosity
μ, σ	mean and variance of the log-normal distribution
ν	kinematic viscosity
ν_{t}	turbulent kinematic viscosity
ρ	mixture density
ρ_{a}	ambient gas density
ρ_{j}	injected gas density
ρ_{k}	partial density of the kth species

$\tilde{\sigma}_{ij}$	resolved stress tensor
$\tilde{\sigma}_{SG_{ij}}$	subgrid-scale stress tensor
τ_c	characteristic chemical reaction time-scale
τ_{ck}	chemical time-scale of reaction k
$\tilde{\tau}_{ij}$	effective stress tensor
χ	instantaneous scalar dissipation rate
χ_e	steady extinction limit
χ_r	scalar dissipation ratio
χ_{st}	scalar dissipation rate at stoichiometric mixture fraction
$\tilde{\chi}$	instantaneous filtered scalar dissipation rate
$\bar{\chi}$	mean scalar dissipation rate
$\bar{\chi}_Z$	time-averaged conditional-mean scalar dissipation rate

Symbols

$CHRR$	chemical heat release rate
$CNVHX$	convective term for mixture enthalpy in the x direction
$CNVHY$	convective term for mixture enthalpy in the y direction
$DELHX$	diffusion term for mixture enthalpy in the x direction
$DELHY$	convective term for mixture enthalpy in the y direction
erf	error function
$G(\ )$	filter function

$P_z(\ )$	subgrid-scale PDF of the mixture fraction
TKE	turbulent kinetic energy
$[\cdot]$	concentration
$\overline{(\ )}$	filtering operation
$\langle\ \rangle$	time average

Superscripts

$f, \widetilde{f}, f'$	total, filtered, and residual components of a variable
f_i', f_i''	first and second derivative of a variable at node i

Abbreviations

DNS	direct numerical simulation
LECT	local equilibrium characteristic time
LES	large-eddy simulation
PaSR	partially-stirred reactor
PSR	perfectly-stirred reactor
PDF	probability density function
RANS	reynolds-averaged Navier-Stokes
RIF	representative interactive flamelet
SGS	subgrid scale
UFPV	unsteady flamelet/progress variable

ABSTRACT

Venugopal, Rishikesh. Ph.D., Purdue University, December, 2008. Numerical Simulations of Flame Dynamics in the Near-Field of High-Reynolds Number Jets. Major Professor: Dr. John Abraham, School of Mechanical Engineering.

Recent experiments in diesel jet flames show that flame lift-off has a significant influence on pollutant formation. Lift-off occurs in the near-field of the jet, which is characterized by complex interactions between turbulence and chemistry. Commonly employed modeling approaches based on Reynolds-averaged Navier-Stokes (RANS) simulations are limited in their capability to predict transient and steady lift-off phenomena, as they ignore effects due to unsteadiness and curvature that are inherent in the near-field.

In the present work, we perform numerical investigations of localized flame dynamics in the near-field ($x/d < 25$) of high-Reynolds number (Re) jets encountered in diesel engine applications. The primary focus is on the exploration of unsteady extinction/reignition phenomena. A dual approach involving large-eddy simulation (LES) of a 70,000-Re variable-density isothermal gaseous fuel jet, and studies of flame-vortex interactions and unsteady flamelets, under diesel engine conditions, is employed in this work.

Results from flame-vortex interaction studies show that in the near-field ($x/d < 25$) of the 70,000-Re jet at radial locations close to the centerline ($r/d < 1.5$), unsteady extinction/reignition phenomena characterize the flame dynamics. Extinction is minimally affected by the vortex-induced curvature, but involves strong unsteady effects leading to extinction limits higher than steady values. On the other hand, reignition is governed by curvature effects, and occurs through

the dynamics of edge flames. In the simulated jet near-field, unsteady effects are observed to diminish with increasing axial locations due to relatively weaker vortices, whereas curvature effects increase due to the presence of relatively thicker flames.

The unsteady flamelet studies show that in stoichiometric regions at radial locations relatively far from the centerline (r/d > 1.0) in the jet near-field, temporary flame weakening/recovery events are likely to occur. Steady flamelet models provide reasonable estimates of the mean temperature, and mean mass fractions of the major species and unburned hydrocarbons (UHCs), but are inadequate for the prediction of mean NO mass fractions. Extrapolation of the analysis to jets with higher global strain rates shows that unsteady effects on the localized flame dynamics are important for the prediction of transient and steady lift-off behavior.

CHAPTER 1. INTRODUCTION

1.1. <u>Background and Motivation</u>

Diesel combustion has been an active area of research over the past two decades with an increasing focus on emissions reduction. As diesel engines are extensively employed in ground and marine transportation, the need to control toxic pollutants, while maintaining or improving their high thermal efficiency, is of central importance. To achieve this, a thorough understanding of spray formation, mixing, combustion and pollutant formation is essential. To this end, significant advances have been made through both experimental and computational efforts. In particular, the development and application of optical diagnostic tools (Dec, 1997; Flynn *et al.*, 1999; Siebers and Higgins, 2001) and multidimensional computational models (Magi, 1987; Amsden, 1993) have provided valuable insights into various aspects of diesel combustion, such as the structure and entrainment characteristics of vaporizing Diesel sprays (Bracco, 1985; Reitz, 1987; Post *et al.*, 1999), autoignition (Wan *et al.*,1997; Gopalakrishnan and Abraham, 2002), and pollutant formation (Pitsch *et al.*, 1996; Gopalakrishnan and Abraham, 2004).

The majority of multidimensional models which are currently being employed solve the Reynolds-averaged Navier-Stokes (RANS) equations with sub-models for turbulence, sprays and combustion. A variety of combustion sub-models such as local equilibrium characteristic time (LECT) (Abraham *et al.*, 1985) models, representative interactive flamelet (RIF) (Pitsch *et al.*, 1995) models, perfectly stirred reactor (PSR) (Senecal *et al.*, 2002) models, partially stirred reactor (PaSR) (Chomiak and Karlsson, 1996) models and flame surface density (Tap and Veynante, 2005) models have been developed. In order to

achieve model closure, each of these approaches assumes a certain physical picture of the combusting diesel jet. For instance, LECT models are based on a mixing-controlled hypothesis for diesel combustion whereas RIF models can incorporate detailed chemical kinetics by assuming that the turbulent flame is comprised of strained laminar diffusion flamelets. On the other hand, PSR models assume turbulent mixing to be much faster than chemistry resulting in locally premixed kinetics-controlled combustion. The appropriateness of these modeling assumptions is often evaluated through comparisons with experimental data within a certain range of chamber conditions. However, the agreement of the model predictions with data in a certain range is by itself not a validation of the presumed physics. Moreover, the agreement of the measured results with computed results using models based on conflicting theories often obscures the understanding of the underlying physical mechanisms. An interesting example is the prediction of flame stabilization or lift-off in diesel jets which occurs in the near-field. Recent experiments in diesel sprays (Siebers and Higgins, 2001; Pickett and Siebers, 2004) have shown that the flame lift-off height is an important measure of the extent of fuel-air mixing prior to combustion and subsequent pollutant distribution in the jet. Computations employing models such as PSR (Kong *et al.*, 2005a, b) and RIF (Venugopal and Abraham, 2007a), which are based on very different theories, have been shown to predict lift-off heights within a given range of chamber conditions. As discussed in a recent review by Venugopal and Abraham (2007b), this suggests that near-field phenomena may result from a combination of several mechanisms, which renders RANS models with a presumed turbulence-chemistry interaction inappropriate.

A major shortcoming of RANS approaches is the inherent lack of unsteadiness and intermittency which are characteristic of turbulent flows. Local fluctuations of fuel and oxidizer concentrations, temperature and scalar dissipation rates can have a significant impact on the flame structure and stabilization in turbulent reacting flows. In this context, with the advent of faster computers and higher-order accurate numerical schemes, large-eddy simulation

(LES) has emerged as a promising tool where large-scale fluctuations are resolved while subgrid scale effects are modeled. Though the efficacy of LES in the prediction of reacting flows is still limited by the reliability of the subgrid scale combustion model, accounting for localized fluctuations of quantities such as scalar dissipation rates have been shown to yield significant improvements over RANS predictions of flame structure and pollutant distributions in jet diffusion flames (Pitsch, 2002; Pitsch, 2006). However, the majority of the commonly employed subgrid scale models in LES, such as flamelet (Pitsch and Steiner, 2000) and flamelet-progress variable (Pierce and Moin, 2004) models, assume a locally 1-D flame structure. These models are also often employed in RANS simulations. Consequently, two-dimensional (2-D) and three-dimensional (3-D) interactions due to turbulence-induced flame curvature cannot be captured. Moreover, detailed understanding of such curvature effects in the near-field of jet diffusion flames, specifically under diesel conditions, is still lacking.

Direct numerical simulation (DNS), on the other hand, offers great potential in understanding turbulence-chemistry interaction. In principle, all the turbulence and chemical scales are fully resolved in a DNS with no-priori assumptions about the flame structure. However, even for relatively low jet exit Reynolds numbers, DNS leads to a massive computational overhead and is impractical for the Reynolds numbers encountered in Diesel applications. Nevertheless, over the past fifteen years, DNS has emerged as a valuable research tool for simulation of reacting flow problems in more simplified canonical configurations such as flame-vortex interactions, reacting mixing layers and isotropic decaying turbulence (Versvisch and Poinsot, 1998). The applicability of widely-employed modeling approaches such as flamelet models for the prediction of phenomena such as auto-ignition and flame extinction can be assessed through DNS. Furthermore, through DNS databases, improved models for RANS and LES applications can be developed. The need for such DNS studies under diesel conditions was recently discussed by Venugopal and Abraham (2007b).

In this work, our primary interest lies in the investigation of phenomena related to flame lift-off in diesel jets. As discussed before, recent experiments (Siebers *et al.*, 2002; Pickett and Siebers, 2004) in diesel jets show that the lift-off height significantly influences soot formation through fuel/air premixing prior to combustion. However, prediction of lift-off heights from a computational viewpoint is challenging. For instance, consider Fig. 1.1 that shows a schematic of the instantaneous flowfield of a lifted jet diffusion flame. The figure shows that lift-off in the near-field of the jet could result from an interplay of a variety of processes, such as *autoignition*, *partially-premixed flame propagation* and *local extinction/reignition*. In particular, Fig.1.1 shows one possible conceptual picture, where autoignited kernels originate at downstream locations in the jet and propagate upstream towards the base of the lifted flame, where local extinction/reignition events occur. Hence, for the conceptual picture shown in Fig. 1.1, the balance between local extinction/reignition events determines the steady lift-off height in the jet.
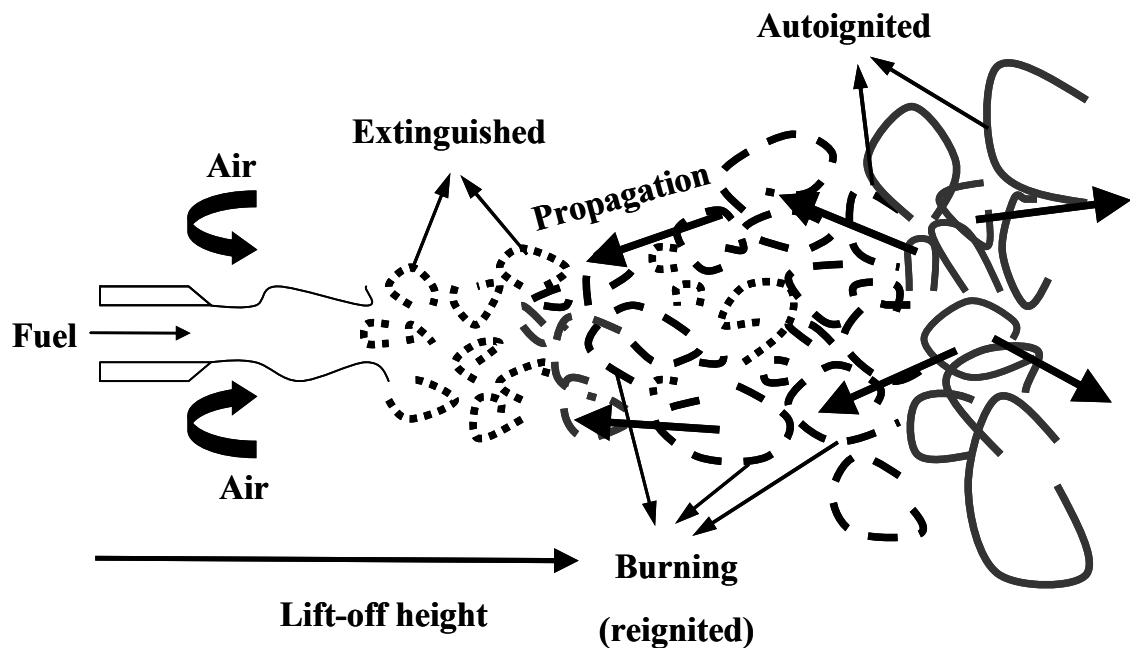
Figure 1.1. Schematic of the instantaneous flowfield of a lifted jet diffusion flame.

The phenomena contributing to lift-off, i.e. autoignition, flame propagation, and local extinction/reignition, are inherently unsteady, and involve 2-D/3-D effects due to the flame curvature. However, as indicated before, commonly employed RANS-based modeling approaches ignore effects due to unsteadiness and curvature on the local flame structure, and hence limited in their capability to describe jet near-field phenomena, such as flame lift-off. Even though LES-based approaches account for unsteadiness, currently employed models in reacting-LES (Pitsch, 2006) do not adequately account for curvature effects on the local flame structure. Hence, this work is focused on the understanding of unsteady and curvature effects on the localized flame dynamics in the near-field of high-Reynolds number (Re) jets, such as those occurring in diesel combustion chambers, While unsteady and curvature effects on all of the contributing phenomena, such as autoignition, flame propagation and extinction/reignition, are important, we primarily focus on extinction/reignition in this work.

Recent DNS studies of jet diffusion flames at relatively low jet Re (< 10,000) (Pantano, 2004; Mizobuchi *et al.*, 2005; Hawkes *et al.*, 2007) using simplified reduced chemical kinetic models show that in the near-field of the jet, local extinction and reignition phenomena are prevalent. Local extinction occurs when the scalar dissipation rate (χ) exceeds a certain critical value (χ_e) leading to loss of heat and radicals from the flame zone. Following local extinction, the extinguished regions can reignite. DNS studies in isotropic decaying turbulence (Sripakagorn *et al.*, 2004) and modeling studies in turbulent CO-H_2 flames (Hewson and Kirstein, 2002) have shown that reignition events occur predominantly through 2-D and 3-D phenomena, such as propagation of edge-flames and engulfment by a neighboring hot environment. However, owing to the relatively low values of Re, these studies are limited to quasi-steady flowfields. In the near-field of high-Re (~ 100,000) jets encountered in diesel applications, it is expected that unsteady effects will be significant, which may alter the flame extinction/reignition characteristics. Moreover, the influence of curvature effects in unsteady flowfields needs clarification. Hence, the present work investigates

extinction/reignition in unsteady flowfields that are representative of the near-field of high-Re jets encountered in diesel combustion.

Experiments in diesel sprays (Siebers and Higgins, 2001; Siebers *et al.*, 2002) show that for a wide range of diesel engine operating conditions, such as injection pressures, chamber densities, temperatures and oxygen concentrations, and orifice diameters, flame lift-off heights lie in the range of 40-400 diameters from the injector orifice. For gaseous fuel jets that are equivalent, i.e. having the same mass and momentum flow rates as the diesel sprays (Iyer and Abraham, 1997), the lift-off heights would fall in the range of 10-100 jet diameters. In this work, we investigate the likely nature of localized flame dynamics in the region up to 25 diameters in a high-Re gaseous fuel jet, which may represent the lift-off region in gaseous jets equivalent to diesel sprays. Experiments (Siebers and Higgins, 2001) and modeling studies (Chomiak and Karlsson, 1996; Venugopal and Abraham, 2007a,b) show that the liquid phase does not have a significant influence on diesel lift-off, except for relatively large orifice diameters (> 200 μm) where the liquid lengths exceed lift-off heights (Siebers and Higgins, 2001; Senecal *et al.*, 2003). Here, we are primarily interested in flame-turbulence interactions relevant for lift-off, and neglect possible effects due to spray-turbulence and spray-flame interactions. It is well-known that the modeling of diesel sprays presents significant challenges and numerical uncertainties (Abraham, 1997; Abraham and Magi, 1999). Hence, we restrict our attention to gaseous fuel jets in order to avoid the uncertainties associated with spray modeling that may influence the conclusions.

In the section that follows, the objectives of the present work are outlined. Thereafter, the approach adopted in this work is discussed in Section 1.3. An outline of the thesis is presented in Section 1.4.

1.2. Objectives

We seek to address the following questions in this work:

1. What are the likely regimes of localized flame dynamics in the near-field of high-Re jets encountered in diesel engine applications?,

2. How do unsteadiness and curvature influence the local flame structure in the near-field of high-Re jets?,

3. What modeling approaches are applicable to predict the localized flame dynamics in the jet near-field?,

4. What are the implications of the findings related to the above questions for transient and steady flame lift-off behavior in diesel jets?

In our opinion, the above questions have not been adequately addressed in the works so far in the literature. These questions are important for the understanding of near-field phenomena in high-Re jets encountered in diesel engines, and for the development of predictive computational tools. Now, we will discuss the approach adopted in the present work to address the questions raised above.

1.3. Approach

A dual approach is employed in this work, which is schematically shown in Fig. 1.2. LES of the near-field (x/d < 30) of a 70,000 Reynolds number isothermal variable-density gaseous fuel jet is performed to estimate mean turbulent length (l) and velocity (q) scales, and time-averaged ($\overline{\chi}$) and instantaneous (χ) time records of conditional-mean scalar dissipation rates. The estimated range of values of l, q and $\overline{\chi}$ are employed to select the initial vortex and flame characteristics in the studies of flame-vortex interactions. In these studies, the detailed effects of a isolated vortex-pair, representative of a turbulent eddy in the jet near-field, on the flame structure are simulated. The flame-vortex interaction studies provide insight into regimes of localized flame dynamics, such as extinction/reignition, effects due to unsteadiness and curvature in the jet near-

field, applicability of modeling approaches, such as flamelet (Peters, 1984) and flamelet/progress variable (Pierce and Moin, 2004; Pitsch and Ihme, 2005) models, and directions for the development for improved modeling approaches.
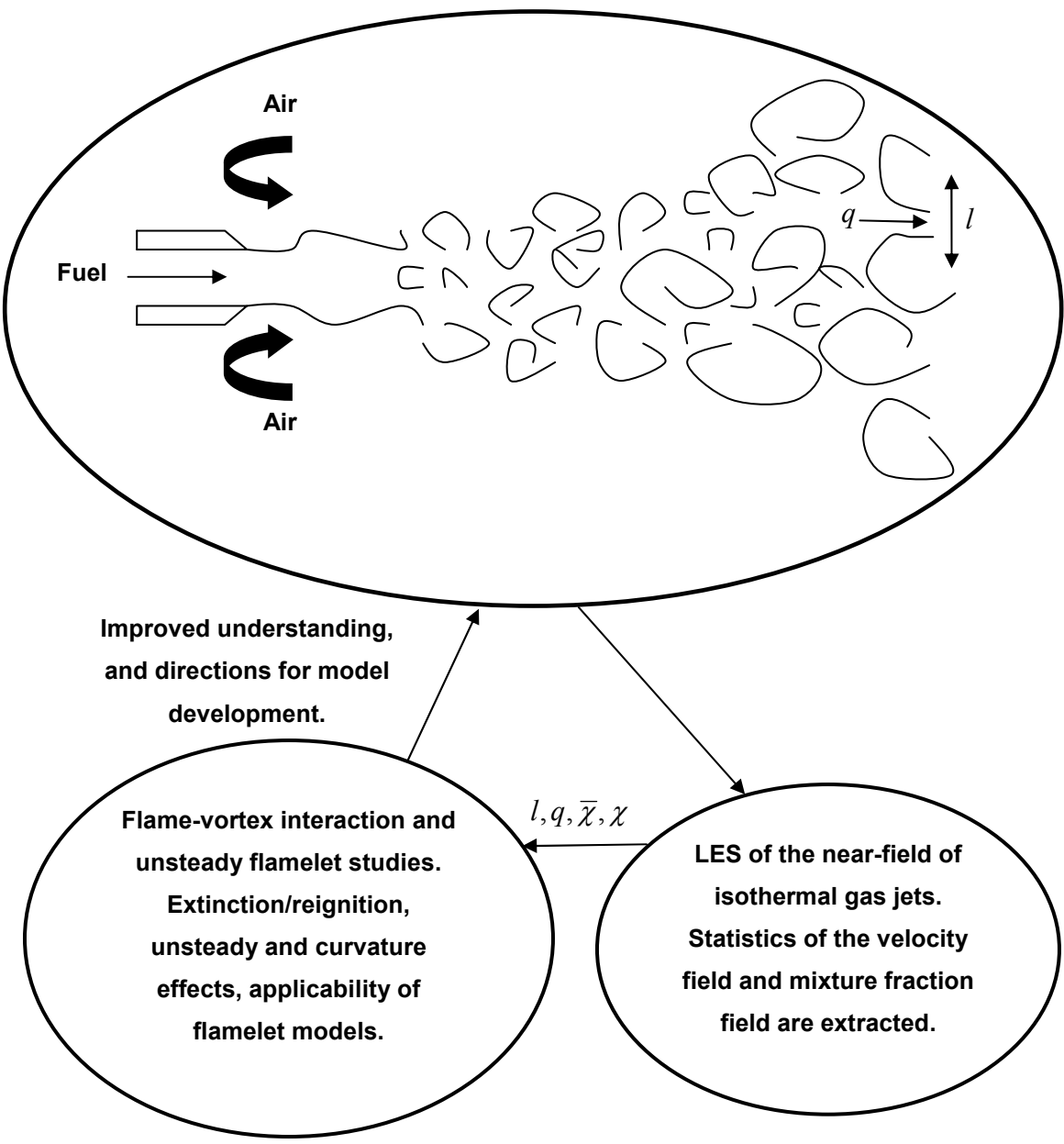
Figure 1.2. Schematic representation of the approach to investigate the near-field flame dynamics in high-Re jets.

In addition, turbulent time records of the scalar dissipation rate (χ) obtained from the unsteady LES flowfield are employed in studies of unsteady flamelets. While the flame-vortex simulations provide insight into the detailed effects due to a single turbulent eddy, the studies of flamelets subjected to χ fluctuations investigate the simultaneous effects of a spectrum of scales on the localized flame dynamics. In particular, the unsteady flamelet studies provide insight into the unsteady responses of the flame temperature, major species and pollutants to χ fluctuations, the applicability of steady flamelet models in unsteady flowfields, and the potential impact of extinction/reignition phenomena on transient and steady lift-off behavior in high-Re jets encountered in diesel applications. Through this coupled approach involving LES, and flame-vortex and unsteady flamelet studies, we seek to gain an improved understanding of the near-field jet flame structure, and the applicability of modeling approaches, such as flamelet models.

The pressures and temperatures simulated in this work are representative of diesel engine combustion chambers. In particular, the LES is performed at a jet-Re of 70,000, which is comparable to those in diesel applications (~ 100,000). The ambient gas (i.e. oxidizer) pressure is 40 bar and the temperature is 1000 K. The injected gas (i.e. fuel) temperature is1000 K and the injected-to-ambient gas density ratio is about 3.5. The flame-vortex and unsteady flamelet studies are performed with the same pressure and temperatures as the LES. These studies also span conditions corresponding to higher-Re jets (~ 400,000), and with lower fuel temperatures (~ 400 K) commonly encountered in diesel engines. The fuel chosen is n-heptane, which is a commonly employed surrogate for practical fuels like diesel. The oxidation chemistry of n-heptane is modeled using both single-step and multistep chemical kinetic mechanisms.

It is evident that the approach outlined above invokes some important assumptions, such as *isothermal* LES, *2-D* flame-vortex simulations, *single-vortex*-flame simulations, and *specific choices* for the simulated pressures and

temperatures. We will discuss these assumptions and their implications on the present findings in detail in Chapter 11.

The LES and flame-vortex interaction studies are performed with an in-house code FLEDS (Flow, Large-eddy and Direct Simulation) (Abraham and Magi, 1997; Viggiano and Magi, 2004; Anders, 2006; Anders *et al.*, 2007). FLEDS employs a sixth-order compact scheme (Lele, 1992) for spatial discretization while time-integration is achieved through a fourth-order accurate compact-storage Runge-Kutta scheme (Carnahan, 1969). Boundary conditions are implemented using the Navier-Stokes characteristic boundary conditions (NSCBC) method of Poinsot and Lele (1992), which is extended to account for multicomponent gaseous mixtures. Chemical kinetic source terms and transport properties are computed through an interface with CHEMKIN subroutines. Details on the numerical schemes and implementation are discussed in Chapter 3.

1.4. <u>Outline of the Thesis</u>

Chapter 2 of the report presents a review of prior experimental and computational work on non-premixed flame-vortex interactions and unsteady response of diffusion flames. In particular, key results from prior studies on extinction and reignition are reviewed. Since this work employs LES to estimate turbulent statistics in the near-field of jets, prior works on LES of gas jets dealing with velocity-field and passive scalar statistics are also discussed.

Chapter 3 presents the problem formulation for the LES study. The filtered governing equations are discussed along with a description of the spatial filter employed in this work. The subgrid scale model equations are presented. The implementation of boundary conditions is discussed. As part of this work, a buffer zone with artificial damping and exponential grid stretching is implemented to prevent vortical structures and spurious pressure waves at the exit outflow boundaries. Parallelization of the code and speed-up are discussed. Problem setup, initialization and simulation parameters are described.

In Chapter 4, the problem formulation for the studies of flame-vortex interactions is discussed. This includes a description of the governing equations, chemical kinetic models, and the problem setup, initialization and non-dimensional parameters governing the flame-vortex interaction.

Results from the LES computation, which form the basis for the flame-vortex interaction and unsteady flamelet studies, are discussed in Chapter 5. Computed time statistics of the velocity-field and mixture fraction field are presented and compared with available experimental data in self-similar jets. To obtain initial conditions for the flame-vortex interaction studies, mean values of turbulent length and velocity scales along with time-averaged conditional-mean scalar dissipation rates are estimated at different axial locations in the jet. In addition, turbulent time records of conditional-mean scalar dissipation rates are computed from the analysis of the unsteady LES flowfield, which are employed in studies focusing on the unsteady response of diffusion flamelets.

The results from the flame-vortex interaction studies employing a single-step kinetic model are presented in Chapters 6 and 7. The physical mechanisms for flame-vortex interaction regimes, such as extinction/reignition, for a baseline case is investigated in Chapter 6. The applicability of flamelet and flamelet/progress variable models to predict vortex-induced extinction/reignition is assessed. In Chapter 7, flame-vortex interaction studies corresponding to several locations in the LES jet near-field are discussed. Non-dimensional numbers governing unsteady and curvature effects are identified, and the nature of variation of these effects in the jet near-field are explored. The results are summarized on an outcome diagram useful to understand the nature of near-field flame dynamics in high-Re jets.

In Chapter 8, flame-vortex interaction studies employing a multistep kinetic mechanism for n-heptane oxidation are presented for a limited set of conditions obtained from the LES. The physical mechanisms for extinction/reignition are investigated, and qualitatively compared to those from the single-step model results discussed in Chapters 6 and 7. Furthermore, the unsteady response of

major products and pollutants to the vortex-induced perturbation is investigated, and the influence of unsteadiness and curvature on product/pollutant formation rates is discussed.

Chapter 9 presents results from studies of diffusion flamelets subjected to turbulent fluctuations of the scalar dissipation corresponding to the near-field of the jet simulated by LES. As a preliminary step towards the understanding of the unsteady flame response, oscillatory perturbations with specified amplitudes and frequencies are considered, The unsteady response of the flame temperature, major species and pollutants is investigated, and the applicability of steady flamelet models for the prediction of temperature and species responses is assessed. Through an extrapolation of the analysis to jets with higher global strain rates, the unsteady flame response and applicability of steady flamelets during local extinction/reignition are explored. In addition, the potential impact of extinction/reignition events on the prediction of steady lift-off heights is discussed.

The implications of the findings from the present work for practical phenomena and turbulent combustion modeling in diesel jet flames are discussed in Chapter 10. In particular, it is shown that recent experimental observations related to transient flame lift-off behavior in diesel jets can be explained in terms of unsteady effects on the localized flame dynamics. Furthermore, implications of the findings from the flame-vortex studies for turbulent combustion modeling in the near-field of diesel jets are discussed. Approaches to incorporate the improved understanding gained from the flame-vortex simulations into RANS/LES combustion sub-models are explored.

Chapter 11 presents the summary and conclusions from this work. Key assumptions invoked in this study, and their implications on the findings are discussed. Directions for future work, some of which relax the assumptions made in this work, are discussed.

CHAPTER 2. LITERATURE REVIEW

2.1. <u>Introduction</u>

As discussed in Chapter 1, this work employs a coupled approach involving the LES of a high-Re number jet, and studies of flame-vortex interactions and unsteady flamelets, to investigate the nature of localized flame dynamics in the near-field of high-Re jets. This chapter presents a review of prior works on non-premixed flame-vortex interactions, LES of jets focusing on turbulent statistics, and the unsteady response of diffusion flames. The primary focus of this work is to characterize regimes, such as local flame extinction/reignition, which are related to jet near-field phenomena, such as flame lift-off. Hence, prior findings in the literature specific to non-premixed flame extinction/reignition are reviewed.

Flame extinction has been a subject of extensive research in the combustion community for decades. Williams (2000) provides a comprehensive review of the progress made in the understanding of flamelet structure and extinction in both premixed and diffusion flames. Diffusion flame extinction can be brought about by various means, e.g., through strain, dilution or radiative losses. Strain-induced extinction occurs when the flame is subjected to a strain rate above a certain value. This concept is most easily understood by considering Fig. 2.1, which shows the classical S-curve behavior of strained diffusion flames. Here T_{max} is the maximum temperature and a is the characteristic strain rate imposed on the flame. The inverse of a may be interpreted as a characteristic mixing time. The upper branch of the S-curve represents burning solutions at low strain rates where the chemical heat release rates exceed diffusive heat losses from the flame-zone. As a increases, T_{max}

decreases and beyond a certain critical value of *a* (point Q in the figure), the flame is quenched leading to a sudden transition to the lower non-burning branch of the S curve. Conversely, ignition occurs when the strain rate decreases to a sufficient value leading to a transition from the lower non-burning branch to the upper burning branch (point I in the figure). The middle branch is an unstable one, which cannot be recovered by the solution of the steady flamelet (i.e. reactive-diffusive) equations. However, as we will clarify in Chapter 6 on the flame-vortex studies, during transient reignition following extinction, flame states in the unstable branch may be observed.
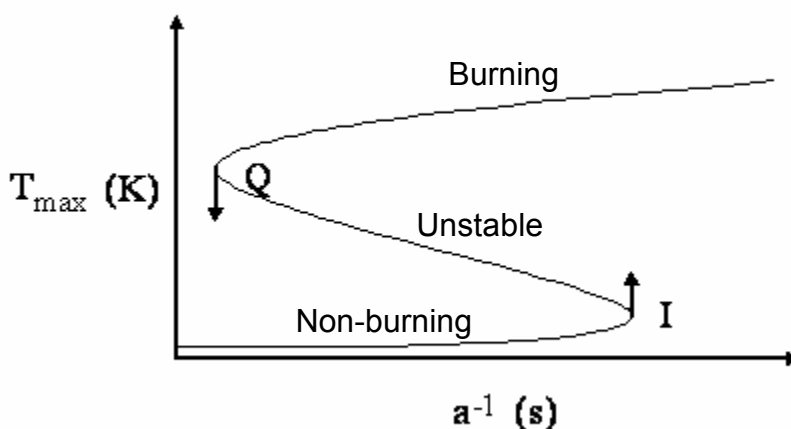
Figure 2.1. S-curve behavior of strained diffusion flames.
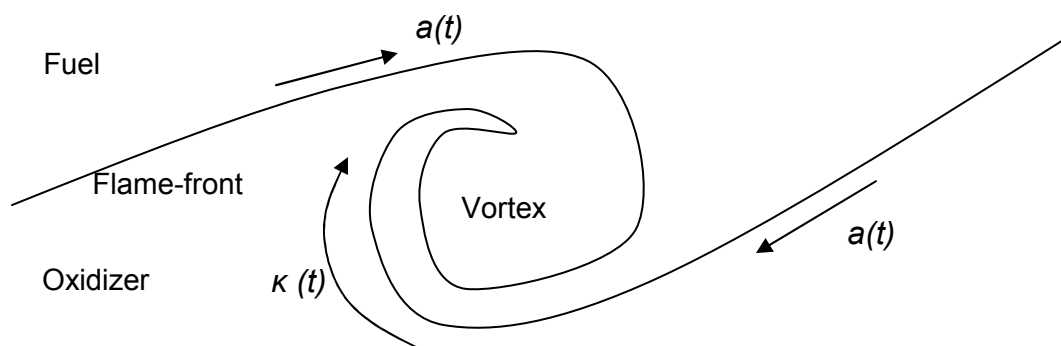
Figure 2.2. Schematic of a non-premixed flame rolled up in a vortex showing unsteadiness and curvature.

In turbulent flames, strain-induced extinction events can occur locally when strain rates become sufficiently high. A simple way to conceptualize strain-induced extinction in turbulent flames is as extinction induced by a vortex. The flame-vortex interaction represents the stretching (strain and curvature) effects of a single length-scale or a turbulent eddy on the flame structure. Figure 2.2 shows a schematic of a non-premixed flame-front rolled up by a vortex. The vortex induces an unsteady effect, represented by the time-dependent strain $a(t)$ and a curvature effect, represented by the time-dependent curvature $\kappa(t)$, on the flame response. The unsteady effect becomes important when the rate of variation of $a(t)$ becomes comparable to or greater than the chemical reaction rate. Under such conditions, the flame responds with a delay to the imposed strain. Moreover, as discussed before, the flame-front can locally extinguish if $a(t)$ exceeds a critical value. The vortex-induced curvature $\kappa(t)$ causes 2-D effects and thickening of the flame-front. Hence, the flame-vortex setup is useful to study the effects due to unsteadiness and curvature on the flame structure. In the section that follows, we will review prior experimental and computational works on vortex-induced flame extinction, which corresponds to flame extinction in unsteady flowfields.

Recent DNS studies of jet diffusion flames in the near-field (Pantano, 2004; Hawkes *et al.*, 2007) have shown that following local extinction, reignition events can occur when extinguished regions transition to a burning state. DNS of diffusion flames evolving in isotropic turbulence (Sripakagorn *et al.*, 2004) has shown that such reignition phenomena may occur as an independent flamelet scenario, which is similar to autoignition shown in Fig. 2.1 (i.e. transition from point I to the burning branch), or through 2-D and 3-D interactions with neighboring burning regions. A detailed understanding of such interactions between burning and non-burning regions following extinction is still lacking. In Section 2.3, we will review some of the recent studies related to reignition in both flame-vortex interactions and other configurations such as isotropic decaying turbulence and jet flames.

Section 2.4 reviews prior works related to the unsteady response of diffusion flames. In Section 2.5, an overview of large-eddy simulation (LES) and subgrid scale modeling is presented. Prior works on LES of non-reacting jets dealing with both velocity field and passive scalar (mixture fraction) statistics are reviewed. The chapter closes with a summary in Section 2.6.

2.2. Extinction in Non-premixed Flame-Vortex Interactions

The dynamics of flames interacting with vortices is a problem of both fundamental and practical interest. From a fundamental viewpoint, a flame-vortex interaction typifies the effects of unsteadiness and curvature on the flame structure, whereas from a practical perspective much of the combustion dynamics in devices like diesel engines and gas turbines occurs in localized reacting shear layers rolled-up in vortices. In addition, the configurational simplicity of a flame-vortex problem allows precise experimentation and detailed numerical investigation through DNS. Such detailed simulations are useful in verifying standard approaches to turbulent combustion modeling and to construct sub-models for turbulence-chemistry interaction. Renard *et al.* (2000) provide a comprehensive review of flame-vortex studies relevant to both premixed and non-premixed flames.

Figures 2.3 (a) and (b) show two commonly employed configurations in studies of non-premixed flame-vortex interactions. When a vortex interacts with a non-premixed flame, several outcomes may be observed such as rollup, straining, wrinkling, dissipation, extinction, partial-premixing and reignition. The majority of the earlier studies on flame-vortex interactions was analytical (Marble, 1985; Karagozian and Marble, 1986) and focused on the enhancement of the rate of fuel consumption due to vortex-induced rollup and straining. The infinitely fast chemistry assumption was employed in these studies and the configuration of a single vortex centered on a diffusion flame (Fig. 2.3(a)) was used. The trends observed in the analytical studies were confirmed by numerical studies,

such as those of Laverdant and Candel (1988) and Ashurst (1989). In addition, the configuration shown in Fig. 2.3(a) has been employed in the numerical studies of Thevenin and Candel (1995) on autoignition in a mixing layer rolled up by a single vortex. It was found that two ignition modes could exist depending on the initial oxidizer temperature and the initial vortex Reynolds number. For high initial temperatures and large values of the Reynolds number, ignition occurred in a premixed-mode in the well-mixed vortex cores while the strain rates in the vortex braids were high enough to prevent ignition. On the other hand, for low initial temperatures and small values of the Reynolds number, ignition occurred in a non-premixed mode in the vortex braids since the vortex cores did not reach a sufficient temperature for ignition.
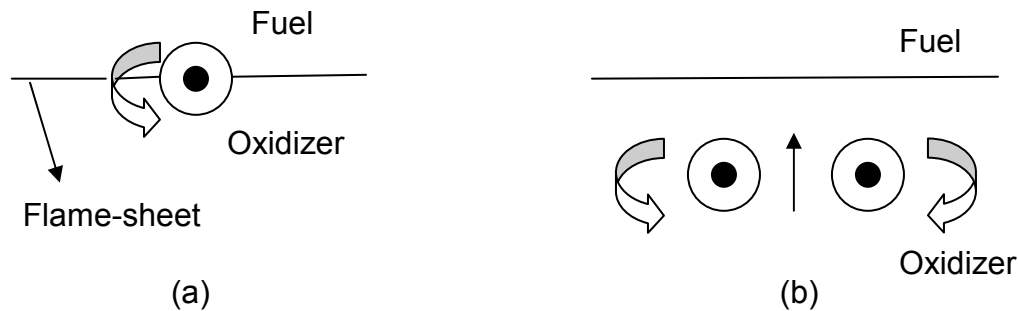
Figure 2.3. Commonly employed configurations for non-premixed flame-vortex interactions; (a) vortex centered on the flame, and (b) counter-rotating vortex-pair allowed to impinge on the flame.

More recently, experimental and computational studies on vortex-induced flame extinction have been performed. The configuration shown in Fig. 2.3(b) is particularly suitable for extinction studies where the vortex-pair is allowed to self-propagate and impinge on the initially-flat diffusion flame. The head-on interaction can then lead to the local disruption of the flame front. This configuration can be generated experimentally in rollup burners, such as those employed in the studies of Thevenin *et al.* (1998), Renard *et al.* (1999) and Santoro *et al.* (2000a) to investigate regimes of flame-vortex interactions.

Thevenin *et al.* (1998) investigated extinction processes in a non-premixed flame-vortex interaction through measurements in a rollup burner. A counterflow diffusion flame with hydrogen diluted with nitrogen on one side and air on the other side was established. Toroidal vortex rings were injected from the air-side and allowed to impinge on the diffusion flame. Effects of the initial vortex velocity, u_v, and the global mixture ratio, Φ_g, were investigated. Φ_g was defined as the ratio between initial mass fraction of fuel on the fuel-side and initial mass fraction of oxygen on the air-side divided by corresponding values for stoichiometric combustion. OH planar-laser-induced-fluorescence (PLIF) was used to detect the presence of the flame.
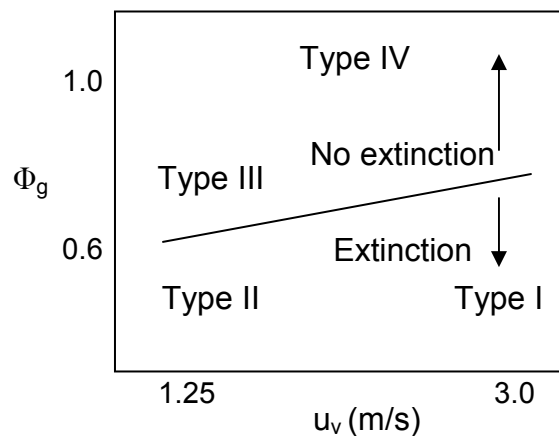
Figure 2.4. Schematic representation of interaction regimes observed by Thevenin *et al.* (1998).

Four interaction regimes were identified across the range of Φ_g and u_v considered. For a very low Φ_g but relatively large values of u_v, global extinction of the flame was observed, which was classified as a type-I interaction. Increasing Φ_g or decreasing u_v lead to a second type of interaction (type –II) where only local extinction of the flame front was observed. For relatively large values of Φ_g and the slowest vortex considered, the flame did not extinguish and but significant rollup and elongation of the flame was observed (type-III). For the

highest Φ_g explored, there was no extinction but the left and right parts of the elongated flame were found to re-connect (type-IV). The measured extinction strain rates were found to be somewhat higher than those estimated from a steady-state asymptotic analysis, which assumes a flame-sheet with infinitely-fast chemistry. The reasonable agreement of the measured results with asymptotics was justified by the absence of significant unsteady effects. In other words, the characteristic reaction time-scales for the flames were shorter than the convective time-scales of the vortices and the flames responded almost immediately to the imposed strain. Consequently, the values of Φ_g and u_v delineating extinction and no-extinction regimes were predicted reasonably well by asymptotics. Fig. 2.4 schematically depicts the interaction diagram proposed by Thevenin *et al.* (1998).

(a)   (b)
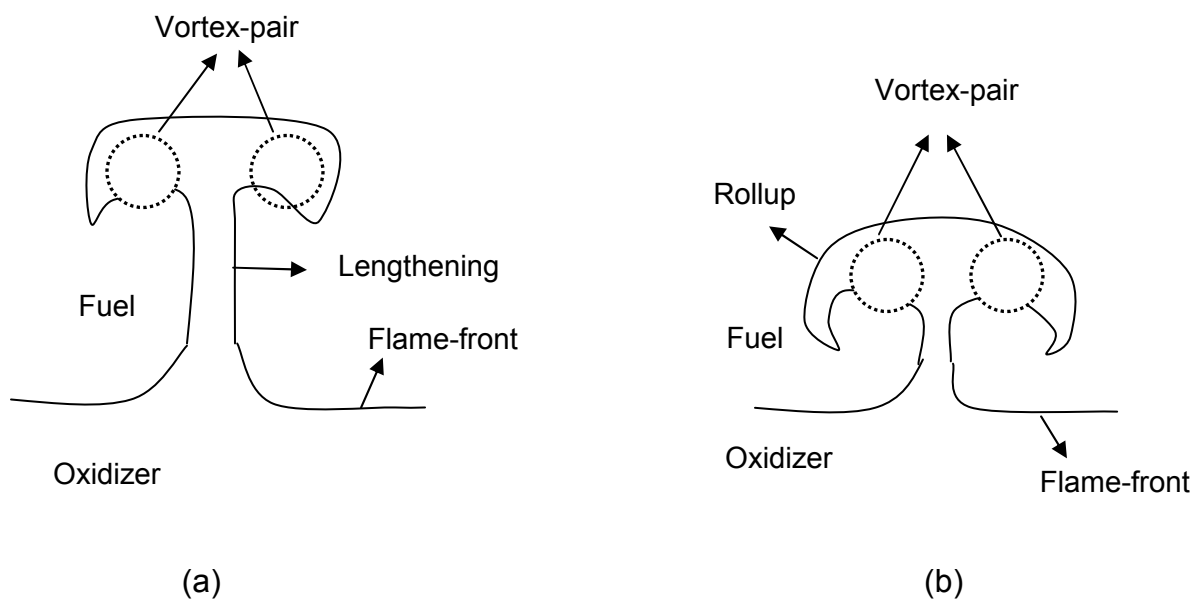
Figure 2.5. Schematic of the flame-vortex interaction outcomes observed by Renard *et al.* (1999) for a (a) fast vortex and (b) slow vortex.

Renard *et al.* (1999) investigated heat-release, extinction and time evolution of the flame surface area during non-premixed flame-vortex interactions

in a similar configuration. It was found that the increase in flame surface area due to the interaction not only depends on u_v, but also on the residence time. Figs. 2.5 (a) and (b) schematically show the flame-vortex interaction outcomes in the experiments of Renard *et al.* (1999) for a fast vortex and a slow vortex, respectively. As seen from the figures, while a fast vortex stretched a flame by lengthening, a slow vortex caused stretching due to rollup. From 2-D DNS computations with multi-step H_2/air chemistry using a similar setup as the experiments, it was shown that the time evolution of the heat release rate and the maximum OH concentration correlated well with each other. Hence, local extinction was detected by a fall in the maximum OH concentration to within 10% of its initial value. OH PLIF images were also employed to compute the flame surface area.

A wider range of vortex length and velocity scales were explored by Thevenin *et al.* (2000) through experiments on diluted H_2/air flames. Eight interaction regimes were identified and characterized by the relative importance of various competing physical phenomena such as dissipation, straining, curvature, wrinkling, rollup and extinction. For relatively small vortex-to-flame length-scale ratios, the vortices were too weak to have a significant impact on the flame while with relatively large length-scale ratios, wrinkling and roll-up were found to be important. For sufficiently high vortex-to-flame velocity-scale ratios, unsteady effects and extinction were observed. In certain cases with relatively large length-scale ratios and moderate velocity-scale ratios, formation of an oxidizer pocket burning on the fuel-side was observed. The limits delineating the various interaction regimes were expressed in terms of the Damkőhler number.

A flame-vortex interaction problem can be employed to assess the accuracy of standard modeling approaches for turbulent combustion. An example of this is the 2-D DNS study of Cuenot and Poinsot (1994) where the range of applicability of the steady-laminar-flamelet approximation (SLFA) was determined. According to the SLFA, the flame structure is essentially 1-D depending only on the mixture fraction and the scalar dissipation rate. The scalar

dissipation rate χ is a measure of the local mixing rate experienced by the flame and can be shown to be proportional to the imposed strain rate (Peters, 1984). In addition, the flame is assumed to respond to changes in χ instantaneously and unsteady effects are ignored.

In the study of Cuenot and Poinsot (1994), the impingement event of a 2-D counter-rotating vortex-pair on initially-flat diffusion flame (see Fig. 2.2(b)) was simulated. Single-step idealized chemistry was employed. Cuenot and Poinsot (1994) compared DNS predictions of temperature response to χ with an asymptotic flamelet library based on the SLFA. This comparison showed that for relatively slow vortices larger than a certain size, the SLFA predictions agreed well with the DNS results. However, as the vortex velocity was increased, unsteady effects became dominant leading to deviations of the SLFA results from the DNS data. Similarly, as the vortex size was decreased, curvature effects were observed leading to disagreement between the SLFA and the DNS predictions. However, for vortices small enough to cause curvature effects, the vortex velocity had to be increased to prevent viscous dissipation. Moreover, since the SLFA ignores both unsteady and curvature effects, disagreement between the SLFA and the DNS predictions could in general result from both the effects. Hence, in the study of Cuenot and Poinsot (1994), unsteady effects and curvature effects could not be separated. The limits of applicability of the SLFA were expressed in terms of the Damkőhler number (Da) based on the vortex time-scale and the chemical time-scale. An important observation from their work was that unsteady effects became significant prior to extinction implying that the SLFA ceases to apply even before extinction occurs. In other words, if Da_e represents the critical Da below which extinction occurs and Da_{SLFA} represents the critical Da below which SLFA ceases to apply i.e. unsteady effects become important, then $Da_e < Da_{SLFA}$. The 2-D DNS results were represented on a regime diagram with the vortex-to-flame velocity-scale ratio and the vortex-to-flame length-scale ratio as axes.

In the recent past, unsteady extinction processes during flame-vortex interactions have received attention. Santoro *et al.* (2000a) explored vortex-induced extinction behavior in gaseous methanol counterflow diffusion flames experimentally. The vortex ring was generated on the oxidizer-side and allowed to impinge on the flame. Formaldehyde (HCHO) PLIF was used to detect local extinction. Extinction strain rates measured were almost twice those of steady limits. To rationalize this observation, Santoro *et al.* (2000a) proposed a two-layer model for the flame-vortex interaction region. The interaction region was characterized in terms of an outer convective-diffusive layer and an inner reactive-diffusive layer. The relevant characteristic time-scales in the outer layer are the mixing time-scale τ_m, proportional to the inverse of the initial strain rate imposed by the counterflow on the flame and the initial vortex turnover time, τ_v. In the inner layer, the relevant time-scales are τ_v and the characteristic chemical time τ_c. For the conditions explored, it was found that $\tau_c < \tau_v < \tau_m$. As a result, the vortex caused unsteady effects in the outer convective-diffusive layer but the inner reactive-diffusive layer behaved in a quasi-steady manner since $\tau_c < \tau_v$. Using a simple analytical model that invoked the constant-density approximation, an expression for the effective scalar dissipation rate experienced by the flame was obtained in terms of the time-dependent strain rate imposed by the vortex. It was shown that the maximum scalar dissipation rate is lower than the peak instantaneous strain rate and a delay exists between the changes in the strain rate and the scalar dissipation rate. Consequently, in terms of the effective scalar dissipation rate, the vortex-induced extinction limit was only about 30 % greater than the quasi-steady limit.

More recently, Oh *et al.* (2004) investigated vortex-induced extinction behavior of diluted methane-air counterflow flames numerically using multi-step reduced kinetic models for methane oxidation. To reduce the computational cost, an augmented reaction mechanism (ARM) derived from the comprehensive Miller-Bowman (MB) mechanism (Miller and Bowman, 1989) for methane

combustion was employed. An ARM is essentially a revised type of reduced reaction mechanism (RRM) where certain number of reactions in the RRM may be lumped to reduce the total number of reactions. The ARM employed by Oh *et al.* (2004) comprised 17 reaction steps among 21 species. Comparisons of steady extinction limits predicted by the ARM showed good agreement with experiments and the MB mechanism. In addition, the unsteady response of the flame to sinusoidal variations in the scalar dissipation rate was found to be similar for the ARM and the MB mechanism.

Flame-vortex simulations were performed with the ARM using the configuration shown in Fig. 2.3(b). Vortices were released from both the fuel and air sides. It was found that for the conditions explored, unsteady scalar dissipation rates at extinction were 3-4 times the steady extinction limit. Using an analysis similar to that of Santoro *et al.* (2000a), order of magnitude estimates of τ_m, τ_v and τ_c were obtained. For the conditions of Oh *et al.* (2004), τ_v was shorter than both τ_m and τ_c implying that both the outer convective-diffusive layer and the inner reactive-diffusive layer in the flame-vortex interaction region were unsteady. This in turn reflected in the relatively large value of the unsteady extinction limit. Moreover, the air-side vortex was found to cause a more rapid extinction of the flame than the fuel-side vortex. In the computations of Oh *et al.* (2004), the methane flame was located on the air-side of the stagnation plane and hence the air-side vortex interacts with the flame earlier relative to the fuel-side vortex. Interaction of the air-side vortex with the flame resulted in its intensification due to enhanced convective transport of vorticity. This in turn resulted in higher strain rates on the flame leading to earlier extinction in the case of the air-side vortex.

As indicated in Section 2.1, local extinction may be followed by reignition events. In recent years, there has been a growing interest in reignition phenomena; both computational and experimental studies have been carried out.

In the section that follows, the reignition processes are discussed and key conclusions from prior works presented.

2.3. <u>Reignition</u>

In turbulent reacting flows, the instantaneous scalar dissipation rate χ is a strongly fluctuating variable (Pitsch, 2006). This implies that we may encounter repeated excursions of χ above and below the steady extinction limit χ_e. As discussed in Section 2.2, values of χ equal to or higher than χ_e can lead to local extinction and destruction of the flame surface. Following extinction, if the value of χ remains below χ_e for a sufficient amount of time allowing the fuel and oxidizer to mix through diffusion, the extinguished regions can reignite leading to the creation of flame surface. This process may be understood as a transition from the point I in the lower branch of the S-curve shown in Fig. 2.1 to the burning upper branch of the curve. However, DNS studies have shown that reignition of the extinguished regions can also depend on the presence of adjacent burning regions. In this section, we will first discuss some of the possible mechanisms for reignition which have been proposed from recent DNS studies and then review some of the prior works on reignition in non-premixed flame-vortex interactions.

The mechanism of reignition is closely related to the evolution of the flame structure after local extinction. Due to the local disruption of the flame front, we encounter extremities of diffusion flames which border a quenched location. The extremity of a diffusion flame adjacent to a quenched location is termed as a "flame-edge" or simply, an "edge-flame" (Buckmaster, 2002). The schematic in Fig. 2.6 shows edge flames formed after local extinction which border extinguished regions. The dynamics of these edge flames plays a decisive role in the mechanisms of reignition of the extinguished regions. Buckmaster (2002) provides a comprehensive review of the characteristics of edge flames. Even though edge-flame dynamics is a fairly well-researched topic, its importance in

reignition phenomena has received attention only recently (Hewson and Kirstein, 2002; Pantano, 2004; Sripakagorn *et al.*, 2004).
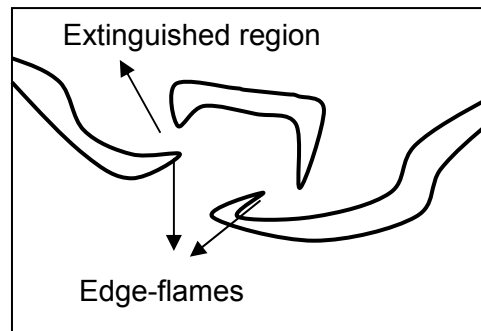
Figure 2.6. Schematic representation of edge-flames formed after local extinction.

To understand the characteristics of edge-flames, consider Figs. 2.7(a)-(c), which schematically show the three different configurations of an edge-flame, depending on the conditions which exist in the adjoining extinguished region. In Figs. 2.7(a)-(c), u is the local flow velocity, u_{EF} is the edge-flame velocity relative to the extinguished mixture and u_{LF} is the resultant edge-flame velocity relative to the laboratory frame. In the extinction mode (Fig. 2.7(a)), an edge-flame recedes away from the extinguished region and leads to the widening of the extinction-hole. In other words, reignition does not occur. The extinction front has a negative displacement speed (away from the extinction-hole) under these conditions. In the propagating ignition mode (Fig. 2.7(b)), the edge-flame displays a positive displacement speed towards the extinguished region and leads to reignition. The edge-flame can also assume a standing triple-flame structure (Fig. 2.7(c)) when u and u_{EF} become equal in magnitude. The triple-flame structure has a lean-premixed branch and a rich-premixed branch which connect at the triple-point. As shown in Fig. 2.7(c), excess fuel from the rich branch and excess oxidizer from the lean branch burn out in a trailing diffusion flame.
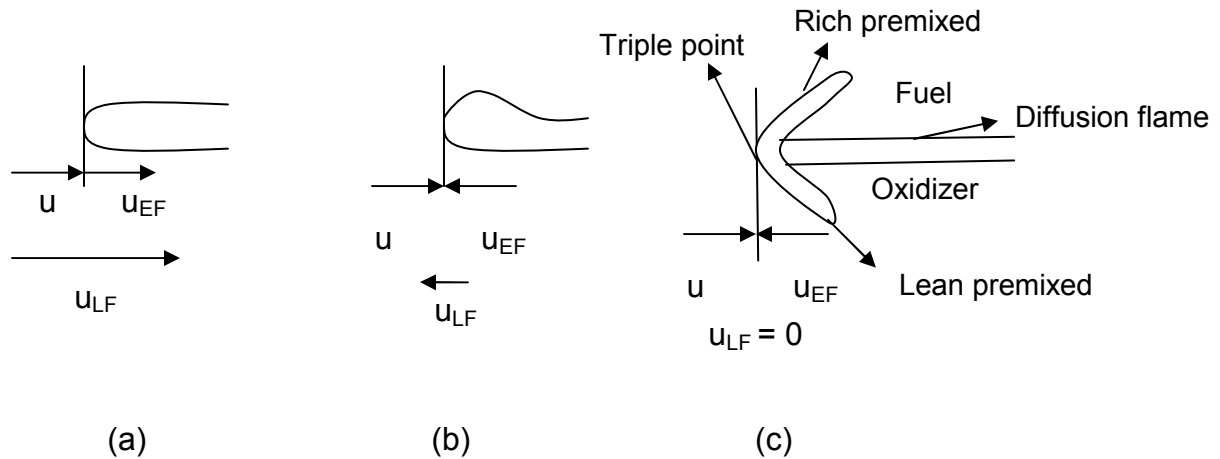
Figure 2.7. Edge-flame configurations, (a) extinction front, (b) ignition front and (c) standing triple-flame.

Edge flames have been investigated to a significant extent through theoretical studies employing activation energy asymptotics (Dold, 1988; Buckmaster, 1996; Daou and Linan, 1998; Ghosal and Versvisch, 2000), numerical studies with simplified (Reutsch *et al.*, 1995) and detailed chemistry (Echekki and Chen, 1998; Im and Chen, 1999; Amantini *et al.*, 2006) and experiments (Philips, 1967; Ko and Chung, 1999; Santoro *et al.*, 2000b). From these studies, it is now understood that the structure of edge flames depends on various parameters such as the Damkőhler number (Da), the Lewis number of the fuel and the ratio of unburned to burned gas density. For values of Da larger than the extinction Damkőhler number Da_e in the adjoining extinguished region, the edge-flame behaves as an ignition front and propagates with a positive displacement speed towards the extinction-hole. An ignition front could have a triple-flame structure for small values of Da but the premixed branches collapse to form a simple edge for intermediate values of Da. However, as Da decreases to values close to Da_e, the edge displacement speed becomes negative transforming the edge into an extinction front.

Santoro *et al.* (2000b) measured propagation rates of edge-flames in counterflow mixing layers. A theoretical framework was also developed using a

thermal diffusive model with constant density and transport properties. It was shown that the scalar dissipation rate and the Da attained a maximum at the center of the stagnation plane and decreased at radial distances away from the center. Consequently, an extinction front was formed bordering the extinction-hole at the center which was found to recede away from the hole. However, at a certain radial distance away from the center, the Da became large enough to transform the extinction front to a propagating edge which eventually stabilized as a triple-flame. Fig. 2.8 shows a schematic representation of the measured results of Santoro *et al.* (2000b). In Fig. 2.8, the edge-speed u_{EF} is normalized by the premixed laminar flame speed u_L. As discussed before, the edge-flame speed rapidly falls as the Da falls close to the extinction value. In the experiments, the propagating edge-flame speed was roughly 2.6 times the laminar flame speed. This ratio scaled with the square root of the unburned to burned gas density ratio, in agreement with the numerical studies of Ruetsch *et al.* (1995). Further details on the structure of edge and triple-flames may be found in Buckmaster (2002) and the references therein.
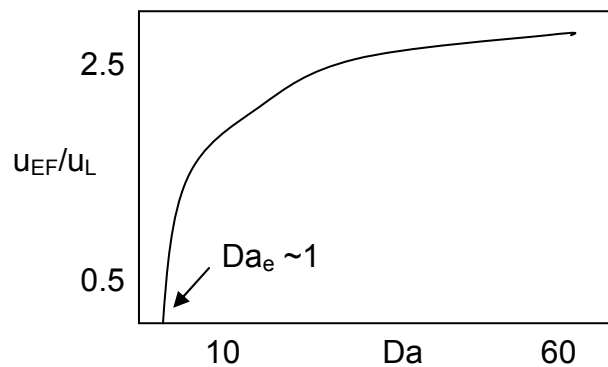
Figure 2.8. Edge-flame speed vs. Da (Santoro *et al.*, 2000b).

The importance of edge-flames in reignition phenomena has been demonstrated in recent DNS studies of jet flames (Pantano, 2004) and diffusion flames evolving in isotropic decaying turbulence (Sripakagorn *et al.*, 2004). Pantano (2004) performed a massively parallel 3-D DNS with approximately 100

million grid points of a combusting methane plane jet in the near-field. The jet exit Reynolds number was relatively low, about 3000 and a 4-step reduced kinetic model for methane combustion (Peters, 1985) was employed. For the parameters chosen for the simulation, local extinction and reignition in the jet were observed. The locations of the flame-edges were identified by the intersections of the isosurfaces of the hydrogen (H) radical with the isosurfaces of the stoichiometric mixture fraction. Flame-edge statistics in the form of joint PDFs of the edge-speed and the instantaneous scalar dissipation rate were computed. The peaks of the joint PDFs were found to occur at the theoretical edge-flame speed (Reutsch *et al.*, 1995), equal to $\left(\sqrt{\rho_{ub}/\rho_b}\right)*u_L$, where ρ_{ub} and ρ_b are the unburned and burned gas densities, respectively, at values of the scalar dissipation rate χ lower than the extinction limit χ_e. However, considerable broadening of the joint PDFs was observed due to unsteady effects. Negative edge-flame speeds were observed for values of χ larger than χ_e.

Sripakagorn *et al.* (2004) performed 3-D DNS of a diffusion flame evolving in isotropic decaying turbulence to simulate extinction and reignition. Single-step idealized chemistry was employed and the thermal diffusive approximation with constant density and transport properties was invoked. Three types of reignition scenarios were identified: an independent flamelet scenario, reignition due to propagation of edge-flames and a third scenario involving engulfment of the extinguished region by a hot neighborhood. The independent flamelet scenario was observed when the excursions of χ above χ_e were relatively small and short-lived. In such cases, the extinguished flamelets reignited without substantial interactions with the neighboring burning flamelets.

However, when the excursions of χ above χ_e were large and lasted for a long time, reignition occurred under the influence of the adjacent burning regions. In particular, two modes of reignition were observed. In the first one, reignition occurred through propagation of edge-flames as ignition fronts towards the

extinguished regions. This was termed as the 'edge-flame propagation' scenario. In the second mode, reignition occurred through turbulent convection of hot gases into the quenched regions. Sripakagorn *et al.* (2004) termed this mode as the 'engulfment' scenario. The classical 1-D flamelet model (Peters, 1984) which ignores interactions between adjacent flamelets failed to predict the edge-flame propagation and engulfment scenarios for reignition. As discussed in the modeling studies of Hewson and Kirstein (2002) on extinction and reignition in jet flames, the edge-flame propagation and engulfment scenarios can be differentiated by the direction of heat transfer from the edge-flames to the extinguished regions.
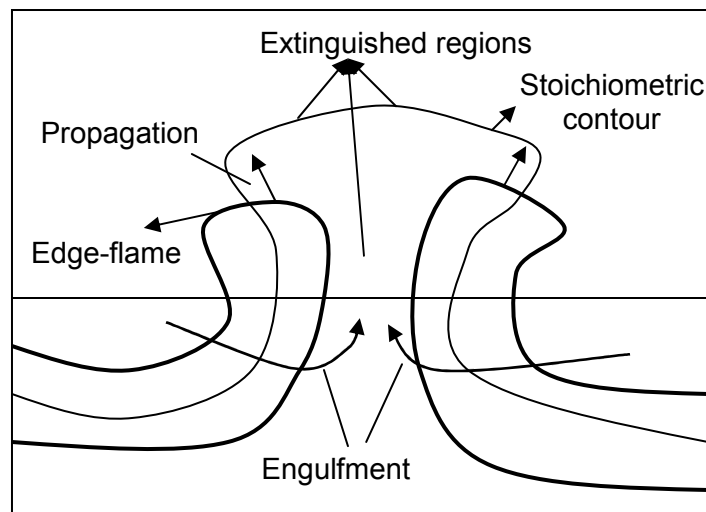
Figure 2.9. Schematic representation of the edge-flame propagation and engulfment scenarios for reignition.

To clarify this, consider Fig. 2.9 which shows a schematic representation of reignition by the two modes. As shown in the figure, heat transfer from the edge flames occurs along the stoichiometric isocontour for the propagation scenario while heat is transferred perpendicular to the stoichiometric contour for the engulfment scenario. Sripakagorn *et al.* (2004) computed the fraction of extinguished flamelets which reignite through the three modes. It was found that the majority of the flamelets reignited through the edge-flame propagation and

engulfment scenarios; propagation being the most dominant mode of reignition. Moreover, the results showed that reignition is relatively slow as compared to extinction. Due to the complexity of the simulated turbulent flowfield in the work of Sripakagorn *et al.* (2004), the effects of individual length-scales and the associated curvature effects on the reignition behavior could not be isolated. The flame-vortex setup employed in the present work is particularly suitable to explore these aspects.

Reignition has received attention, to a limited extent, through experimental and computational studies of flame-vortex interactions. As discussed before, the flame-vortex setup allows detailed investigation of effects due to unsteadiness, curvature and chemical kinetics on the flame structure. Santoro *et al.* (2002) performed experiments on diluted methanol spray counterflow diffusion flames with vortices injected from both the fuel and oxidizer sides. Based on the overall stoichiometry, the flame was located on the fuel-side. The fuel droplets were found to completely vaporize before reaching the flame. Local extinction followed by reignition was observed for the range of vortex circulations employed. The robustness of the spray flame to vortex-induced extinction was compared to that of a gaseous flame. The comparison showed that the spray flame was relatively weaker than the gaseous flame and extinguished at lower vortex circulations. This inherent weakness of the spray flame relative to the gaseous flame was attributed to the additional heat loss due to the latent heat of vaporization of the fuel droplets. Since the flame was located on the fuel-side of the stagnation plane, vortices injected from the air-side had to pass through the stagnation plane prior to interaction with the flame. Consequently, the air-side vortices were considerably weakened due to stretching at the stagnation plane and were much less effective in causing extinction than the fuel-side vortices. Following extinction, an annular extinction-hole was formed at the center which was bordered by two flame-edges on either side of the vertical centerline. Subsequently, the extinction-hole was healed by the propagation of the edge-flames. When the vortices approached the flame from the oxidizer-side, the

reignition time was found to be significantly different for the spray and gaseous flames. The spray flames required more time to reignite following extinction. This observation was attributed to the fact that in the case of spray flames, the fuel droplets in the extinguished region were displaced from the centerline by the air-side vortex. This fuel-depletion effect increased the time required for reignition to occur for the spray flames. On the hand, the differences in reignition times between spray and gaseous flames were minimal for fuel-side vortices since the availability of the fuel droplets in the reigniting region was not affected due to the vortex-induced flow.

Recently, Herrmanns *et al.* (2007) computationally investigated the dynamics of flame-edges formed by the local extinction of non-premixed flame-sheets in counterflow mixing layers by axisymmetric vortex rings. A mathematical model which employed the constant density approximation was employed. The evolution of the velocity-field, derived from potential flow theory, was obtained by superimposing the axisymmetric velocity-field due to the vortex ring on the unperturbed strained flow in the mixing layer. The evolution of the mixture fraction Z was obtained by integrating a transport equation for Z derived with the assumptions of constant density and constant transport properties. The location of the flame-sheet was determined by the location of the stoichiometric surface. The flame-edges were presumed to propagate with a well-defined velocity which was expressed as a function of the local Damkőhler number. The flame-vortex ring interaction was described in terms of four non-dimensional numbers based on the flame and vortex characteristics: a Peclet number for the unperturbed flow, a flame-robustness parameter indicating how far the initial flame is from extinction, the overall air-to-fuel stoichiometric ratio, and a non-dimensional vortex circulation. Despite the simplicity of the model, good qualitative agreement was reported with experimental visualization. The model results showed that for the case of strong vortices interacting with robust flames, i.e., flames initially far from extinction, axial extinction followed by reignition occurred. Moreover, the dynamics of the flame-edges were predominantly controlled by the vortex-

induced convective velocities and much less dependent on the robustness of the flame. However, for the case of weak flames interacting with weak vortices, as in the case of the experiments of Santoro *et al.* (2002), the model predictions did not agree well with the experimental visualization. This disagreement was attributed to failure of the constant property model to describe the dissipation of the relatively weak vortex due to contact with hot gases in the flame. Moreover, phenomena such as focusing of the edge-flames due to the vortex-induced flow which can lead to mutual annihilation events during reignition could not be captured by the model. Evidence of such mutual interactions between edge-flames during reignition will be shown in the present work.

Experimental and computational studies on extinction and reignition have also been reported in a double-vortex-flame configuration. The experiments (Amantini *et al.*, 2005), which were performed on gaseous methanol-air counterflow flames subjected to two impinging counter-rotating vortices from the fuel and air sides, showed that following local extinction, the resulting flame-edges are initially advected away from the extinction-hole due to vortex-induced radial velocities but subsequently propagate towards the hole leading to reignition. Similar trends were observed by Yoo and Im (2005), who performed a 2-D DNS study on a similar configuration with H_2/air flames. The edge-displacement speed was found to be negative in the initial phase of reignition for a limited duration due to enthalpy loss in the transverse direction in the presence of large strain. Early transient effects were found to be significant in the determination of the edge-flame speed.

It is important to note that the flame-vortex interaction studies provide insight into the detailed effects of a single turbulent eddy on the local flame structure. However, flamelets in the near-field of the jet are likely to encounter a spectrum of turbulent scales. Hence, in order to gain insight into the simultaneous effects due to a spectrum of scales, we perform studies of unsteady flamelets (Chapter 9) subjected to scalar dissipation rate (χ) fluctuations. These fluctuations are obtained as turbulent time records generated

from the analysis of the unsteady flowfield of the 70,000 Reynolds jet computed using LES. In the section that follows, we briefly review prior works focusing on the unsteady response of diffusion flames to temporal variations in the strain rate.

2.4. <u>Unsteady Response of Diffusion Flames</u>

The effect of flow unsteadiness on the structure of counterflow diffusion flames has received considerable attention in the last two decades (Im *et al.*, 1995; Egolfopoulos and Campbell, 1996; Kistler *et al.*, 1998; Im *et al.*, 1999; Welle *et al.*, 2003). These studies have been carried out by imposing oscillatory strain rates on the flames. Two major conclusions from these studies are: a) at high frequencies of the imposed perturbation, the flame becomes relatively insensitive due to increased phase lag, and (b) this insensitivity may lead to extinction strain rates higher than steady limits.

Egolfopoulos and Campbell(1996) performed numerical investigations of counterflow methane-air flames subject to velocity and fuel mass fraction oscillations at the nozzle exits. It was shown that the phase lag associated with the flame response at high frequencies results from the attenuation of the oscillations imposed in the outer convective layer, by diffusion in the inner diffusive-reactive layer. In other words, the unsteady response of diffusion flames is diffusion-limited. In another numerical study involving counterflow methane-air flames, Im *et al.(*1999) investigated the chemical response of species including pollutants like carbon monoxide (CO) and nitrogen oxides (NOx) to oscillating strain rate under conditions far from extinction. Their studies showed that owing to relatively slow characteristic chemical time-scales, the response of CO and NOx is weak at high frequencies. Furthermore, the authors showed that the scalar dissipation rate (χ) is a more appropriate parameter to characterize unsteady flames than the strain rate, since χ accounts for the diffusion-limited flame response. In this context, the studies reported in the present work in

Chapter 9 employ the flamelet formulation, where χ directly appears as a parameter incorporating the effects due to flow-unsteadiness. Note that in addition to the numerical works discussed above, recent experiments (Welle *et al.*, 2003) on propane-air diffusion flames have also confirmed the diffusion-limited frequency response of diffusion flames to strain rate oscillations, resulting in an increased lag at high frequencies.

Oscillatory perturbation studies have also focused on unsteady flame extinction. For instance, Im *et al.* (1995) compared the unsteady response of near-extinction flames and flames in the Burke-Schumann limit, i.e. infinitely fast chemistry. Near-extinction flames were shown to be more sensitive to flow-unsteadiness, and the heat-release rate response of these flames exhibited a phase-lag to the imposed strain rate oscillation. Unsteady extinction in counterflow hydrogen/air flames in the presence of sinusoidal strain was studied numerically and experimentally by Kistler *et al.* (1998) These studies showed that for strongly burning flames, i.e. flames initially far from extinction, the unsteady extinction strain rates increasingly deviate from steady values at relatively high frequencies, due to the delayed response of the flames. Note that some of the findings discussed above, such as the distinction between unsteady and steady extinction limits, were reviewed in the context of the flame-vortex interactions as well in the previous section. Essentially, the vortex may be thought of as a strain rate perturbation on the flame with a time-dependent amplitude and frequency that are related to the length and velocity scales of the vortex.

In Chapter 9, we will investigate the response of diffusion flamelets to turbulent fluctuations of the scalar dissipation rate. As a preliminary step towards the understanding of the unsteady flame response, we will consider oscillatory perturbations similar to the studies reviewed above. In addition to unsteady extinction, we will clarify the effects of unsteadiness on reignition, which has not received attention in the literature so far. Furthermore, while the studies reviewed above investigated simpler fuels like methane, we will focus on n-heptane, which is a commonly employed surrogate for practical fuels like diesel. The unsteady

response of the flame temperature, major species and pollutants during extinction/reignition is investigated, and the applicability of steady flamelets in unsteady flowfields is assessed.

In the next section, an overview of the LES methodology and subgrid scale modeling is presented. Key results from some of the prior LES studies focusing on velocity-field and passive scalar statistics are discussed.

<div style="text-align:center">

2.5. <u>Large-eddy Simulation of Jets</u>

</div>

Large-eddy simulation (LES) has emerged as an important research tool in recent years. LES is increasingly being applied to a variety of complex flows with unsteadiness, streamline curvature, recirculation, swirl, and combustion, which may occur in practical applications such as gas turbines and internal combustion engines. Progress in the development of LES-based models has been reviewed by several authors (Rogallo and Moin, 1984; Lesieur and Metais, 1996; Piomelli, 1999; Meneveau and Katz, 2000; Pitsch, 2006, Oefelein, 2006). The central concept in LES is to fully resolve the large-scale energy-containing eddies of the simulated turbulent flowfield. These large-scale motions are strongly dependent on the flow geometry and boundary conditions. On the other hand, the small-scale motions are not resolved but modeled through a subgrid scale (SGS) model. While this leads to a significant saving in computational cost in comparison to a DNS where the entire spectrum of turbulent scales is resolved, the additional justification for SGS modeling relies on the premise that the small-scales are isotropic, universal and carry a relatively small fraction of the total energy.

The LES methodology involves the application of a spatial filtering operation to the instantaneous turbulent flowfield, which removes turbulent motions of length-scales smaller than the filter width Δ. The governing (filtered) equations for the remaining large-scale motions are then discretized and solved on a mesh with spacing of the order of or smaller than Δ. As indicated by Pope (2004), this methodology of resolving the large-scales while modeling the small

scales seems to be compelling for the transport of momentum, heat and mass in free shear flows at high values of Re. In such flows, the transported quantities of interest and the rate-controlling processes are determined by the large-scale motions which then cascade down to the statistically isotropic and more universal smaller scales, at least in the Richardson-Kolmogorov point of view. However, this may not be the case in applications such as turbulent combustion. In these applications, the rate-controlling processes of molecular mixing and chemical reactions occur at the smallest scales and therefore need to be modeled. Accordingly, the reliability of the LES technique is then closely linked to the reliability of the SGS model, as in the case of RANS. In fact, most LES combustion models are formulated on similar lines as RANS models. LES-based models for turbulent combustion were recently reviewed by Pitsch (2006).

Various SGS models for LES have been formulated and tested, the simplest and widely employed being the Smagorinsky model (Smagorinsky, 1963). The Smagorinsky model employs an eddy-viscosity-type closure based on a mixing length hypothesis and requires the specification of a model constant C_s, which typically lies in the range 0.11-0.23 (Piomelli, 1999). Even though the Smagorinsky model has been widely employed for computations of jets (Morris *et al.*, 1997; Bogey *et al.*, 2003; Suto *et al.*, 2004; Andersson *et al.*, 2005; Anders *et al.*, 2007) with reasonable accuracy, it has been found to be overly dissipative which could hinder transition to turbulence (Gago *et al.*, 2003). The model is particularly unsuitable for wall-bounded flows where it does not produce the correct limiting behavior near the wall (Lesieur and Metais, 1996).

To overcome these limitations of the Smagorinsky model, dynamic models (Germano *et al.*, 1991; Piomelli, 1999) have been developed in which the model constant is computed as a function of space and time as the simulation progresses. This removes the need to adjust the model constant depending on the flow geometry as in the case of the Smagorinsky model. Dynamic models assume scale invariance which allows the computation of a dynamic model coefficient using information from the resolved scales by performing a test filter

operation, with typically twice the grid filter width. The dynamic Smagorinsky model has been shown to yield superior performance relative to the constant-coefficient model for flows in rotating channels, mixing layers, scalar mixing in co-annular jets and turbulent boundary layers (Meneveau and Katz, 2000 and the references therein). However, apart from the added computational cost of performing the test filter operation to compute the dynamic coefficient, the dynamic procedure leads to a high degree of variability in the computed eddy viscosity, including negative values which could lead to numerical instabilities. Remedies to get rid of such instabilities have been proposed (Germano *et al.*, 1991; Ghosal *et al.*, 1995) such as averaging along directions of statistical homogeneity. In addition to dynamic models, scale-similar and mixed models have been developed which are reviewed by Piomelli (1999), among others. Scale-similar models are based on the premise that the most active subgrid scales are close to the grid cut-off wavenumber and that they interact with scales just above the cutoff. These largest subgrid scales are then computed by filtering the SGS scales. Scale-similar models tend to underestimate the dissipation and hence mixed models have been developed which add the scale-similar SGS stress contribution to the standard Smagorinsky model.

LES studies have also been reported in the literature without an explicit SGS model. Examples are those by Visbal and Rizzetta (2002) and Visbal *et al.* (2003). In these studies, the spatial filter employed played the role of an implicit SGS model and provided the required smoothing and dissipation to prevent the pile-up of energy at the small-scales. Moreover, it was concluded that the SGS model did not have a significant influence on the results. Uzun (2003) compared centerline mean velocity profiles, growth rates, Reynolds stresses and far-field jet noise with a dynamic SGS model and without an explicit SGS model for a jet with an exit Reynolds number of 400,000. The comparisons showed that the jet growth rate is faster without the SGS model. In addition, the peak centerline turbulence intensities were higher without the SGS model, which lead to higher noise levels. Moreover, analysis of the temporal spectra of the streamline velocity

fluctuations showed more energy at higher frequencies (finer scales) when the SGS model was not used. On the other hand, the lower frequencies (larger scales) were found to be more energetic with the dynamic SGS model. In other words, the eddy viscosity of the dynamic model caused a reduction of the turbulent kinetic energy at the finer scales. Uzun (2003) did not give a definitive conclusion as to which approach is the best but reported that the use of the dynamic SGS model increased the computational cost by about 50 %. Another example of LES without SGS modeling is the monotone-integrated large-eddy simulation (MILES) approach (Boris *et al.*, 1992). In MILES, the Navier-Stokes equations are solved on a grid which is relatively coarse and no explicit SGS model is used. The numerical scheme is constructed to be stable and non-oscillatory in the regions of inadequate resolution.

Now we will review some of the prior LES studies specifically related to jets. In recent years, LES studies in the near-field of high-Reynolds number jets have been performed. DeBonius and Scott (2002) report LES computation in the near-field up to about 20 diameters downstream of the nozzle exit, of a Mach 1.4, 1.2×10^6 Reynolds number round jet. The computational grid employed modeled both the nozzle geometry and the external jet flowfield. A relatively coarse grid with about 1.5 million grid points and a finer grid with about 2.3 million points were employed. Fourth order accurate time-stepping and central differencing schemes along with a sixth order spatial filter were used. The compressible form of the constant-coefficient Smagorinsky model was used as the SGS model. The simulation performed on 16 processors on a Silicon Graphics Power Challenge machine required about 2 months of calendar time. The computations underpredicted the potential core was by about 1.5 jet diameters relative to experiments. The authors attribute the shorter computed potential core to inadequate dissipation from the SGS model. Both the grids employed resulted in a rate of centerline velocity decay close to the measurements. In addition, two-point space correlations were computed to estimate integral length-scales in the jet. The computed integral length-scales were approximately $d_j/2$, where d_j is the

jet diameter. Two-point space time correlations were also computed to estimate the convection velocity of the turbulent structures. The convection velocities ranged from $0.57U_j$ – $0.71U_j$, where U_j is the injection velocity depending on the separation distance. The convection velocity was found to decrease with increasing separation distance due to viscous effects.

Bogey *et al.* (2003) investigated the near-field of a 65000 Reynolds number, 0.9 Mach number round jet using compressible large-eddy simulation. They employed a seven-point stencil dispersion-relation-preserving (DRP) finite-difference scheme to discretize the Euler (convective) fluxes, a standard 2nd-order finite difference scheme for the viscous terms and 4th-order Runge-Kutta scheme for time integration. The constant-coefficient Smagorinsky SGS model was employed and the jet was forced at the inlet using a vortex-ring perturbation to trigger transition to turbulence. The perturbation was divergence-free, temporally random and generated turbulence intensities around 4% locally in the shear layer. These intensities were strong enough, so that a potential core similar to that for high-Reynolds number jets, of about $10.4r_o$, where r_o is the inlet jet radius, was observed. A velocity decay constant of 5.5 and a spreading rate of 0.096 were reported which agreed well with experimental data. Furthermore, the radial profiles of the normalized Reynolds-stresses at axial locations beyond $15r_o$ were well superimposed, indicating self-similarity. Integral length-scales were computed using two-point space correlations. In the self-similar region, a linear increase of the computed integral length-scale with axial distance was observed, in agreement with the measured trends reported by Wygnanski and Fiedler (1969). Moreover, the longitudinal length-scale L_{11} was found to be about 2.4 times the transverse length-scale L_{22}, somewhat higher than the factor of 2 typical of homogenous isotropic turbulence. In addition, the computed energy spectrum showed a $k^{-5/3}$ decay. The grid cutoff wavenumber was shown to lie in the inertial range thereby supporting the assumption of the SGS model.

In addition to statistics of the velocity field, LES has been employed in the recent past to investigate passive scalar transport in the near-field of jets.

Ribault *et al.* (2001) performed LES of a 3000 Reynolds number plane jet to investigate passive scalar statistics. The relatively low Reynolds number was chosen to compare with experiments and DNS. Dynamic Smagorinsky and dynamic mixed SGS models were employed in the filtered equations for momentum and the scalar. A 4th-order compact scheme was used for spatial discretization along with 4th –order spatial filtering while a 4th-order Runge-Kutta scheme was employed for time advancement. The 3-D grid measured 12 (axial) x 15 x 4 in inlet jet slot-width units with 61 (axial) x 105 x 16 grid points. This grid comprised of a factor of 22 fewer points than the corresponding DNS. At the jet inlet, a broadband forcing representative of isotropic turbulence was introduced to facilitate transition. Ribault *et al.* (2001) investigated two types of errors in terms of the jet half-width; the numerical error which was defined as the difference between a coarse-resolution LES and a fine-resolution LES with the same filter width, and the modeling error which was defined as the difference between the fine LES and the DNS results. The analysis of these two types of errors showed that while the relative magnitudes were about the same, the signs were opposite.
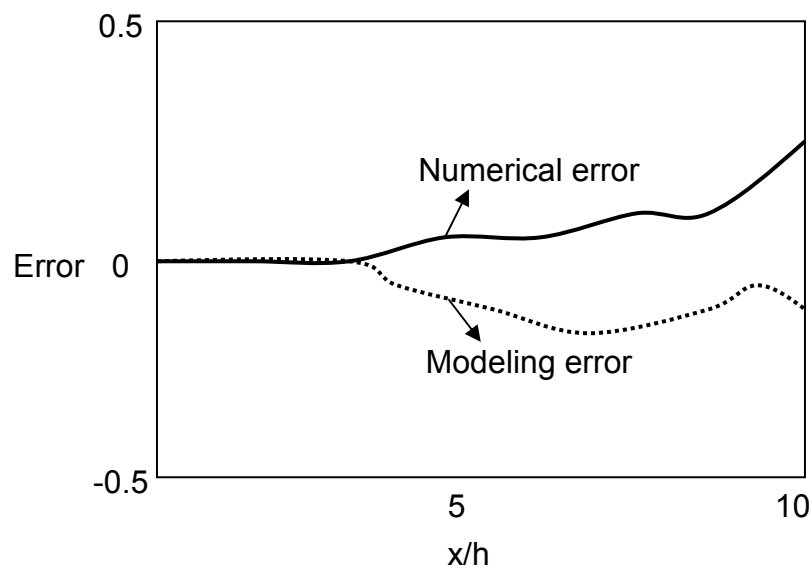
Figure 2.10. Schematic representation of the error analysis reported by Ribault *et al.* (2001); h is the jet inlet slot width.

Figure 2.10 shows a schematic of the findings of Ribault *et al.* (2001). As shown in the figure, the numerical error assists the SGS model and the total error is less than the modeling error. Ribault *et al.* (2001) computed statistics of the passive scalar which include mean and RMS values, higher moments such as skewness and kurtosis and probability density functions (PDFs). The computed decay rate of the mean passive scalar along the jet centerline compared favorably with both experiments and the DNS results. The results with the dynamic Smagorinsky model were slightly closer to the DNS. The PDFs were computed at different axial locations and different radial locations at each axial location using the filtered passive scalar field and compared to those obtained with the DNS. It was found that at axial locations close to the jet exit, for instance at x/h =1, the PDFs exhibited a *marching* behavior. This implies that the most probable value across the mixing layer follows (or marches along) the local mean value of the scalar. This type of PDF is representative of small-scale mixing. The marching behavior was also confirmed in the DNS. However, at downstream locations, for instance at x/h =7, the PDFs showed a *non-marching* behavior where the most probable value approximately remained the same while the mean value decreased across the shear layer. At even greater axial locations such as x/d = 11.5, the PDFs were found to be *tilted* where marching behavior was observed close to the centerline but secondary peaks corresponding to unmixed fluid occurred at radial locations away from the centerline. The overall qualitative behavior in the PDFs computed from the LES flowfield was in good agreement with the DNS results. However, the peaks were lower in magnitude and the PDFs were wider in the LES, suggesting additional mixing due to subgrid fluctuations. Moreover, the DNS flowfield showed strong patches of unmixed fluid at the jet centerline at downstream axial locations which were absent in the LES.

The present study investigates statistics of the velocity and passive scalar (mixture fraction) fields in the near-field of gaseous fuel jets under diesel engine conditions. These conditions are characterized by high pressures and relatively large density ratios between the injected and the ambient fluids. Studies in the

near-field of jets under diesel conditions are limited in the literature. A recent example is the LES performed by Anders *et al.* (2007). The near-field of a 80,000 Reynolds number gaseous n-heptane jet injected into air was investigated. The 3-D computational domain measured 32 (axial) x16x16 in terms of the jet exit diameter with 400 (axial) x 128 x 128 grid points. The constant-coefficient Smagorinsky SGS model was employed. The spatial discretization was achieved with a 6th–order compact scheme while time-integration was performed with a 4th–order Runge-Kutta scheme. A 6th–order tridiagonal spatial filter was employed. The jet was forced at the inlet with a vortex-ring perturbation similar to the one used by Bogey *et al.* (2003). The Navier-Stokes characteristic boundary conditions method (Poinsot and Lele, 1992) was extended to account for multi-component transport and used to impose subsonic inflow conditions at the jet inlet and non-reflective outflow conditions at all the other boundaries. The simulated pressure was 40 bar and the injected-to-ambient gas density ratio was about 3.5. The transient development of the head-vortex ring and the transition to turbulence was examined through instantaneous contours of vorticity. The implemented LES model predicted a potential core of about 8 diameters. The jet half-width was computed from the time and azimuthally-averaged data. A spreading rate of about 0.12 was estimated which is higher than the experimental reported range of 0.086-0.096. This discrepancy was attributed to the lack of self-similarity in the simulated near-field region of the jet.

2.6. <u>Summary</u>

In this chapter, prior works on non-premixed flame-vortex interactions, and the unsteady response of non-premixed flames were reviewed. Since the present work is focused on the investigation of flame extinction/reignition, prior findings in the literature related to extinction/reignition were discussed. The review emphasized the differences between vortex-induced extinction and quasi-steady extinction. In particular, extinction in the presence of a vortex may be characterized by unsteady effects. Due to unsteadiness in the flame response,

we may encounter extinction scalar dissipation rates greater than steady limits. Some of the possible mechanisms leading to reignition following local extinction were discussed. The importance of edge-flame dynamics in reignition phenomena was demonstrated. Studies so far have not investigated the effects due to unsteadiness and curvature on reignition phenomena, which are important in the context of modeling, and validity of modeling approaches, such as flamelet models. The present work clarifies unsteady and curvature effects on extinction/reignition in the context of flame-vortex interactions, and explores the nature of variation of these effects in the near-field of high-Re jets.

An overview of the LES methodology and subgrid scale modeling was presented. Key results from some of the recent studies on velocity field and passive scalar statistics were discussed. In this work, LES of the near-field of a high-Re isothermal gaseous fuel jet is carried out to estimate length-scales, velocity scales and scalar dissipation rates; which are then used to select vortex and flame characteristics for the flame-vortex studies. Even though estimates of length-scales and velocity-scales are available from LES studies in the literature (Bogey *et al*., 2003; Uzun, 2003) at values of Re comparable to those employed here, these studies have not focused on mixture fraction statistics and scalar dissipation rates. Moreover, these studies have not been performed under diesel conditions, i.e., under high pressures and large density ratios between the injected and the ambient fluids. Hence, we employ a LES model recently employed by Anders *et al.* (2007) to investigate jets under diesel conditions. In the chapter that follows, the problem formulation for the LES of a 70,000-Re variable-density isothermal round gas jet is presented. This includes a description of the governing equations, numerical discretization and filtering schemes, subgrid scale model, and the computational setup for the LES.

CHAPTER 3. PROBLEM FORMULATION: LES STUDIES

3.1. Introduction

This chapter deals with the problem formulation for the LES of the near-field of a high-Re number gaseous fuel jet under diesel conditions. In Section 3.2, the formulation of the LES equations is discussed briefly. The subgrid scale model equations are presented in Section 3.3. The spatial filtering scheme is discussed in Section 3.4. Thereafter, the inlet perturbation employed to trigger transition to turbulence is discussed in Section 3.5. Thereafter, the spatial and temporal discretization schemes, and the boundary conditions are presented in Sections 3.6 and 3.7, respectively. The numerical grid, initial conditions and the speed-up of the 3-D code are discussed in Section 3.8. In this section, the implementation of a buffer layer required to prevent fluctuations and vortical structures at the exit boundary is discussed. The chapter closes with a summary in Section 3.9.

3.2. Filtered Governing Equations

The LES methodology involves the application of a spatial filter to the flowfield to remove turbulent motions below the filter width. These unresolved turbulent motions are often referred to as subgrid scales since the filter width is typically chosen to be of the order of the grid size. The effects of the subgrid scale (SGS) motions on the resolved scales are then accounted for through a SGS model. Similar to Reynolds decomposition which is employed in Reynolds-averaged Navier-Stokes (RANS) modeling, any variable f is decomposed into *filtered (or resolved)* $\widetilde{f}$ and *residual (or subgrid scale)* f' components, so that

$$f = \tilde{f} + f'. \tag{3.1}$$

In Eq. (3.1), $\tilde{f}$ is a density-weighted (Favre) filtered variable since we are interested in compressible flows in this work. $\tilde{f}$ is defined as

$$\tilde{f} = \frac{\overline{\rho f}}{\overline{\rho}}, \tag{3.2}$$

where the filtering operation is denoted by the overbar. The Favre-filtering operation can be expressed as a convolution volume integral given by

$$\tilde{f} = \frac{1}{\overline{\rho}} \iiint_V G(\mathbf{x} - \mathbf{x}')\rho(\mathbf{x}')f(\mathbf{x}')d\mathbf{x}', \tag{3.3}$$

where G denotes the filter function. The specific filtering scheme employed in this work will be discussed later. The present work employs a 3-D non-uniform Cartesian grid. The local filter width Δ is determined in terms of the local grid-spacing Δ_x, Δ_y and Δ_z along x, y and z directions, respectively, using the expression:

$$\Delta = \sqrt[3]{\left(\Delta_x \Delta_y \Delta_z\right)}. \tag{3.4}$$

To derive the filtered continuity and momentum equations, the Favre-filtering rules are applied to the equations with the assumption that the filtering operation commutes with differentiation, which is not strictly valid for non-uniform grids (Moin *et al.*, 1991). The resulting continuity and momentum equations, in terms of Favre-filtered variables are given by

$$\frac{\partial \overline{\rho}}{\partial t} + \frac{\partial}{\partial x_j}\left(\overline{\rho}\tilde{u}_j\right) = 0, \tag{3.5}$$

$$\frac{\partial}{\partial t}\left(\overline{\rho}\tilde{u}_i\right) + \frac{\partial}{\partial x_j}\left(\overline{\rho}\tilde{u}_i\tilde{u}_j\right) = -\frac{\partial \overline{p}}{\partial x_j} + \frac{\partial \tilde{\tau}_{ij}}{\partial x_j}, \tag{3.6}$$

where $\tilde{\tau}_{ij}$ is the effective stress tensor given by the sum of the resolved stress $\tilde{\sigma}_{ij}$ and the SGS stress $\tilde{\sigma}_{SG_{ij}}$ as

$$\tilde{\tau}_{ij} = \tilde{\sigma}_{ij} + \tilde{\sigma}_{SG_{ij}}. \tag{3.7}$$

Using an eddy-viscosity model, $\tilde{\tau}_{ij}$ can be written as

$$\tilde{\tau}_{ij} = \tilde{\mu}_{eff}\left[\left(\frac{\partial \tilde{u}_i}{\partial x_j} + \frac{\partial \tilde{u}_j}{\partial x_i}\right) - \frac{2}{3}\frac{\partial \tilde{u}_k}{\partial x_k}\delta_{ij}\right] + \frac{1}{3}\tilde{\tau}_{kk}\delta_{ij}, \tag{3.8}$$

where $\tilde{\mu}_{eff}$ is the effective dynamic viscosity, given by

$$\tilde{\mu}_{eff} = \tilde{\mu} + \tilde{\mu}_T. \tag{3.9}$$

Here, $\tilde{\mu}_T$ is the eddy-viscosity. In this work, closure for $\tilde{\mu}_T$ is obtained from the constant-coefficient Smagorinsky SGS model. The filtered energy and species equations can be obtained in a similar fashion. The final forms of the filtered energy and species equations, respectively, implemented in the FLEDS code are given below:

$$\frac{\partial}{\partial t}(\overline{\rho}\tilde{e}) + \frac{\partial}{\partial x_j}\left[(\overline{\rho}\tilde{e} + \overline{p})\tilde{u}_j\right] = \frac{\partial}{\partial x_j}(\tilde{\tau}_{ij}\tilde{u}_i) + \frac{\partial}{\partial x_j}\left(\tilde{\lambda}_{eff}\frac{\partial \tilde{T}}{\partial x_j}\right) + \frac{\partial}{\partial x_j}\left[\overline{\rho}\sum_k\left(\tilde{h}_k\tilde{D}_{eff}\frac{\partial \tilde{Y}_k}{\partial x_j}\right)\right], \tag{3.10}$$

$$\frac{\partial}{\partial x_j}(\overline{\rho}\tilde{Y}_k) + \frac{\partial}{\partial x_j}(\overline{\rho}\tilde{Y}_k\tilde{u}_j) = \frac{\partial}{\partial x_j}\left(\overline{\rho}\tilde{D}_{eff}\frac{\partial \tilde{Y}_k}{\partial x_j}\right). \tag{3.11}$$

The LES studies performed in this work are non-reacting and hence chemical kinetic source terms do not appear in Eqs. (3.10) and (3.11). Note that with the eddy-viscosity model, the filtered governing equations and the exact equations (see Eqs. (4.1)-(4.4)) have analogous forms, with effective transport properties replacing the molecular transport properties in the filtered equations. Now, we will discuss the closure expressions for the effective properties using the SGS model.

3.3. The Smagorinsky Model

In this work, the constant-coefficient Smagorinsky model (Smagorinsky, 1963) is used as the SGS model. The SGS eddy-viscosity $\tilde{\mu}_T$ is modeled as

$$\tilde{\mu}_T = C\overline{\rho}\,\Delta^2\left|\tilde{S}\right|^2, \tag{3.12}$$

where $\left|\tilde{S}\right| = \left(2\tilde{S}_{ij}\tilde{S}_{ij}\right)^{1/2}$, $\tilde{S}_{ij}$ being the strain-rate tensor, and Δ is the local filter-width. In Eq. (3.12), C is a model constant, set equal to 0.012 in this work. This value of C has been employed in prior LES studies of jets (Speziale *et al.*, 1988; Morris *et al.*, 1997; Andersson *et al.*, 2005). The effective stress tensor is given by

$$\tilde{\tau}_{ij} = \tilde{\mu}_{\text{eff}}\left[2\tilde{S}_{ij} - \frac{2}{3}\tilde{S}_{kk}\delta_{ij}\right] - \frac{2}{3}C_{I}\bar{\rho}\,\Delta^2\left|\tilde{S}\right|^2\delta_{ij}, \qquad (3.13)$$

where C_1 is a model constant, chosen to be equal to 0.0066. In addition, the turbulent Prandtl number Pr_t and the turbulent Schmidt number Sc_t are specified to compute the SGS thermal and mass diffusivities. In the present work, we choose $Pr_t = 0.7$ and $Sc_t = 0.9$. The values of C_1, Pr_t and Sc_t chosen here are identical to those employed in the LES studies of Speziale *et al.* (1988), Morris *et al.*(1997), Andersson *et al.*(2005) and Anders *et al.*(2007).

3.4. Spatial Filtering

Spatial filtering is employed to get rid of fluctuations close to the grid-scale. In this context, the spatial filter plays a similar role as that of the SGS model by removing small-scale fluctuations and preventing energy pile-up. In Section 2.4 of Chapter 2, prior works in the literature without an explicit SGS model where the spatial filter was used to dissipate the small-scale fluctuations were discussed. In this work, the filtering scheme developed by Lele (1992) is employed.

Let f be a flow variable and $\bar{f}$ be the corresponding filtered variable. Then, the filtering operation involves the solution of the following system of equations:

$$\beta\bar{f}_{i-2} + \alpha\bar{f}_{i-1} + \bar{f}_i + \alpha\bar{f}_{i+1} + \alpha\bar{f}_{i+2} = af_i + \frac{d}{2}\left(f_{i-3} + f_{i+3}\right) + \frac{c}{2}\left(f_{i+2} + f_{i-2}\right) + \frac{b}{2}\left(f_{i+1} + f_{i-1}\right). \quad (3.14)$$

For 6th-order accuracy, the coefficients of the scheme are given by (Lele, 1992)

$$a = \frac{1}{16}(11 + 10\alpha - 10\beta), \tag{3.15}$$

$$b = \frac{1}{32}(15 + 34\alpha + 30\beta), \tag{3.16}$$

$$c = \frac{1}{16}(-3 + 6\alpha + 26\beta), \tag{3.17}$$

$$d = \frac{1}{32}(1 - 2\alpha + 2\beta). \tag{3.18}$$

Setting $\beta = 0$ results in a tri-diagonal system of equations which is solved using the TDMA. The filter parameter α decides the cut-off wavelength for the implemented filter. It may be seen from Eqs. (3.14)-(3.18) that with $\beta = 0$ and $\alpha = 0.5$, there is no filtering action since $a = 1;\ b = 1;\ c = 0;\ d = 0$. Following Uzun (2003) and Anders (2006), a value of $\alpha = 0.45$ is used in the present investigation. It can be shown through the determination of the filter transfer function that values of α closer to 0.5 lead to the filtering of shorter wavelengths while lower values of α cause the filtering of larger wavelengths.

3.5. Inlet Perturbation

In LES, inflow forcing is typically employed to numerically trigger transition to turbulence, even at sufficiently high Reynolds numbers. As discussed in Chapter 2, various types of forcing techniques have been employed in the literature. In this work, we employ the vortex ring perturbation technique recently developed by Bogey *et al.* (2003) in their LES studies of jet aeroacoustics. This technique minimizes spurious acoustic waves produced by the perturbation.

The vortex ring is introduced at 0.4 jet diameters into the domain. The axial and radial velocity components of the vortex ring are given by (Bogey *et al.*, 2003)

$$U_{xo} = 2\left(\frac{r_o}{r}\right)\left(\frac{r - r_o}{\Delta_o}\right)\exp\left(-\ln(2)\left(\frac{\Delta(x,r)}{\Delta_o}\right)^2\right), \tag{3.19}$$

$$U_{\mathrm{ro}} = -2\left(\frac{r_{\mathrm{o}}}{r}\right)\left(\frac{x-x_{\mathrm{o}}}{\Delta_{\mathrm{o}}}\right)\exp\left(-\ln(2)\left(\frac{\Delta(x,r)}{\Delta_{\mathrm{o}}}\right)^2\right). \tag{3.20}$$

Here, r and $\Delta(x,r)$ are the radial distances from the origin and the center of the vortex ring Δ_o, respectively. Hence,

$$r = \sqrt{\left(y^2+z^2\right)}, \tag{3.21}$$

$$\Delta(x,r) = \sqrt{\left((x-x_{\mathrm{o}})^2 + (r-r_{\mathrm{o}})^2\right)}. \tag{3.22}$$

The vortex ring velocity is superimposed on the main flow at every time-step as an azimuthal random function with 10 modes. Hence, the resultant axial and radial velocities are given by

$$u_{\mathrm{x}} = u_{\mathrm{x}} + \sum_{n=0}^{9} C_{\mathrm{B}}\varepsilon_{\mathrm{n}}\cos(n\theta+\varphi_{\mathrm{n}})U_{\mathrm{xo}}U_{\mathrm{j}}, \tag{3.23}$$

$$u_r = u_{\mathrm{r}} + \sum_{n=0}^{9} C_{\mathrm{B}}\varepsilon_{\mathrm{n}}\cos(n\theta+\varphi_{\mathrm{n}})U_{\mathrm{ro}}U_{\mathrm{j}}, \tag{3.24}$$

where U_{j} is the centerline velocity of the jet at the inlet. In Eqs. (3.23) and (3.24), ε_{n} is the random amplitude restricted to lie between -1 and 1 and φ_{n} is the random phase lying between 0 and 2π. Similar to the works of Bogey *et al.* (2003) and Anders *et al.* (2007), C_{B} is set equal to 0.01. Now, we will briefly discuss the spatial and temporal discretization schemes, and the boundary conditions employed in the LES study.

3.6. Spatial and Temporal Discretization

FLEDS discretizes the governing equations on a non-uniform 3-D Cartesian grid. The non-uniform physical space is transformed into a uniform cubed computational space. For spatial discretization, the 6th-order non-dissipative compact scheme developed by Lele (1992) is employed. The resulting discretized equations are solved using the tri-diagonal matrix algorithm

(TDMA). For interior nodes, the following 6th-order central scheme is employed to compute the first derivatives for Euler fluxes:

$$\frac{1}{3}f'_{i-1} + f'_i + \frac{1}{3}f'_{i+1} = \frac{7}{9h}\left(f_{i+1} - f_{i-1}\right) + \frac{1}{36h}\left(f_{i+2} - f_{i-2}\right),$$ (3.25)

where h denotes the grid-spacing in the direction of differentiation. The 2nd derivatives for the viscous terms at the interior nodes are computed using the 6th-order central scheme given below:

$$\frac{2}{11}f''_{i-1} + f''_i + \frac{2}{11}f''_{i+1} = \frac{12}{11h^2}\left(f_{i+1} - 2f_i + f_{i-1}\right) + \frac{3}{44h^2}\left(f_{i+2} - 2f_i + f_{i-2}\right).$$ (3.26)

For the near-boundary nodes, the formulation for both the 1st and 2nd derivatives reduces to 3rd-order one-sided and 4th-order central schemes. Further details may be found in Lele (1992) and Anders (2006).

Time integration is performed using a compact storage 4th-order Runge Kutta (RK-4) scheme (Carnahan, 1969). The RK-4 constants employed in the FLEDS code are adopted from Gill (1951). Time-advancement of a variable y is achieved as follows:

$$y^{n+1} = y^n + \frac{h}{6}\left[k_1 + 2\left(1 - \frac{1}{\sqrt{2}}\right)k_2 + 2\left(1 + \frac{1}{\sqrt{2}}\right)k_3 + k_4\right],$$ (3.27)

where the superscript n stands for the value at the nth time-step. If the time increment function is denoted by $f(t, y)$ and the time-step by Δ_t, the four-stage variables are given by

$$k_1 = f\left(t^n, y^n\right),$$ (3.28)

$$k_2 = f\left(t^n + \frac{1}{2}\Delta_t, y^n + \frac{1}{2}\Delta_t k_1\right),$$ (3.29)

$$k_3 = f\left(t^n + \frac{1}{2}\Delta_t, y^n + \left(-\frac{1}{2} + \frac{1}{\sqrt{2}}\right)\Delta_t k_1 + \left(1 - \frac{1}{\sqrt{2}}\right)\Delta_t k_2\right),$$ (3.30)

$$k_4 = f\left(t^n + \Delta_t, y^n - \frac{1}{\sqrt{2}}\Delta_t k_2 + \left(1 + \frac{1}{\sqrt{2}}\right)\Delta_t k_3\right).$$ (3.31)

The Courant-Friedrichs Lewey (CFL) criterion is employed to impose a limitation on the time-step from stability considerations. Δ_t is estimated using the expression

$$\Delta_t = CFL\left[\frac{\delta_{ix}\delta_{iy}\delta_{iz}}{\delta_{ix}\delta_{iy} + \delta_{iy}\delta_{iz} + \delta_{ix}\delta_{iz}}\right],$$ (3.33)

where CFL denotes the CFL number, chosen to be equal to 0.9 in this work, and δ_{ix} is estimated as

$$\delta_{ix} = \frac{\Delta_x\Delta_y\Delta_z}{\left(|u_i|+c\right)\Delta_y\Delta_z + \left(\dfrac{2\lambda}{c_p}+\mu\right)\dfrac{\Delta_x}{\rho}}.$$ (3.34)

Here, Δ_x, Δ_y and Δ_z denote the grid-spacing in x, y and z directions, respectively and c is the speed of sound. Expressions analogous to Eq. (3.34) are used for computing δ_{iy} and δ_{iz}.

3.7. Boundary Conditions

The boundary conditions implemented in the code are based on the Navier-Stokes characteristic boundary conditions (NSCBC) method developed by Poinsot and Lele (1992). In the present case, the NSCBC method is extended to account for multi-component gas transport (Anders *et al.*, 2007). The NSCBC method involves the application of characteristic wave analysis to the Navier-Stokes equations. This allows the estimation of the amplitudes and velocities of the characteristic waves crossing a given boundary. For example, consider Fig. 3.1, which shows the five characteristic waves entering and leaving the computational domain for subsonic flow. In Fig. 3.1, λ_1 represents the velocity of the wave moving in the negative x_1 direction, λ_2 is the speed of the entropy waves, λ_3 and λ_4 are the velocities of *v* and *w* advection, respectively, and λ_5 is the velocity of the wave moving in the positive x_1 direction.
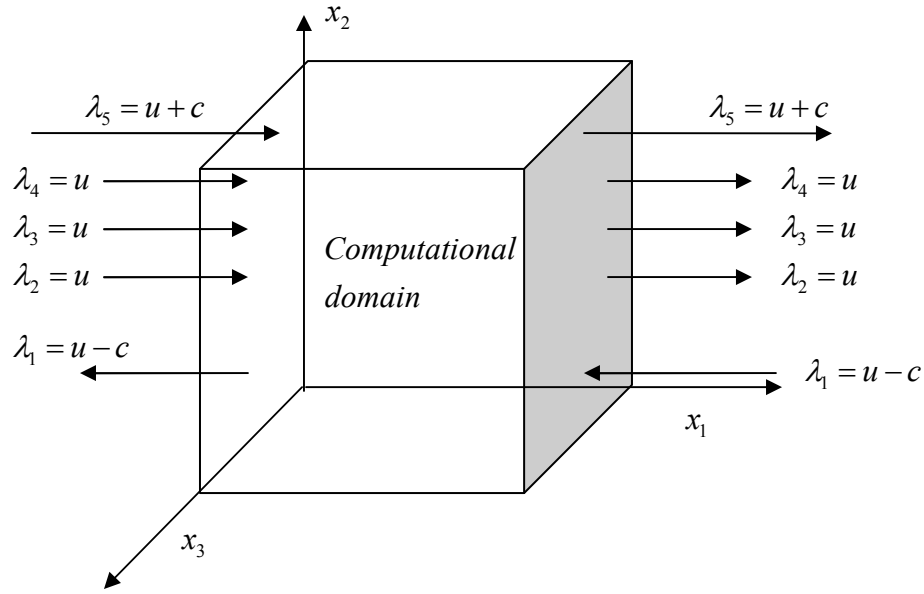
Figure 3.1. Schematic representation of the characteristic waves entering and
leaving the computational domain.

The transformed continuity, momentum and energy equations after the
application of the characteristic wave analysis are advanced in time to determine
the boundary conditions for the next time-step for the species partial densities ρ_k,
momentum densities m_i in each of the three Cartesian directions and the total
energy ρe. For instance, using waves in the x_1 direction, the transformed
continuity and momentum equations are given by:

$$\frac{\partial \rho_k}{\partial t} + d_1^k + \frac{\partial (m_2)}{\partial x_2} + \frac{\partial (m_3)}{\partial x_3} = 0, \tag{3.35}$$

$$\frac{\partial (m_1)}{\partial t} + u_1 \sum_k d_1^k + \rho d_3 + \frac{\partial (m_1 u_2)}{\partial x_2} + \frac{\partial (m_1 u_3)}{\partial x_3} = \frac{\partial \tau_{1j}}{\partial x_j}, \tag{3.36}$$

$$\frac{\partial (m_2)}{\partial t} + u_2 \sum_k d_1^k + \rho d_4 + \frac{\partial (m_2 u_2)}{\partial x_2} + \frac{\partial (m_2 u_3)}{\partial x_3} = \frac{\partial \tau_{2j}}{\partial x_j}, \tag{3.37}$$

$$\frac{\partial (m_3)}{\partial t} + u_3 \sum_k d_1^k + \rho d_5 + \frac{\partial (m_3 u_2)}{\partial x_2} + \frac{\partial (m_3 u_3)}{\partial x_3} = \frac{\partial \tau_{3j}}{\partial x_j}. \tag{3.38}$$

To advance Eqs. (3.18)- (3.21) along with the energy equation in time, the vector **d** should be known. Following Poinsot and Lele (1992), the components of **d** are estimated from the wave amplitudes $\Psi_{1...5}$ as

$$d_1^k = \frac{1}{c^2}\left[\Psi_2^k + \frac{Y_k}{2}\left(\Psi_5 + \Psi_1\right)\right], \tag{3.39}$$

$$d_2 = \frac{1}{2}\left(\Psi_5 + \Psi_1\right), \tag{3.40}$$

$$d_3 = \frac{1}{2\rho c}\left(\Psi_5 - \Psi_1\right), \tag{3.41}$$

$$d_4 = \Psi_3, \tag{3.42}$$

$$d_5 = \Psi_4. \tag{3.43}$$

The wave amplitudes Ψ_i are related to the wave velocities λ_i shown in Fig. 3.1 according to the relations

$$\Psi_1 = \lambda_1\left(\frac{\partial p}{\partial x_1} - \rho c \frac{\partial u_1}{\partial x_1}\right), \tag{3.44}$$

$$\Psi_2^k = \lambda_2\left(c^2 \frac{\partial \rho_k}{\partial x_1} - Y_k \frac{\partial p}{\partial x_1}\right), \tag{3.45}$$

$$\Psi_3 = \lambda_3 \frac{\partial u_2}{\partial x_1}, \tag{3.46}$$

$$\Psi_4 = \lambda_4 \frac{\partial u_3}{\partial x_1}, \tag{3.47}$$

$$\Psi_5 = \lambda_5\left(\frac{\partial p}{\partial x_1} + \rho c \frac{\partial u_1}{\partial x_1}\right). \tag{3.48}$$

Now, we will briefly discuss the implementation of the non-reflective outflow and subsonic inflow boundary conditions (BCs), which are employed in the LES study.

3.7.1. Outflow BC

In the LES, outflow BCs are imposed on all the boundaries except the inlet boundary. The pressure at infinity is imposed and the spatial derivatives of the tangential stresses and the normal heat flux along the direction normal to the boundary are set to zero. The set of equations (3.35)-(3.38) along with the energy equation are advanced in time to determine the BCs at the next time-step. All the wave amplitudes except Ψ_1 are computed using the equations (3.45)-(3.48). Since Ψ_1 represents the amplitude of the waves entering the domain, a perfectly non-reflecting boundary would set this amplitude to zero. However, Poinsot and Lele (1992) indicate that this leads to an ill-posed problem since the mean pressure for the flow is not known. Hence, a partially-reflecting BC is implemented which allows waves reflected from infinity at a specified pressure to determine the mean pressure in the flow. Accordingly, Ψ_1 is expressed as a function of the difference between the outlet pressure p and the specified pressure at infinity p_∞ as given below:

$$\Psi_1 = K(p - p_\infty),\qquad(3.49)$$

where the constant K is given by

$$K = \frac{\sigma(1 - M^2)c}{L}.\qquad(3.50)$$

Here, M is the Mach number, L is a characteristic length, and σ is a constant, set equal to 0.25 (Poinsot and Lele, 1992) in the present study. Further details on the NSCBC method may be found in Poinsot and Lele (1992) and Anders et al. (2007).

3.7.2. Subsonic Inflow BC

A subsonic inflow condition is used at the jet inlet boundary while non-reflective outflow conditions are implemented at all the other boundaries. For the inflow BC, Poinsot and Lele (1992) derive the so called local one-dimensional inviscid relations (LODI) to determine the amplitudes of the characteristic waves.

The LODI are obtained when transverse and viscous terms are neglected in the conservation equations. The authors indicate that the LODI are not physical but merely compatibility conditions between choices made for the physical boundary conditions and the amplitudes of the waves crossing the boundary. One set of LODI are given below:

$$\frac{\partial \rho}{\partial t} + \frac{1}{c^2}\left[\sum_k \Psi_2^k + \frac{1}{2}\left(\Psi_5 - \Psi_1\right)\right] = 0, \tag{3.51}$$

$$\frac{\partial p}{\partial t} + \frac{1}{2}\left(\Psi_5 + \Psi_1\right) = 0, \tag{3.52}$$

$$\frac{\partial u_1}{\partial t} + \frac{1}{2\rho c}\left(\Psi_5 - \Psi_1\right) = 0, \tag{3.53}$$

$$\frac{\partial u_2}{\partial t} + \Psi_3 = 0, \tag{3.54}$$

$$\frac{\partial u_3}{\partial t} + \Psi_4 = 0. \tag{3.55}$$

In the equations above, $\Psi_{1..5}$ represent the amplitudes of the five characteristic waves entering and leaving the domain. At the inflow boundary, the three velocity components, temperature and the species mass fraction profiles along with their derivatives are specified. Of the five wave amplitudes, Ψ_1 is determined from the interior points using Eq. (3.44). The remaining amplitudes are determined using the LODI. For instance, knowing Ψ_1 and the specified values of the velocity component u_1 and its time-derivative $\frac{du_1}{dt}$ at the boundary, we can compute the incoming wave Ψ_5 in the positive x_1 direction (see Fig. 3.1) from Eq. (3.53) as

$$\Psi_5 = \Psi_1 - 2\rho c \frac{du_1}{dt}. \tag{3.56}$$

Since the three velocity components and the temperature are specified, the characteristic wave analysis needs to be applied only to the continuity equation to determine the new density. Hence, the density is computed from the equation

$$\frac{\partial \rho}{\partial t} + \frac{1}{c^2}\left[\sum_k \Psi_2^k + \frac{1}{2}(\Psi_5 + \Psi_1)\right] + \frac{\partial}{\partial x_2}(\rho u_2) + \frac{\partial}{\partial x_3}(\rho u_3) = 0. \tag{3.57}$$

3.8. Computational Setup

3.8.1. Numerical Grid

The LES is performed on a computational domain measuring 40 x 14 x 14, in terms of exit jet diameter. The center z-x plane of the 3-D numerical grid is shown in Fig. 3.2. As indicated in Fig. 3.2, the physical region of the grid where the jet flowfield of interest is simulated extends up to 25 jet diameters in the axial direction. Beyond this distance, a buffer region is implemented with exponential grid-stretching and artificial damping. This buffer zone is required to prevent fluctuations and vortical structures from reaching the outflow boundary when the jet exits the domain. The presence of strong fluctuations at the outflow boundary could result in undesired reflections that could in turn lead to numerical instabilities. The implementation of the buffer zone in the present work is similar to that of Uzun (2003). In this zone, the turbulent flowfield is forced towards a smooth target solution by the addition of extra source terms to the right-hand side of the governing equations. For example, if f is the variable of interest and f_{target} is the target solution, then the artificial damping term is implemented as follows (Uzun, 2003):

$$\frac{\partial f}{\partial t} = RHS - \left[\chi(x)\left(f - f_{\text{target}}\right)\right]. \tag{3.58}$$

In Eq. (3.58), the damping factor $\chi(x)$ is given by

$$\chi(x) = \chi_{\max}\left(\frac{x - x_{\text{phy}}}{x_{\max} - x_{\text{phy}}}\right)^3, \tag{3.59}$$

where x is the axial location, x_{phy} is the axial extent of the physical part of the grid, which is 25 jet diameters in the present case, $x_{\max}$ is the maximum extent of

the domain, equal to 40 jet diameters, and the constant χ_{max} is set equal to 1. The target solution employed here is the self-similar solution for an incompressible turbulent round jet (Pope, 2000). Note from Fig. 3.2 that the grid is significantly stretched in the buffer layer which provides additional dissipation in the relatively coarse computational cells.
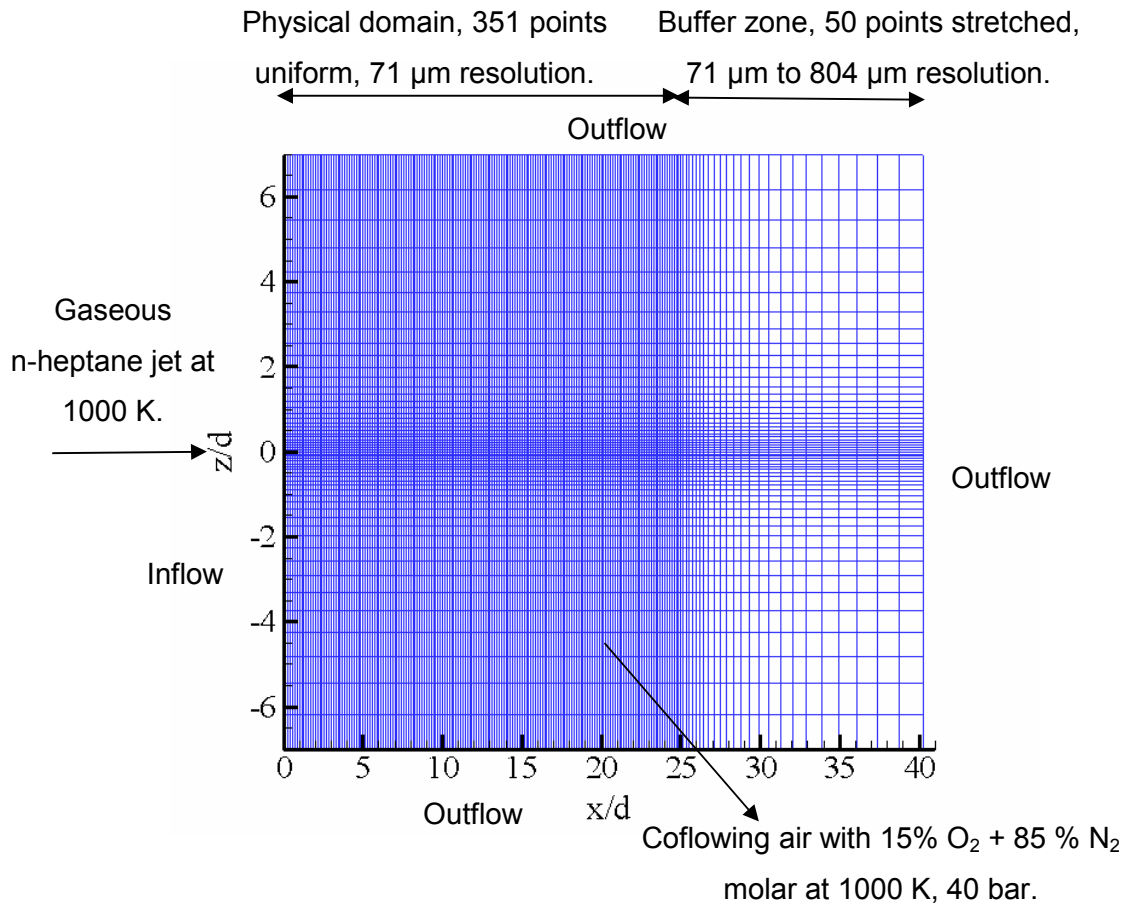
Figure 3.2. The numerical grid employed in the 3-D LES studies, center z-x plane (every 2nd grid-point shown).

As shown in Fig. 3.2, the grid comprises 401 (axial) x 113 x 113 grid points, which leads to a total of about 5.1 million points. The jet exit Reynolds number simulated is about 70,000 and the exit diameter d is 1 mm. The physical

part of the domain up to about 25 jet diameters has 351 points in the axial direction. This results in a uniform resolution of about 71 μm, which is about 0.07d. The grid is stretched exponentially beyond 25d to form a buffer zone where the maximum resolution increases to about 0.8d. In the transverse y and z directions, the grid is stretched from the center to the boundaries. The resolution varies from about 0.026d to about 0.44d. This places about 26 cells in the nozzle radius. The simulated near-field region of the jet, the jet exit Reynolds number and the numerical resolution employed here are comparable to those in the LES studies of Uzun (2003) and Anders (2006).

3.8.2. Initial Conditions

The initial conditions in the chamber are representative of diesel chambers; pressure is 40 bar and the temperatures of the injected (n-heptane) and ambient gases are 1000 K. This leads to an injected-to-ambient gas density ratio of about 3.5. The exit jet diameter is 1 mm and the jet exit Re of 70,000 corresponds to an injection velocity U_j of 42.5 m/s. This injection velocity is significantly lower than in modern diesel engines (~ 400 m/s) but the Re is comparable due to the relatively large value of the jet diameter. The ambient gas in the chamber is 15 % O_2 and 85 % N_2 by molar composition. A relatively small co-flow velocity of 0.425 m/s is imparted to the ambient gas. The maximum initial Mach number in the domain is about 0.15. Hence, compressibility effects are not expected to be significant. In this work, we are primarily interested in the statistically stationary jet structure which is amenable to time statistics. The transient development of the jet is not of interest here. Hence, the flowfield is initialized with the steady self-similar solution of an incompressible turbulent round jet. Then, perturbations are introduced close to the inlet to trigger transition to an instantaneous turbulent flowfield corresponding to the conditions being simulated. An approximate mean axial velocity profile for the self-similar jet is given by (Pope, 2000)

$$\frac{U(x,r)}{U_0(x)} = \left(1 + a\eta^2\right)^{-2},$$ (3.60)

where U is the mean axial velocity, U_0 is the mean jet centerline velocity, a is a constant, equal to 47 based on a jet spreading rate of 0.094, and η is the similarity variable, defined as

$$\eta = \frac{r}{r_{1/2}(x)}.$$ (3.61)

In Eq. (3.61), $r_{1/2}(x)$ is the jet half-radius, which increases linearly with axial distance x in the jet as follows:

$$\frac{dr_{1/2}}{dx} = S,$$ (3.62)

where S is the jet spreading rate, assumed to be equal to 0.094. The centerline velocity $U_0(x)$ is assumed to decay with x according to the expression below

$$\frac{U_0(x)}{U_j} = \frac{Bd}{x - x_0},$$ (3.63)

where d is the jet exit diameter. The decay constant B is chosen to be equal to 5.5, within the range reported in the experiments of Wygnanski and Fiedler (1969) and Panchapakesan and Lumley (1993a), and the virtual origin x_0 is assumed to be zero. The mean radial velocity V is given by the expression (Pope, 2000)

$$\frac{V(x,r)}{U_0} = \frac{1}{2}\frac{\left(\eta - a\eta^3\right)}{\left(1 + a\eta^2\right)^2}.$$ (3.64)

Similar profiles are employed for the species mass fractions.

Figure 3.3 shows the contours of axial velocity in the center z-x plane at the start of the computation in the physical part of the domain up to 25d. The self-similar profiles discussed above are implemented after about x/d = 5 to simulate the presence of a potential core region. In the potential core region, a hyperbolic tangent profile is used along the transverse directions to ensure a smooth

variation from the injected jet velocity to the co-flow air velocity. The inlet jet shear thickness δ_θ is $0.15 r_0$, where r_0 is jet exit radius.
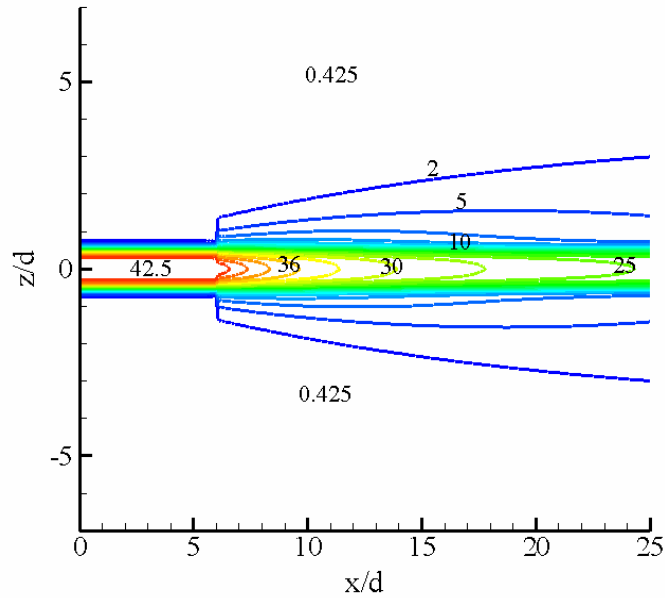
Figure 3.3. Initial contours of axial velocity (m/s).
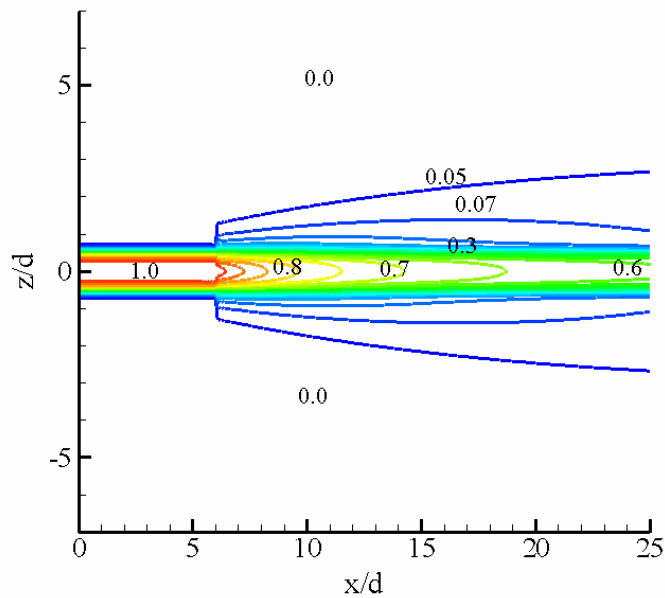
Figure 3.4. Initial contours of mixture fraction in the jet.

Note that the chosen grid places about 6 grid points in the jet shear layer. The measurements of Zaman (1985) show that the ratio δ_θ / r_0 is typically less than 0.01. However, as indicated by Bogey *et al.* (2003), numerical studies in the literature report values around 0.1 due to resolution requirements. Figure 3.4 shows the initial contours of the mixture fraction in the jet. In the present case, the mixture fraction is the same as the fuel mass fraction since the flow is non-reacting. The stoichiometric mixture fraction contour is also shown which is about 0.05. Note that the self-similar profiles employed here are used only as initial guesses and have no bearing on the instantaneous flowfield which develops during the simulation and the time statistics which are performed subsequently.

3.8.3. 3-D Code Speed-up

Computations were performed on the Tungsten Xeon Cluster, which is part of the National Center for Supercomputing Applications (NCSA) to assess the speed-up of the 3-D version of the FLEDS code. Figure 3.5 shows the speed-up as a function of the number of processors. The ideal linear behavior is also shown for comparison. Here, speed-up is defined as the CPU time with 16 processors to the CPU time with a higher number of processors. Figure 3.5 shows that the actual speed-up curve deviates from the ideal linear behavior beyond 32 processors. This reflects the increasing importance of communication time relative to the computational time as the number of processors increases. Moreover, the size of the computational domain also plays a role by influencing the ratio of boundary to interior nodes. It is expected that the scaling will improve as the size of the simulation domain increases.

Note that due to the non-local nature of the 6th-order compact scheme (Lele, 1992), the derivatives are computed through matrix inversion employing the tridiagonal matrix algorithm (TDMA). In the version of the FLEDS code employed in the present work, the implementation of the TDMA involves a sequential communication of the tridiagonal coefficients among the processors.

Since the TDMA routines are called several times every time-step when large number of processors are employed, this sequential implementation affects the speed-up of the code. One possible approach (Magi, 2008) is to replace the compact scheme with a non-compact finite-difference scheme, such as the recent 13-point stencil scheme proposed by Bogey and Bailly (2004), in routines where the TDMA is called for a relatively large number of times. For instance, non-compact schemes can be employed in routines that compute the diffusive terms of the governing equations. Alternative parallelization strategies, such as the transposition strategy (Uzun, 2003), can also be explored to improve the speed-up performance of the code.

The LES computation reported in this work is performed on the NCSA Tungsten cluster with 128 3.2 GHz Intel Xeon processors. The CPU time per time-step is about 14 s. The numerical time-step is approximately 1.65×10^{-8} s. Hence, for a simulation time of about 4.15 milliseconds, the total CPU time is about 42 days.
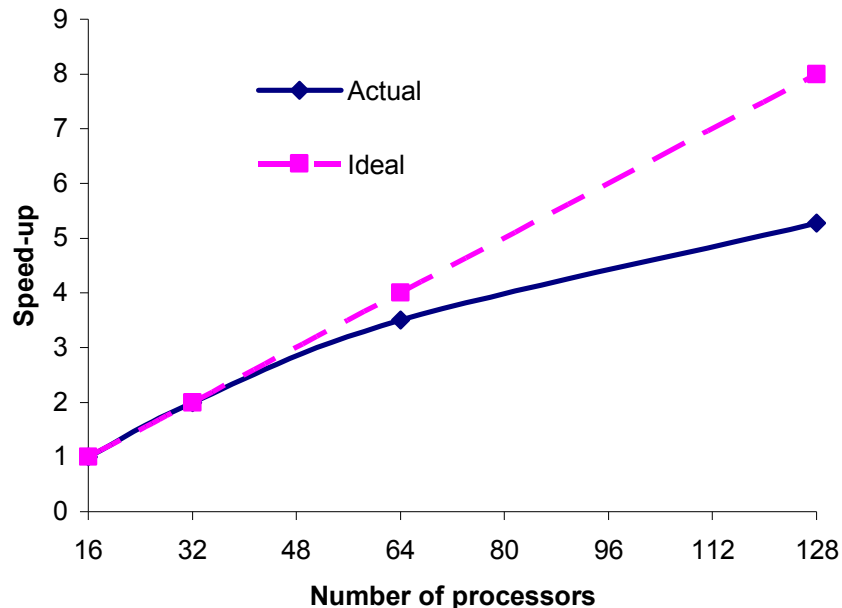
Figure 3.5. Speed-up of the 3-D code as a function of the number of processors.

3.9. <u>Summary</u>

The problem formulation for the LES study performed in this work was presented in this chapter. The filtered governing equations are solved with a 6th-order compact finite-difference scheme and 4th-order time-integration. A 6th-order tri-diagonal spatial filter is employed to remove fluctuations close to the grid-scale. In addition, a constant-coefficient Smagorinsky SGS model is used for the closure of the SGS stress terms. Subsonic inflow and non-reflective outflow boundary conditions are implemented using the NSCBC method. The jet is forced with a vortex ring perturbation at the inlet to trigger transition to turbulence. A buffer zone with exponential stretching and artificial damping is implemented to get rid of fluctuations near the outflow boundary. The jet exit Reynolds number simulated is 70,000. The injected-to-ambient gas density ratio is about 3.5. The temperature and pressure in the domain are chosen to be 1000 K and 40 bar, respectively, to simulate diesel engine conditions. The near-field region of interest is up to 25 jet diameters and a 3-D non-uniform grid with about 5.1 million points is employed.

In the chapter that follows, problem formulation for the studies of flame-vortex interactions is presented. This includes a description of the governing equations, computational set up and conditions.

CHAPTER 4. PROBLEM FORMULATION: FLAME-VORTEX STUDIES

4.1. <u>Introduction</u>

In this chapter, the problem formulation for the studies of flame-vortex interactions is presented. In Section 4.2, the numerics is briefly discussed, which includes the governing equations, numerical schemes and boundary conditions. Chemical kinetic models employed in the flame-vortex simulations are described in Section 4.3. Thereafter, the computational setup is outlined in Section 4.4, which includes a discussion of the initial conditions and important non-dimensional numbers for the flame-vortex interaction studies. The chapter closes with a summary in Section 4.5.

4.2. <u>Numerics</u>

The numerical code employed in this work is the flow, large-eddy and direct simulation (FLEDS) code (Abraham and Magi, 1997; Viggiano and Magi, 2004; Anders, 2006). FLEDS solves the time-dependent conservation equations for chemically reacting flows. For instance, the continuity and momentum equations are given by

$$\frac{\partial \rho}{\partial t} + \frac{\partial}{\partial x_j}(\rho u_j) = 0 , \tag{4.1}$$

$$\frac{\partial}{\partial t}(\rho u_i) + \frac{\partial}{\partial x_j}(\rho u_i u_j) = -\frac{\partial p}{\partial x_i} + \frac{\partial \sigma_{ij}}{\partial x_j} , \tag{4.2}$$

where σ_{ij} is the viscous stress tensor given by $\sigma_{ij} = \mu\left[\left(\frac{\partial u_i}{\partial x_j} + \frac{\partial u_j}{\partial x_i}\right) - \frac{2}{3}\frac{\partial u_k}{\partial x_k}\delta_{ij}\right]$.

The pressure p is determined from the equation of state for ideal gases

$$p = \rho R T, \tag{4.3}$$

where R is the specific gas constant. The energy equation is cast in terms of the total specific energy e, given by

$$e = \frac{1}{2} u_i u_i + u_e, \tag{4.4}$$

where u_e stands for the specific internal energy, as

$$\frac{\partial}{\partial t}(\rho e) + \frac{\partial}{\partial x_j}\left[(\rho e + p) u_j\right] = \frac{\partial}{\partial x_j}(\sigma_{ij} u_j) + \frac{\partial}{\partial x_j}\left(\lambda \frac{\partial T}{\partial x_j}\right) + \frac{\partial}{\partial x_j}\left[\rho \sum_k \left(h_k D_k \frac{\partial Y_k}{\partial x_j}\right)\right] + \sum_k \dot{w}_k h_k^0. \tag{4.5}$$

In Eq. (4.5), h_k, D_k, Y_k, $\dot{w}_k$ and h_k^0 are the specific enthalpy, mass diffusivity, mass fraction, production/destruction rate and standard specific enthalpy of the kth species, respectively. Soret and Dufour effects have been neglected in Eq. (4.5). In addition, the species conservation equation is solved in terms of Y_k as

$$\frac{\partial}{\partial t}(\rho Y_k) + \frac{\partial}{\partial x_j}(\rho Y_k u_j) = \frac{\partial}{\partial x_j}\left(\rho D_k \frac{\partial Y_k}{\partial x_j}\right) + \dot{w}_k. \tag{4.6}$$

In the FLEDS code, molecular transport properties and chemical kinetic source terms are computed through an interface with the CHEMKIN library of sub-routines. In the present work, mass diffusivities D_k are computed using either the simplified unity Lewis number (UL) model or the mixture-averaged (MA) model. In the UL model, the mass diffusivities of all the species are assumed to be equal to the thermal diffusivity of the mixture. Hence, D_k is computed as

$$D_k = \alpha = \frac{\lambda}{\rho c_p}. \tag{4.7}$$

On the other hand, in the MA model, the diffusivity of species k, D_{km}, is computed using the expression (Bird *et al.*, 1960)

$$D_{km} = \frac{1 - Y_k}{\displaystyle\sum_{j \neq i}^{N} \frac{X_j}{D_{ji}}} \tag{4.8}$$

Here, D_{ji} is the binary diffusion coefficient between species i and j and X_j is the mole fraction of species j.

Similar to the LES (see Section 3.6), spatial discretization is achieved through a 6th-order compact finite-difference scheme (Lele, 1992), while time integration is performed using a 4th-order Runge-Kutta scheme (Carnahan, 1962). Non-reflecting outflow boundary conditions, which were discussed in Section 3.7.1, are imposed at all the boundaries. Now, we will discuss the chemical kinetic models employed in the flame-vortex interaction studies to compute the chemical kinetic source terms.

4.3. Chemical Kinetic Models

As stated in Chapter 1, we are primarily interested in conditions representative of diesel engine combustion chambers in this work. Hence, we choose a commonly employed diesel fuel surrogate, n-heptane, as the fuel. Our primary objective is to characterize the likely nature of localized flame dynamics in the near-field of high-Reynolds number jets through non-dimensional numbers, and assess the applicability of modeling approaches, such as flamelet models. Since the objective is not to quantify the flame structure in the jet near-field, a single-step chemistry model is chosen for the majority of the flame-vortex interaction studies in this work. The single-step kinetic model is useful to identify regimes of flame-vortex interaction and physical mechanisms through well-defined non-dimensional numbers (to be discussed in Section 4.4). However, in order to assess whether the physical mechanisms revealed by the single-step model are valid with realistic multistep chemistry, computations with a skeletal 56-step n-heptane mechanism (Peters *et al.*, 2002) for a limited set of conditions are also performed. Below, the single-step and the multistep kinetic models employed in this work are discussed.

4.3.1. Single-step Kinetic Model

We consider an irreversible single-step reaction given by

$$F + \nu_O O_2 \rightarrow \nu_P P,$$ (4.9)

where F represents the fuel and P represents the primary products of combustion and ν denotes the stoichiometric coefficient. If F represents n-heptane, C_7H_{16}, which is a commonly employed surrogate for practical fuels like Diesel, then the single-step reaction is of the form:

$$C_7H_{16} + 11O_2 \rightarrow 7CO_2 + 8H_2O.$$ (4.10)

In the single-step model, conservation equations are solved for five species: C_7H_{16}, O_2, N_2, CO_2 and H_2O. The single-step reaction rate $\dot{w}_F$ (mol/cm^{3}s) is given by the Arrhenius expression

$$\dot{w}_F = AT^b[C_7H_{16}]^m[O_2]^n e^{-E_a/R_u T},$$ (4.11)

where A is the pre-exponential factor, equal to 5.1×10^{11} in cm-mole-s units, T is the temperature, b is the temperature exponent, equal to zero in this case, m and n are reaction orders with respect to the fuel and O_2, respectively, which are assumed to be unity in this model, E_a is the activation energy, equal to 100000 J/mol, R_u is the universal gas constant, and $[C_7H_{16}]$ and $[O_2]$ are the concentrations of C_7H_{16} and O_2 in mol/cm^3, respectively. These values are chosen to give a steady extinction scalar dissipation rate χ_e in agreement with detailed kinetic models for n-heptane oxidation (Seiser *et al.*, 2000; Peters *et al.*, 2002) and are close to those reported in prior DNS studies of n-heptane flames under the pressures and temperatures employed here (Sreedhara and Lakshmisha, 2000).

It is important to note that the single-step kinetic model employed here is not intended to reproduce realistic n-heptane chemistry. The single-step model parameters result in a unique chemical time-scale and Damköhler number, which can then be used to study the coupling between the fluid flow and chemistry. The

chemical time-scale τ_c from the single-step model is estimated as (Safta and Madnia, 2002)

$$\tau_c = \left(\frac{\dot{w}_P MW_{\text{mix}}}{\rho}\right)^{-1} = \left(\frac{\nu_P AT^b [C_7 H_{16}]^m [O_2]^n \exp\left(-\dfrac{E_a}{R_u T}\right) MW_{\text{mix}}}{\rho}\right)^{-1} , \qquad (4.12)$$

where $\dot{w}_P$ is the reaction rate based on the product, MW_{mix} is the mixture molecular weight, and ρ is the mixture mass density. Here, we estimate τ_c based on CO_2 as the product of combustion. In Section 4.4, we will employ τ_c to define the Damköhler number, which represents the coupling between mixing and chemistry.

4.3.2. Multistep Kinetic Model

We model n-heptane oxidation chemistry with a skeletal mechanism comprising 34 species among 56 reaction steps, developed by Peters *et al.* (2002). This 56-step mechanism captures first- and second-stage ignition. It was shown by Peters *et al.* that this mechanism predicts autoignition delay times in n-heptane-air mixtures with adequate accuracy for pressures up to 42 bar. Since we are interested in predicting critical regimes, such as extinction/reignition and partially-premixed combustion, we have assessed the accuracy of the mechanism in predicting non-premixed flame structure, extinction, and partially-premixed flame structure through comparisons with available experimental data in n-heptane flames at 1 bar. These results are discussed below.

For non-premixed flame structure and extinction, we consider the experimental data reported by Seiser *et al.* (1998) for counterflow gaseous n-heptane/air flames. Seiser *et al.* report profiles of temperatures and major species mole fractions for a counterflow diffusion flame with 15 % molar n-heptane and 85 % molar N_2 at 338 K on one side (x = 0), and air at 298 K on the other side (x = 1) . The fuel and oxidizer-side velocities are 0.342 m/s and 0.375

m/s, respectively. The OPPDIFF code (Kee *et al.*, 1999) is employed to compute the steady-state structure of the non-premixed flame.

(a)

(b)

(c)
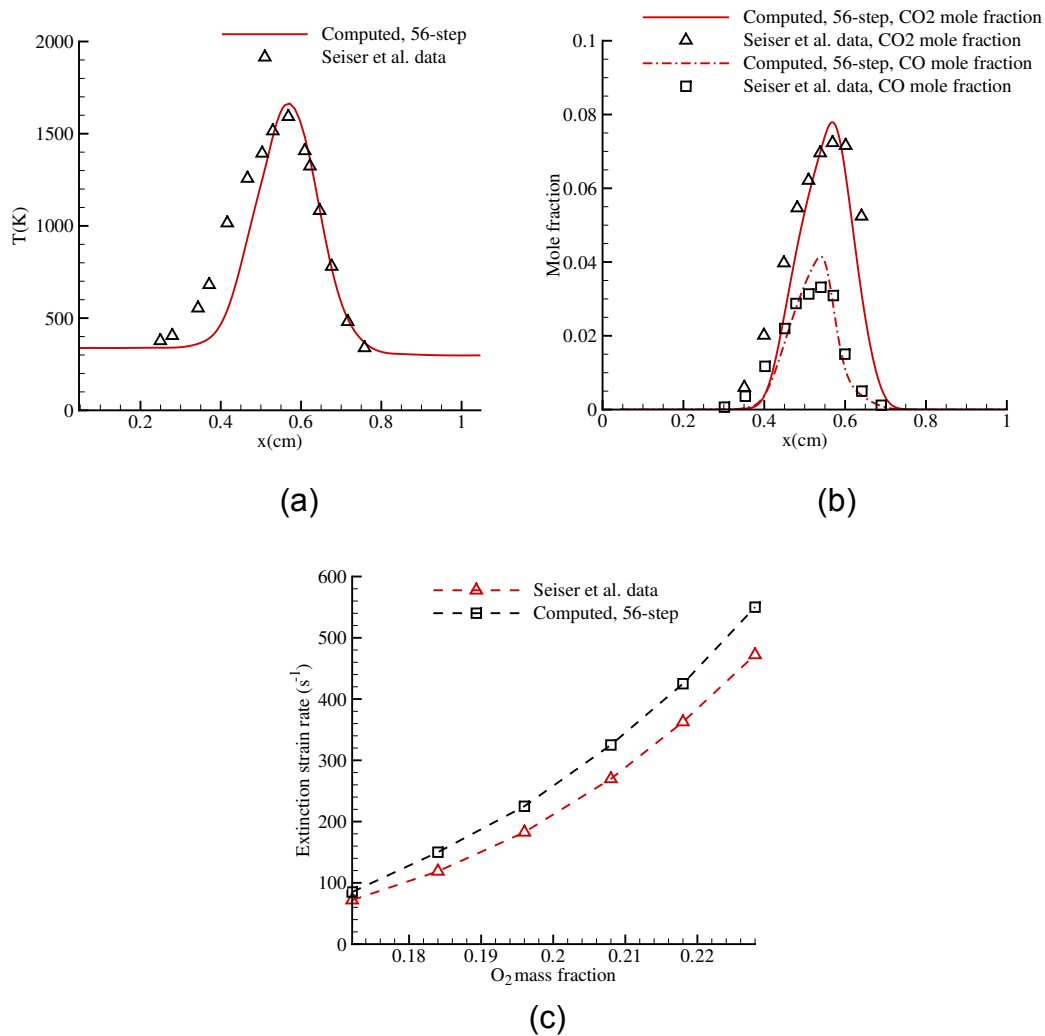
Figure 4.1. Non-premixed flame structure and extinction, computed with the 56-step mechanism and compared with the measured data of Seiser *et al.* (1998); (a) temperature, (b) mole fractions of CO_2 and CO, and (d) extinction strain rates as a function of O_2 mass fraction.

Figure 4.1(a) compares the computed temperature profile using the 56-step mechanism with the measured data. Note that about 250 grid points were employed to obtain a grid-independent solution. Figure 4.1(a) shows that the mechanism predicts the peak temperature and its location within 5% even though

some discrepancies are observed on the fuel-side. Figure 4.1(b) compares the computed profiles of CO_2 and CO mole fractions with the measured data. The agreement of the peak values is within 8 % for CO_2 and within 15 % for CO. In addition, we compared profiles of other major species such as H_2O and H_2, and C-1 and C-3 hydrocarbons like CH_4 and C_3H_6 and found that the values predicted by the mechanism are within 25 % of the measured values. To compute extinction strain rates, the fuel and oxidizer-side velocities are gradually varied; starting from a steady-state burning solution in OPPDIFF, until a turning point leading to a non-burning solution is observed. Figure 4.1(c) compares the computed and measured extinction strain rates as a function of O_2 mass fraction on the air-side. The mechanism captures the qualitative behavior well and the predicted values lie within 20 % of the measurements.
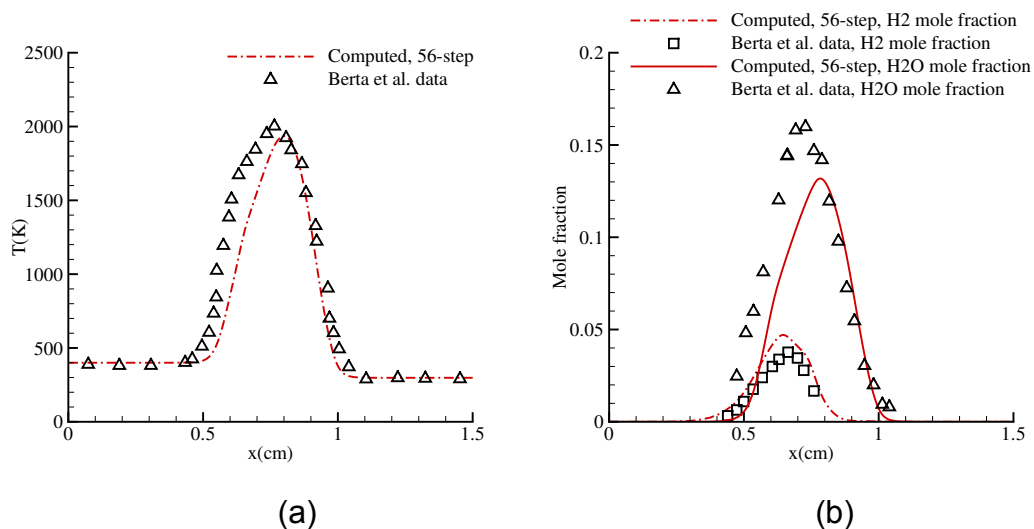
Figure 4.2. Comparison of computed and measured data for a n-heptane counterflow partially-premixed flame with $\Phi = 10$, $a_g = 100$ /s; (a) temperature, and (b) H_2 and H_2O mole fractions.

To assess the ability of the 56-step mechanism to predict partially-premixed flame structure, we consider the recent experimental data reported by Berta *et al.* (2005). In these experiments, temperatures and species concentrations in counterflow flames established with a partially-premixed n-

heptane/air mixture at a given equivalence ratio Φ and 400 K at one end (x = 0), and air at 298 K on the other end (x = 1.5) were measured. We compared the measured data with computed data for cases with $\Phi = \infty$ (non-premixed), 4 and 10 at a global strain rate a_g of 100 /s. For brevity, we present the temperature and H_2 and H_2O mole fraction comparisons in Figs. 4.2(a) and (b), respectively, for the Φ = 10 case. Note that the agreement with experimental data is within 6 % with respect to the peak temperature, whereas the computed H_2O and H_2 peak mass fractions agree within 25 % with the measured values. Moreover, the 56-step mechanism predicts the locations of the peak temperature and H_2O/H_2 peak mass fractions within 10 % of the experimental data. These comparisons lend credence to the applicability of the 56-step mechanism to predict non-premixed and partially-premixed flame structures, and extinction.

Note, however, that in the present work we are employing the mechanism at a relatively high pressure of 40 bar. To the best of our knowledge, there is no experimental data in the literature on n-heptane flame structure and extinction under high pressures. This leads to a certain degree of uncertainty with respect to chemical kinetics in this work, and hence we will defer from drawing specific conclusions about the reaction pathways and chemical species governing the unsteady flame structure. Nevertheless, as shown in prior experimental and numerical studies on flame-vortex interactions (Cuenot and Poinsot, 1994; Thevenin et al., 2000), the interaction outcomes are predominantly governed by non-dimensional numbers such as the Damkőhler number and the Reynolds number. Hence, it is expected that the flame-vortex interaction regimes observed with the 56-step mechanism, such as extinction, reignition and pocket formation (see Chapter 8), will be observed even with a different kinetic model if the controlling non-dimensional numbers are the same. In fact, this is confirmed by the qualitative agreement between the single-step (Chapters 6 and 7) and kinetic model (Chapter 8) results with respect to physical mechanisms for extinction/reignition. It is therefore useful to interpret the 56-step n-heptane

mechanism as one with a specific set of chemical time scales (Damkőhler numbers).

4.4. <u>Computational Setup</u>

4.4.1. Initial Conditions

Figure 4.3 shows a schematic of the computational setup. The computational domain is 2-D and measures 2.5 mm x 2.5 mm. A uniform grid with 350x350 points is employed resulting in a resolution of about 7.1 μm. A mass-diffusion layer between the fuel and diluted air (15 % O_2 + 85% N_2 molar) is formed using a hyperbolic tangent profile according to the relation

$$f = \left(\frac{f_1 + f_2}{2}\right) + \left(\frac{f_2 - f_1}{2}\right)\tanh\left(\frac{y - y_c}{\delta}\right), \tag{4.13}$$

where f is the mass fraction of a given species at a particular location, and f_1 and f_2 are the mass fractions of the species on the fuel and air-sides, respectively, y and y_c are the y-coordinates of a given location and the center, respectively, and δ is the thickness of the hyperbolic-tangent profile, which is chosen to be 120 μm in this work. Based on the LES statistics (discussed in Chapter 5), the initial vortex length-scales (d_v in Fig. 4.3) simulated lie in the range of 100-600 μm, and the initial diffusion layer thicknesses (δ) lie in the range of 150-500 μm. Hence, the chosen resolution resolves the relevant length scales of the flame-vortex interaction by at least 15 cells, which is consistent with the typical choice of about 10 cells to resolve the relevant length scales in DNS studies (Vervisch and Poinsot, 1998). Note that for the larger vortices (d_v > 200 μm) and thicker diffusion layers (δ > 200 μm) employed, larger domains (5 mm x 5mm) with the same resolution, i.e. 7.1 μm, are used. In addition, the domain sizes chosen are at least 8 times larger than the simulated vortices in either direction to minimize boundary effects. Furthermore, our recent studies

(Venugopal and Abraham, 2008b) show that the chosen resolution is sufficient to adequately describe the physical mechanisms governing extinction/reignition for the conditions employed here.
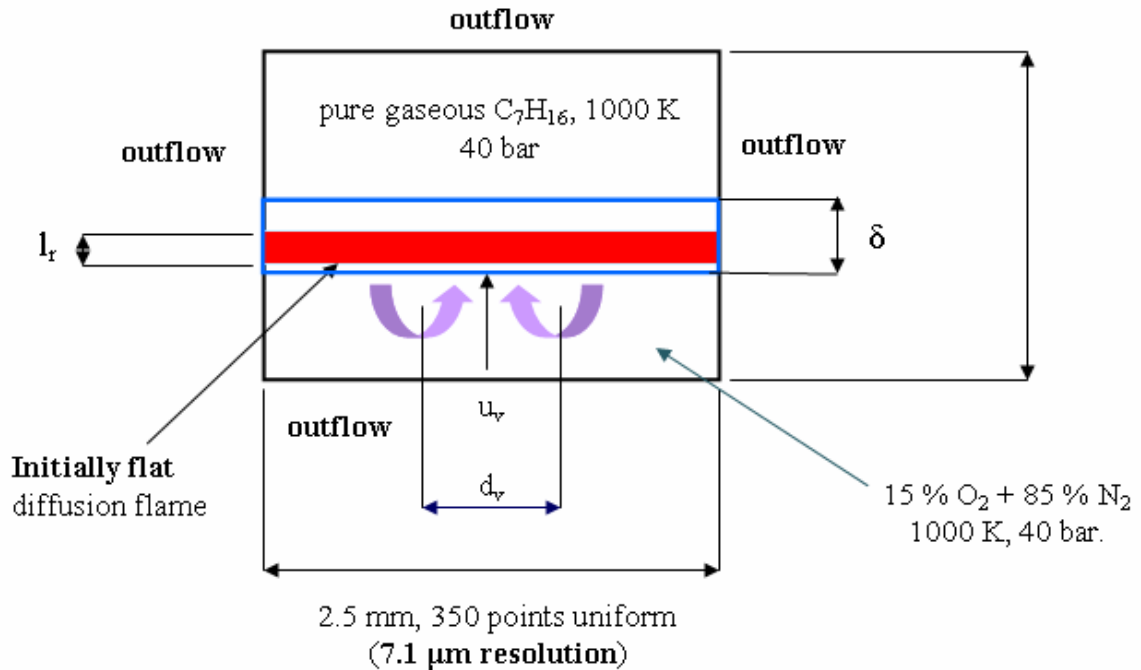
Figure 4.3. Schematic of the computational set up for the flame-vortex simulations.

The fuel-side and the air-side temperatures are equal to 1000 K. The simulated pressure is 40 bar, which is representative of diesel engine combustion chambers. Note that lower fuel temperatures (~ 400 K) are typical in diesel applications. In the LES study, a higher fuel temperature is chosen to minimize the density gradients resulting from relatively large values of the injected-to-ambient gas density ratio, which is about 3.5 with T_{fuel} = 1000 K, as against about 8 with T_{fuel} = 400 K. Even though the choice of a lower density ratio (due to a higher fuel temperature) affects the predicted statistics in the isothermal jet computed with LES, the statistics are expected to show scaling behavior with respect to the density ratio (Pitts, 1991; Abraham, 1996). On the other hand, the

higher fuel temperature (= 1000 K) would lead to shorter chemical time scales and stronger flames. We will discuss the implications of choosing a higher fuel temperature for the findings from the flame-vortex simulations (Chapters 6 and 7) through comparisons with our recent studies (Venugopal and Abraham, 2008a,b) employing a lower fuel temperature (= 450 K).

To obtain initial conditions for the diffusion flame, we employ a 1-D laminar flamelet-code (Gopalakrishnan and Abraham, 2002) which solves the following time-dependent flamelet equations in mixture fraction Z space (Peters, 1984):

$$\rho \frac{\partial Y_i}{\partial t} = \rho \frac{\chi}{2} \frac{\partial^2 Y_i}{\partial Z^2} + \dot{w}_i, \tag{4.14}$$

$$\rho \frac{\partial T}{\partial t} = \rho \frac{\chi}{2} \frac{\partial^2 T}{\partial Z^2} + \frac{1}{c_p} \frac{\partial p}{\partial t} - \sum_{i=1}^{n} \frac{h_i^0}{c_p} \dot{w}_i, \tag{4.15}$$

where p is the gas pressure, T is the temperature, ρ is the mixture mass density, Y_i, $\dot{w}_i$ and h_i^0 are the mass fraction, production/destruction rate and standard specific enthalpy of species i, respectively, and c_p is the mixture specific heat. Here, unity species Lewis numbers are assumed and χ is the instantaneous scalar dissipation rate, which is assumed to depend on Z according to the relation (Peters, 1984)

$$\chi = \frac{\chi_{st} \exp\{-2[erfc^{-1}(2Z)]^2\}}{\exp\{-2[erfc^{-1}(2Z_{st})]^2\}}, \tag{4.16}$$

where Z_{st} is the stoichiometric mixture fraction and χ_{st} is the scalar dissipation rate at Z_{st}. Using χ_{st} as an input parameter and air and fuel-side temperatures and pressure identical to the 2-D DNS setup, steady-state profiles of Y_i and T are obtained as functions of Z and initialized on the 2-D grid. Note that this flamelet-code has been employed in several prior studies focusing in diesel jet flames (Gopalakrishnan and Abraham, 2002, 2004; Venugopal and Abraham, 2007a), and is used for the unsteady flamelet studies discussed in Chapter 9.
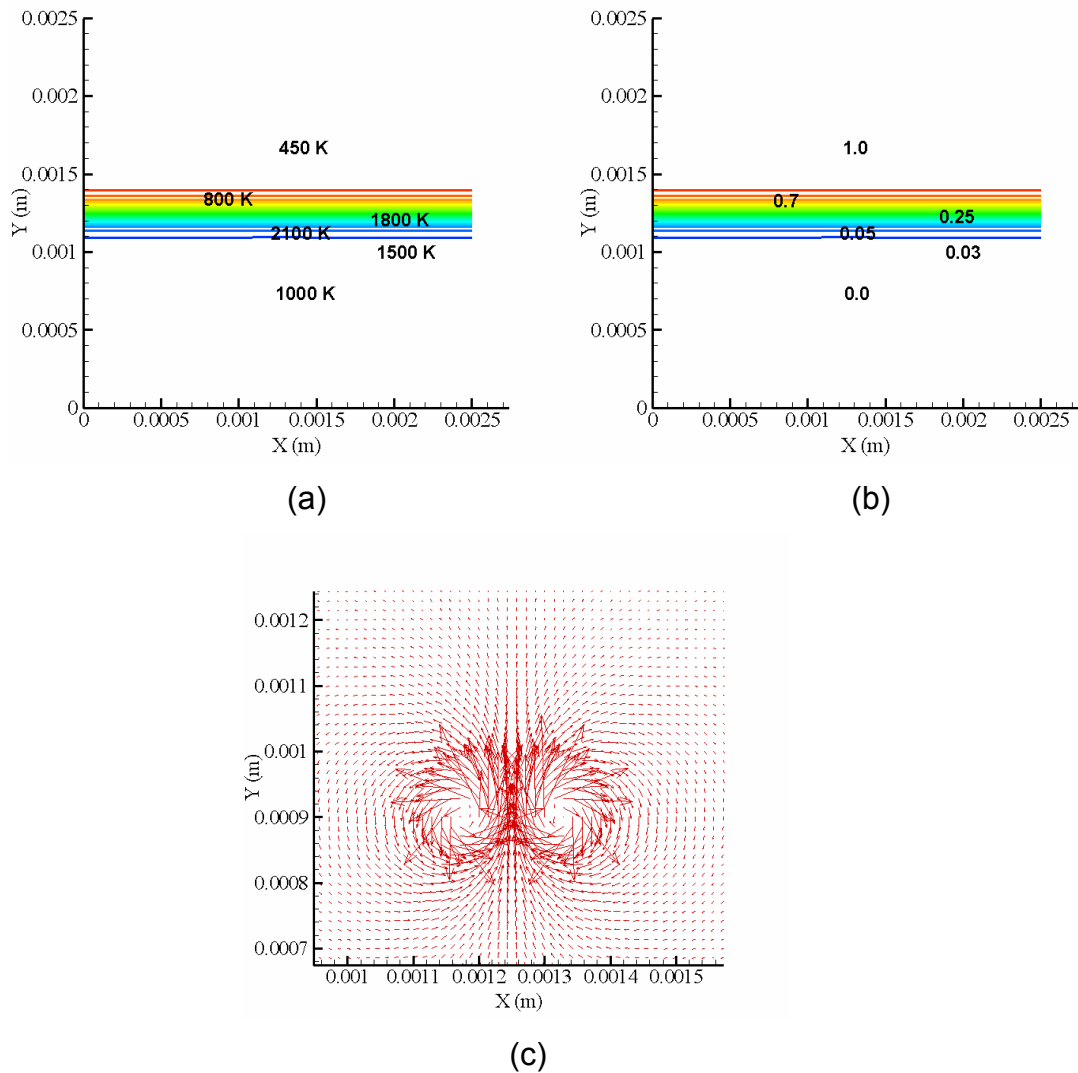
Figure 4.4. Initial conditions; (a) T (K) contours, (b) Z contours and (c) velocity vectors (every 2nd vector is shown).

The T and Z contours in the initial unperturbed flame are shown in Figs. 4.4 (a) and (b), respectively. Note that the peak temperatures are attained close to Z_{st}, which is about 0.05 for the diluted n-heptane-air diffusion flame considered here. Each vortex of the counter-rotating vortex-pair is superimposed on the initial flowfield as an Oseen-Hammel vortex (Renard *et al.*, 2000) according to the expression

$$u_\theta = \frac{\Gamma}{2\pi r}\left(1 - \exp\left(-\frac{r^2}{\sigma^2}\right)\right), \qquad (4.17)$$

where u_θ is the circumferential velocity, Γ is the circulation, r is the radial distance from the vortex center, and σ is the core radius, which is sufficiently small compared to the initial vortex diameter d_v to begin with ($\sigma < 0.3 d_v$), and thereafter increases with time due to viscous action. In Eq. (4.17), Γ is an input parameter that characterizes the velocity-scale u_v of the vortex-pair and the Reynolds number of the vortex. This technique of impulsively starting the vortex has been employed in prior flame-vortex interaction studies (Cuenot and Poinsot, 1994; Renard *et al.*, 1999) . As discussed by Vera and Linan (2004), the velocity-scale u_v of the vortex-pair is the self-propagation velocity, given by

$$u_v = \frac{\Gamma}{2\pi d_v} . \qquad (4.18)$$

All the vortices considered in this study are initialized at a distance of about 2.5δ from the peak temperature location in the flame. Though this location lies in the thermal layer, we found that the vortex strength is negligibly affected due to viscous dissipation prior to interaction with the flame owing to the relatively high vortex Reynolds numbers employed (> 100). Figure 4.4(c) shows the initial velocity vectors for the simulated vortex-pair. Now, we will discuss the important non-dimensional numbers which characterize the problem.

4.4.2. Non-dimensionalization

The following non-dimensional numbers, which govern the flame-vortex interaction, can be constructed from the vortex and flame scales shown in Fig. 4.3:

(a) Flame Damkőhler number Da**.** Based on the stoichiometric scalar dissipation rate χ_{st} and a chemical time-scale τ_c (see Eq. (4.12)) for the flame, a flame Damkőhler number Da can be defined as:

$$Da = \left(\chi_{st} \tau_c \right)^{-1}, \tag{4.19}$$

where τ_c is also estimated at Z_{st} similar to χ_{st}.

Note that in Eq. (4.19), χ_{st} and τ_c are instantaneous quantities and vary as a function of time and space along the stoichiometric isocontour during the flame-vortex interaction. The initial value of this Damkőhler number, Da_i, is a measure of the strength of the unperturbed flame. Based on the time-averaged conditional mean scalar dissipation rates computed with LES in the near-field (x/d < 25) of the 70,000 Reynolds number jet (see Chapter 5), and the chemical time scales from the single-step model, estimated values of Da_i lie in the range of 10-100. In Chapter 6, we will employ a flame extinction criterion based on Da that is suitable for unsteady flames.

(b) Length-scale ratio l_r. A vortex-to-flame length-scale ratio l_r can be defined as

$$l_r = \frac{d_v}{\delta}, \tag{4.20}$$

where d_v is the initial diameter of the vortex-pair, as shown in Fig. 4.3 and δ is the initial thickness of the diffusion layer, which serves as a length-scale for the initial flame. Based on the mean integral and Taylor length scales, and the mean diffusion length scales estimated from the LES in the jet near-field, l_r varies in the range 0.3-3.0, which represents vortices smaller and larger than the initial flames. It will be shown in Chapters 6 and 7 that l_r characterizes the effects due to the vortex-induced curvature on the flame structure.

(c) Velocity-scale ratio u_{fv}. Based on the velocity scales for the vortex and the flame, we can define a vortex-to-flame velocity scale ratio u_{fv} as

$$u_{fv} = \frac{u_v}{u_f}, \tag{4.21}$$

where u_v is the self-induced propagation speed of the vortex-pair (see Eq. (4.18)), and u_f is a velocity-scale for the flame, estimated as

$$u_f = \frac{\delta}{\tau_c}. \tag{4.22}$$

u_{fv} is a measure of unsteady effects caused by the vortex on the flame-response and varies in the range 1.0-6.0 in this work, based on the LES statistics estimated in the near-field of the 70,000 Reynolds number jet.

(d) Vortex Reynolds number Re_v. A Reynolds number Re_v can be defined for the vortex-pair as

$$Re = \frac{u_v \cdot d_v}{v}, \tag{4.23}$$

where v is the kinematic viscosity. In the present study, the estimated range of d_v and u_v from the LES result in Re_v values in the range of 60-2000. Note that prior works have considered values of Re_v up to about 600. The implications of the relatively high values of Re_v employed here are discussed in Chapters 6 and 7. Moreover, since Re_v depends on both d_v and u_v, it represents the combined effects of unsteadiness and curvature.

(e) Scalar dissipation ratio χ_r. In addition to u_{fv}, we define a scalar dissipation ratio χ_r as a measure of unsteady effects, where

$$\chi_r = \frac{\chi_{st}}{\chi_e}. \tag{4.24}$$

In Eq. (4.24), χ_e is the steady extinction limit (Peters and Williams, 1983), which is estimated using the 1-D flame code described in Section 4.4.1 by gradually increasing the scalar dissipation rate till extinction is observed. Note that χ_{st} is the instantaneous scalar dissipation rate during the flame-vortex interaction. It will be shown in the flame-vortex (Chapters 6 and 7) and the unsteady flamelet

(Chapter 9) studies that values of χ_r greater than unity at extinction represent effects due to unsteadiness, which result in unsteady extinction limits higher than steady values.

In addition, a non-dimensional time t* defined as t* = t/t$_{eddy}$ is employed, where t$_{eddy}$ is the initial vortex (or eddy) turnover time-scale($\sim d_v/u_v$).

4.4.3. 2-D Code Speed-up
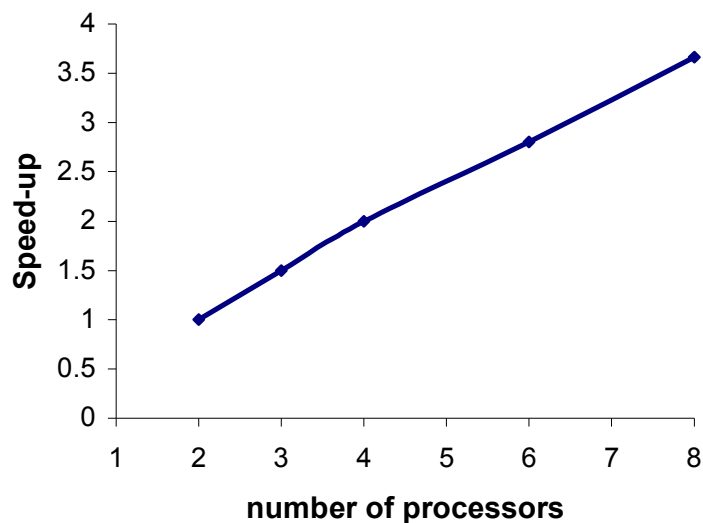
Figure 4.5. Speed-up performance of the 2-D flame-vortex code.

The parallelization of the FLEDS code was discussed in Section 3.8.3. The flame-vortex interaction studies are performed on an IBM-SP with 373 MHz POWER3-II processors. Figure 4.5 shows the speed-up performance of the 2-D code with up to 8 processors. In Fig. 4.5, the speed-up is computed as the ratio of the CPU time with a given processor to the CPU time with 2 processors. It is observed that the speed-up is very nearly linear. As discussed in Section 3.8.3 in the context of the speed-up with the 3-D code, the increase in the communication time relative to the computational time with higher number of processors (> 32)

affects the speed-up. The flame-vortex simulations are performed with 8 processors. On an average (i.e. over a range of vortex and flame characteristics), the CPU time for the simulations is about 6 days.

4.5. Summary

In this chapter, the problem formulation for the flame-vortex interaction studies was presented. Similar to the LES, a 6th-order compact finite-difference scheme is employed for spatial discretization while time-integration is performed with a compact storage 4th-order Runge-Kutta scheme. Non-reflecting NSCBC outflow BCs are employed at all the boundaries. The 2-D computational domain is initialized with a 1-D diffusion flame and a counter-rotating vortex-pair is allowed to self-propagate towards the flame. Chemistry is modeled through both single-step and multistep kinetic models. The simulated pressures and temperatures are representative of diesel engine combustion chambers. The initial vortex and flame characteristics, and the range of governing non-dimensional numbers for the flame-vortex interaction are derived from mean temporal statistics computed with LES at different locations in the jet.

In the chapter that follows, results from the LES of the near-field of a 70,000 Reynolds number variable-density round jet are presented. Turbulent statistics of the velocity and mixture fraction fields are computed, and compared with available experimental data in self-similar jets. Statistics of interest, i.e. l, q and χ are estimated at different locations in the jet near-field.

CHAPTER 5. LES OF THE NEAR-FIELD OF A HIGH-REYNOLDS NUMBER VARIABLE-DENSITY ROUND JET

5.1. <u>Introduction</u>

In this chapter, results from the LES of a 70,000-Re variable-density round gaseous fuel jet are presented. The jet is isothermal and the near-field of interest is about 25 jet diameters in the axial direction. The problem formulation comprising numerical methods, computational setup and initialization for the LES were described in Chapter 3. In this work, the LES of the jet near-field is employed to estimate (temporal) mean turbulent length and velocity scales, and time-averaged and turbulent time records of conditional-mean scalar dissipation rates. While the mean length and velocity scales, and the time-averaged conditional mean scalar dissipation rates are used to select vortex and flame characteristics in the flame-vortex studies (Chapters 6 and 7), the turbulent time records of conditional mean scalar dissipation rates are employed in studies of diffusion flamelets subjected to scalar dissipation rate fluctuations (Chapter 9). The coupling between the LES, and the flame-vortex and unsteady flamelet studies provides useful insight into the near-field flame dynamics in high-Reynolds number jets encountered in diesel engine applications.

In Section 5.2, the salient features of the instantaneous flowfield of the jet are discussed. Thereafter, in Section 5.3, turbulent statistics of the velocity-field obtained by temporal and spatial (azimuthal) averaging are presented which includes mean velocities, centerline decay and spreading rates, turbulence intensities, velocity-scales, autocorrelations and integral length-scales. Mean scalar dissipation rates and statistics of the mixture fraction field are discussed in Section 5.4. In both Sections 5.3 and 5.4, the computed results are compared

with published experimental data for self-similar isothermal round jets. The chapter closes with summary and conclusions in Section 5.5.

5.2. Instantaneous Flowfield

Recall from Section 3.7 that the LES is performed on a 3-D stretched Cartesian grid in a domain measuring 40x14x14 in terms of jet exit diameters with 401x113x113 grid points. The first 25 diameters form the physical part of the computational domain, beyond which a buffer region with exponential grid-stretching and artificial damping is employed to remove fluctuations and spurious pressure waves at the outflow boundary. The jet diameter d is 1 mm and the Reynolds number based on d and the injection velocity U_{inj} of 42.5 m/s is about 70,000. Gaseous n-heptane at 1000 K is injected into an ambient comprising 15% O_2 and 85% N_2 by mole fraction at 1000 K. A relatively small co-flow velocity of 0.425 m/s is employed in the ambient.

Figure 5.1 shows the isosurface of the instantaneous filtered stoichiometric mixture fraction, $\widetilde{Z} = 0.05$, in the jet at 2.45 ms after start of injection (ASI). We observe a potential core region which is essentially laminar followed by transition to turbulence and growth of coherent vortex structures. Beyond 25 diameters, the structures dissipate in the buffer region due to the relatively coarse grid and artificial damping. Fig. 5.2 shows three isocontours of $\widetilde{Z}$ on the center z-x plane at 2.45 ASI. The $\widetilde{Z} = 0.05$ contour appears significantly wrinkled and stretched in the figure. The potential core region (region of uniform $\widetilde{Z}$ in the axial direction) is observed to extend up to about 8 diameters.

Figure 5.3 shows the isocontours of the instantaneous vorticity $\widetilde{\Omega}$ in the jet at 2.45 ASI. The development of fine-scale turbulence following the potential core is evident. This is possibly due to vortex-pairing and breakdown (Pope, 2000). We also observe streaks of high values of $\widetilde{\Omega}$ (darker contours), for instance $\widetilde{\Omega} = 200,000\,\text{s}^{-1}$, indicating regions of high shear.
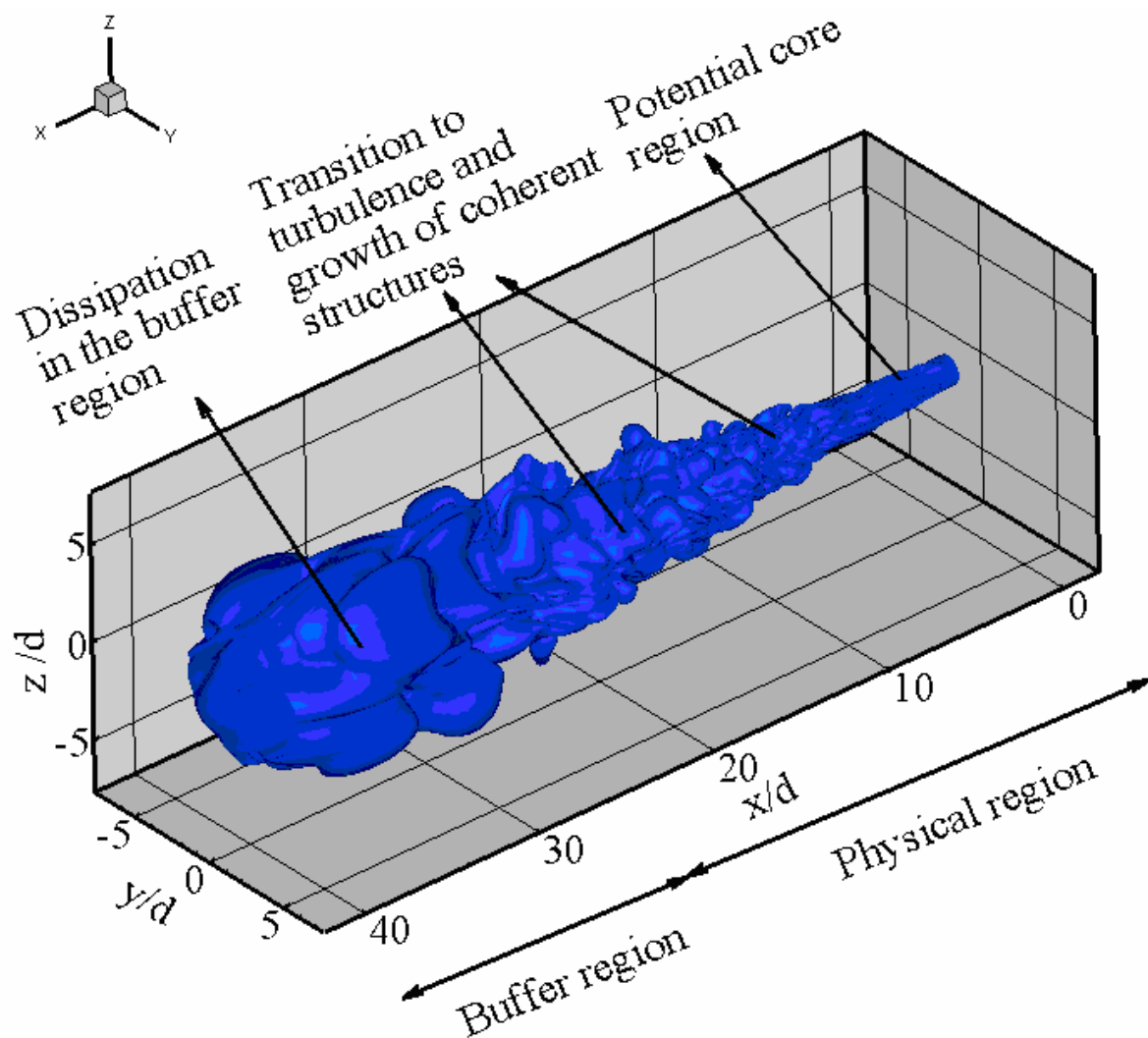
Figure 5.1. Isosurface of $\widetilde{Z} = 0.05$ in the jet at 2.45 ms.
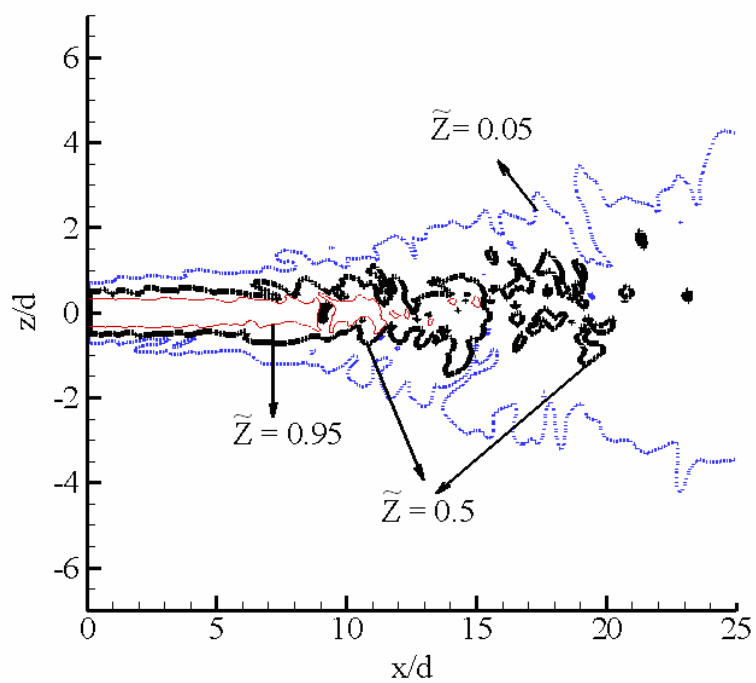
Figure 5.2. Isocontours of $\widetilde{Z}$ in the center z-x plane at 2.45 ms.
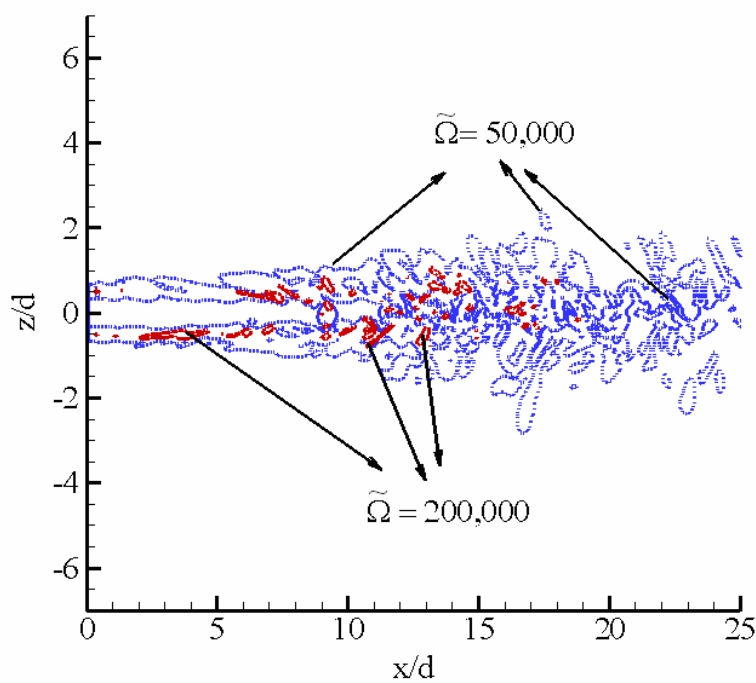
Figure 5.3. Isocontours of vorticity $\widetilde{\Omega}$ (1/s) at 2.45 ms ASI.
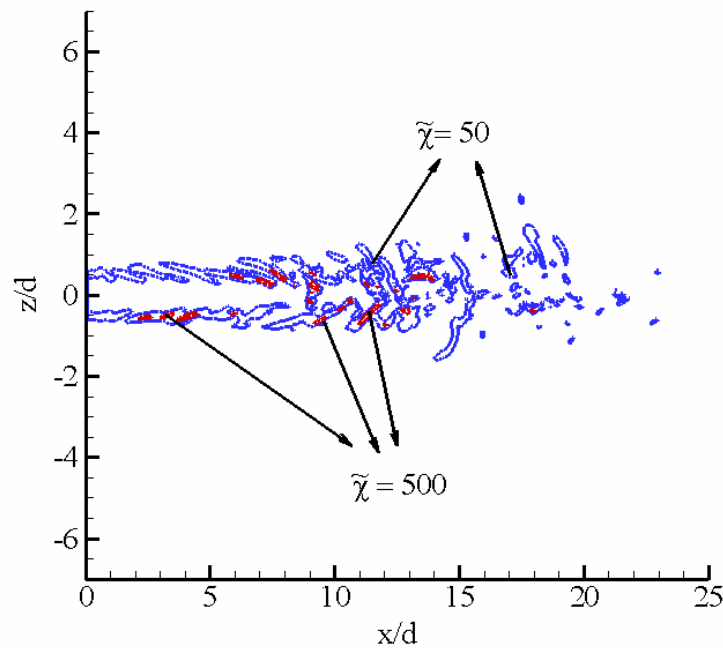
Figure 5.4. Isocontours of the filtered scalar dissipation rate $\widetilde{\chi}$ (1/s) at 2.45 ms ASI.

The isocontours of the filtered scalar dissipation rate $\widetilde{\chi}$ is shown in Fig. 5.4. Following Girimaji and Zhou (1996), $\widetilde{\chi}$ is modeled as

$$\widetilde{\chi} = 2(D_t + D_l)(\nabla\widetilde{Z})^2,$$ (5.1)

where D_l is the laminar mass diffusivity and D_t is the turbulent mass diffusivity of the mixture, estimated as

$$D_t = \frac{v_t}{Sc_t}.$$ (5.2)

In Eq. (5.2), v_t is the eddy viscosity computed from the constant-coefficient Smagorinsky subgrid scale model (see Eq. (3.12)), and Sc_t is the turbulent Schmidt number, assumed to be 0.9 in this work. The model expression given by Eq. (5.1) accounts for interactions between the subgrid scales but not for interactions between the resolved and the subgrid (unresolved) scales of

turbulent motion. Hence, effects such as backscatter are not represented in this model for $\tilde{\chi}$. Neglecting the interactions between the resolved and the unresolved scales is, however, reasonable at relatively high-Reynolds numbers with an adequate inertial sub-range, such as the present case, where most of the scalar dissipation occurs at the subgrid scales. Figure 5.4 shows that like in the case of $\tilde{\Omega}$ (see Fig. 5.3), relatively high values of $\tilde{\chi}$ are interspersed between relatively low values. The strong spatial fluctuations of $\tilde{\chi}$ are evident in Fig. 5.5, which shows $\tilde{\chi}$ along the centerline of the jet as a function of the axial distance. Such fluctuations could potentially lead to extinction and reignition in a reacting jet. We will characterize the fluctuations of $\tilde{\chi}$ in detail later.
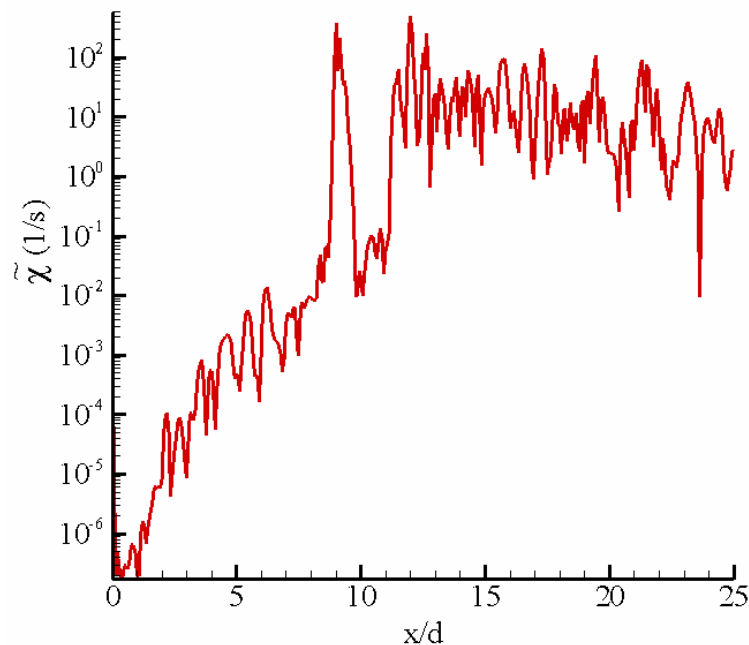
Figure 5.5. $\tilde{\chi}$ (1/s) vs. x/d along the centerline of the jet at 2.45 ms ASI.

5.3. Mean Flowfield

To estimate mean turbulent statistics of the velocity field and the mixture fraction field, time averaging of the instantaneous flowfield is performed. In

addition, since a round jet is axisymmetric in the mean, azimuthal (theta) averaging is also performed to generate axisymmetric results. In the present work, 3-D instantaneous data of the quantities of interest were collected every 0.01 ms and averaging was performed over 346 such datasets, i.e., over 3.46 ms. If the flow time of the jet is of the order of $L/U_{\text{inj}} = 0.025\ m/42.5\ m/s \sim 0.59\ ms$, where L is the length of the physical part of the domain, the averaging time is about 6 flow times. The transients exited the physical part of the domain by 0.8 ms ASI and then averaging was performed from 0.8 ms to 3.73 ms. We will first discuss statistics computed from the velocity field and then focus on the mixture fraction field.

5.3.1. Velocity-field Statistics

Figures 5.6 and 5.7 show the isocontours of the mean axial velocity U and the mean turbulent kinetic energy TKE in the jet. U and TKE are computed according to the following set of equations:

$$U = \langle u_1 \rangle = \frac{\sum\limits_{n=1}^{N} u_1^n}{N},$$

$$TKE = 0.5 \left\langle \sum_{k=1}^{3} u_k'^2 \right\rangle = 0.5 \left\langle \sum_{k=1}^{3} u_k^2 \right\rangle - 0.5 \left\langle \sum_{k=1}^{3} u_k \right\rangle^2. \tag{5.3}$$

In Eq. (5.3), u_k^n is the instantaneous filtered velocity at the nth time-interval in the kth Cartesian direction (k=1 is the axial direction and k=2, 3 denote transverse directions), $\langle\ \rangle$ denotes time-averaging, N is the total number of time-intervals considered, and u_k' is the instantaneous velocity fluctuation in the kth Cartesian direction. The mean contours shown in the figures are similar to those that may be obtained from Reynolds-averaged Navier Stokes (RANS) modeling. As expected, U decreases as we proceed downstream in the axial direction and radially away from the center of the jet. Figure 5.7 shows that the TKE reaches a maximum value at a certain distance ($x/d \sim 11$) beyond the potential core in the

jet shear layers. Beyond this axial distance, the TKE decays as we proceed downstream in the jet.
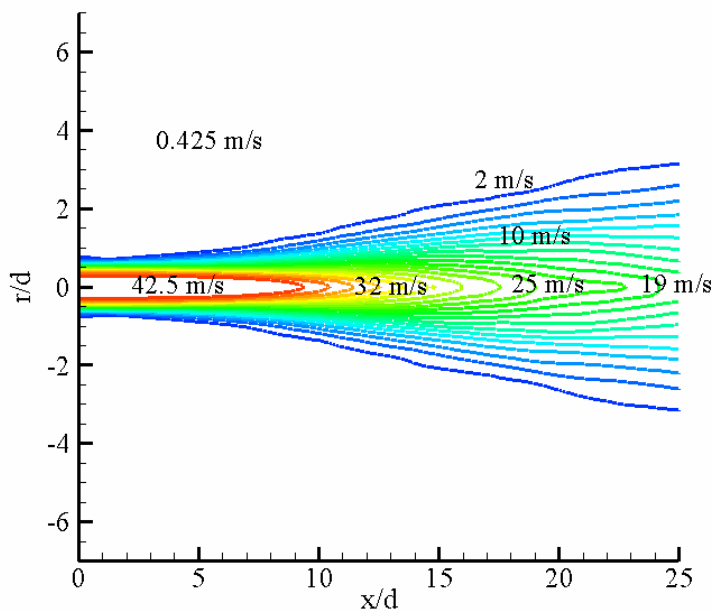
Figure 5.6. Isocontours of mean axial velocity U (m/s) in the jet.
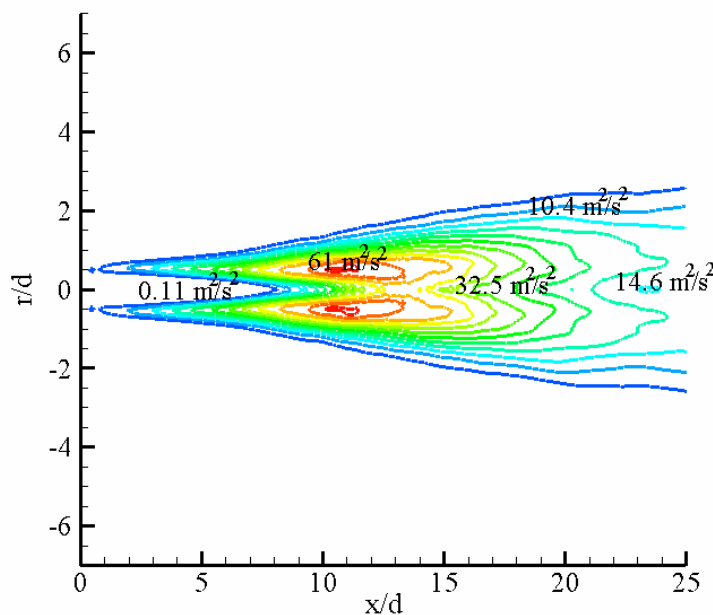
Figure 5.7. Isocontours of mean turbulent kinetic energy TKE (m^2/s^2).
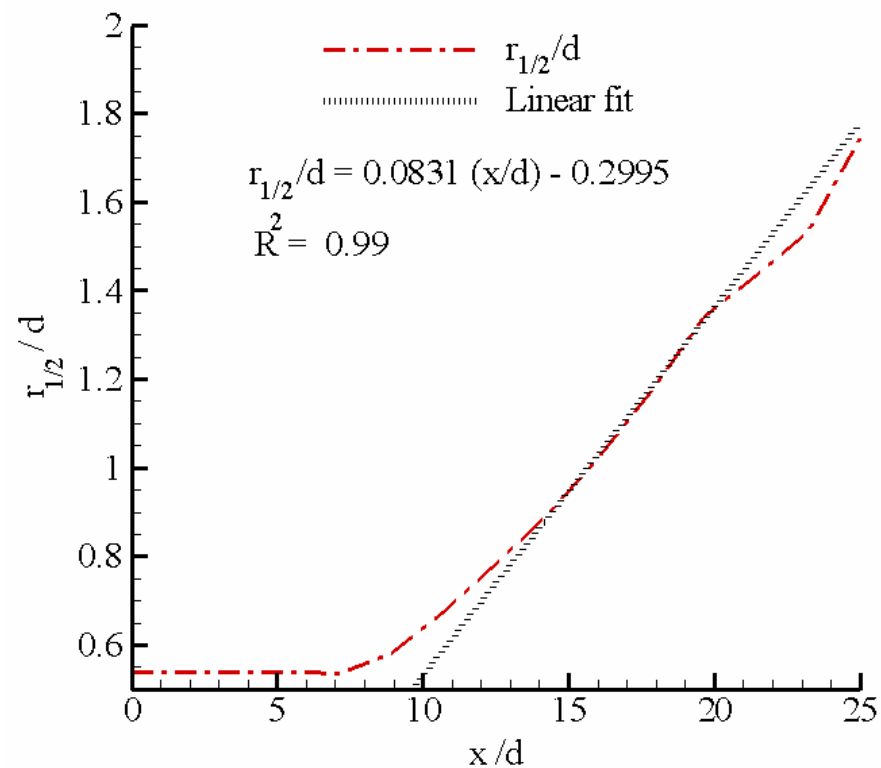
Figure 5.8. Jet half-width $r_{1/2}/d$ as a function of axial distance x/d.

The spreading rate and the centerline velocity decay rate were estimated from the mean axial velocity. Figure 5.8 shows the normalized jet half-width $r_{1/2}/d$ based on U plotted as a function of the axial distance x/d. Beyond the potential core of about 8 jet diameters, $r_{1/2}/d$ increases as expected. Note that in Fig. 5.8, $r_{1/2}$ is computed through interpolation between two radial locations at a given axial location in the jet where U/U_{cl} is close to 0.5. The computed spreading rate, given by the slope of a linear fit to the data, is about 0.0831 in the region $14 \leq x/d \leq 20$, as shown in Fig. 5.8. This value agrees within 25 % with the measured range of 0.094-0.102 reported by Hussein *et al.* (1994) and is about 15 % lower the value of 0.096 reported by Panchapakesan and Lumley (1993a)

through measurements in the self-similar region of round jets. Experiments (Wygnanski and Fiedler, 1969; Panchapakesan and Lumley, 1993a; Hussein *et al.*, 1994) indicate that self-similarity of the mean velocities is achieved only beyond 30 diameters. Hence, apart from the inadequacies of the subgrid-scale model, the lack of self-similarity in the simulated near-field of the jet may be responsible for the discrepancy between the computed and measured values of the spreading rate.
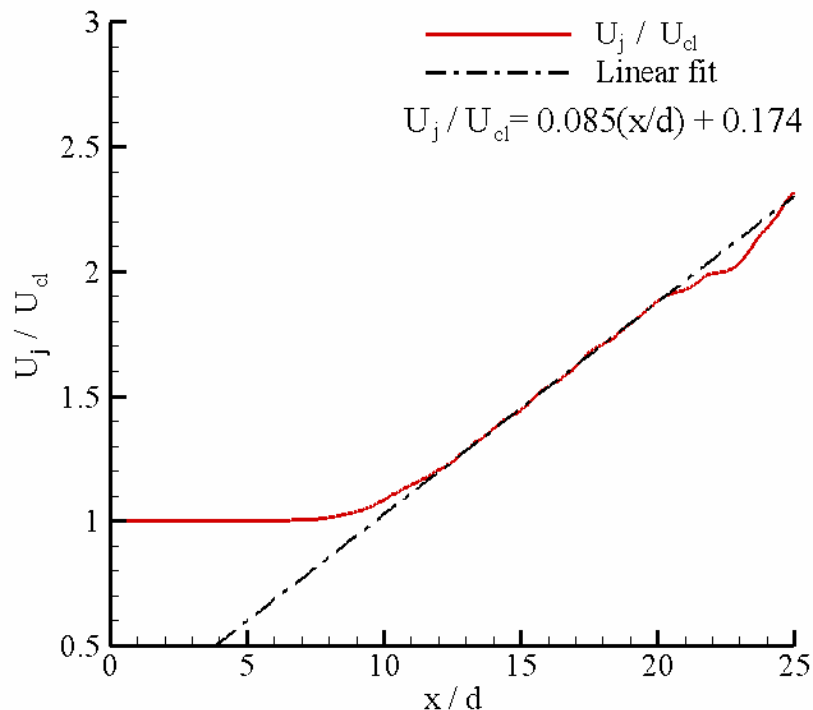
Figure 5.9. U_j/U_{cl} as a function of x/d in the jet.

To investigate the decay rate of the mean centerline velocity U_{cl}, consider Fig. 5.9 that shows the ratio, U_j/U_{cl} where U_j is the injection velocity, as a function of the axial distance in the jet. The velocity decay constant, given by the inverse of the slope of a linear fit to the data, is estimated to be about 11.76 (~1/ 0.085) in the region $14 \leq x/d \leq 20$. As indicated in the experiments of

Panchapakesan and Lumley (1993b) on helium jets injected into air, the decay constant shows a dependence on the injected-to-ambient gas density ratio, ρ_j / ρ_a. In the present case, ρ_j / ρ_a is about 3.5. Hence, we need to account for the density-ratio effect before comparing with the constant-density experimental data. This is achieved by introducing the effective diameter, d_e as

$$d_e = d \cdot \left(\rho_j / \rho_a \right)^{1/2}. \tag{5.4}$$

Hence, the computed decay constant after accounting for the density-ratio effects is $11.76 / (3.5)^{1/2} \sim 6.32$. This value agrees within 10 % with the range 5.8-5.9 reported by Hussein *et al*. (1994) for their 95,500 Reynolds number jet, and is about 5 % higher than the value of 6.06 reported by Panchapakesan and Lumley (1993a) for their 11,000 Reynolds number jet in the self-similar region.
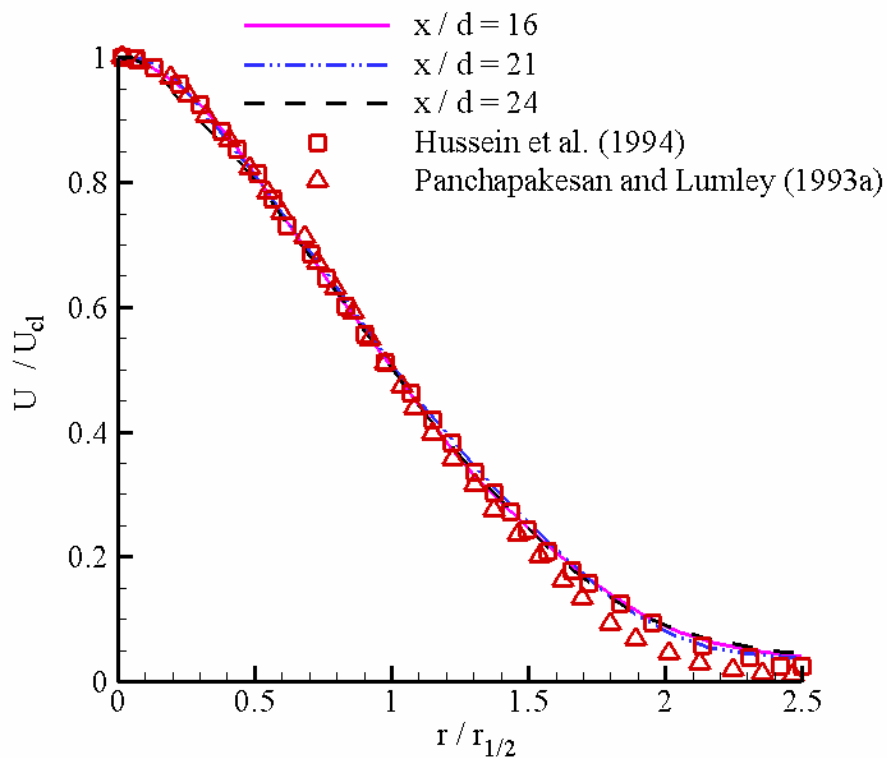
Figure 5.10. Computed normalized radial profiles of U compared to experiments.

To investigate self-similarity of U in the jet, consider Fig. 5.10 which compares the computed radial profiles of U at different axial locations with the self-similar profiles reported in the experiments of Panchapakesan and Lumley (1993a) and Hussein *et al.* (1994). U is normalized by the centerline velocity U_{cl} whereas the radial location r is normalized by the jet half-width $r_{1/2}$. We observe that the computed profiles are nearly superimposed for $x/d = 21$ and $x/d = 24$, indicating self-similarity. The computed values are within 6% of the experimental ones.
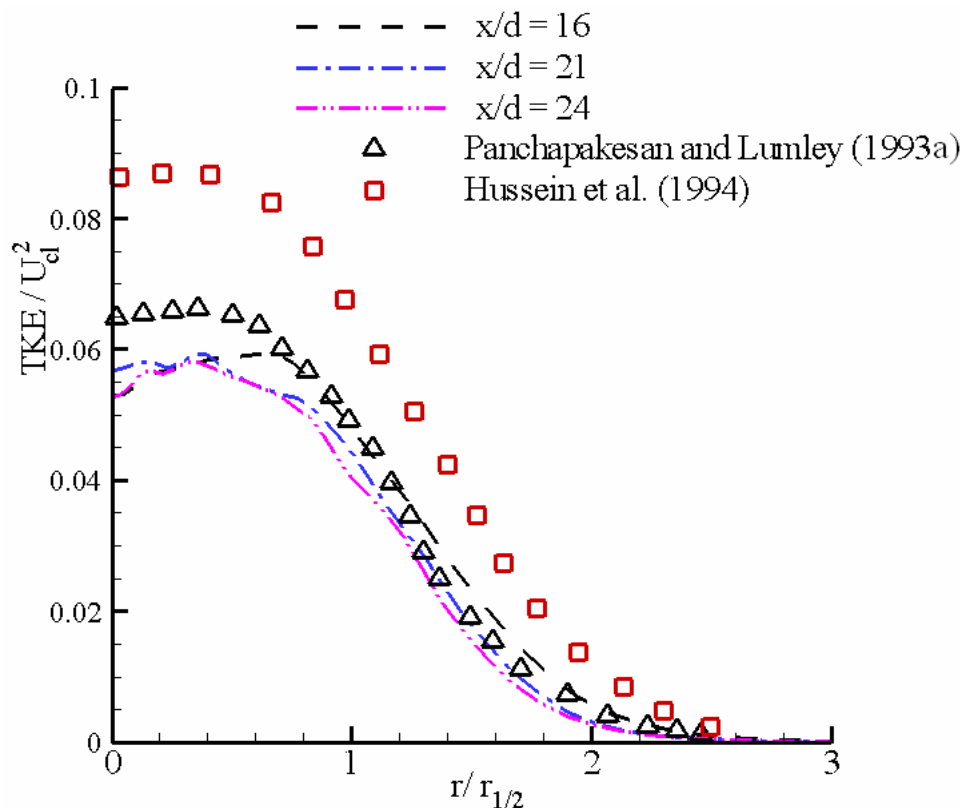
Figure 5.11. Computed radial profiles of normalized *TKE* at different axial positions in the jet.

Figure 5.11 shows the computed radial profiles of the mean turbulent kinetic energy *TKE* (see Eq. (5.3)) at three different axial locations in the jet. The *TKE* has been normalized by U_{cl}^2. The measured profiles of Panchapakesan and

Lumley (1993a) and Hussein *et al.* (1994) in the self-similar region are also shown for comparison. The measured profiles of TKE were obtained from the trace of the normal Reynolds stresses reported in the experiments. We observe from the figure that unlike the profiles of U, the TKE profiles are not superimposed even beyond $x/d = 20$ indicating that the jet has not achieved self-similarity with respect to the TKE. The computed values agree within 15 % with the data of Panchapakesan and Lumley (1993a) in their 11,000 Reynolds number jet but deviations up to 31 % are observed with the profile of Hussein *et al.* (1994) in their 95,500 Reynolds number jet . The experiments of Wygnanski and Fiedler (1969) indicate that the Reynolds stresses (and hence the TKE) show self-similar behavior only beyond 50 jet diameters. Hence, quantitative agreement of the computed profiles with the measured profiles in self-similar jets is not expected. Moreover, we observe discrepancies up to 30 % between the two sets of experimental data in Fig. 5.11 Hussein *et al.* (1994) attribute these differences to differences in the jet Reynolds number, which was 95,500 in the case of Hussein *et al.* (1994) and 11,000 in the case of Panchapakesan and Lumley (1993a).

It is also likely that the chosen constant of the Smagorinsky subgrid-scale model, 0.012, underestimates the eddy viscosity and hence the Reynolds stresses and the TKE. Uzun (2003) demonstrates that the computed Reynolds stresses are highly sensitive to the choice of the model constant and reports better agreement with a constant of 0.018. Similarly, Bogey *et al.* (2003) show good agreement with the self-similar profile of Hussein *et al.* (1994) with a constant of 0.0381. It is therefore possible that with a value higher than 0.012 for the Smagorinsky constant, the computed profiles may be closer to the experimental data. Uzun (2003) also indicates additional factors such as the influence of inlet conditions used in the LES and effects due to the nozzle geometry which are not accounted for in the computations. It is encouraging, however, that the values compare reasonably well with those of Panchapakesan

and Lumley (1993a), and the radial location of the peak TKE and the shape of the profile are close to those in the measured data.

From the knowledge of the TKE, the velocity-scales in the jet can be estimated. In the present work, the mean velocity-scale q is computed as

$$q = \left(2TKE\right)^{1/2}. \tag{5.5}$$

Fig. 5.12 shows the radial profiles of the local turbulence intensity, q/U, in the jet at various axial locations. Similar to the TKE, as we move downstream in the jet, the peak intensity decays and the peak value is attained at radial locations farther from the centerline.
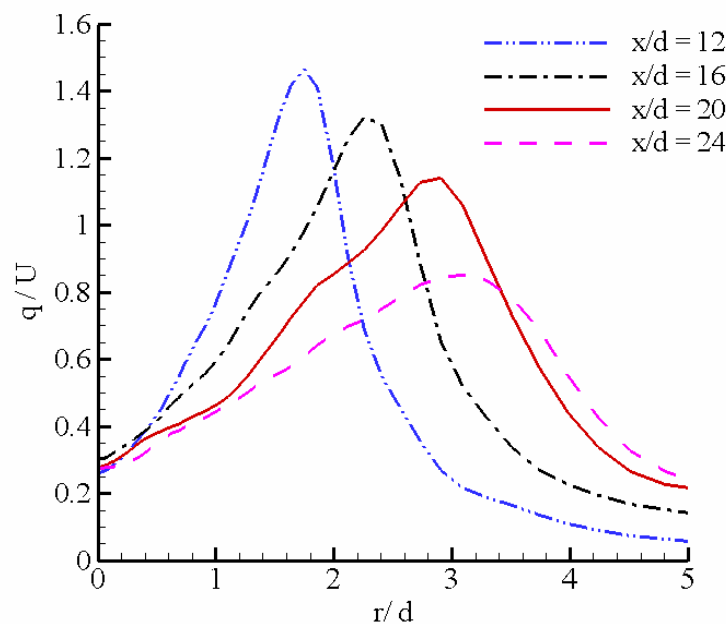
Figure 5.12. Radial profiles of turbulence intensity in the jet at different axial locations.

In addition to the mean velocity-scales, we are interested in estimating the mean integral length-scales in this work. The integral length-scales can be computed from two-point correlations of the fluctuating velocities (Pope, 2000).

For instance, the longitudinal normalized two-point autocorrelation $R_{11}(r,x,y,z)$ is given by the expression

$$R_{11}(s,x,y,z) = \frac{\langle u'(x+s,y,z) \cdot u'(x,y,z) \rangle}{\langle u'^2(x+s,y,z) \rangle^{1/2} \cdot \langle u'^2(x,y,z) \rangle^{1/2}},$$ (5.6)

where s is the separation distance. For homogenous turbulence, R_{11} is only a function of s but this may not be true in general in the present case. From the knowledge of R_{11}, the longitudinal integral length-scale $L_{11}(x,y,z)$ is estimated as:

$$L_{11}(x,y,z) = \int_{s=0}^{s=s_{max}} |R_{11}(s,x,y,z)| \, ds,$$ (5.7)

where s_{max} is the maximum value of the separation distance considered. Wygnanski and Fiedler (1969) report measured values of R_{11} up to $s = 0.2 \cdot x$. Hence, we choose $s_{max} = 0.2 \cdot x$ in the computation of the integral given by Eq. (5.7) for all the jet locations investigated.
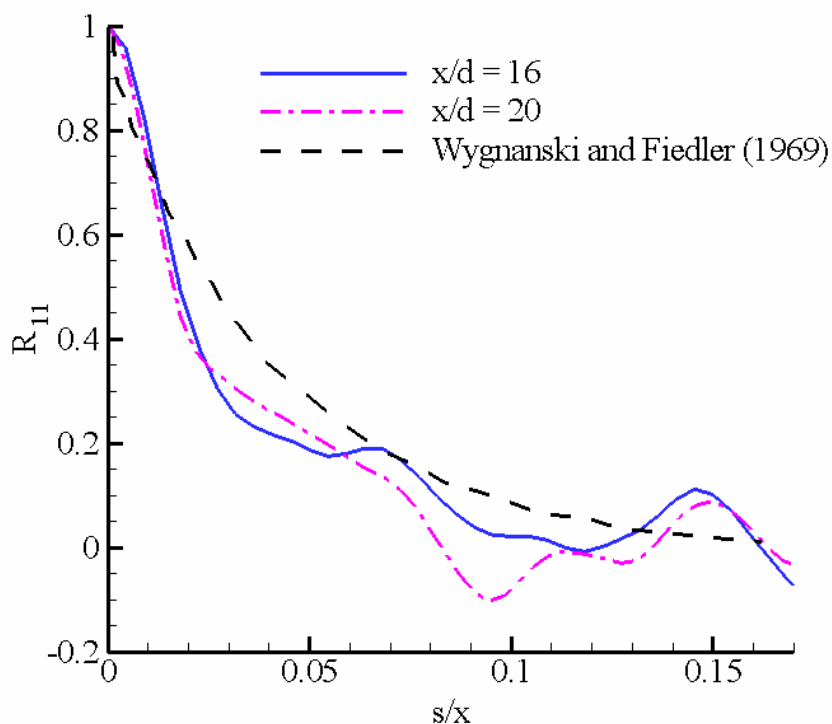
Figure 5.13. R_{11} as a function of s/x on the jet centerline.

Figure 5.13 shows the computed values of R_{11} as a function of s/x on the jet centerline at x/d = 16 and x/d = 20. The measured values of R_{11} reported by Wygnanski and Fiedler (1969) in the self-similar region of the jet ($x/d > 30$) are also shown for comparison. We observe trends similar to the experiments but quantitative differences are evident. As expected, R_{11} decreases as s increases and decreases to values close to zero at large s. Negative values of R_{11} are observed only in the computed data and not in the experiments for the range of separation distances shown. Moreover, the x dependence of R_{11} suggests that the turbulence is not homogenous in the computed jet. Using Eq. (5.7), it is estimated as $L_{11}/x = 0.0335$ at x/d = 16 and $L_{11}/x = 0.0315$ at x/d = 20. These estimates are about 12.3 % and about 17.5 % lower than the value $L_{11}/x = 0.0382$ reported by Wygnanski and Fiedler (1969) on the jet centerline in the self-similar jet.
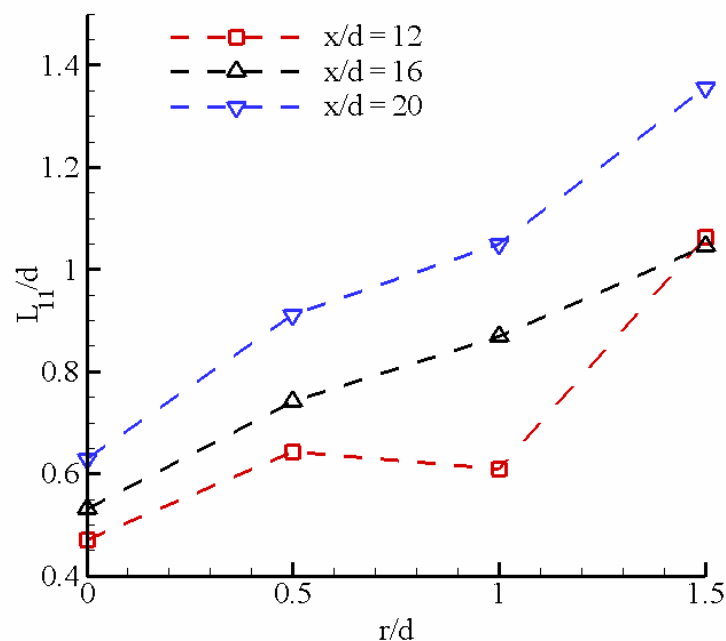
Figure 5.14. L_{11}/d as a function of r/d at different axial locations in the jet.
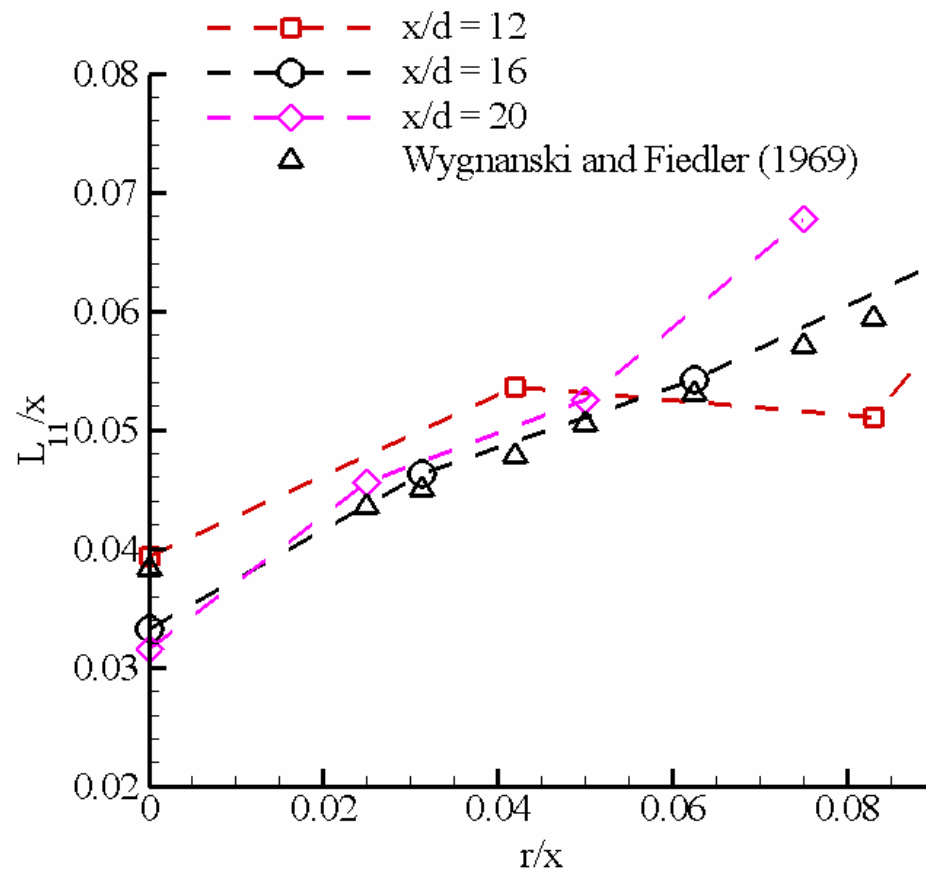
Figure 5.15. L_{11}/x as a function of r/x at different axial locations compared with the self-similar profile reported by Wygnanski and Fiedler (1969).

Figure 5.14 shows L_{11}/d as a function of r/d at three axial locations in the jet. For $x/d=16$ and $x/d=20$, L_{11} increases as x increases and as we move radially out from the centerline. However, at $x/d=12$, it appears from the limited set of computed data that L_{11} slightly decreases from $r/d=0.5$ to $r/d=1.0$ before increasing again. Note that the axial location, $x/d=12$, represents the mixing region relatively close to the potential core region ($x/d\sim8$). Similar trends were observed in the measurements of Davies *et al.* (1962) in the mixing region of round jets just downstream of the potential core region where the integral length-scales were found to decrease across the jet

shear layers. In Fig. 5.15, the normalized length-scales L_{11}/x as a function of r/x at the three axial locations are shown along with the measured data points of Wygnanski and Fiedler (1969) in the self-similar region. The quantitative agreement with the measured values is within 20 % at $x/d=16$ and $x/d=20$.

From the analysis so far, we observe that closer to the jet orifice, the characteristic length-scales (L_{11}) are smaller while the turbulence intensities (q) are larger. In the flame-vortex studies discussed in Chapters 6 and 7, we will relate L_{11} and q to the length-scale and the velocity-scale of the vortex, respectively. The implications of the nature of variation of L_{11} and q in the jet near-field for effects due to unsteadiness and curvature, and the applicability of commonly employed modeling approaches such as flamelet models will be investigated.

In addition to L_{11}, two other length-scales of interest are the Kolmogorov length-scale η and the Taylor micro-scale λ. η represents the smallest and most dissipative scale of turbulence at which turbulent straining is just overcome by molecular viscous action (i.e. $Re_\eta=1$). In the context of reacting flows, η is closely related to the validity of modeling approaches such as flamelet models since these models assume that reaction zones are thinner than η (and hence all the scales of turbulence) and therefore embedded within the turbulent eddies. On the other hand, λ lies in-between L_{11} and η in high Reynolds number turbulence but does not have a clear physical interpretation (Pope, 2000). However, λ is widely used in turbulence literature to characterize the turbulent Reynolds number in canonical flow problems like isotropic turbulence. From the knowledge of L_{11}, η and λ can be estimated using the following relations:

$$\eta=\left(L_{11}\right)^{1/4}\left(\frac{\nu}{u_1'}\right)^{3/4}, \tag{5.8}$$

$$\lambda=\left(\frac{15L_{11}\nu}{u_1'}\right)^{1/2}. \tag{5.9}$$

In Eq. (5.8) and Eq. (5.9), v is the laminar kinematic viscosity and $u_1^{'}$ is the root-mean-square axial velocity fluctuation. Note that Eq. (5.9) assumes isotropic turbulence.
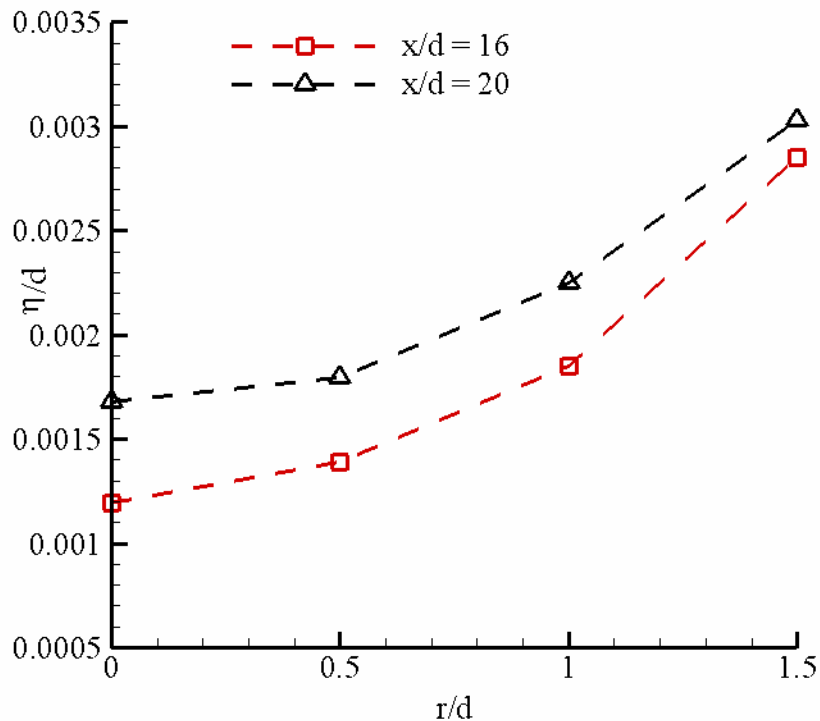
Figure 5.16. η/d as a function of r/d at different axial locations in the jet.

Figure 5.16 shows η/d as a function of r/d at two axial locations in the jet. Similar to the trends observed for L_{11}, η increases with both x and r. The values of η are of the order of $(1/1000)^{\text{th}}$ of a diameter, which is order of micrometers in the present case with $d = 1\,\text{mm}$. The normalized Taylor micro-scale, λ/d, is shown in Fig. 5.17 as a function of r/d at $x/d = 16$ and $x/d = 20$. Values of λ lie in-between L_{11} and η as expected and are roughly 2-3 times smaller than L_{11} and about an order of magnitude higher than η for the jet locations shown in the figure. This significant gap between η and λ is expected

from Eqs. (5.8) and (5.9) for the relatively high jet Reynolds numbers simulated here. The estimated values of L_{11}, λ and η provide us with a range of values for the choice of the vortex length-scales in the studies of flame-vortex interactions.
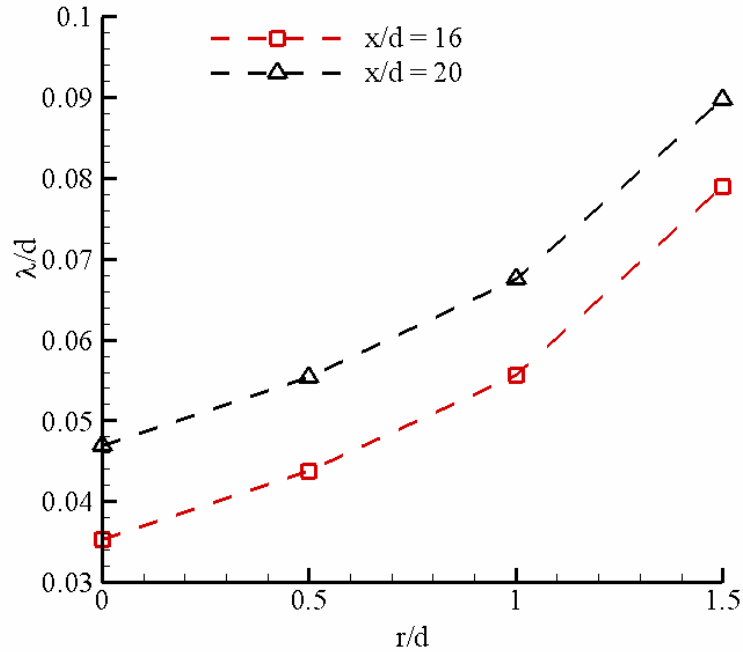
Figure 5.17. λ/d as a function of r/d at different axial locations in the jet.

5.3.2. Mixture Fraction Statistics

We will now focus on the statistics computed from the filtered mixture fraction ($\widetilde{Z}$) field. As in the case of the velocity field, we will discuss the computed jet spreading rate based on the mean filtered mixture fraction $\overline{Z}$, the decay rate of centerline $\overline{Z}$, and the filtered variance $\overline{Z}^{"2}$. The estimates from the LES will be compared to available experimental data in the literature. In addition, we are interested in the estimates of the mean scalar dissipation rates. The estimated mean scalar dissipation rate and the characteristic chemical time-scale from a single-step kinetic model are used to select an initial Damköhler number in the studies of flame-vortex interactions. Furthermore, we will characterize the

fluctuations and the probability density functions (PDFs) of the scalar dissipation rate, which can then be employed to study the unsteady response of diffusion flamelets.
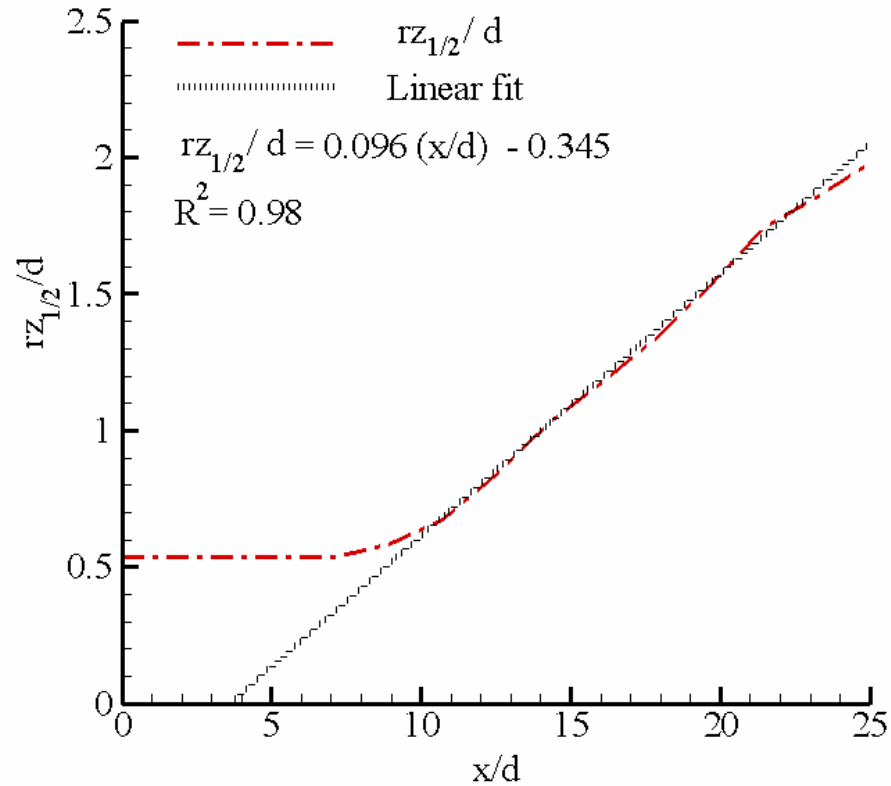
Figure 5.18. $rz_{1/2}/d$ as a function of x/d in the jet.

The jet half-width based on $\bar{Z}$, $rz_{1/2}$, is shown as a function of x/d in Fig. 5.18. As in the case of the velocity-field, the jet is observed to spread linearly. The spreading rate, estimated as the slope of the linear fit to the computed data in the region $14 \le x/d \le 20$, is about 0.096. This value lies within the range of 0.097-0.115 reported in the experiments on variable-density jets of methane and propane with jet exit Reynolds numbers in the range 4000-25000 (Birch *et al.*, 1978; Pitts and Kashiwagi, 1984; Richards and Pitts, 1993) in the region $10 < x/d < 70$.
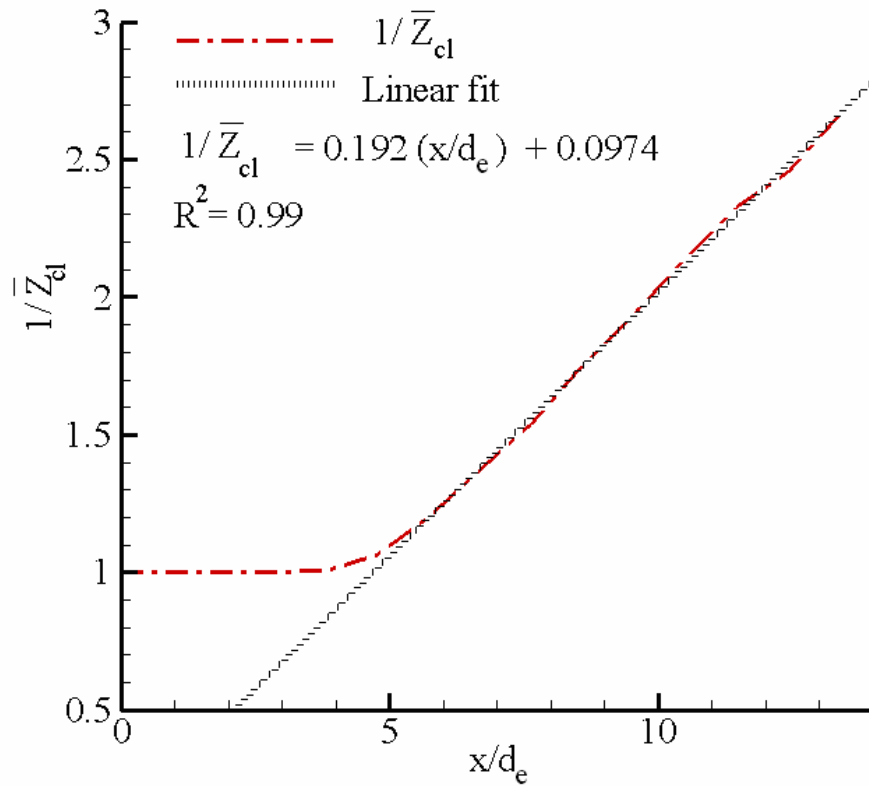
Figure 5.19. $1/\overline{Z}_{cl}$ as a function of x/d_e in the jet.

The reciprocal of the centerline mixture fraction, $1/\overline{Z}_{cl}$, is shown in Fig. 5.19 as a function of x/d_e, where d_e is an effective jet diameter introduced in Eq. (5.4). In the present case with $\rho_j/\rho_a = 3.46$, $d_e = 1.86d$. A decay rate of 0.192 is estimated from the linear fit to the computed data, which is reasonably close (within 25 %) to the range 0.212-0.25 reported in the measurements (Richards and Pitts, 1993; Pitts and Kashiwagi, 1984; Birch *et al.*, 1978) in the region from 10 to 100 jet diameters. Note that this decay rate is higher than the value of 0.1563 (~1 / 6.4) observed for the decay of U_{cl}. A likely reason could be the higher (about 10 %) value of the mixture fraction diffusivity D_t in comparison to the momentum diffusivity ν_t (i.e. $Sc_t = 0.9$).
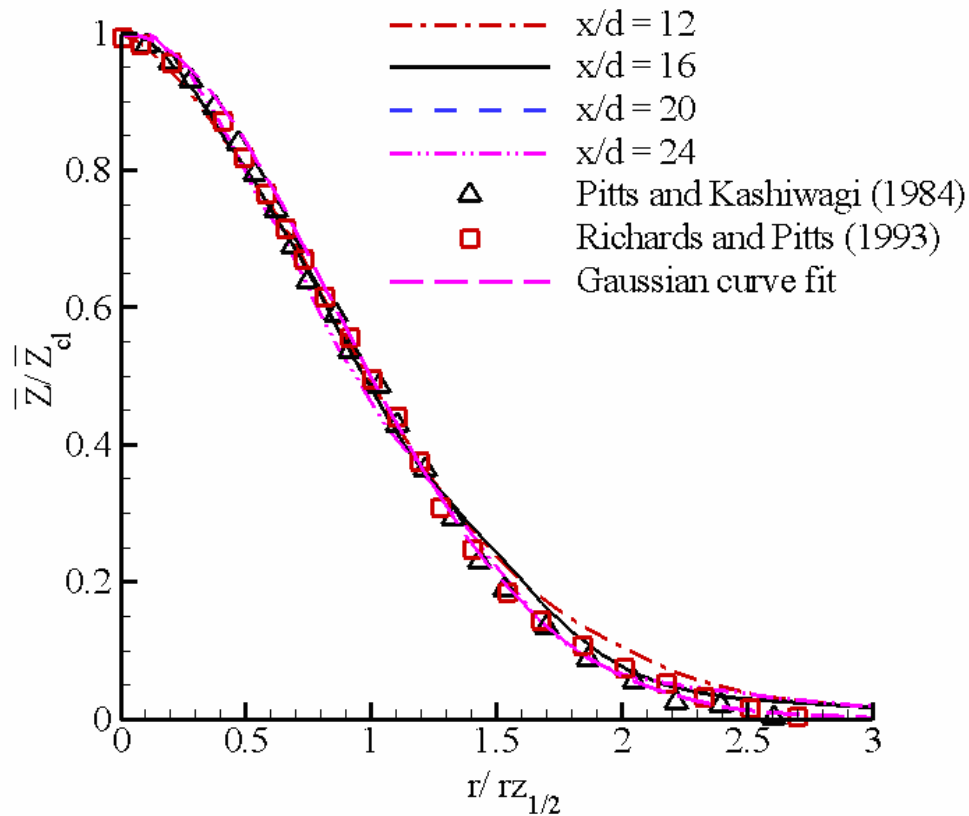
Figure 5.20. Radial profiles of normalized $\overline{Z}$ in the jet.

Let us now consider the radial profiles of $\overline{Z}$ to investigate self-similarity of the mixture fraction field. Figure 5.20 shows the radial profiles of $\overline{Z}/\overline{Z}_{cl}$ as a function of $r/rz_{1/2}$ at various axial locations in the jet. We observe good agreement of the computed data with the self-similar profiles reported by Richards and Pitts (1993) for a 25,000 Reynolds number propane jet and Pitts and Kashiwagi (1984) for a 4000 Reynolds number methane jet. Also shown in Fig. 7.20 is a Gaussian curve fit to the experimental data of Richards and Pitts (1993) and Pitts and Kashiwagi (1984),

$$\frac{\overline{Z}}{\overline{Z}_{cl}} = \exp\left(-0.693\left(\frac{r}{rz_{1/2}}\right)^2\right), \tag{5.10}$$

which provides a good approximation even in the present case. The computed profiles are well superimposed beyond $x/d = 16$ indicating self-similarity.
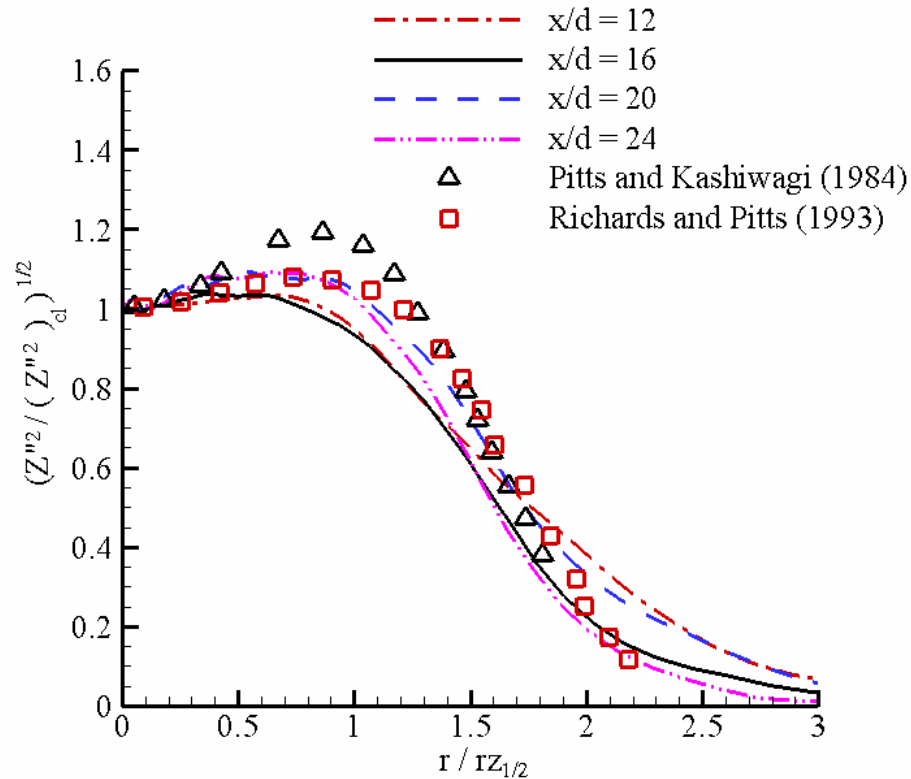
Figure 5.21. $\left(\overline{Z}''^2 /\left(\overline{Z}''^2\right)_{cl}\right)^{1/2}$ as a function of $r/rz_{1/2}$ at different axial locations in the jet.

To investigate self-similarity of the mixture fraction variance, consider Fig. 5.21 which shows the square-root of the normalized mixture fraction variance calculated from the filtered mixture fraction field, $\left(\overline{Z}''^2 /\left(\overline{Z}''^2\right)_{cl}\right)^{1/2}$, as a function of $r/rz_{1/2}$ at different axial locations in the jet. The profiles are not superimposed, especially at larger values of $r/rz_{1/2}$, indicating that the variance-field has not reached self-similarity in the simulated near-field of the jet. However, the computed profiles are reasonably close to the self-similar profiles reported in the measurements in the region $0 < r/rz_{1/2} < 2$, though deviations are observed at

larger values of $r/rz_{1/2}$. Comparing with Fig. 5.11 which shows the radial profiles of the normalized TKE, the quantitative agreement with the self-similar profiles is much better for the mixture fraction variance.

Now, we will focus on the statistics of the scalar dissipation rate χ, a quantity of central importance in the modeling and discussion of non-premixed turbulent combustion. Experimental data on scalar dissipation rates in non-reacting jets is limited in the literature. Due to the lack of normalization in the measured data, the comparison with the computed LES results will be more focused on qualitative trends rather than quantitative estimates. From the available experimental data on scalar dissipation, such as those of Namazian *et al.* (1988) and Effelsberg and Peters (1988) on non-reacting propane jets (Re_{jet} = 4000-10,000) in the region $x/d < 60$, the following observations can be made:

1. The mean scalar dissipation rate $\overline{\chi}$ decreases with downstream distance in the jet.

2. The radial profiles of $\overline{\chi}$ exhibit a double-peak structure which gradually vanishes as we proceed downstream in the jet. Moreover, the peak values of $\overline{\chi}$ are found in the jet shear layers.

3. The log-normal distribution is a good approximation for the PDF of χ.

We will now investigate the scalar dissipation rates computed from the LES flowfield.

The instantaneous filtered scalar dissipation rate $\tilde{\chi}$ is computed using the model expression given by Eq. (5.1). However, in the flamelet equations discussed in Section 4.3, the instantaneous scalar dissipation rate χ corresponds to a certain value of the mixture fraction Z. Since $\tilde{Z}$ is a fluctuating quantity in the LES flowfield, the χ value relevant to the flamelet equations is then the conditional value, χ_Z, subject to the condition that $\tilde{Z} = Z$ at a given location in the jet. Following Bushe and Steiner (1999), χ_Z can be related to the unconditional value $\tilde{\chi}$ using the expression

$$\tilde{\chi} = \int_{Z=0}^{Z=1} \chi_Z P_Z\left(Z, \bar{Z}, \bar{Z}''^2\right) dZ, \tag{5.11}$$

where P_Z is the subgrid-scale probability-density-function (PDF) of the mixture fraction, which in general is a function of $\bar{Z}$ and $\bar{Z}''^2$. In the present work, we assume that P_Z is a beta PDF P_{beta}, shown to be a good estimate for the subgrid-scale PDF of the mixture fraction in reacting DNS studies of homogenous turbulence (Madnia and Givi, 1993; Wall *et al.*, 2000). P_{beta} has also been widely employed in LES studies of reacting jets (Pitsch and Steiner, 2000a, b). P_{beta} is given by

$$P_{\text{beta}}(Z) = \frac{(Z)^{\alpha-1}(1-Z)^{\beta-1}\,\Gamma(\alpha+\beta)}{\Gamma(\alpha)\Gamma(\beta)}, \tag{5.12}$$

where Γ is the gamma function and the parameters α and β are related to $\bar{Z}$ and $\bar{Z}''^2$ through the relations

$$\alpha = \bar{Z}\gamma, \tag{5.13}$$

and

$$\beta = (1-\bar{Z})\gamma, \tag{5.14}$$

where

$$\gamma = \frac{\bar{Z}(1-\bar{Z})}{\bar{Z}''^2}. \tag{5.15}$$

However, in order to explicitly solve for χ_Z, we need to know its functional dependence on Z. As suggested by Peters (2000), the functional dependence is usually assumed to be the same as in steady counterflows

$$\chi_Z = \chi_{\text{st}} f(Z), \tag{5.16}$$

where χ_{st} is the conditional scalar dissipation rate at the stoichiometric mixture fraction Z_{st} and $f(Z)$ has the form

$$f(Z) = \frac{\exp\{-2[erfc^{-1}(2Z)]^2\}}{\exp\{-2[erfc^{-1}(2Z_{st})]^2\}}. \tag{5.17}$$

Since P_{beta} is not defined at $Z=0$ and $Z=1$, P_Z was assumed to be a delta function at these two points in the Z space. With these presumed forms for P_Z and $f(Z)$, we can compute χ_{st} by the inversion of the integral in Eq. (7.11) as

$$\chi_{\text{st}} = \frac{\tilde{\chi}}{\int\limits_{Z=0}^{Z=1} f(Z) P_Z\left(Z, \bar{Z}, \bar{Z}''^2\right) dZ}. \tag{5.18}$$

To avoid the computation of the expensive gamma functions online during the averaging process, the integral in Eq. (5.18) was pre-computed and a 2-D look-up table was generated with discrete values of the integral for given values of $\bar{Z}$ and $\bar{Z}''^2$. Hence, during the computation of the statistics from the 3-D instantaneous data, the values of the integral corresponding to the values of $\bar{Z}$ and $\bar{Z}''^2$ at a given location in the jet were simply evaluated through 2-D interpolation.

Figure 5.22 shows the isocontours of the mean filtered scalar dissipation rate $\bar{\chi}$ in the jet. We observe trends similar to the experimental observations discussed before. From the shown isocontours, we observe that along the jet centerline, values of $\bar{\chi}$ increase initially in the mixing region just downstream of the potential core $(x/d \sim 8)$ up to about 13 jet diameters and then decrease as turbulent mixing decreases the scalar gradients. The radial profiles of $\bar{\chi}$ at different axial locations are shown in Fig. 5.23. We observe the characteristic double-peak structure of the profiles as in the experiments of Namazian *et al.* (1988) which becomes less prominent as we proceed downstream in the jet. Except at $x/d = 12$ where $\bar{\chi}$ peaks at the centerline, the peak values of $\bar{\chi}$ are observed to occur in the jet shear layer and move closer to the centerline as x increases from $16d$ to $24d$.
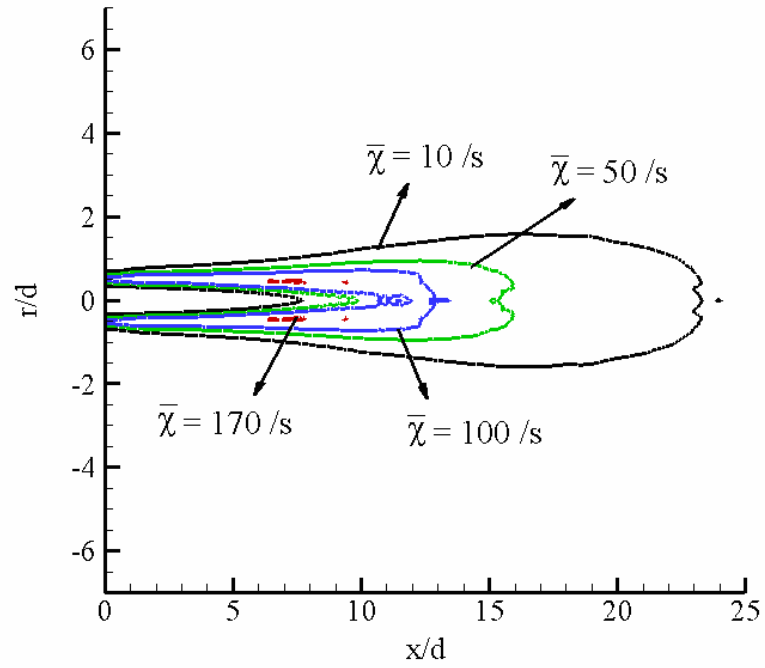
Figure 5.22. Isocontours of $\overline{\chi}$ (1/s) in the jet.
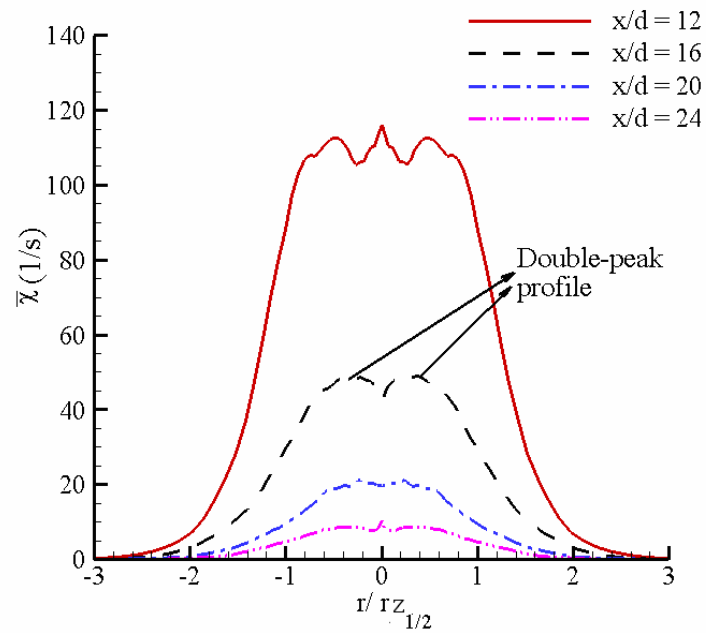
Figure 5.23. $\overline{\chi}$ (1/s) as a function of $r / rz_{1/2}$ in the jet at different axial locations.

Figure 5.23 shows the radial profiles of the conditional mean value, $\overline{\chi}_Z$, in the jet at different axial locations. We observe trends similar to $\overline{\chi}$ but the values of $\overline{\chi}_Z$ are significantly higher than $\overline{\chi}$. The lower values of $\overline{\chi}$ in Fig. 5.23 reflect the effect of the subgrid-scale PDF P_Z, which essentially attenuates $\overline{\chi}_Z$ by the probability of attaining a certain value of Z at a given location in the jet flowfield. Moreover, $\overline{\chi}_Z$ consistently peaks in the jet shear layer at all the axial locations shown and the double-peak structure is much more prominent compared to $\overline{\chi}$ (see Fig. 5.23). Both $\overline{\chi}$ and $\overline{\chi}_Z$ are observed to decay strongly as we proceed downstream in the jet from $x/d = 12$ to $x/d = 24$ in qualitative agreement with experiments. We will employ these computed values of $\overline{\chi}_Z$ at different jet locations in the studies of flame-vortex interactions.
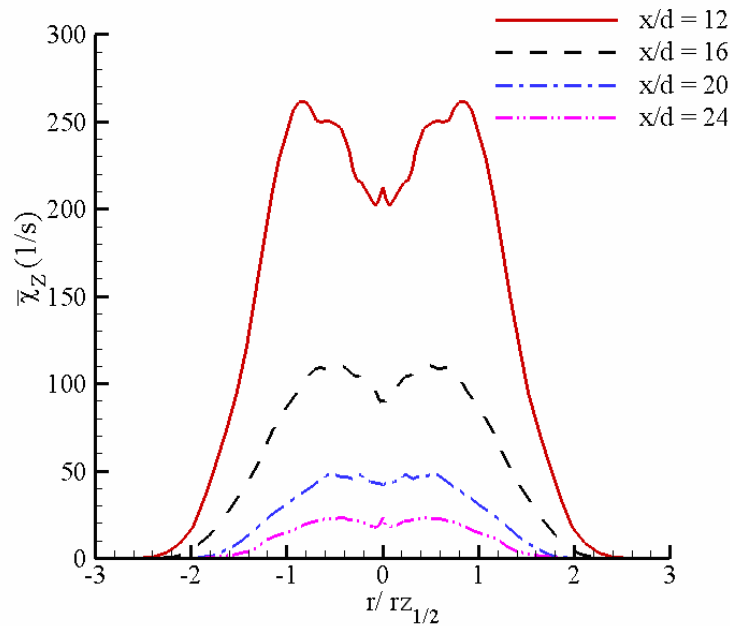
Figure 5.24. $\overline{\chi}_Z$ (1/s) as a function of $r/rz_{1/2}$ in the jet at different axial locations.

Let us now investigate the fluctuations and PDFs of $\widetilde{\chi}$ at different locations in the jet. Instantaneous time-record of $\widetilde{\chi}$ was collected over 100,000 time-steps at given locations in the jet. For instance, consider Fig. 5.25, which

shows the time-record of $\tilde{\chi}$ on the jet centerline at $x/d = 12$. We observe strong fluctuations of $\tilde{\chi}$ but the repeated bursts of relatively high values are often followed by relatively low values.
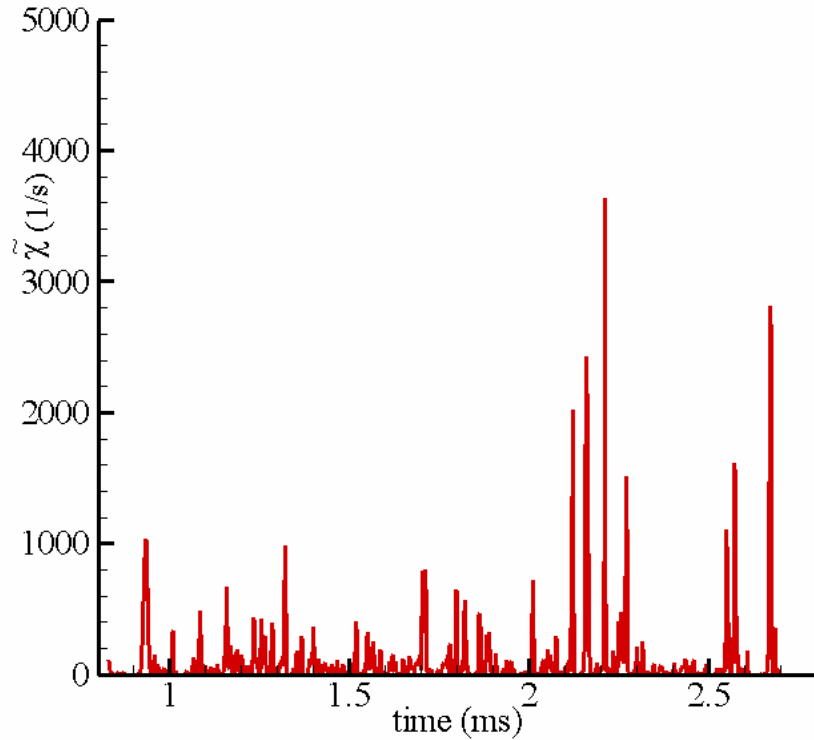
Figure 5.25. $\tilde{\chi}$ (1/s) as a function of time (ms) on the jet centerline at x/d = 12.

To explore the possible implications of the fluctuations of the scalar dissipation rate on the flame-response, consider Fig. 5.26, which shows the scalar dissipation ratio χ_r as a function of time at $x/d = 12$ on the jet centerline. Recall from Eq. (4.48) that χ_r is the ratio of the instantaneous scalar dissipation rate at stoichiometric mixture fraction χ_{st} to the steady extinction limit χ_e. It will be shown in the flame-vortex interaction studies presented in Chapters 6 and 7 that excursions of χ_{st} above χ_e (i.e. $\chi_r > 1$) and below χ_e (i.e. $\chi_r < 1$) are important for extinction and reignition. Moreover, burning flames with values of

χ_r greater than unity (i.e. $\chi_{st} > \chi_e$) represent effects due to unsteadiness, which render the unsteady flame more resistant to extinction. In LES, χ_{st} is the instantaneous conditional scalar dissipation rate, conditioned at the stoichiometric mixture fraction, computed using Eq. (5.18). In Fig. 5.26, χ_{st} is normalized by $\chi_e = 500$ 1/s, the steady extinction limit from a flamelet calculation using the single-step kinetic model for the pressures and temperatures simulated here.
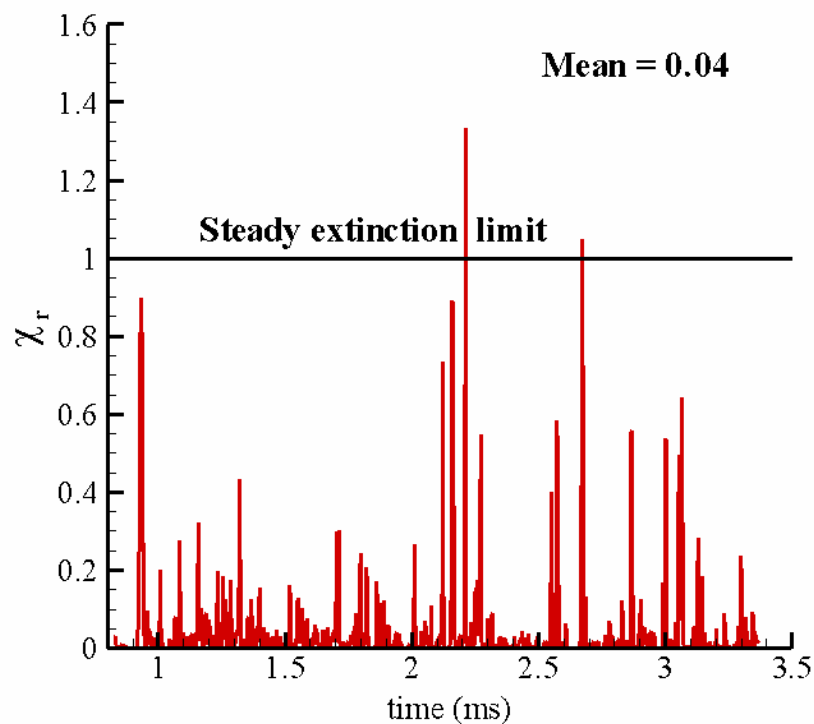
Figure 5.26. χ_r as a function of time (ms) on the jet centerline at x/d = 12.

We observe excursions of χ_r above and below 1 but it is interesting that the excursions above 1 are significantly short-lived. This in turn is reflected in the mean value being relatively small, equal to only about 0.04. In other words, a RANS calculation employing this mean value would predict a burning flamelet at

this jet location. However, we will show from flame-vortex interaction studies discussed in Chapters 6 and 7 that transient local extinction/reignition events are probable at $x/d = 12$ close to the jet centerline.
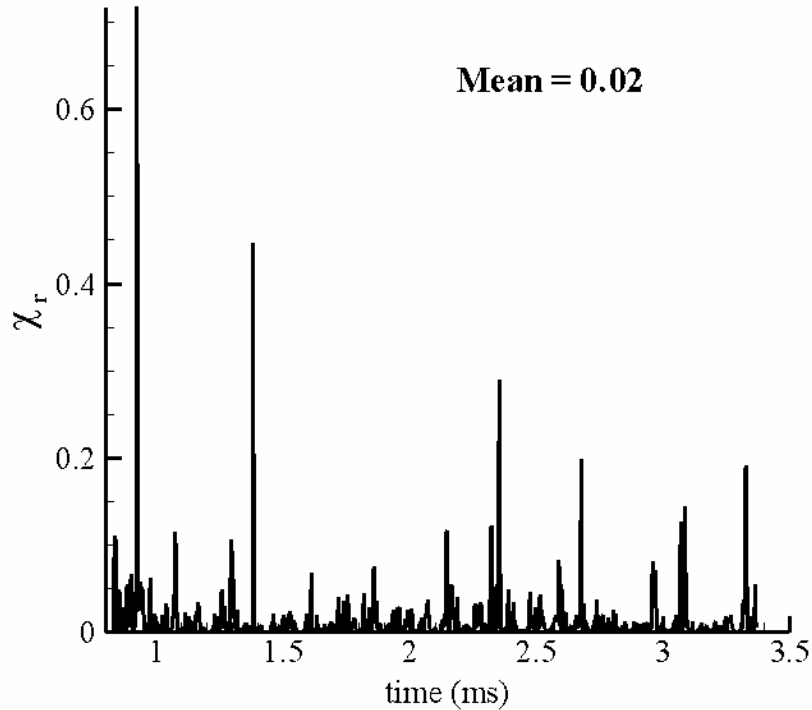
Figure 5.27. χ_r as a function of time (ms) on the jet centerline at x/d = 16.

Figures 5.27 and 5.28 show χ_r as a function of time at the downstream axial locations of $x/d = 16$ and $x/d = 20$, respectively, on the jet centerline. As shown before, $\overline{\chi}$ and $\overline{\chi}_z$ will decrease as we proceed downstream in the jet. As a result, the excursions of χ_r above 1 do not occur at $x/d = 16$ and $x/d = 20$, implying that instantaneous local extinction on the jet centerline is not expected at these axial locations. As discussed in Chapters 6 and 7, the flame-vortex interaction studies reveal similar trends, in that the tendency for local extinction decreases as we proceed downstream in the jet. However, note that the scenarios explored in Chapters 6 and 7 are interactions of isolated vortices with

flames, whereas the time records shown in Figs. 5.26-5.28 may be interpreted as superpositions of χ_r values due to interactions of multiple vortices (eddies) locally with the flames. In this context, Chapter 9 reports studies investigating the response of flamelets to fluctuating time records of χ_r.
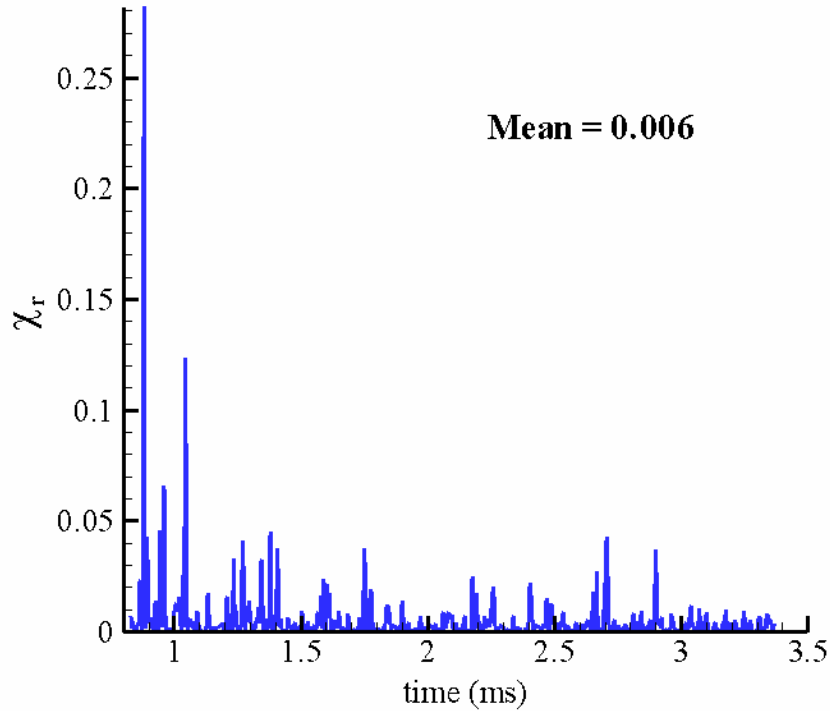
Figure 5.28. χ_r as a function of time (ms) on the jet centerline at x/d = 20.

Let us now consider the PDF of $\tilde{\chi}$ computed from the instantaneous time-record at different locations in the jet. Data collected over 100,000 time-steps were used for the evaluation of the PDF. Due to the high degree of variability of χ_{st}, it is convenient to compute the PDF of $\ln(\chi_{st})$. In addition, a normal distribution for $\ln(\chi_{st})$, $P_N(\ln(\chi_{st}))$, where

$$P_N(\ln(\chi_{st})) = \frac{1}{\sqrt{2\pi}\sigma} \exp\left(-\frac{(\ln(\chi_{st}) - \mu)^2}{2\sigma^2}\right), \tag{5.19}$$

is computed for comparison with the computed PDF. In Eq. (5.19), μ and σ represent the mean and RMS values of $\ln(\chi_{st})$, respectively.
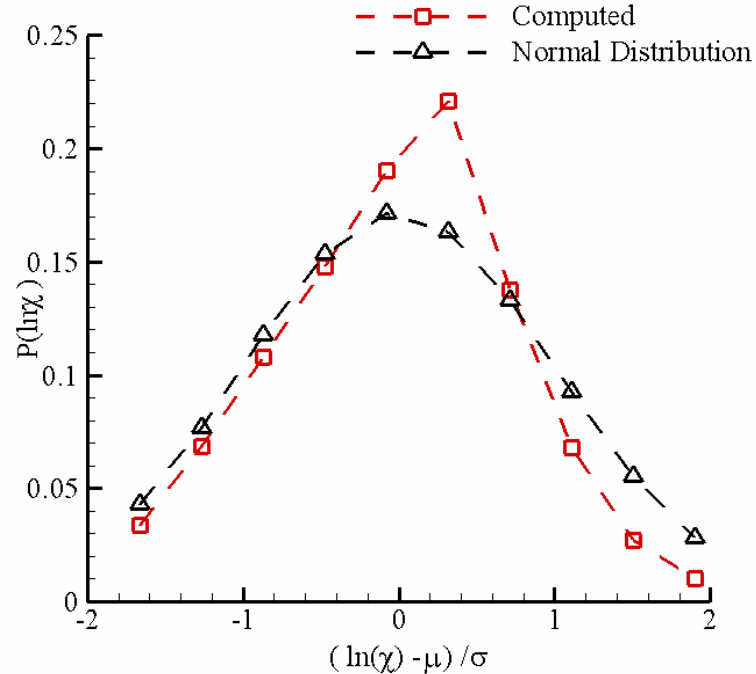
Figure 5.29. Computed PDF compared with a normal distribution on the jet centerline at x/d = 12.

Figures 5.29-5.31 show the computed PDFs at the axial locations of x/d = 12, x/d = 16 and x/d = 20 on the jet centerline, respectively. The normal distribution given by Eq. (5.19) is also shown for comparison. We observe that there is reasonable agreement of the computed PDF with the normal distribution, and the overall agreement improves as we advance downstream in the axial direction. However, even at downstream jet locations (i.e. x/d = 16, 20), it is observed that the normal distribution deviates particularly at the tails of the PDFs, i.e. for relatively high and low values of χ_{st}. Interestingly, these values represent low probability events, which are important for local extinction/reignition, as discussed in Chapter 9. These events are specific to the simulated jet, and not captured by a universal distribution, such as the normal distribution.
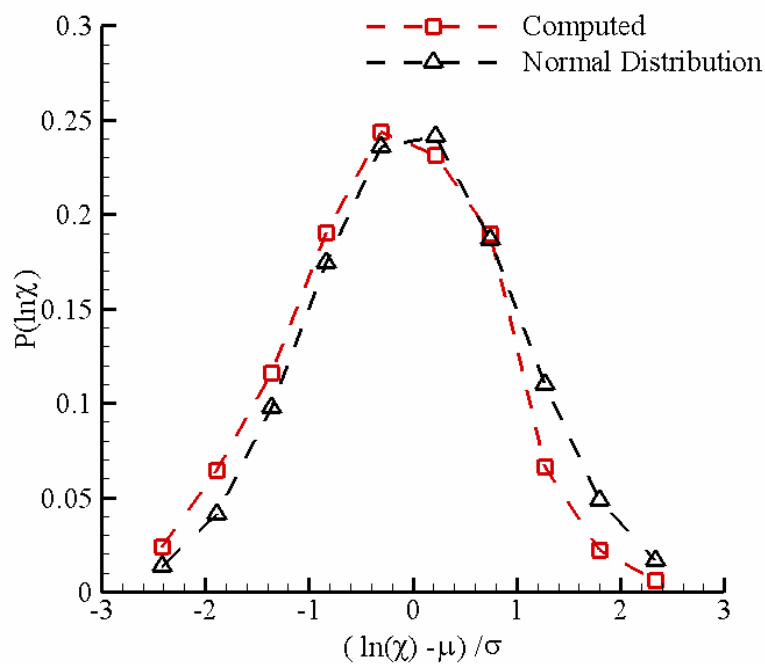
Figure 5.30. Computed PDF compared with a normal distribution on the jet centerline at x/d = 16.
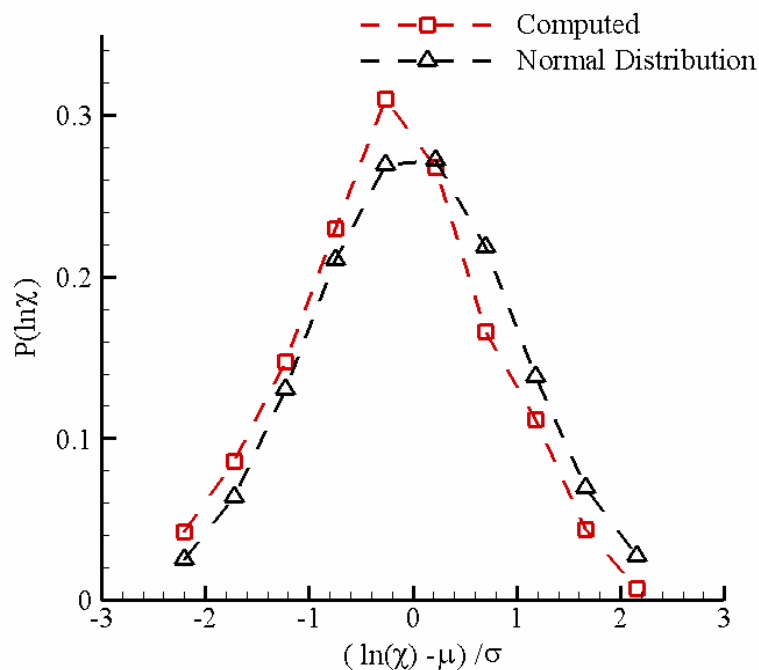
Figure 5.31. Computed PDF compared with a normal distribution on the jet centerline at x/d = 20.
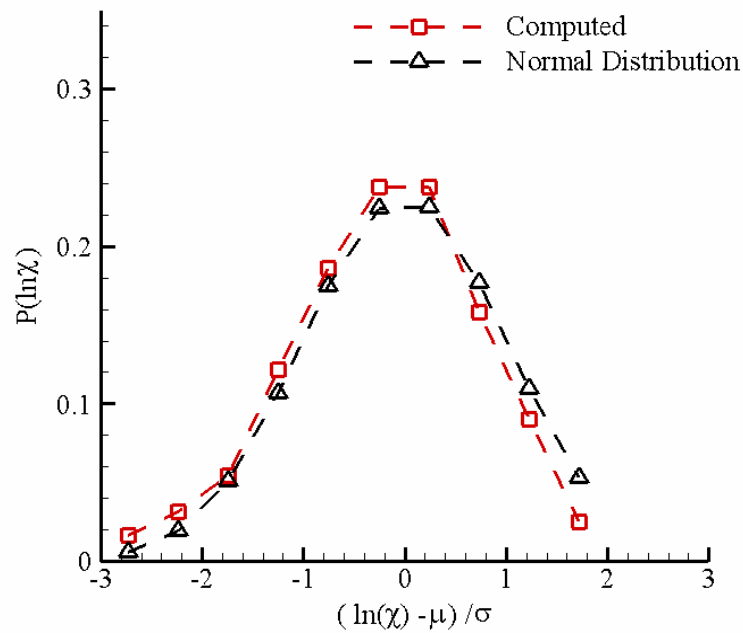
Figure 5.32.   Computed PDF compared with a normal distribution at the jet location, r/d = 0.5, x/d = 12.
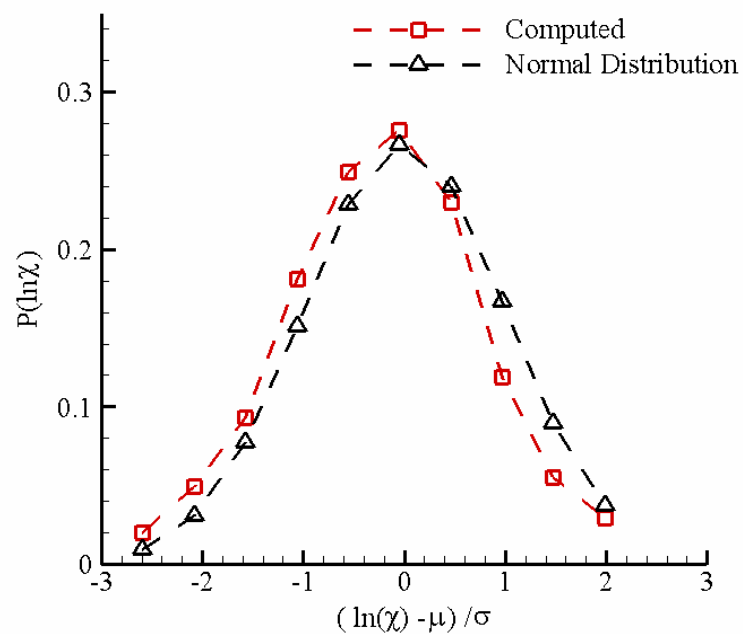
Figure 5.33.   Computed PDF compared with a normal distribution at the jet location, r/d = 0.5, x/d = 16.
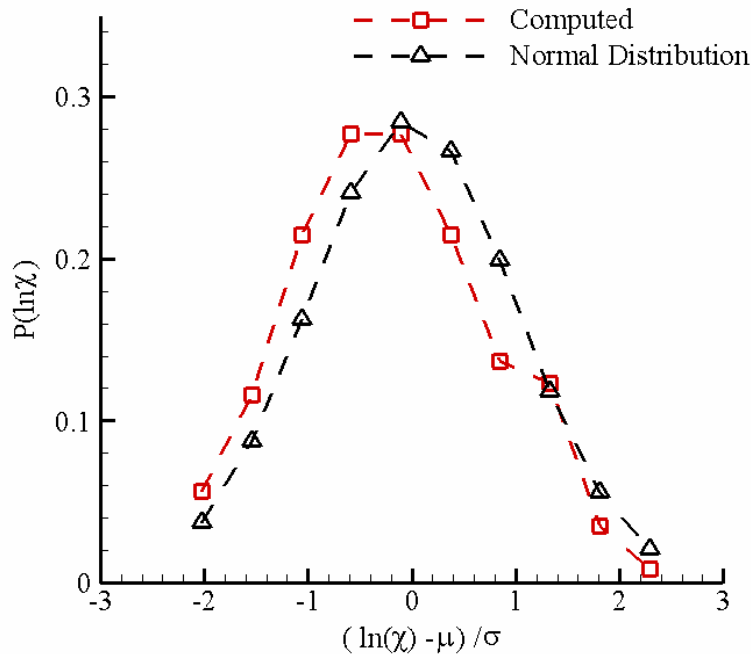
Figure 5.34. Computed PDF compared with a normal distribution at the jet
location, r/d = 0.5, x/d = 20.

Figures 5.32-5.34 compare the computed PDFs with the normal distribution at the radial location of $r/d = 0.5$ at the axial locations of $x/d = 12$, $x/d = 16$ and $x/d = 20$, respectively. Similar to the trends observed on the jet centerline, the normal distribution provides a good approximation to the computed PDFs. Moreover, comparing Fig. 5.29 and Fig. 5.32, we observe that the quantitative agreement with the normal distribution improves as we move radially out from the jet centerline ($r/d = 0$) to $r/d = 0.5$ at $x/d = 12$. These trends with respect to the computed PDFs are in good qualitative agreement with the experiments of Namazian *et al.* (1988) and Effelsberg and Peters (1988) where log-normality of the χ_{st} distribution was reported. Moreover, the values of the RMS σ of $\ln(\chi_{st})$ were found to lie in the 1.2-2.2 in the simulated near-field region of the jet, which lies within the range of 0.6-1.7 reported by Effelsberg and Peters (1988) in the region up to $x/d = 50$. RANS-based interactive flamelet

models (Pitsch and Peters, 1995; Gopalakrishnan and Abraham, 2002) typically employ a log-normal distribution with $\sigma = 1$ to mimic the fluctuations of χ.

5.4. <u>Summary and Conclusions</u>

In this chapter, results from the LES in the near-field ($x/d < 25$) of a 70,000 Reynolds number, variable-density, isothermal gaseous fuel round jet were presented. Turbulent statistics of the velocity and the mixture fraction fields were computed to estimate mean length-scales, velocity-scales and scalar dissipation rates at different locations on the jet centerline and the jet shear layers. The computed statistics were compared with published experimental results in the literature in the self-similar region of isothermal round jets. The computed statistics form the basis for the studies of flame-vortex interactions and unsteady flamelets that follow in subsequent chapters.

The statistics computed from the velocity-field included first (mean) and second (variance) moments. The jet was observed to spread linearly and the estimated spreading rate of 0.083 in the region $14 \leq x/d \leq 20$ was lower than the range of 0.094-0.102 reported in the experiments on self-similar jets. The decay constant of the mean centerline velocity in this region was estimated to be about 6.3, which is within 10 % of the values reported in measurements. Apart from the inadequacies of the constant-coefficient Smagorinsky model, the discrepancy of the computed values relative to the measured ones may be attributed to the lack of self-similarity in the near-field region of the jet. However, the normalized radial profiles of the mean axial velocity showed good agreement with measured self-similar profiles and were reasonably super-imposed beyond 20 jet diameters. The normalized radial profiles of the mean turbulent kinetic energy TKE lacked self-similarity. The computed values were within 15 % of the measured values reported by Panchapakesan and Lumley (1993a) but larger deviations upto 31 % were observed from the values reported by Hussein *et al.* (1994). Based on the prior studies of Uzun (2003) on the sensitivity of the Reynolds stresses on the

Smagorinsky constant, it is likely that the value of 0.012 employed in the present work under-estimates the eddy viscosity and hence the Reynolds stresses and the TKE. Mean velocity-scales representative of vortex velocity-scales in the 2-D DNS of flame-vortex interactions were estimated.

Mean longitudinal integral length-scales, Taylor micro-scales and the Kolmogorov length-scales were estimated at different axial and radial locations in the jet. While the integral length-scales were estimated from two-point auto-correlations of the fluctuating axial velocities, the Taylor and Kolmogorov length-scales were estimated from scaling relations in isotropic turbulence. For axial distances greater than 12 jet diameters, the integral length-scales were found to increase as we proceed downstream in the axial direction and radially away from the centerline. The computed values agreed within 20 % with the measured values of Wygnanski and Fiedler (1969) in self-similar jets. The variation of the Taylor and the Kolmogorov scales along the axial and radial directions showed similar trends as those of the integral length-scales. The expected large gap between the Taylor and the Kolmogorov length-scales at the relatively high jet Reynolds numbers employed here was confirmed.

Statistics of the mixture fraction field were computed which included means and variances of the filtered mixture fraction and conditional means and PDFs of the filtered scalar dissipation rate. The computed values of the jet spreading rate and decay rate of the centerline mixture fraction were within 25 % of the measured values in self-similar jets. Beyond an axial distance of 16 jet diameters, the normalized radial profiles of the mean mixture fraction were well super-imposed and showed good agreement with the measured self-similar profiles. A Gaussian curve-fit suggested in prior experimental studies (Pitts and Kashiwagi, 1984) was found to be a good approximation to the computed profiles. In contrast to the TKE, the radial profiles of the normalized mixture fraction variance compared favorably with the reported self-similar profiles in the experiments.

Unconditional and conditional means of the scalar dissipation rate, a statistic of the mixture fraction relevant to reacting flows, were estimated. The conditional means were estimated from the unconditional filtered values by the presumption of a beta PDF for the subgrid-scale PDF of the mixture fraction. Both the unconditional and conditional means showed trends in good qualitative agreement with the experiments on non-reacting round jets, In particular, the values initially increase beyond the potential core up to a certain distance in the jet ($x/d \sim 12$) and then decay strongly due to turbulent mixing. Consistent with experiments, the radial profiles showed a double-peak structure which became less prominent as we proceed downstream along the axial direction in the jet. The conditional mean scalar dissipation rates estimated at different locations in the jet flowfield will be employed in the future studies of flame-vortex interactions.

The fluctuations of the scalar dissipation rate were characterized at different axial locations in the jet. Significant excursions of the instantaneous conditional values above the steady extinction limit were observed at upstream axial locations ($x/d = 12$) closer to the centerline ($r/d < 1$). However, these overshoots were short-lived and the mean values remained much lower than the extinction limit (< 0.1 χ_e). The time-records of the conditional scalar dissipation rates obtained across the jet near-field are employed in studies focusing on the unsteady response of diffusion flamelets in Chapter 9.

To further assess the accuracy of the LES model for the prediction of the scalar statistics, PDFs of χ_{st} were computed from the instantaneous time-records at different locations in the jet and compared with the log-normal distribution reported in experiments. The comparisons showed that the log-normal distribution is a reasonable approximation to the computed PDFs. The quantitative agreement with the log-normal distribution improved as we proceed downstream in the axial direction and radially out from the centerline. The computed variances of the log-normal distributions from the filtered values were found to lie in a range comparable to that reported in the experiments of Effelsberg and Peters (1988).

In the chapters that follow (Chapters 6 and 7), we will employ the temporal mean values of length scales, velocity scales and scalar dissipation rates in the studies of flame-vortex interactions corresponding to different locations in the jet near-field. Physical mechanisms for regimes, such as local extinction and reignition, will be investigated, and the applicability of modeling approaches, such as flamelet and flamelet/progress variable models, will be assessed.

CHAPTER 6. FLAME-VORTEX INTERACTIONS

6.1. Introduction

In this chapter, results from studies of flame-vortex interactions are presented. As discussed in Chapter 1, the vortex and flame characteristics employed in the flame-vortex studies are selected from the mean statistics computed from the LES flowfield at different axial locations in the jet. Recall from Section 3.3 that the problem setup consists of an initially-flat diffusion flame which is allowed to interact with a counter-rotating vortex-pair. The fluid mechanics of the flame-vortex interaction is investigated for a baseline case characterized by the following set of non-dimensional numbers: $l_r = 1.5$; $u_r = 5.85$; $Re = 540$; $Da_i = 30$. This set of non-dimensional numbers is obtained by averaging the temporal mean length-scale, velocity-scale and conditional mean scalar dissipation rate computed with LES across the radial region $0 \leq r/d \leq 1.5$ at the jet axial location, x/d = 12. Note that the radial region close to the jet centerline is chosen as the most energetic eddies (capable of causing flame extinction/reignition) are expected to occur in this region.

With respect to length scales in the selected jet near-field region (i.e. x/d = 12 and $0 \leq r/d \leq 1.5$), the selected vortex is sized about 36 % of the mean integral length-scale (L_{11}) and about 3 times the mean Taylor length-scale (λ). Moreover, the velocity-scale for the vortex is assumed to be equal to the mean velocity-scale (u') in the selected jet near-field region. Hence, the chosen vortex characteristics represent inertial scales in the turbulent energy spectrum, and the flame-vortex interactions reported in this chapter represent localized interactions of inertial scales with the flamelets. The simulated pressure is 40 bar and the fuel-side and oxidizer-side temperatures are 1000 K. These conditions are

identical to those in the LES jet. The single-step kinetic model discussed in Section 3.3 is employed with gaseous n-heptane as the representative fuel.

In the section that follows, the sequence of events that occur during the flame-vortex interaction is described. It will be shown that the transient flame-response can be categorized into an extinction phase and a reignition phase. The extinction and the reignition phases are discussed in Sections 6.3 and 6.4, respectively. In each of these sections, the relative importance of convection and diffusion processes is investigated and the applicability of 1-D transient diffusion flamelet libraries to predict the flame-response is assessed. In Section 6.5, a modeling framework to predict extinction and reignition observed in the flame-vortex simulations is evaluated, and implications for turbulent combustion modeling are discussed. The chapter closes with summary and conclusions in Section 6.6. Results from flame-vortex studies employing higher vortex Reynolds numbers than that discussed in this chapter may be accessed in a recent publication (Venugopal and Abraham, 2008a), some of which are discussed in Section 7.2 of Chapter 7.

6.2. Transient Flame-response

Figures 6.1 (a)-(f) show the sequence of events that occur during the flame-vortex interaction at the selected location in the jet in terms of temperature contours. The stoichiometric isocontour ($Z = 0.05$) is also indicated in these figures. Recall from Section 3.3 that in Figs. 6.1 (a)-(f), t* represents the physical time non-dimensionalized by the eddy turnover time-scale. The frames have been magnified for clarity. Figure 6.1(a) shows the initial temperature contours with the velocity vectors overlaid (only every 2nd vector is shown for clarity). When the vortex impinges on the flat flame, it induces curvature and strain. This is evident in Fig. 6.1(b) where the portion of the diffusion flame interacting with the vortex becomes curved and the flame thickness decreases. Subsequently, local extinction occurs along the symmetry axis as shown in Fig. 6.1(c), with peak temperatures falling below 1400 K along this axis.
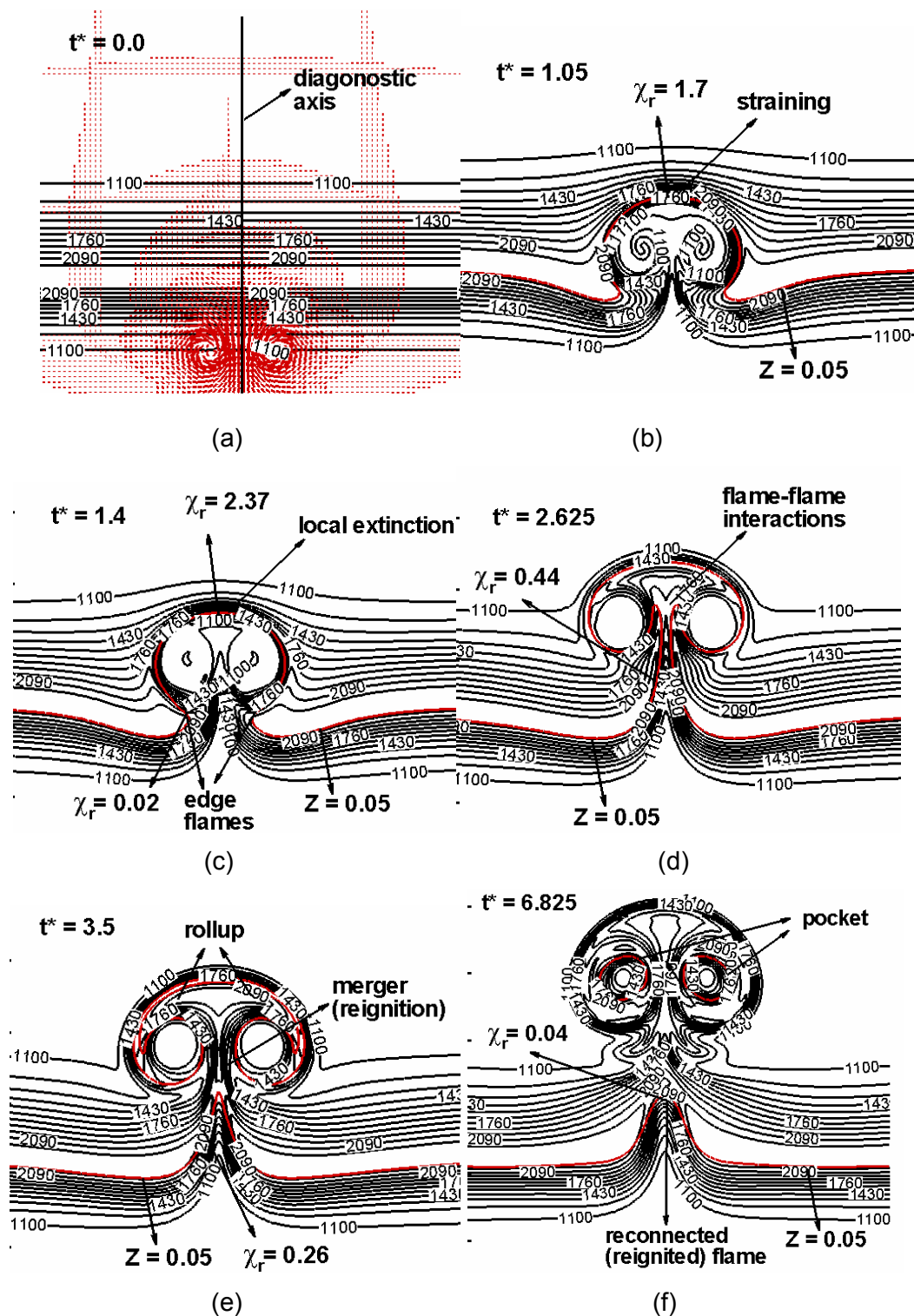
Figure 6.1. Evolution of temperature (K) during the flame-vortex interaction.

We will discuss the extinction characteristics in greater detail in terms of an unsteady scalar dissipation rate and the Damkőhler number in the next section. It is seen from Fig. 6.1(c) that the quenched region is bordered by two distinct flame-edges on either side of the symmetry line. Recall from the literature review in Chapter 2 that edge-flames are extremities of diffusion flames which border extinguished regions. As the vortex convects through the flame, the edge-flames are advected and rolled up by the vortex-induced flow. At the same time, we observe from Fig. 6.1(d) that the proximity of the flame-edges leads to lateral (i.e. in the X-direction) flame-flame interactions. We will quantify the flame-flame interactions in terms of convection and diffusion processes along the vertical centerline later. The lateral interactions lead to lateral propagation and subsequent merger of the edge-flames, as shown in Fig. 6.1(e). A reconnected diffusion flame is eventually established by about $t^* = 6.825$ (Fig. 6(f)). In Fig. 6.1(f), we also observe a pocket of oxidizer detached from the re-connected flame on the fuel-side, which would eventually burn out in the core of the vortex.

This sequence of events involving unsteady flame-flame interactions leading to the re-establishment of the original diffusion flame may be characterized as the *reignition phase*. Hence, the unsteady flame-vortex interaction at the selected location in the jet can be categorized into the two phases, the extinction phase and the reignition phase. We will now focus on the evolution of the flame structure and the mixing field during each of the two phases. We will also assess the applicability of the 1-D transient diffusion flamelet model to predict the flame-response during extinction and reignition. In the analysis below, the vertical centerline is chosen as the diagnostic axis (see Fig. 6.1(a)).

6.3. <u>The Extinction Phase</u>
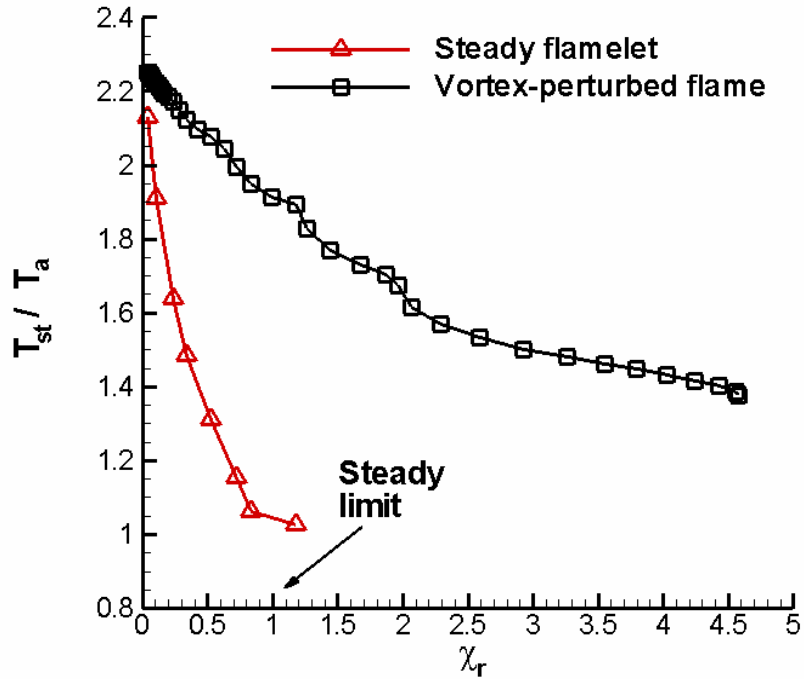
Figure 6.2. T_{st}/T_a as a function of χ_r during the extinction phase.

Figure 6.2 shows the temperature T_{st} as a function of the scalar dissipation rate χ_{st} at the stoichiometric mixture fraction Z_{st} along the diagnostic axis. The instantaneous scalar dissipation rate χ is computed as

$$\chi = 2D_Z(|\nabla Z|^2), \tag{6.1}$$

where the mixture fraction diffusivity $D_Z = \lambda/(\rho c_p)$ with the unity Lewis number assumption. In Fig. 6.2, T_{st} has been normalized by the air-side temperature T_a and χ_{st} have been normalized by the steady extinction limit χ_e to give χ_r (Eq. (3.48)). Here, χ_e is estimated using the 1-D laminar flame code described in Section 3.3. Starting from a burning solution, χ is gradually increased till peak temperatures fall within 10 % of the frozen flow solution ($T = 1000\text{ K}$). With this

extinction criterion, χ_e is about 500 s^{-1} for the kinetic parameters chosen for the single-step model. From Fig. 6.2, we observe that T_{st} decreases as χ_{st} increases and subsequently drops to values within 40 % of T_a, indicating that the vortex-perturbed flame is approaching local extinction. The temperature response resembles the upper-branch of the well-known S-curve behavior of strained diffusion flames (Seshadri and Williams, 1978).
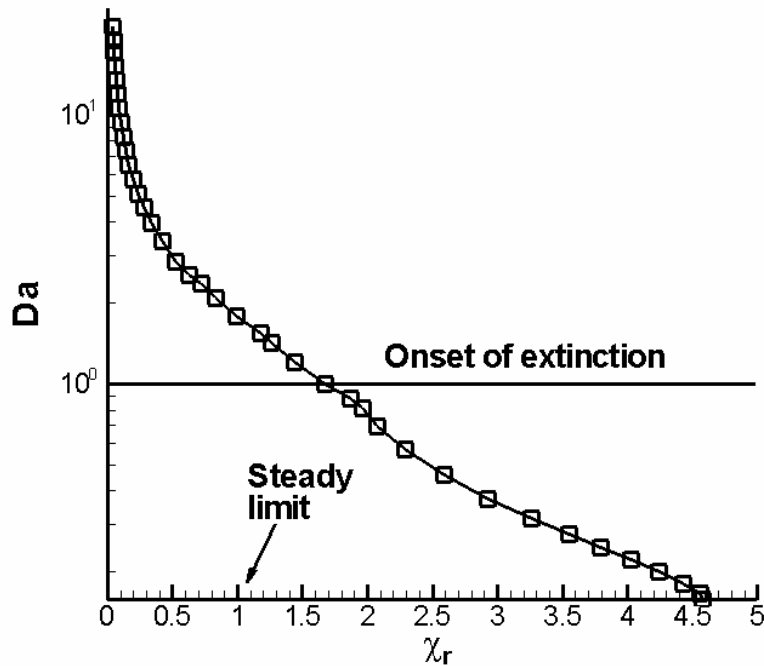
Figure 6.3. Da as a function of χ_r during the extinction phase.

However, we observe from the figure that the vortex-perturbed flame responds very differently than a steady laminar flamelet. In particular, it is seen that the vortex-perturbed flame withstands scalar dissipation rates much higher than the steady limit, and the temperatures do not fall to the frozen limit even at χ_{st} values as high as $4.5\chi_e$. This behavior arises from the vortex-induced unsteadiness on the flame response, which causes the unsteady flame to respond with a phase-lag to the imposed scalar dissipation, and renders it more

resistant to extinction. Figure 6.2 clearly shows that *steady flamelet* libraries commonly used for turbulence-chemistry closure are not applicable in the present case.

Figure 6.3 shows the variation of the instantaneous flame Damkőhler number Da (see Eq. (3.48)) as a function of χ_r along the vertical centerline. We observe trends similar to the temperature response. In this study, for consistency across the range of conditions explored, we choose $Da = 1$ as the criterion for the onset of local extinction. This criterion is discussed by Peters (2000), and marks the onset of extinction when the instantaneous mixing time represented by χ_{st}^{-1} becomes equal to the instantaneous chemical time τ_c. Furthermore, the $Da = 1$ criterion is meaningful in the present case since extinction is strain-induced, and occurs when the mixing time-scale becomes shorter than chemical time-scale.

Deviations of unsteady vortex-induced extinction from quasi-steady extinction have been reported in recent works, for instance, in the experiments of Santoro *et al.* (2000a) in vortex-perturbed gaseous methanol counterflow flames, and in the computations of Oh *et al.* (2004) involving vortex-induced extinction of dilute methane-air counterflow flames. Santoro *et al.* (2000a) found that the unsteady extinction scalar dissipation rate is about 30 % greater than the steady limit. On the other hand, Oh *et al.* (2004) reported unsteady extinction limits as much as 4 times the steady values. An important distinction between the conditions studied by Santoro *et al.* and Oh *et al.* is the relative ordering of the characteristic chemical and vortex time-scales. While in the case of Santoro *et al.*, the chemical time scales were shorter than the vortex time scales, Oh *et al.* considered vortices with time scales shorter than the chemical time scales. This shows that as the vortex time scales become shorter than the chemical time scales, the unsteady extinction limit would increasingly deviate from the steady values. In the present case, the characteristic chemical-to-vortex time-scale ratio is about 3.9 ($\sim l_r / u_{fv}$), implying that vortex time scales are shorter than chemical time scales. Hence, consistent with the results of Oh *et al.* (2004), we observe

significant deviations between the unsteady and steady extinction limits. Furthermore, since the unsteady flame response is expected to be dependent on the time-history of the scalar dissipation rate, it is intuitive that the unsteady extinction limit would be flow-dependent. In the next chapter, where we consider vortex and flame characteristics varying across the jet flowfield, we will clarify the non-dimensional numbers that control the unsteady flame response and extinction limits.
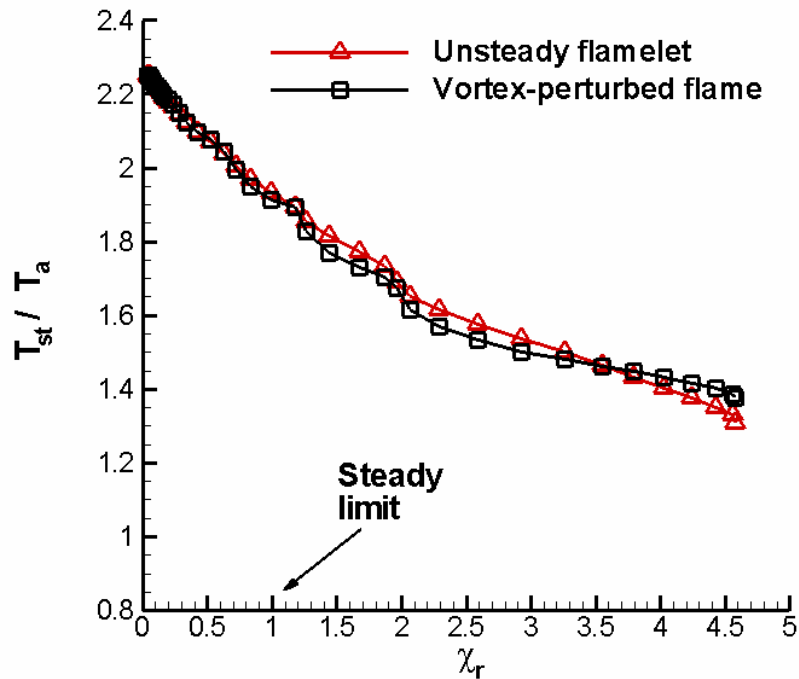
Figure 6.4. T_{st}/T_a as a function of χ_r with the unsteady flamelet model and flame-vortex simulation.

It is interesting to compare the temperature response with predictions using an *unsteady flamelet* model. Here, by 'unsteady flamelet', we refer to the time-dependent flamelet equations given by Eqs. (3.38) and (3.39) where χ varies as a function of both Z and time. The 1-D laminar flame code discussed in Section 3.3 is employed along with the single-step kinetic model. The

instantaneous scalar dissipation rate $\chi(Z,t)$ (see Eq. (6.1)) is extracted from the flame-vortex flowfield along the vertical centerline and used as an input in the flame code. Figs. 6.4 and 6.5 show the normalized temperature T_{st}/T_a and the CO_2 mass fraction Y_{CO_2} as a function of χ_r, respectively, computed using the unsteady flamelet model compared with the results from the flame-vortex simulation. We observe that the model predictions agree well with the flame-vortex results with respect to both T_{st} and Y_{CO_2}, indicating that the model captures effects due to unsteadiness. In other words, the flame behaves as a 1-D unsteady flamelet in the extinction phase.
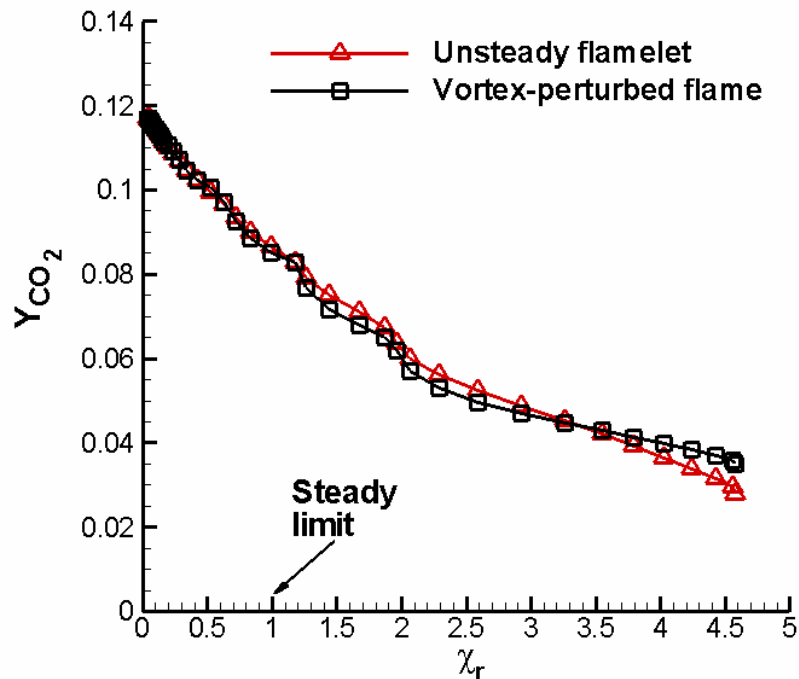
Figure 5.6. Y_{CO_2} as a function of χ_r with the unsteady flamelet model and flame-vortex simulation.

Concurrent with this discussion on the comparison of the flame-vortex results with the flamelet model, it is interesting to investigate the nature of heat

loss mechanisms that lead to extinction. The convective and diffusive heat fluxes are computed using the expressions:

$$CNVHX = \rho u \frac{\partial h}{\partial x},$$

$$CNVHY = \rho v \frac{\partial h}{\partial y},$$

$$DELHX = \frac{\partial}{\partial x}\left(\frac{\lambda}{c_p} \frac{\partial h}{\partial x} \right),$$

$$DELHY = \frac{\partial}{\partial y}\left(\frac{\lambda}{c_p} \frac{\partial h}{\partial y} \right).$$

(6.2)
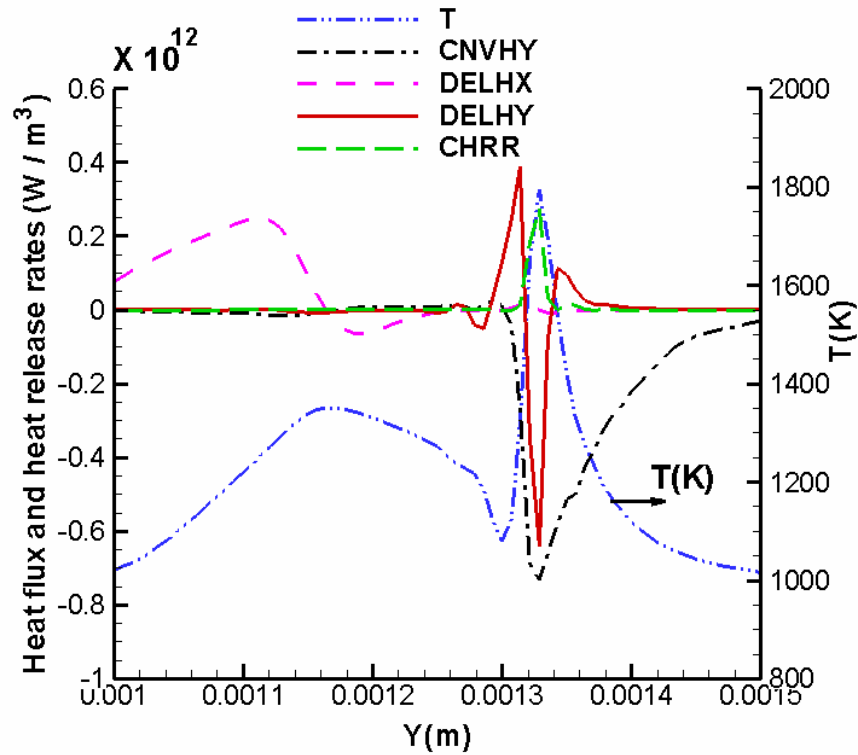
Figure 6.6. Comparison of convective and diffusive heat fluxes and the heat release rate (W/m³) at t* = 1.4. The temperature T is shown on the right axis.

In Eq. (6.2), *CNVHX* and *CNVHY* are convective terms for the mixture specific enthalpy h in the X and Y directions, respectively, *DELHX* and *DELHY* are the diffusion terms for h in the X and Y directions, respectively, and ρ, u, v,

λ and c_p are the mixture density, X-velocity, Y-velocity, mixture thermal conductivity and mixture specific heat, respectively. Figure 6.6 compares the heat-flux terms given by Eq. (6.2) and the chemical heat release rate $CHRR$ along the vertical centerline at t* = 1.4, a time-instant close to extinction. $CHRR$ is computed as

$$CHRR = \left| \sum_{i=1}^{N} \dot{w}_i h_i^0 \right|, \qquad (6.3)$$

where N is the total number of species. In Fig. 6.6, the temperature is also shown on the right axis. We observe from Fig. 6.6 that the dominant mode of heat loss is the convective term $CNVHY$, followed by the diffusive term $DELHY$ along the y-direction. $CNVHX$ is zero since the diagnostic axis is a symmetry line and is not shown in Fig. 6.6. Moreover, $CHRR$ is smaller in magnitude than $CNVHY$, implying that the flame is approaching extinction. $DELHX$, which is essentially a curvature term, is negligibly small in comparison to $CNVHY$ and $DELHY$ in the extinguishing region ($0.0013 < Y < 0.0014$). This indicates that curvature effects are minimal up to extinction; this is consistent with the agreement between the flame-vortex and the flamelet model predictions, since the curvature term is absent in the flamelet calculations. In the context of the flamelet equations given by Eqs. (3.38) and (3.39), the convective terms do not directly appear as a result of the flamelet-transformation with unity species Lewis numbers (Peters, 1984), but affect the magnitude of χ through mixture fraction gradients (see Eq. (6.1)). Note, however, that the hump in the temperature profile on the left (oxidizer) side upstream of the flame is caused by heat addition due to the curvature term $DELHX$.

Figure 6.7 shows the mixture fraction Z along the vertical centerline along with the temperature T on the right-hand axis. It is seen that the heat addition due to $DELHX$ occurs at sufficiently lean fractions ($Z \leq 0.01$) and does not affect the extinction behavior. In other words, the vortex-induced re-circulation results in very little partial-premixing up to extinction and the flame can essentially be modeled as a 1-D unsteady diffusion flamelet.
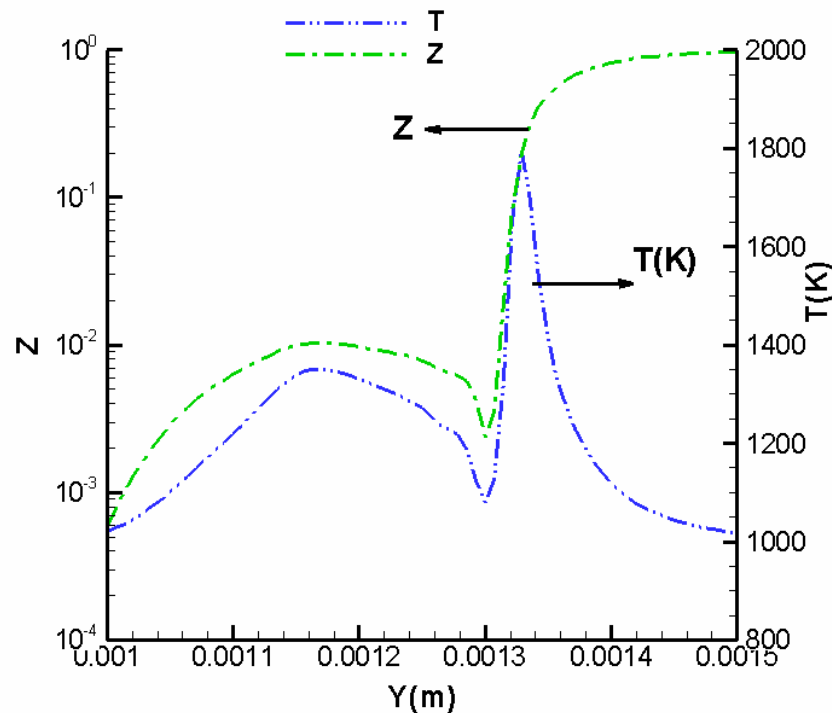
Figure 6.7. Z and T along the vertical centerline at t* = 1.4.

6.4. The Reignition Phase

Let us now examine the unsteady flame-response during the reignition phase. The time-evolution of the temperature T, the mixture fraction Z and the scalar dissipation rate χ along the vertical centerline is shown in Figs. 6.8(a), (b) and (c), respectively. In these figures, only the reigniting region is shown for clarity. From Fig. 6.8(a) which shows the evolution of temperature, we notice that beyond t* = 1.4, the extinguished region begins to reignite and by t* = 3.5, the peak temperature becomes comparable to that of the original diffusion flame. At t* = 1.4, we observe from Fig. 6.8(b) that the quenched region is essentially diluted with the oxidizer, indicated by values of Z well below Z_{st} (~ 0.05). As time progresses, Z evolves from lean to flammable and rich fractions due to partial-premixing in the wake of the vortex-induced flow. In other words, the re-

connected diffusion flame is formed through a transient partially-premixed flame structure.

(a)

(b)

(c)
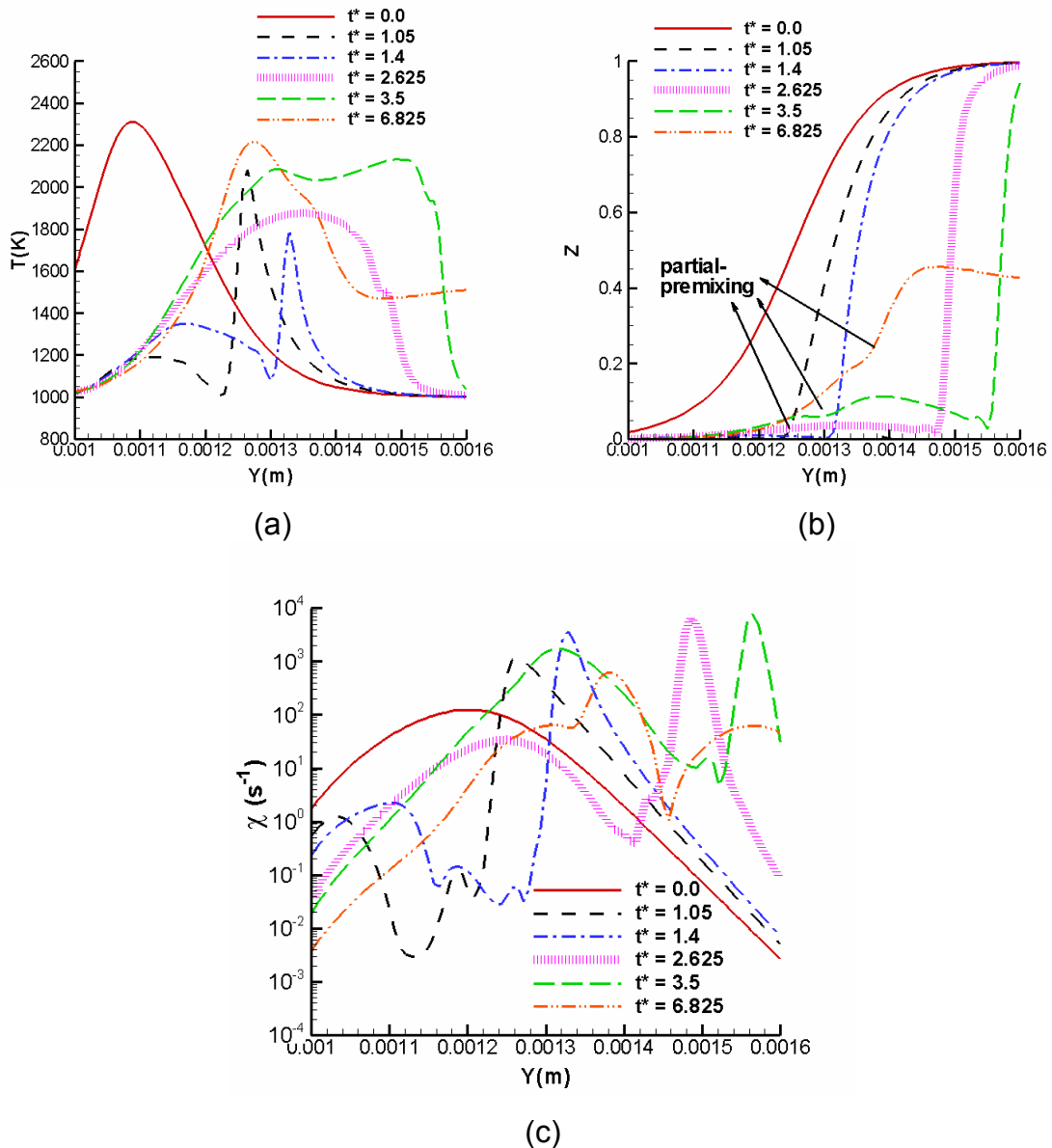
Figure 6.8. Time-evolution of (a) the temperature, (b) the mixture fraction and (c) the scalar dissipation rate along the vertical centerline during the reignition phase.

The effect of partial-premixing is evident in the time-evolution of χ shown in Fig. 6.8(c). It is observed that at the onset of reignition (t* = 1.4), χ values are

relatively small (< 0.1) in the reigniting region ($0.0011 < Y < 0.0013$) due to dilution by the oxidizer. Thereafter, as flammable fractions are created (t* = 2.625, 3.5), χ values increase in the reigniting region ($0.0011 < Y < 0.0015$). It is interesting to note that as we advance in time from t* = 1.4 to 3.5, Figs. 6.8(a) and (c) show that both T and χ increase in the reigniting regions. In the context of the S-curve shown in Fig. 2.1, this corresponds to a transition from the lower (non-burning) to the upper (burning) branch via the unstable branch. This behavior cannot be recovered with a steady flamelet model which would predict a sudden transition from the non-burning branch (point I in Fig. 2.1) to the burning branch once χ has fallen below a certain value.

Computations with the unsteady 1-D flame code described in Section 3.3 show that for the range of values of χ encountered in the reigniting region ($0.0011 < Y < 0.0015$), for instance at t* = 1.4, the autoignition delay times are much longer (of the order of 10t$_{eddy}$), whereas reignition occurs within a time-interval of about 2t$_{eddy}$ (from t* = 1.4 to 3.5) in the flame-vortex simulation. In other words, it is unlikely that the reignition process occurs through an independent flamelet scenario (Sripakagorn *et al.*, 2004) where the individual flamelets reignite without interactions with the neighboring burning regions. It will be shown in Chapter 7 that l_r has a significant effect of the mode of reignition. Essentially, for relatively small values of l_r (< 3.0, for instance, as explained in Chapter 7), mutual interactions between edge flames are strong enough to cause reignition before autoignition can occur. As seen from the temperature snapshots in Figs. 6.1(c)-(e), lateral interactions involving the rolled up flame-edges bordering the quenched regions play an important role during the reignition phase. We will now quantify these specific interactions in terms of convection and diffusion processes.

(a) t* = 1.4   (b) t* = 2.625

(c) t* = 3.5
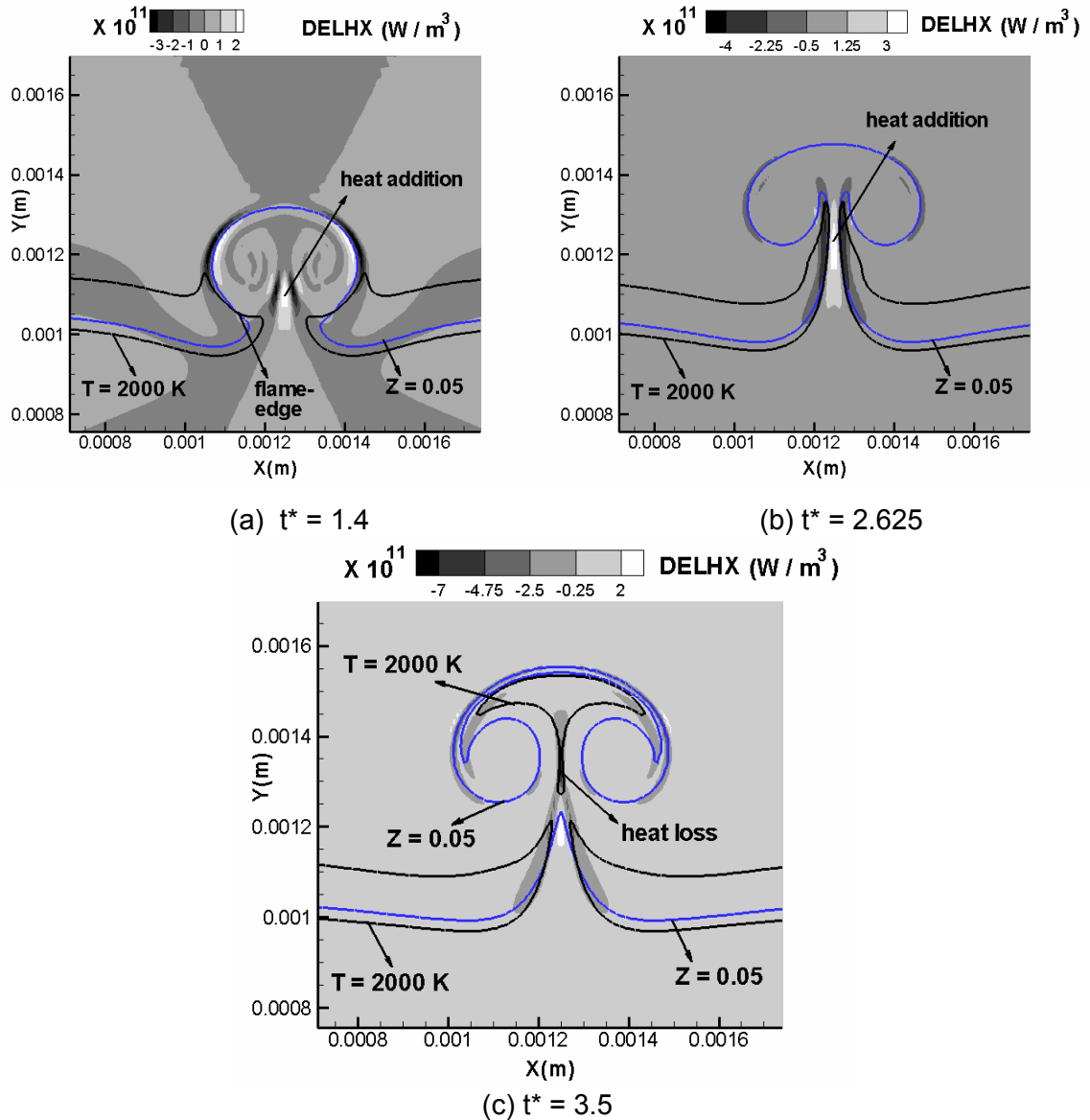
Figure 6.9. Contours of the lateral heat diffusion term $DELHX$ (W/m^3) during the reignition phase. Isocontours of $T = 2000\,K$ and $Z = 0.05$ are shown to define the flame-edge location.

Figures 6.9(a)-(c) show the contours of the lateral heat diffusion term $DELHX$ at t* = 1.4, 2.625 and 3.5, respectively. Following Pantano (2004), the position of the flame-edge can be found by the intersection of the isocontour of a reacting scalar with the Z_{st} isocontour. In Figs. 6.9(a)-(c), a temperature contour of 2000 K has been chosen along with the $Z_{st} = 0.05$ contour to define the edge

location. This choice is arbitrary but provides a reference location for the flame-edge. As shown in Figs. 6.9(a) and 6.9(b), *DELHX* contributes towards heat transfer to the extinguished points along the vertical centerline from the adjoining edge-flames. In addition to *DELHX*, lateral diffusion of species would promote partial-premixing and creation of flammable fractions in the quenched locations along the symmetry line (see Fig. 6.8(b)). This leads to the lateral propagation and the merger of the two parallel edge-flames, which is evident in Figs. 6.1(c) and (d). Note from Fig. 6.9(c) that during the final stages of the reignition phase, *DELHX* becomes negative in the region $0.00125 < Y < 0.00135$ as rich fractions are formed in this region due to partial-premixing (see Fig. 6.8(b)). In other words, *DELHX* contributes to heat loss from the reignited flame-elements that are rich to the colder regions around the vortical oxidizer pocket. This leads to local annihilation events in the merged flame (see Figs. 6.1(d) and 6.1(e)). Fig. 6.9(c) also shows that by t* = 3.5, sufficient mixing has occurred to form stoichiometric fractions in the reigniting region and a re-connected diffusion flame is eventually established.

The flame-flame interactions involving merger and annihilation of parallel flames observed here are qualitatively similar to those observed in the recent numerical work on premixed kernel-vortex interactions by Gokula and Echekki (2006). Figures 6.10(a) and (b) compare the relative magnitudes of the various heat flux terms and the chemical heat release rate *CHRR* at t* = 2.625 and 3.5, respectively, during the reignition phase along the vertical centerline. It is seen from Fig. 6.10(a) that the curvature term *DELHX* is of leading order and even larger in magnitude than the convective term *CNVHY* in the reigniting region, and the normal heat diffusion term *DELHY* is negligibly small in this region. Recall from our discussion of extinction (Fig. 6.6) that this is different from the trend observed in the extinguishing region. Essentially, the reigniting region is substantially diluted by the oxidizer following extinction as a result of which gradients in the Y direction are negligible in the early phase of reignition. On the other hand, the presence of the adjoining rolled-up edge-flames leads to strong

gradients in the X (lateral) direction thereby leading to the dominance of *DELHX* over *DELHY* .
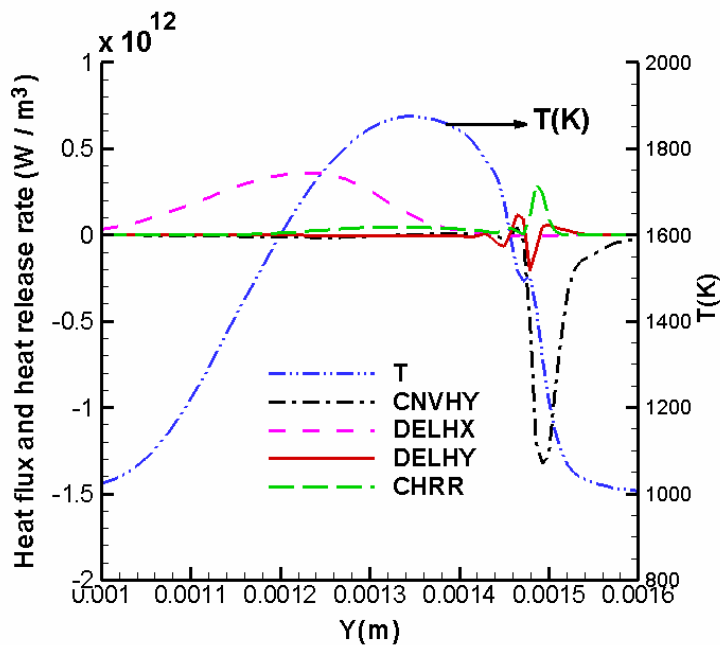
(a)
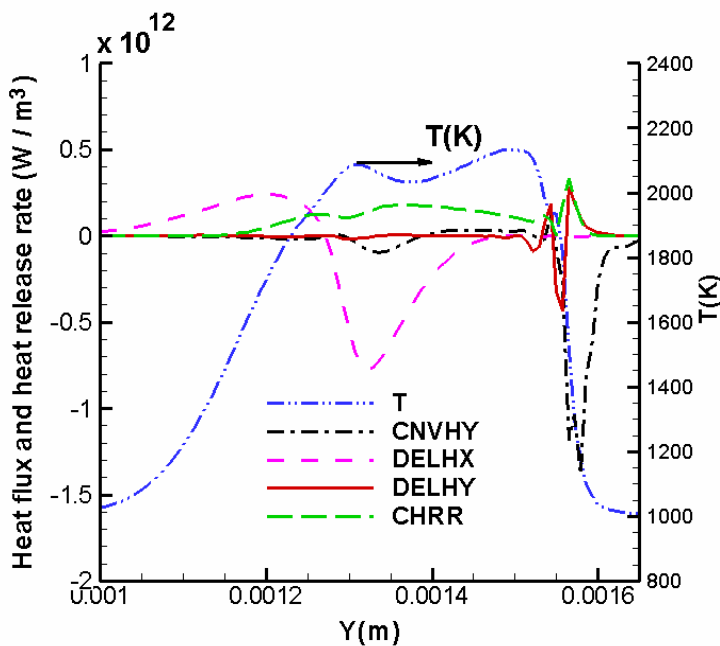
(b)

Figure 6.10. Comparison of heat fluxes (W/m^3) and the chemical heat release rate (W/m^3) along the vertical centerline during the reignition phase at (a) t* = 2.625, and (b) t* = 3.5.

Figure 6.10(b) represents a later stage during reignition. In the region $0.00125 < Y < 0.00145$, we observe that in addition to $CNVHY$, $DELHX$ makes a significant contribution to heat loss from the reignited but richer fractions formed by partial-premixing which leads to the local annihilation of the merged flame in this region, as discussed before. These results clearly indicate that the classical thin-flame assumption with non-negligible gradients only in the flame-normal direction (Peters, 1984), that leads to the 1-D flamelet equations represented by Eqs. (3.38) and (3.39), break down during the reignition phase. In other words, 2-D interactions with neighboring burning regions are found to be critical during reignition. It is interesting that the results are in good qualitative agreement with the edge-flame propagation and engulfment scenarios reported in the DNS of extinction-reignition dynamics in isotropic decaying turbulence performed by Sripakagorn *et al.* (2004), where lateral interactions were found to be important.

Figures 6.11(a)-(c) show the influence of the instantaneous scalar dissipation rate χ on the edge-flame dynamics during the reignition phase. Recall that the χ_r values shown in the figures at the edge locations are obtained by normalizing χ by the steady extinction limit χ_e. In Fig. 6.11(a), we observe that soon after local extinction, χ_r values in the vicinity of the flame-edges are relatively small, favoring their propagation into the adjoining quenched region. Aided by the vortex-induced flow, the edges are advected into the extinguished regions, where they promote heat addition due to lateral (X) heat and species diffusion (see Figs. 6.9(b) and 6.10(b)). However, the straining caused by the vortex leads to relatively high values of χ_r along the stoichiometric contour (Fig. 6.11(b)). This causes the edge-flames to recede away from the extinguished region, as shown by the increased separation distance between the edges in Fig. 6.11(c). We can also interpret this as negative propagation due to high values of scalar dissipation (Santoro *et al.*, 2000a). In Fig. 6.11(c), we observe that the effect of the vortex-induced flow has decreased and χ_r values at the flame-edge

locations have fallen to relatively low values. This leads to conditions favorable for edge-flame propagation and the diffusion flame is eventually re-established. Hence, the dynamics of the edge-flames is strongly influenced by the variations of χ relative to χ_e in the reigniting regions.

(a) t* = 1.4

(b) t* = 2.625

(c) t* = 3.5
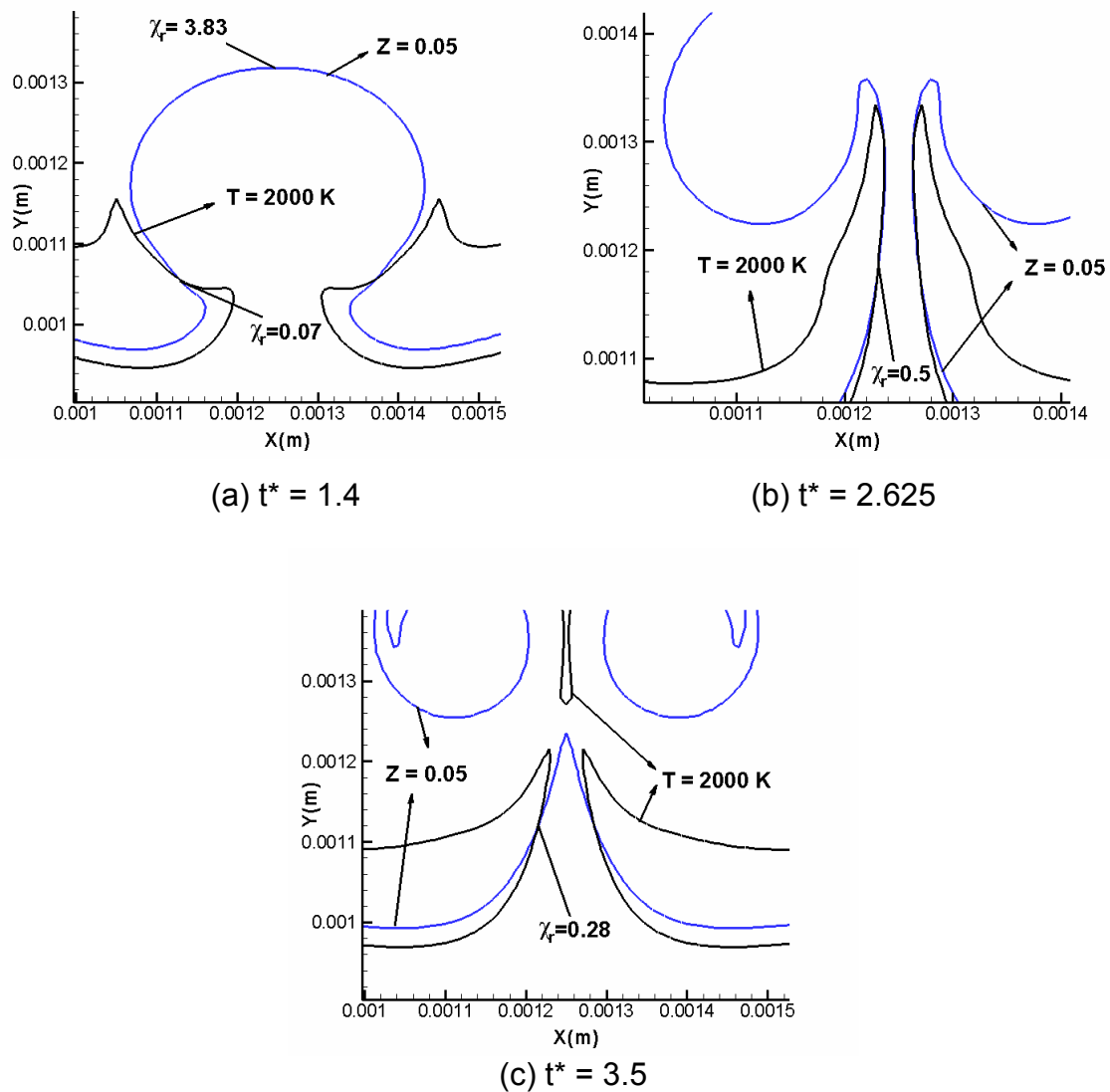
Figure 6.11. Influence of scalar dissipation on the edge-flame dynamics at different times during the reignition phase.

There are important differences between the reignition scenario observed here and that observed in the experiments of Santoro *et al.* (2000a). In the experiments, the vortex was relatively weak and had very little influence on the edge-flame dynamics due to almost complete dissipation after local extinction. Flame-flame interactions and local annihilation events observed in the present DNS were not reported. Moreover, in the absence of the vortex-induced flow, reignition occurred solely by the propagation of the edge-flames as ignition fronts along the stoichiometric contour. In the present case, flame-flame interactions enhance the mixing processes in the extinguished regions and greatly reduce the distance over which the edge-flames have to propagate to re-establish the diffusion flame. It is intuitive that as the vortex Reynolds number decreases, the importance of flame-flame interactions relative to edge-flame propagation would decrease.

Finally, it is interesting to consider the relative time scales over which extinction and reignition occur. Through a qualitative examination of the temperature snapshots such as those in Figs. 6.1(a)-(f), it is estimated that extinction occurs over a period of $t^* \sim 1.4$ ($t \sim 1.4 t_{eddy}$). On the other hand, the reignition phase occurs over a time interval of about $5.4 t_{eddy}$. Hence, consistent with the modeling studies of Hewson and Kerstein (2002) on extinction and reignition in turbulent jet flames, reignition is relatively slow compared to extinction. However, as discussed before, the rate of reignition would be even slower if the process occurred through an independent-flamelet scenario.

Note that in the present work, we have simulated a relatively high pressure of 40 bar to represent diesel engine conditions. The primary influence of the higher pressure is on molecular transport properties such as the kinematic viscosity, which is accounted for in the Reynolds number. The Damköhler number represents the kinetic effects of high-pressure (i.e. higher reaction rates and shorter chemical time scales). Note, however, that the focus of the present work is to investigate the flame-vortex interaction regimes through non-dimensional numbers, and not to assess the kinetic effects of pressure on these

regimes (such as extinction/reignition). Reliable multi-step kinetic models validated over a wide range of pressures would be required, which to the best of our knowledge, do not exist in the current literature. Hence, the predominant effect of the high-pressure in our work is hydrodynamic, and this effect would show scaling behavior. Furthermore, the chosen fuel-side temperature of 1000 K is much higher than those typically employed in diesel chambers (~ 400 K). In Chapter 7, we will present results from flame-vortex interaction studies with lower fuel-side temperatures (Venugopal and Abraham, 2008a) closer to diesel conditions in addition to the studies corresponding to the LES jet (i.e. with a fuel temperature of 1000 K). The implications of using a higher fuel temperature and the associated lower fuel-to-oxidizer density ratio will also be discussed.

6.5. <u>A Modeling Approach for Flame Extinction and Reignition</u>

From the flame-vortex simulation results discussed in this chapter, it is evident that unsteady flamelet models satisfactorily predict local extinction, but are inadequate to predict reignition through edge-flame dynamics following extinction. In this section, we will evaluate the recently developed flamelet/progress variable (FPV) approach (Pierce and Moin, 2004; Pitsch and Ihme, 2005) for the prediction of extinction and reignition. In Section 6.5.1, the theoretical framework is discussed, and the predictive capability of the model is demonstrated through comparisons of the model results with the flame-vortex simulation results. Thereafter, in Section 6.5.2, possible approaches for the implementation of the modeling framework as a RANS/LES combustion sub-model are discussed.

6.5.1. Theoretical Framework

Let us consider Fig. 6.12, which shows the stoichiometric temperature T_{st} as a function of the stoichiometric scalar dissipation rate χ_{st} along the vertical

centerline. The steady extinction limit χ_e is indicated on the figure. We observe three distinct parts of the T_{st}-χ_{st} state diagram, which are labeled as I, II and III. Part I represents the extinction phase discussed in Section 6.3, during which the unsteady flame withstands scalar dissipation rates well above the steady limit. Part II represents the early phase of reignition following extinction, where the edge flames are rolled up and transfer heat to the extinguished regions through lateral diffusion. Consequently, in spite of the relatively high values of χ_{st}, T_{st} begins to increase. As discussed in Section 6.4, the rate of partial-premixing in the reigniting region becomes high enough to cause secondary extinction events, and stoichiometric regions with relatively low mixing rates (i.e. low χ_{st}) are formed in the reconnecting region. Thereafter, the evolution of the reconnecting region is represented by Part III of the diagram, where the reconnected flame gradually relaxes beck to the initial state.
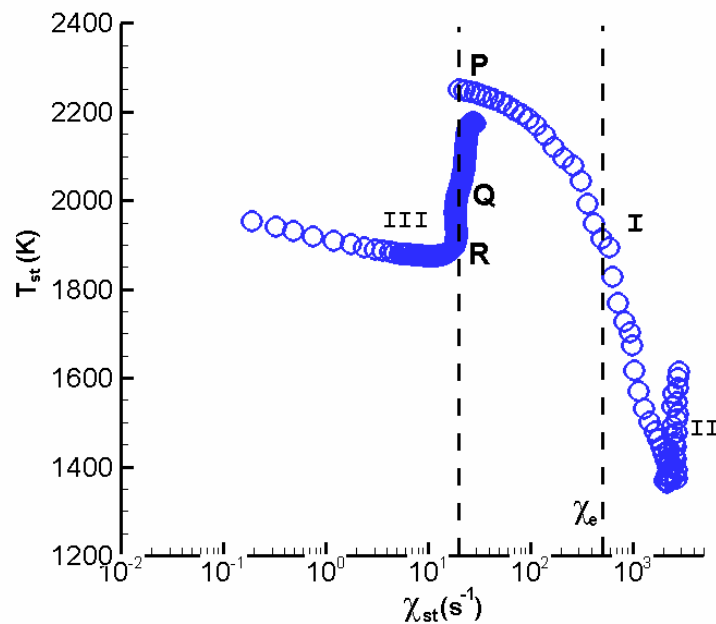
Figure 6.12. T_{st}-χ_{st} state diagram representing states during extinction and reignition along the vertical centerline during the flame-vortex interaction.

It is interesting to note from Fig. 6.12 that the parameterization commonly employed in flamelet models, i.e. $T_{st} = fn(\chi_{st})$, does not uniquely represent all the states during transient extinction/reignition. For instance, points P, Q and R indicated in Fig. 6.12 have the same value of χ_{st}, but different values of T_{st}. Hence, in order to predict extinction/reignition, we require a parameterization that is unique.
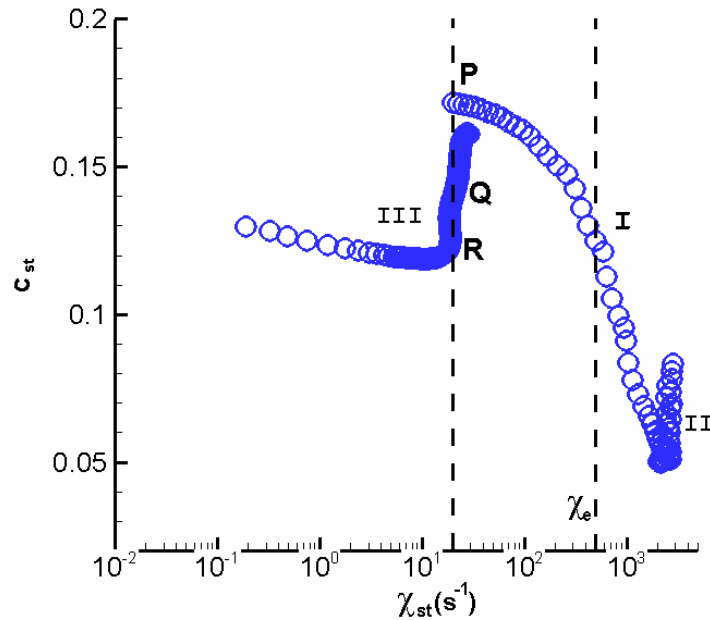
Figure 6.13. c_{st} - χ_{st} state diagram representing states during extinction and reignition along the vertical centerline during the flame-vortex interaction.

One approach is to introduce a reactive scalar, such as a reaction progress variable, which allows us to uniquely identify all the states during extinction/reignition. Following the recent work of Pierce and Moin (2004), this progress variable c can be estimated as the sum of major species mass fractions, which for the single-step model is given by

$$c = Y_{CO_2} + Y_{H_2O} .$$
$$(6.4)$$

Figure 6.13 shows the stoichiometric progress variable c_{st} as a function of χ_{st} along the vertical centerline. Since c_{st} is a reactive scalar, we observe trends similar to T_{st}. In addition, it is seen that points P, Q and R with a given value of χ_{st} can be uniquely identified using c_{st}. In other words, a parameterization of the form, $T_{st} = fn(\chi_{st}, c_{st})$, can represent all the states during extinction and reignition. Pierce and Moin (2004) recently developed a steady form of this approach, called the *flamelet/progress variable* (FPV) model, and assumed reignition to occur through autoignition. Note, however, that the present results show that unsteady effects on the flame-response could be significant and result in extinction scalar dissipation rates higher than steady limits, and that reignition could occur through edge-flame dynamics rather than autoignition Now, we will investigate whether an *unsteady flamelet/progress variable* (UFPV) model (Pitsch and Ihme, 2005) with the parameterization given by $T_{st} = fn(\chi_{st}, c_{st})$ can describe the states during extinction and reignition in the flame-vortex simulations.
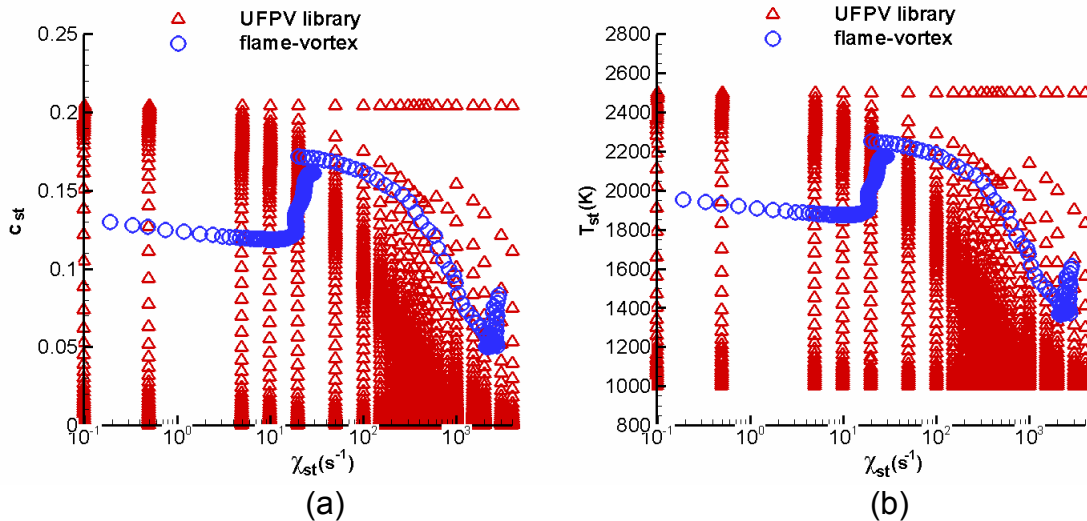
Figure 6.14. Flame states stored in the UFPV library in terms of the (a) c_{st}-χ_{st} diagram, and (b) the T_{st}-χ_{st} diagram.

To generate a UFPV library, we employ the unsteady flamelet equations (see Eqs. (4.14) and (4.14)) and tabulate various values of c, T and Y_i (from the burning branch to the frozen branch) for given values of χ. For instance, consider Figs. 6. 14(a) and (b), which show the states stored in the library for c_{st} and T_{st}, respectively. Results from the flame-vortex simulation are also indicated as circles in the figures. Note that we have employed 23 values of χ_{st} and 100 $(c, T, Y_i)_{st}$ states for each value of χ_{st} to generate the library. Due to the high degree of unsteadiness in the flame response, the values of χ_{st} span a relatively wide range of $2 \times 10^{-4} \chi_e - 8\chi_e$, where $\chi_e = 500 \text{ s}^{-1}$ for the baseline case discussed here. We observe from the figures that the flame-vortex states lie within the library, and are fairly close to the state points in the library.
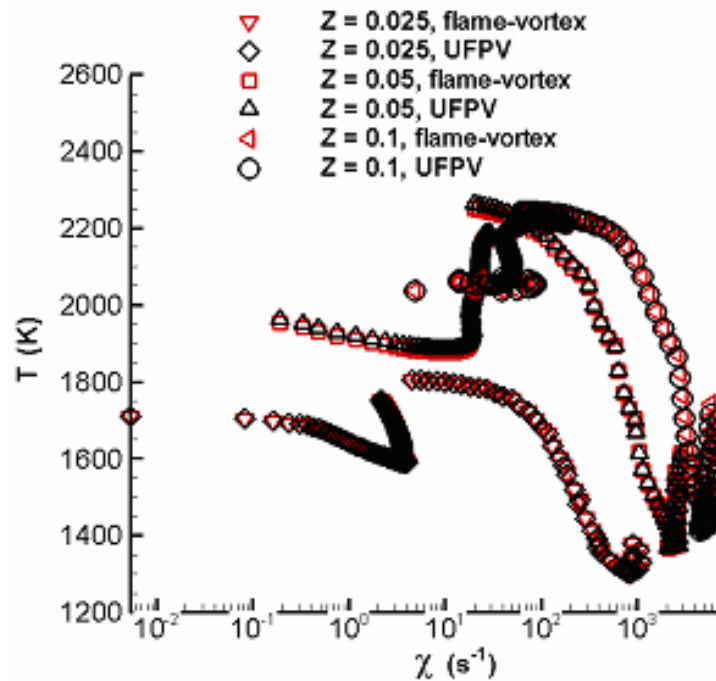
Figure 6.15. UFPV model results compared with the flame-vortex simulation results for three values of Z.

Figure 6.15 compares the predicted values of the temperature T using the UFPV model with the flame-vortex simulation results for three mixture fractions, $Z = 0.05$ (stoichiometric, $Z = 0.025$ (lean), and $Z = 0.1$ (rich). Note that libraries similar those shown in Figs. 6.14(a) and (b) were generated for the lean and rich fractions as well. For a given value of Z, the UFPV model results are obtained through 2-D interpolation based on χ and c estimated from the flame-vortex simulation along the vertical centerline as a function of time. We observe excellent agreement between the UFPV model predictions and the flame-vortex interaction results for all the three values of Z. Similar agreement was obtained with respect to species mass fractions as well. Note that in the case of detailed chemistry, the UFPV library could be relatively large. However, once the library is generated, the computational costs involved are primarily due to interpolation, which would be much lower than those due to direct integration with detailed chemistry.

Hence, the present work shows that the UFPV model can adequately describe unsteady flame extinction and reignition scenarios, provided the instantaneous scalar dissipation rate $\chi(Z,t)$ and the progress variable $c(Z,\chi,t)$ are specified as model parameters. Note that prior works so far in the literature have not assessed the accuracy of the UFPV model to predict unsteady extinction/reignition. We will now discuss possible approaches to implement the UFPV approach as a RANS/LES combustion sub-model.

6.5.2. Extension to RANS/LES Sub-model

In the case of the flame-vortex simulations, which are quasi-laminar (i.e. include only one flow length-scale and time-scale), the model parameters for the UFPV model (χ and c) can be computed exactly and passed on the UFPV library to obtain the predicted temperature and species mass fractions. In a turbulent jet flame simulation employing RANS or LES where not all of the relevant flow and chemical scales are resolved, χ and c have to be estimated

through sub-models. Below, we discuss possible approaches to implement the UFPV model as a RANS/LES combustion sub-model. The ideas presented here are similar to those discussed in the recent LES studies of Pitsch and Ihme (2005) employing the UFPV model for the simulation of a coaxial jet combustor.

In the theoretical framework developed in Section 6.5.1, we showed that the parameterization employed in the UFPV model of the form $\phi = fn(Z, \chi, c)$, where ϕ is a reactive scalar, provides a unique description of the unsteady flame states encountered during extinction and reignition. Now, with a suitable choice for c, such as the sum of major species mass fractions (Pierce and Moin, 2004), the set of values given by the function form $\phi = fn(Z, \chi, c)$ can be generated using the unsteady flamelet equations (Eqs. (4.3) and (4.4)), and stored in the form of a UFPV library. In the previous section, we demonstrated the application of UFPV libraries for three values of the mixture fraction (see Fig. 6.15). Moreover, as discussed by Peters (2000), the variables computed with the flamelet equations may be interpreted as conditional means $\langle \phi \rangle$. Hence, we can express the unconditional values $\widetilde{\phi}$ in the turbulent flowfield as

$$\widetilde{\phi} = \int\int\int \langle \phi(Z, \chi, c) \rangle \widetilde{P}(Z, \chi, c) dZ d\chi dc , \tag{6.5}$$

where $\widetilde{P}(Z, \chi, c)$ is the joint subgrid PDF of Z, χ and c. With the assumption of statistical independence between Z, χ and c, and the subgrid PDFs of χ and c to be described by delta functions (Pierce and Moin, 2004; Pitsch and Ihme, 2005), we obtain the closure expression for the joint PDF as

$$\widetilde{P}(Z, \chi, c) = \widetilde{P}(Z) \cdot \delta(\chi - \langle \chi \rangle) \cdot \delta(c - \langle c \rangle), \tag{6.6}$$

where $\langle \chi \rangle$ and $\langle c \rangle$ are the conditional means of χ and c, respectively, and $\widetilde{P}(Z)$ is the subgrid PDF of Z, which is typically assumed to be a beta function (Peters, 2000; Pitsch, 2006).

Now, as discussed in Chapter 5 on the LES results, and similar to Eq. (6.5), the conditional means can be related to the unconditional values using

$$\tilde{\chi} = \int \langle \chi \rangle \widetilde{P}(Z) dZ \, , \tag{6.7}$$

and

$$\tilde{c} = \int \int \langle c \rangle \widetilde{P}(Z, \chi) dZ d\chi \, . \tag{6.8}$$

Again, the statistical independence of Z and χ can be invoked to simplify the integrand in Eq. (6.8).

Hence, using a UFPV library with Z, $\langle \chi \rangle$ and $\langle c \rangle$ as parameters, we can precompute $\tilde{\phi}$, $\tilde{\chi}$ and $\tilde{c}$ using Eqs. (6.5)-(6.8), and express the possible sets of turbulent flame states as $\tilde{\phi}_{\text{library}} = g(\widetilde{Z}, \tilde{\chi}, \tilde{c})$, where g is the functional form given by the integrand of Eq. (6.5). Now, while $\widetilde{Z}$ and $\tilde{c}$ in the turbulent flowfield can be estimated through modeled transport equations (Pierce and Moin, 2004), $\tilde{\chi}$ can be computed using an algebraic model (see Eq. (5.3)), as in Chapter 5. Note that in contrast to $\widetilde{Z}$, the transport equation for $\tilde{c}$ will not be source-free, since $\tilde{c}$ is a reactive scalar. The mean/filtered source term for $\tilde{c}$, $\tilde{w}_c$, can be expressed as (Pierce and Moin, 2004)

$$\tilde{w}_c = \int \int \int \langle \dot{w}_c(Z, \chi, c) \rangle \widetilde{P}(Z, \chi, c) dZ d\chi dc \, , \tag{6.9}$$

where $\langle \dot{w}_c(Z, \chi, c) \rangle$ is the conditional mean source term for c. In the work of Pierce and Moin (2004) employing the steady FPV model, $\langle \dot{w}_c(Z, c) \rangle$ was precomputed using the steady flamelet equations and stored in the flamelet library for look-up. The same approach can be extended to the UFPV model as well to tabulate $\langle \dot{w}_c(Z, \chi, c) \rangle$ from the unsteady flamelet equations. Hence, with this closure approximation for the source-term, $\tilde{c}$ can be computed using a transport equation in the RANS/LES flowfield. Furthermore, with $\widetilde{Z}$, $\tilde{\chi}$ and $\tilde{c}$ known in each computational cell, 3-D interpolation with the UFPV library (i.e. $\tilde{\phi}_{\text{library}} = g(\widetilde{Z}, \tilde{\chi}, \tilde{c})$) can then be employed to obtain the predicted filtered/mean values of the reactive scalars.

Note that the approach of Pierce and Moin(2004) involving the tabulation of $\langle \dot{w}_c(Z, \chi, c) \rangle$ using the flamelet equations can account for reignition through autoignition, but not through mechanisms such as edge-flame dynamics, which were shown to be important in the present work. In Chapter 10, we will indicate one possible approach to account for edge-flame effects in the modeling of the progress variable. In addition, modeling of the subgrid PDF of the progress variable (i.e. $P(\tilde{c})$) would require consideration. The recent modeling results of Ihme *et al.* (2005) employing the steady FPV model compared with the DNS database of Sripakagorn *et al.* (2004) show sensitivity to the modeling choices for $P(\tilde{c})$. For instance, it was shown that a beta function for $P(\tilde{c})$ provides a more accurate description of the extinction/reignition scenarios observed by Sripakagorn *et al.* (2004) as compared to a delta function assumed in the studies of Pierce and Moin (2004). This further implies that we need model closure for the conditional variance of the progress variable, which is a parameter for the beta-PDF. Finally, the fidelity of the UFPV model to predict turbulent flame extinction/reignition and associated phenomena such as lift-off in a large-scale jet flame would also depend on the sub-models for turbulence and chemistry.

6.6. Summary and Conclusions

In this chapter, results from a baseline flame-vortex simulation were discussed. The conditions simulated were characterized by the following set of non-dimensional numbers: $l_r = 1.5;\ u_{fv} = 5.85;\ \mathrm{Re} = 540;\ Da_i = 30$, which were estimated from the temporal mean statistics computed using LES at the jet location, x/d = 12, computed as an average over the radial region, $0 \leq r/d \leq 1.5$. The pressure was 40 bar and the fuel-side and air-side temperatures were 1000 K. A single-step chemical mechanism was employed. The influence of the chemical mechanism on the conclusions will be discussed in Chapter 8. Under these conditions, local extinction followed by reignition was observed

during the flame-vortex interaction. The flame-response during the extinction phase showed strong unsteady effects owing to the relatively large value of the chemical-to-vortex time-scale ratio, $\tau_c * u_v / d_v$ (~ 4.0). Consistent with prior experimental and numerical works, the unsteady flame was found to extinguish at scalar dissipation rates much higher than the steady extinction limit. Comparisons of the flame-vortex results along the symmetry axis with the predictions of a transient 1-D diffusion flamelet library showed good agreement. In other words, effects due to vortex-induced curvature and partial-premixing were found to be minimal during the extinction phase and the flame essentially behaves as a 1-D unsteady flamelet.

The flame-response during the reignition phase showed significant differences from the extinction phase. Through a sequence of unsteady events involving 2-D flame-flame interactions, merger of the edge-flames formed after local extinction, and the local annihilation of the merged flame, the original diffusion flame was re-established. These interactions were characterized by lateral (X direction) diffusion of heat and species from the rolled-up edge-flames to the adjoining quenched regions. The analysis showed that the 1-D flamelet model which ignores curvature effects is not applicable during the reignition phase. In particular, the flame loses its 1-D flamelet structure due to significant levels of partial-premixing in the wake of the vortex-induced flow. The dynamics of the edge-flames were strongly influenced by the evolution of the instantaneous scalar dissipation rate in the reigniting region. In Chapter 7, we will consider a wider range of conditions estimated from the mean statistics computed with LES, including conditions (such as lower fuel temperatures and larger fuel-to-oxidizer density ratios) that are closer to diesel combustion chambers. In addition, the implications of specific choices, such as the higher fuel temperature (= 1000 K), on the flame-vortex interaction outcomes will be discussed.

The recently developed unsteady flamelet progress/variable (UFPV) model (Pitsch and Ihme, 2005) was assessed for the prediction of unsteady extinction and reignition observed in the flame-vortex simulations. It was shown

that a tabulated UFPV library can accurately describe extinction and reignition, provided the instantaneous scalar dissipation rate and the instantaneous progress variable are specified as model parameters. Hence, from a fundamental (flame-vortex interaction) point of view, the present work shows that the UFPV model is an improvement over steady flamelet models for the prediction of local extinction and reignition. Possible approaches to implement the UFPV model as a combustion sub-model for RANS/LES were discussed. Directions for incorporating edge flame effects into the UFPV model to predict reignition scenarios observed in the present work will be discussed in Chapter 10.

In the chapter that follows, effects due to unsteadiness and curvature on the extinction and reignition scenarios are explored through parametric studies involving a range of vortex length scales, velocity scales and scalar dissipation rates. This range of vortex and flame characteristics is selected from the statistics computed with LES at different locations in the jet. A regime diagram for localized flame dynamics in the jet near-field showing the combined effects of unsteadiness and curvature will be constructed from the coupled LES-flame-vortex studies.

CHAPTER 7. UNSTEADY AND CURVATURE EFFECTS IN FLAME-VORTEX INTERACTIONS

7.1. <u>Introduction</u>

In this chapter, effects due to unsteadiness and curvature on the localized flame dynamics in the jet near field are explored through parametric studies of flame-vortex interactions corresponding to different locations in the LES jet flowfield. Table 7.1 shows the non-dimensional numbers that characterize the flame-vortex interaction, which were introduced in Chapter 4. These non-dimensional numbers are constructed using the initial vortex length-scale (d_v), initial vortex velocity-scale (u_v) and the initial stoichiometric scalar dissipation rate ($\chi_{st,i}$) as parameters. The simulated range for these three parameters is obtained from temporal mean statistics in the computed LES jet near field region ($12 \le x/d \le 20$). At each axial location, the radial region of interest is $0 \le r/d \le 1.5$, which represents a region close to the jet centerline, and the chosen parameters (i.e. d_v, u_v, $\chi_{st,i}$) are computed as averages over this radial region. The radial region close to the jet centerline is chosen as we expect the most energetic eddies capable of causing flame extinction/reignition to occur in this region. The estimated values for d_v, u_v, and $\chi_{st,i}$ in the region, $12 \le x/d \le 20$ and $0 \le r/d \le 1.5$, lie in the range of 90-600 μm, 2-9 m/s, and 2-18 s^{-1}, respectively.

Note that the simulated values of d_v at each axial location in the radial region of interest lie in the range of $(0.1-0.7)L_{11}$, where L_{11} is the mean turbulent integral length-scale. In terms of the mean Taylor length-scale λ, the range of d_v simulated is approximately $(1.5-9.0)\lambda$. Hence, the length-scales of the chosen vortices represent the inertial scales of the turbulent spectrum fairly well.

Moreover, $\chi_{st,i}$ is assumed to be equal to the average stoichiometric conditional-mean scalar dissipation rate in the radial region $0 \leq r/d \leq 1.5$ at a given axial location, and decides the initial thickness (δ) of the diffusion layer. The values of δ corresponding to the estimated values of $\chi_{st,i}$ lie in the range of 120-440 μm.

Table 7.1 Non-dimensional numbers for the flame-vortex interaction studies.

Numbers	Effect	Range simulated $(12 \leq x/d \leq 20)$
Length-scale ratio, $l_r = d_v / \delta$	Curvature	**0.3-3.0**
Velocity-scale ratio, $u_{fv} = u_v / u_f$	Unsteadiness	**1.0-6.0**
Damkőhler number, Da $= \chi_{st}^{-1}/ \tau_c$	Extinction, Da <1	Initial value (strength of the flame): **10-100**
Reynolds number, $Re_v = u_v * d_v/\nu$	Unsteadiness, curvature and viscous	**60-2000** (Prior works, **Re_v< 600**)
Scalar dissipation ratio, $\chi_r = \chi_{st}/\chi_e$	Unsteadiness	Computed during the simulation
t* = t/t_eddy		

From Table 7.1, the estimated values of d_v and δ result in values of l_r in the range of 0.3-3.0. Variation in l_r across the jet can be correlated with variation in curvature, and this range estimated from mean LES statistics (0.3-3.0) represents vortices (eddies) that are smaller and larger than the mean local diffusion layer thickness δ. The simulated values of u_v lie in the range of $(0.5-1.0)u'$, where u' is the mean turbulent velocity-scale. This leads to values of u_{fv} in the range of 1.0-6.0, as indicated in Table 7.1. As we will show in Section 7.2, the lower limit of u_v selected (i.e. ~ $0.5u'$) roughly corresponds to the weakest vortex for the simulated range of Reynolds numbers that can cause

extinction of the flames for the pressures and temperatures considered here. Variation in u_{fv} represents effects due to unsteadiness, and the relatively large values (> 1.0) shown in Table 7.1 suggest that unsteady effects on the flame-response may be important.

As discussed in Chapter 6, the instantaneous flame Damköhler number Da is used to identify local extinction ($Da < 1$), and the initial value Da_{i} is a measure of the robustness of the initial flame. We observe from Table 7.1 that Da_{i} varies In the range of 10-100, and represents highly-strained to moderately-strained flames. However, note that variation of Da_{i} occurs due to a variation in δ (and hence $\chi_{\text{st,i}}$), and therefore would affect the values of l_{r} and u_{fv} as well, for given characteristics of the vortex (d_{v} and u_{v}). In addition to u_{fv}, the scalar dissipation ratio χ_{r} is also a measure of unsteadiness, and can be used to express the magnitude of the unsteady extinction limit relative to the steady value. Note that χ_{r} is an instantaneous quantity that is computed during the simulation (i.e. it is not known a-priori), but we will show that the trends in χ_{r} can in general be related to l_{r} and u_{fv}. In addition to Da, the vortex Reynolds number Re_{v} defined in Table 7.1 is a derived non-dimensional number that includes both the effects of unsteadiness and curvature due to its dependence on d_{v} and u_{v}. Furthermore, as in Chapter 6, the physical time is normalized by the characteristic vortex (or eddy) turnover time ($= d_{\text{v}} / u_{\text{v}}$) to yield t*.

The single-step kinetic model discussed in Section 3.3 is employed in the simulations discussed in this chapter, but we will also present results with a multi-step kinetic model in the Chapter 8 to assess the influence of the kinetics on the conclusions drawn here. In the rest of this chapter, the unsteady and curvature effects at an axial location x/d=12 are discussed in Sections 7.2 and 7.3, respectively. In Section 7.4, results from simulations corresponding to different axial locations in the jet near field are presented. Thereafter, outcome diagrams relevant for local jet near-field flame dynamics, and the implications of the

present results for turbulent combustion modeling are discussed in Section 7.5. Note that the jet considered in the present work has a Reynolds number of 70,000, whereas the Reynolds numbers encountered in practical engines could be an order of magnitude higher. During the discussion of the results, we will comment on the applicability of the present results to higher Reynolds number jets. We will also indicate the implications of some of the choices made for the simulated conditions, such as the fuel- and oxidizer-side temperatures, and the fuel-to-oxidizer density ratio. The chapter closes with summary and conclusions in Section 7.6.

7.2. Unsteady Effects on Flame-Vortex Interactions
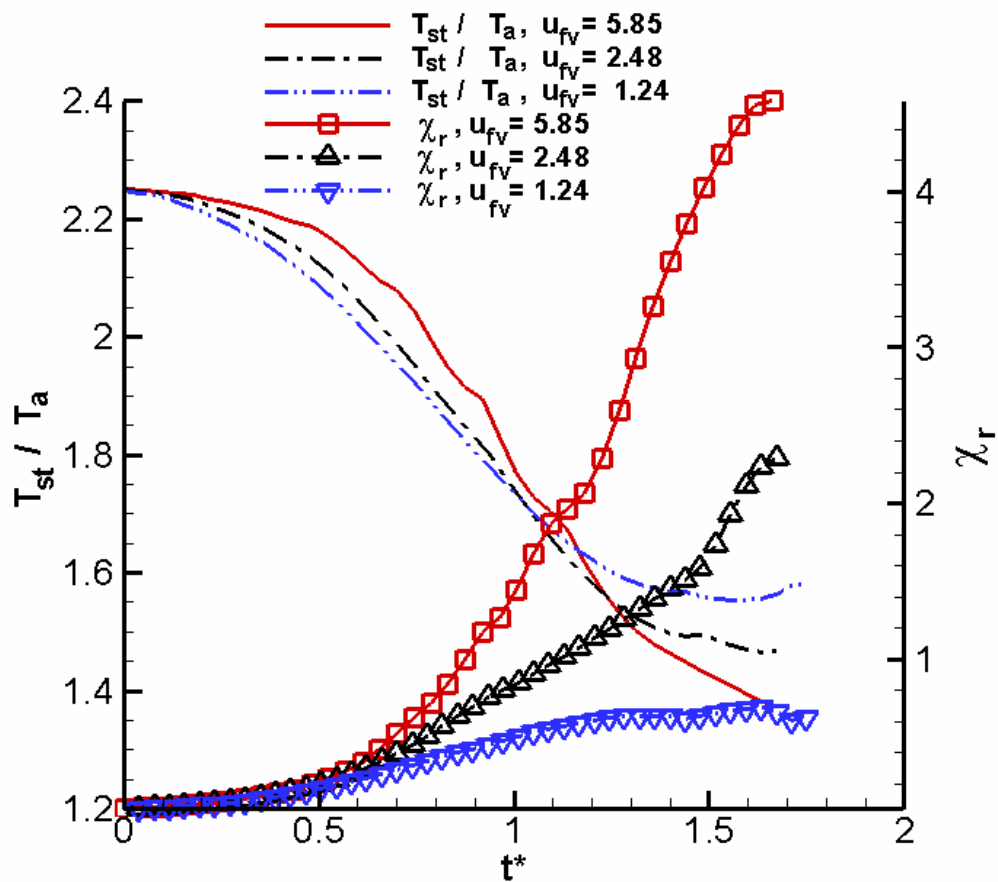
Figure 7.1. T_{st}/T_a and χ_r as a function of t* for different u_{fv} during the extinction phase.

To investigate effects due to unsteadiness, we vary Re_v in the range of 120-540 by changing u_{fv} in the range of 1.0-6.0, while maintaining l_r at 1.5 and Da_i at 30. In other words, the highest Re_v case represents the fastest vortex. Note that $l_r = 1.5$ corresponds to a vortex that is sized about 36 % of the mean turbulent integral length scale (L_{11}) at the axial location x/d = 12, close to the jet centerline ($0 < r/d < 1.5$).

Figure 7.1 shows the time-evolution of the normalized temperature T_{st}/T_a and the scalar dissipation ratio χ_r for three values of u_{fv}. We observe higher values and rates of increase of χ_r as u_{fv} increases. Moreover, the increasing unsteadiness in the flame response at higher values of u_{fv} is also evident. For instance, at t* = 1, we observe higher temperatures for the $u_{fv} = 5.85$ case relative to the $u_{fv} = 1.24$ case, even though the corresponding χ_r values are higher when $u_{fv} = 5.85$. This shows that at higher values of u_{fv}, the unsteady flame responds with a greater delay. However, as χ_r increases to relatively large values (> 2.0), the $u_{fv} = 5.85$ flame is driven towards extinction, while in the other two cases, the flame temperatures begin to recover.

Figure 7.2 compares the unsteady cases with steady flamelet predictions. We observe that the vortex-perturbed flame-response is closer to that of a steady flame as u_{fv} decreases, but unsteady effects are still dominant for the range of conditions simulated. Figure 7.3 shows the variation of Da as a function of χ_r for the three values of u_{fv}. We observe that the unsteady extinction limit (defined at the onset of extinction, $Da = 1$) decreases from about 1.8 χ_e to about 1.2 χ_e as u_{fv} decreases from 5.85 to 2.48. This trend is in qualitative agreement with the numerical results of Oh *et al.* (2004). In other words, the unsteady limit is flow-dependent, and governed by the vortex-to-flame velocity-scale ratio (u_{fv}) for given values of l_r and Da_i. Also, Fig. 7.3 shows that the $u_{fv} = 1.24$ vortex is not

strong enough to locally extinguish the flame, since Da remains of order 2 before increasing due to flame recovery. Note that in the present case, the fuel and oxidizer temperatures are both assumed to be equal to 1000 K. However, it is typical in diesel engine applications to inject cold fuel (~ 400 K) into a hot oxidizer (~ 1000 K). Lower fuel temperatures would give rise to weaker flames (i.e. lower Da_i), and hence larger values of u_{fv} for given characteristics of the vortex. Extrapolating from Fig. 7.3, this would lead to greater deviations of the unsteady extinction limit from the steady limit.
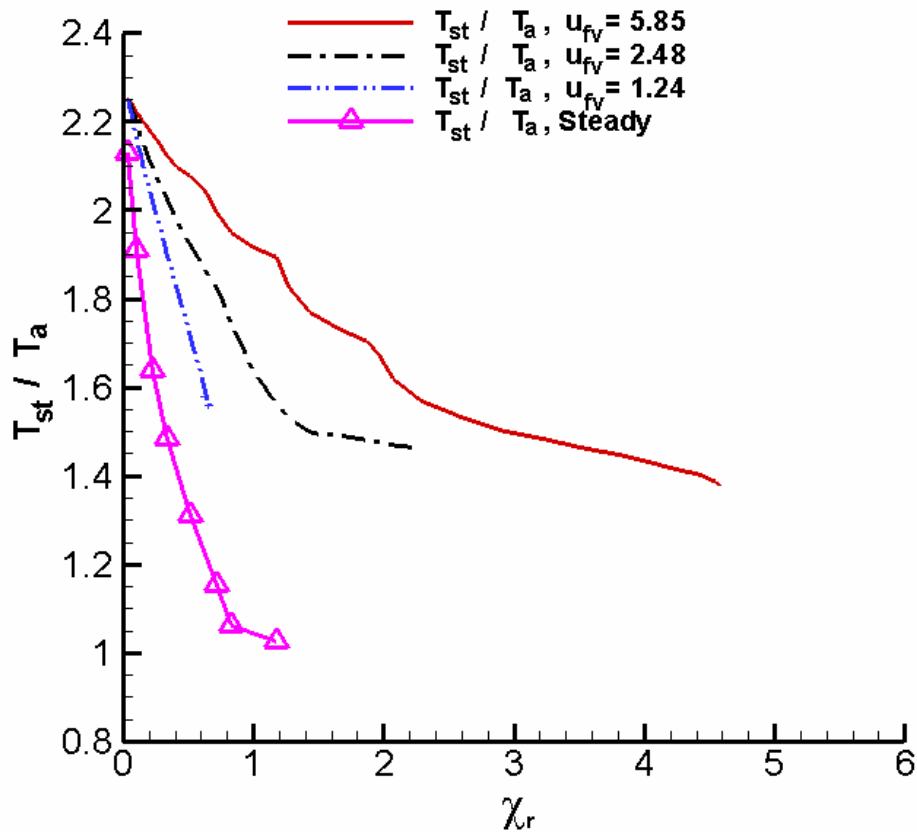
Figure 7.2. T_{st}/T_a as a function of χ_r for different u_{fv} compared with steady flamelet predictions during the extinction phase.
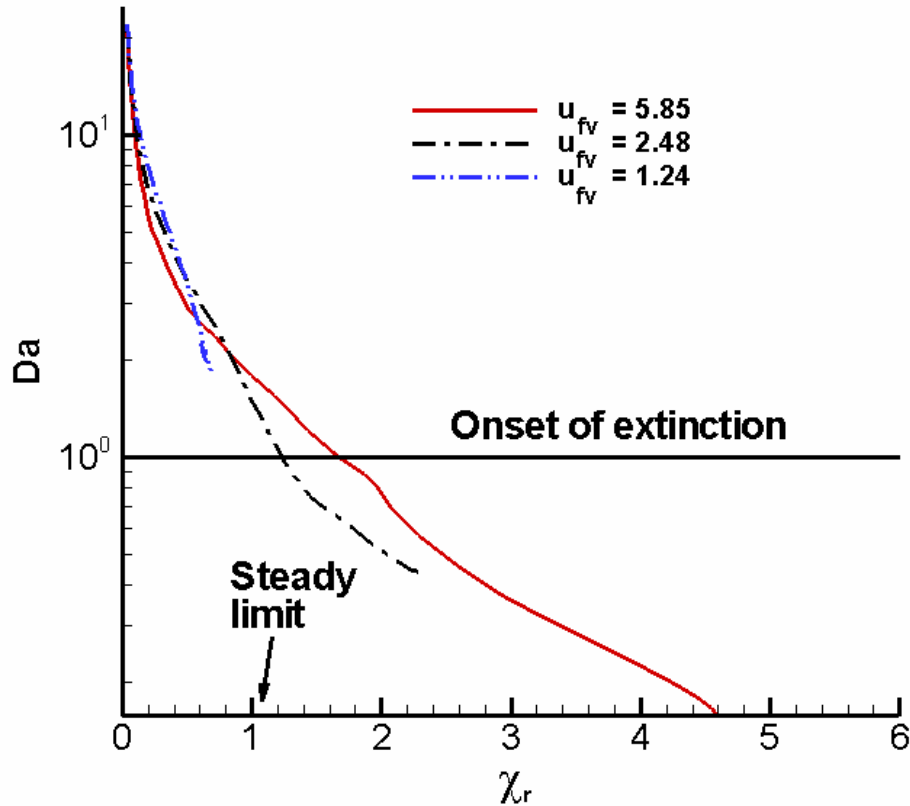
Figure 7.3. Da as a function of χ_r for different u_{fv} during the extinction phase.

To confirm this, consider Fig. 7.4, which shows Da as a function of χ_r for a wider range of vortex Reynolds numbers (Re_v) and u_{fv} (51-205) from our recent flame-vortex interaction studies (Venugopal and Abraham, 2008a). In these studies, we considered interactions between relatively strong vortices with relatively weak (or strained) flames ($Da_i \sim 10$) established between the fuel at 450 K and the oxidizer at 1000 K. Due to the relatively large values of u_{fv} (51-205), we observe unsteady extinction limits (at $Da = 1$) as much as 6 times the steady value. Hence, it is expected that in higher Reynolds number jets under practical engine conditions (i.e. with cold fuel and hot oxidizer), relatively strong vortices would interact with relatively weak (or strained) flames resulting in strong

unsteady effects in the flame-response. Note that for the weaker (and relatively strained) flames simulated in the results of Fig. 7.4, the steady extinction limit is $\chi_e = 130\,\text{s}^{-1}$, which is roughly 0.3 times the steady limit for the flamelets corresponding to the LES jet (i.e. fuel temperature = 1000 K), where $\chi_e = 500\,\text{s}^{-1}$ .Hence, the magnitude of the unsteady limit (at $Da = 1$) for the weaker flames (~ 6 χ_e) is about 780 s^{-1}, whereas it is about 1.8 χ_e (as discussed before), i.e. 900 s^{-1} for the stronger flames with a fuel-side temperature of 1000 K. Hence, the relative magnitudes of the unsteady limits confirm the intuitive expectation that weaker flames extinguish at lower scalar dissipation rates. However, greater departure of the unsteady limit from the steady limit (i.e. higher values of χ_r at extinction) for the weaker flames indicates a greater delay (i.e. unsteady effects) in the flame-response.
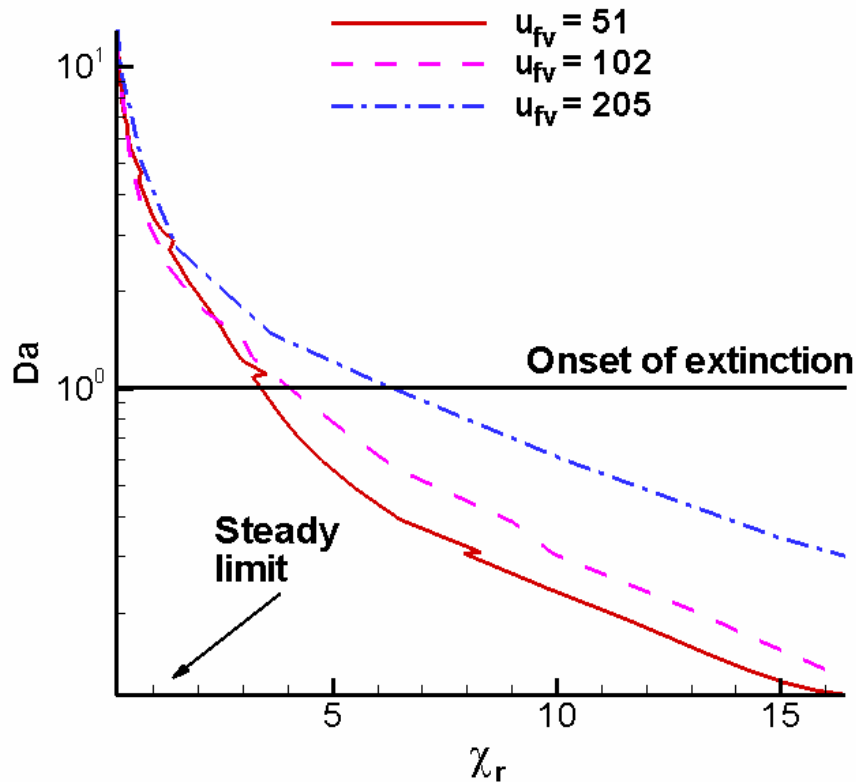
Figure 7.4. Da as a function of χ_r for higher values of u_{fv} (51-205) during the extinction phase (Venugopal and Abraham, 2008a).

In addition, note that the choice of fuel-side and oxidizer-side temperatures influences the fuel-to-oxidizer density ratio. For instance, with $T_f = 450\,\text{K}$ and $T_a = 1000\,\text{K}$, the density ratio is about 7.7, whereas with $T_f = 1000\,\text{K}$ and $T_a = 1000\,\text{K}$, the density ratio is about 3.5. Qualitative comparisons between prior studies with $T_f = 450\,\text{K}$ (Venugopal and Abraham, 2008a) and the present results with $T_f = 1000\,\text{K}$ indicate that the primary effect of the density ratio is to modify the residence time for the flame-vortex interaction. Essentially, the air-side vortex would penetrate much faster in a less dense fuel medium ($T_f = 1000\,\text{K}$), and would therefore be associated with shorter residence times. Hence, we can employ jet scaling laws for the vortex "jet", and achieve comparable residence times for the $T_f = 450\,\text{K}$ and the $T_f = 1000\,\text{K}$ cases by scaling the vortex velocity. Similar scaling can be employed for fuel-side vortices as well. In other words, with different density ratios, we would expect different time scales for extinction and reignition, but the physical mechanisms would remain unaffected. Hence, while the fuel-side and oxidizer-side temperatures primarily affect the flame strength and the non-dimensional numbers Da_i and u_{fv}, the fuel-to-oxidizer density ratio (ρ_j / ρ_a) appears as an additional parameter governing the flame-vortex residence time.

Before we proceed to the discussion of unsteady effects during reignition, it is important to note that the results presented here are based on interactions of air-side vortices with the diffusion flames. In a high-Re jet, the intermittent nature of the shear layers may lead to the entrainment of unmixed fluid in the form of oxidizer eddies which may then interact with the embedded flamelets. The present flame-vortex interaction studies provide insights into such scenarios. However, it is also possible that high-speed fuel eddies (i.e. strong fuel-side vortices) may impact the flamelets. The interactions of fuel-side vortices with the diffusion flames may show some interesting differences from those involving air-side vortices. For instance, the recent numerical results of Oh *et al.* (2004) show that unsteady extinction limits may be different with air-side and fuel-side

vortices, due to differences in the time history of the scalar dissipation rate. However, note that the trends observed here with respect to unsteady effects, i.e. decreasing unsteadiness with decreasing vortex velocities, would remain the same with both air-side and fuel-side vortices. Moreover, in the present case, owing to fuel-to-oxidizer density ratios greater than unity (~3.5), the denser fuel-side vortex may penetrate the diffusion layer more effectively than an air-side vortex, and hence would be associated with shorter residence times. Later in this section, we will discuss some of the possible differences between air-side and fuel-side vortices with respect to reignition.

Let us now consider the effects of unsteadiness on the reignition phase. The edge-flame dynamics during the interaction of the $u_{\mathrm{fv}} = 2.48$ vortex is compared with the baseline case ($u_{\mathrm{fv}} = 5.85$) discussed in Chapter 6. Figures 7.5(a)-(c) show the isocontours, $T = 2000 \ \mathrm{K}$ and $Z = 0.05$, at different instants of time during the reignition phase when $u_{\mathrm{fv}} = 2.48$. Values of χ_{r} at the edge locations are also indicated in these figures. Comparing with Figs. 6.11(a)-(c) which show the edge-flame dynamics for the $u_{\mathrm{fv}} = 5.85$ case at the corresponding times, we observe some important differences. Firstly, values of χ_{r} experienced by the flame edges are much lower with the slower vortex ($u_{\mathrm{fv}} = 2.48$). Consequently, the flame edges are rolled up to a greater extent, as seen through comparisons of Figs. 7.5(b) and (c), and Figs. 6.11(b) and (c). The lower values of χ_{r} favor edge flame propagation, and Fig. 7.5(c) shows that the reconnected flame is formed by t* = 3.5. Note, however, that since t_eddy ($= d_{\mathrm{v}} / u_{\mathrm{v}}$) increases by 2.25 times as u_{fv} decreases from 5.85 to 2.48, reignition occurs over a longer physical time with the slower vortex.

(a) t* = 1.4

(b) t* = 2.625

(c) t* = 3.5
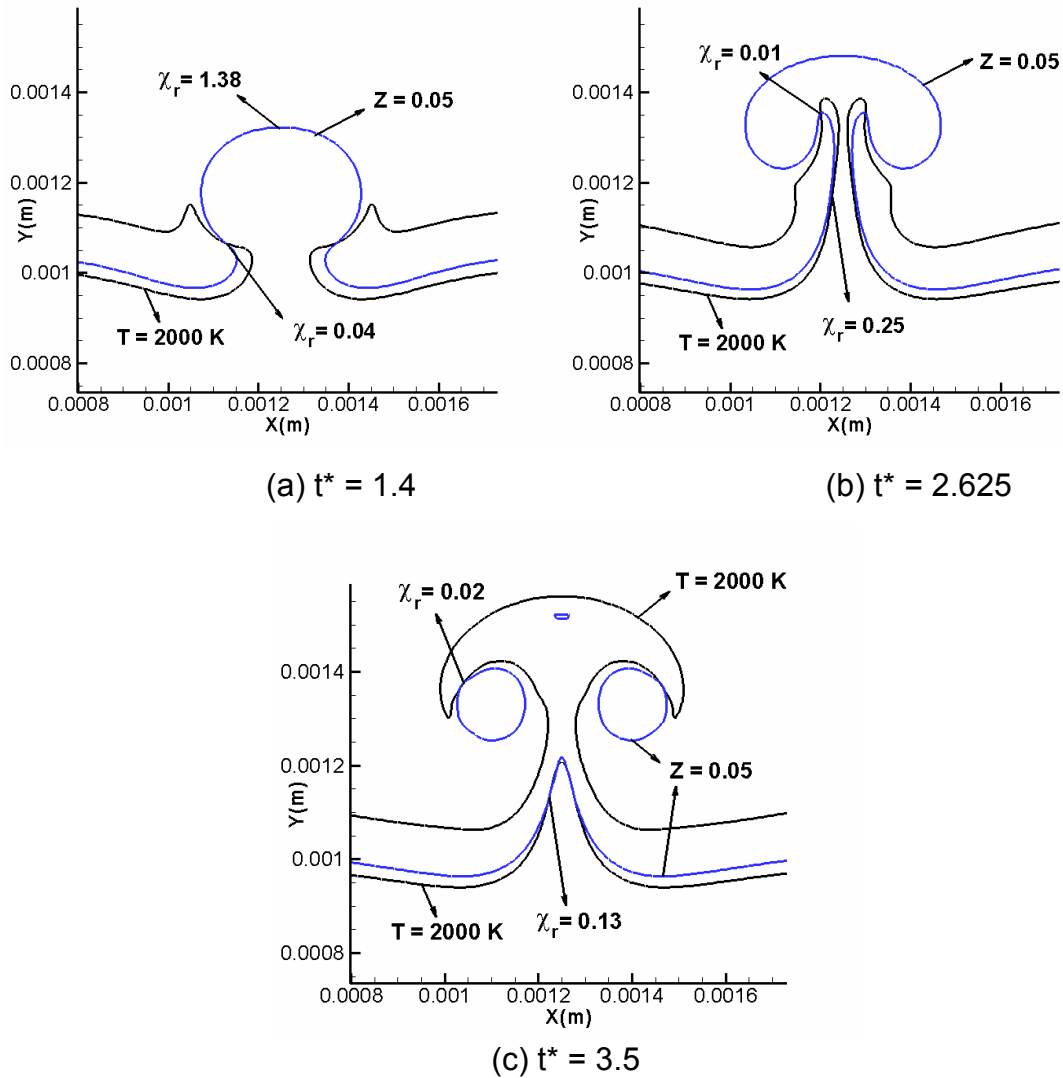
Figure 7.5. Isocontours of $T = 2000\,\text{K}$ and $Z = 0.05$ to show edge-flame dynamics at different times during the reignition phase for $u_{\text{fv}} = 2.48, l_{\text{r}} = 1.5, Da_{\text{i}} = 30$.

These comparisons between the $u_{\text{fv}} = 5.85$ and $u_{\text{fv}} = 2.48$ cases show that as the velocity-scale ratio decreases, effects due to unsteadiness decrease, which lead to greater flame roll-up, but slower rates of extinction and reignition. Note that the choice of $T_{\text{f}} = 1000\,\text{K}$ and $T_{\text{a}} = 1000\,\text{K}$ essentially leads to a single-stage autoignition behavior, whereas with $T_{\text{f}} = 450\,\text{K}$ and $T_{\text{a}} = 1000\,\text{K}$, n-heptane

autoignition would show two-stage behavior (Liu *et al.*, 2005). However, our recent flame-vortex studies employing a multi-step chemistry model for n-heptane (Venugopal and Abraham, 2008b) and with $T_f = 450\,\text{K}$ and $T_a = 1000\,\text{K}$, show that for flame-vortex interactions relevant to the near field of diesel jet flames, reignition is likely to occur through edge-flame dynamics, and not autoignition. Essentially, the mode of reignition (autoignition or edge flame dynamics) is governed by non-dimensional numbers l_r and u_{fv}. It will be shown that in Section 7.3 that l_r has a significant effect on reignition, and for relatively small values of l_r (< 3.0), mutual interactions between edge flames are strong enough to cause reignition before normal (to the flame) diffusion can lead to autoignition. Moreover, for the range of u_{fv} values simulated in this work (1.0-6.0), excursions of χ_{st} above χ_e are significant (i.e. $\chi_r \gg 1$), such that reignition cannot occur without lateral (i.e. along the flame surface) interactions between extinguished and neighboring burning regions. Recent DNS of Sripakagorn *et al.* (2004) in reacting isotropic turbulence also supports this latter fact, and we will confirm the same in Chapter 9 focusing on extinction/reignition under oscillatory scalar dissipation rates.

As discussed earlier, employing fuel-side vortices may show some differences from air-side vortices. For given vortex characteristics (d_v and u_v), a fuel-side vortex would penetrate more effectively through the diffusion layer (since the fuel is about 3.5 times more dense than the oxidizer), and result in relatively shorter residence times. Hence, the tendency for reignition may decrease in comparison to an air-side vortex. In addition, since the stoichiometric mixture fraction in the present heptane/air flame is about 0.05 (i.e. closer to Z = 0 than Z =1), it would take much longer for the extinguished regions diluted with the fuel (Z =1) to premix and form flammable fractions before reignition can occur. Therefore, it may be expected that for given vortex characteristics, air-side vortices are more likely to cause reignition following extinction in comparison to fuel-side vortices. Nevertheless, the trends observed here for reignition with

respect to u_{fv} and l_r would hold true for fuel-side vortices as well. Hence, it is reasonable to expect that the mechanism of reignition through edge flame interactions as revealed in this work for the simulated range of non-dimensional numbers is generally valid, and minimally affected by specific choices, such as fuel- and oxidizer-side temperatures, fuel-to-oxidizer density ratios, and air-side vortices, However, exploration of the dependence of the unsteady extinction limits and the rates of extinction/reignition on the above factors would be useful and interesting avenues for future work.

7.3. Curvature Effects on Flame-Vortex Interactions
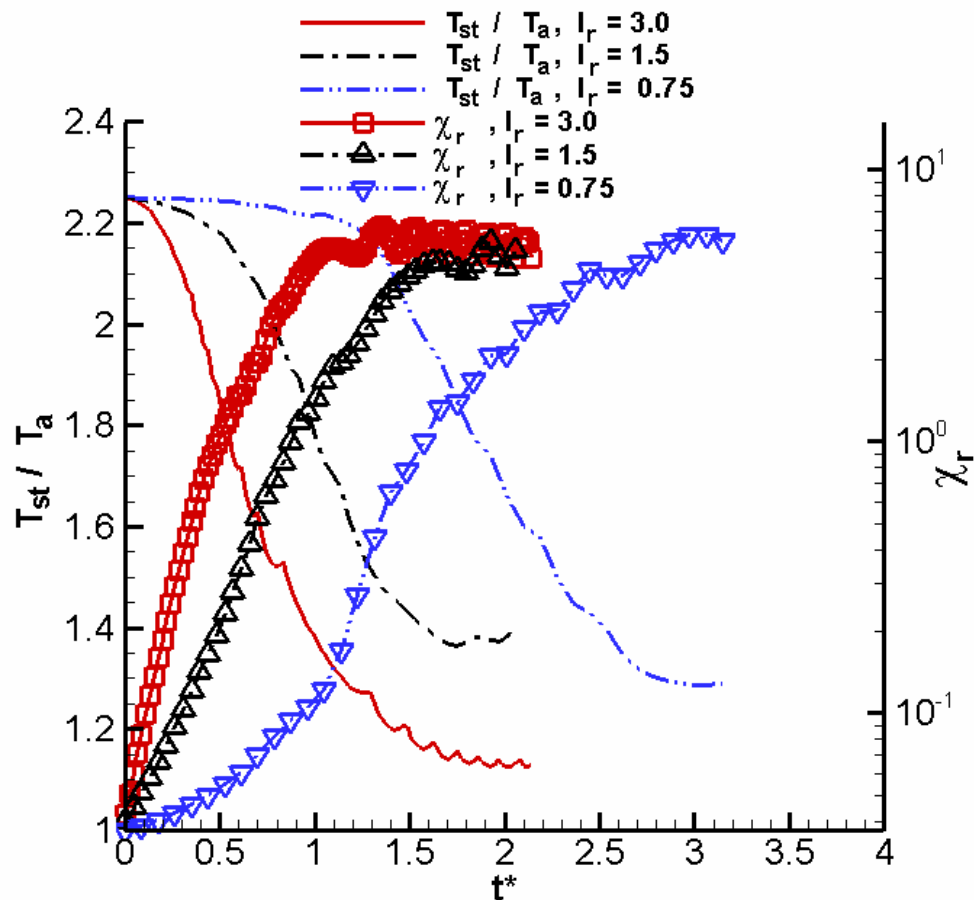
Figure 7.6. T_{st}/T_a and χ_r as a function of t* for different l_r during the extinction phase.

In this section, we will explore effects due to curvature on flame-vortex dynamics, through variation of the length-scale ratio l_r. In particular, l_r is varied in the range of 0.75-3.0, while maintaining u_{fv} and Da_i constant at 5.85 and 30, respectively. In other words, the largest vortex represents the highest Reynolds number. As mentioned before in Section 7.1, note that with respect to the local integral length-scale L_{11}, the simulated range for l_r corresponds to $d_v / L_{11} = 0.18 - 0.72$. Hence, we are considering length scales which are at least 20 % of L_{11}. As before, we will first characterize the flame-response during the extinction phase and then discuss the reignition phase.

To assess effects due to curvature, cases with $l_r = 3.0$ and 0.75 were simulated in addition to the baseline case with $l_r = 1.5$, which was discussed in the previous chapter. Figure 7.6 shows the time-evolution of the normalized temperature T_{st} / T_a and the scalar dissipation ratio χ_r for the three cases during the extinction phase. It is observed that the vortex length-scale has a significant effect on the time-history of χ_r, and consequently the time-scale for extinction. We observe the largest vortex ($l_r = 3.0$) causes extinction over a time-scale of 2t*, whereas with the smallest vortex ($l_r = 0.75$), extinction occurs over about 3t*. However, since t$_{eddy}$ increases by a factor of 4 from the smallest to the largest vortex, the extinction time-scale may in fact be shortest for the smallest vortex.

This is clarified in Fig. 7.7, which shows the normalized temperature and the scalar dissipation ratio as a function of t*^{1}, where t*^{1} is obtained by normalizing the physical time elapsed by the turnover time for the baseline case ($l_r = 1.5$). Essentially, t*^{1} is equivalent to the actual physical time elapsed. From Fig. 7.7, we notice that the extinction time-scale becomes shorter as the vortex size decreases. This is attributed to the higher rate of increase of χ_r with smaller vortices (for instance, for 0.4< t*^{1}< 1.4 in Fig. 7.5), which induce sharper velocity gradients or strain rates (hydrodynamic effects). Prior experiments in vortex-

perturbed diluted hydrogen flames (Thevenin *et al.*, 1998) have also confirmed the decrease in extinction time scales with decrease in the vortex size.
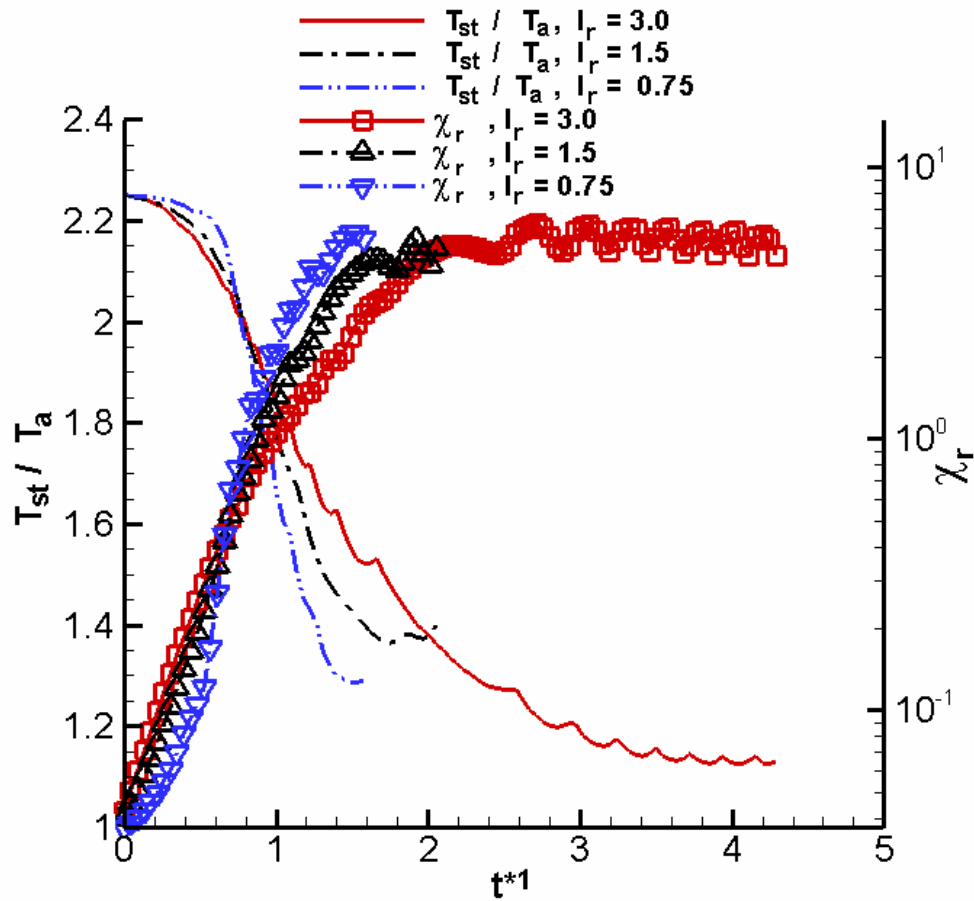
Figure 7.7. T_{st} / T_a and χ_r as a function of t*^{1} for different l_r during the extinction phase.

Figure 7.8 shows the instantaneous flame Damkőhler number Da as a function of χ_r for the three different vortex sizes employed. We observe that the unsteady extinction limit (defined at $Da = 1$) is nearly the same for all the three cases, implying that curvature has a minimal effect on the unsteady limit. Hence, the vortex length-scale predominantly affects the time-scale over which extinction occurs.
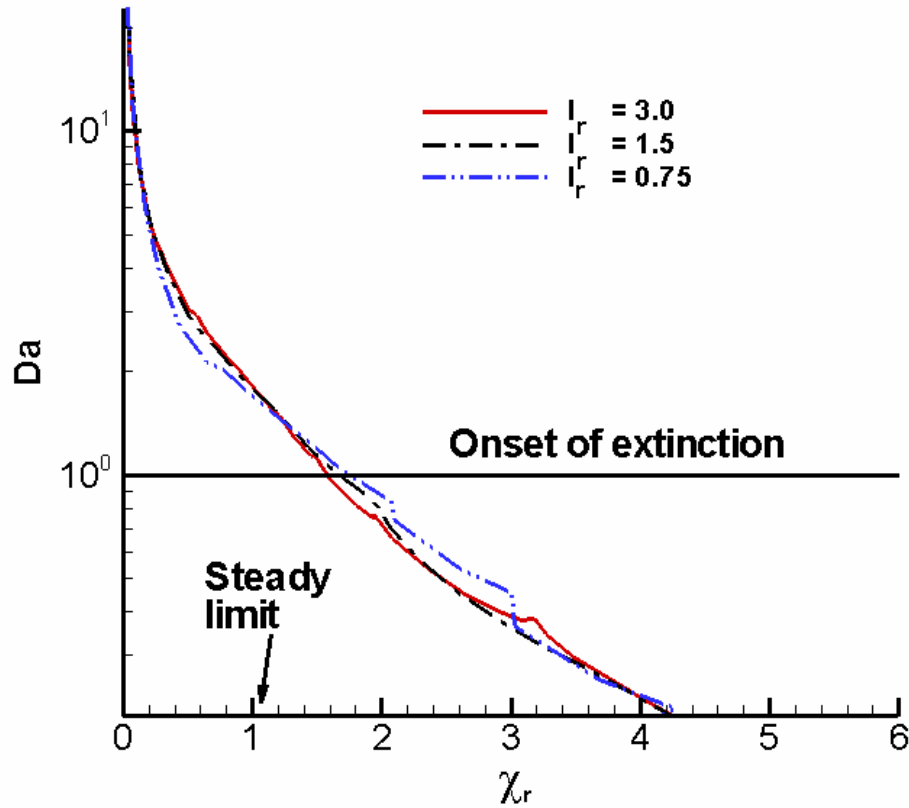
Figure 7.8. Da as a function of χ_r for different l_r during the extinction phase.

To explore whether these trends with respect to curvature effects on extinction are valid for higher values of Re_v (up to 1410) and u_{fv} (~200), consider Fig. 7.9, which shows flame-vortex interaction results (Venugopal and Abraham, 2008a) under engine conditions ($T_f = 450\,\text{K}$ and $T_a = 1000\,\text{K}$, and fuel-to-oxidizer density ratio ~8), and $u_{fv} = 205$ and $l_r = 1.0 - 4.0$. We observe trends similar to those in Fig. 7.8, i.e. the unsteady extinction limit is minimally affected by the vortex length-scale. However, as discussed before, due to higher values of u_{fv} and lower values of Da_i, χ_r values at extinction (~6) are much higher, indicating stronger unsteady effects.
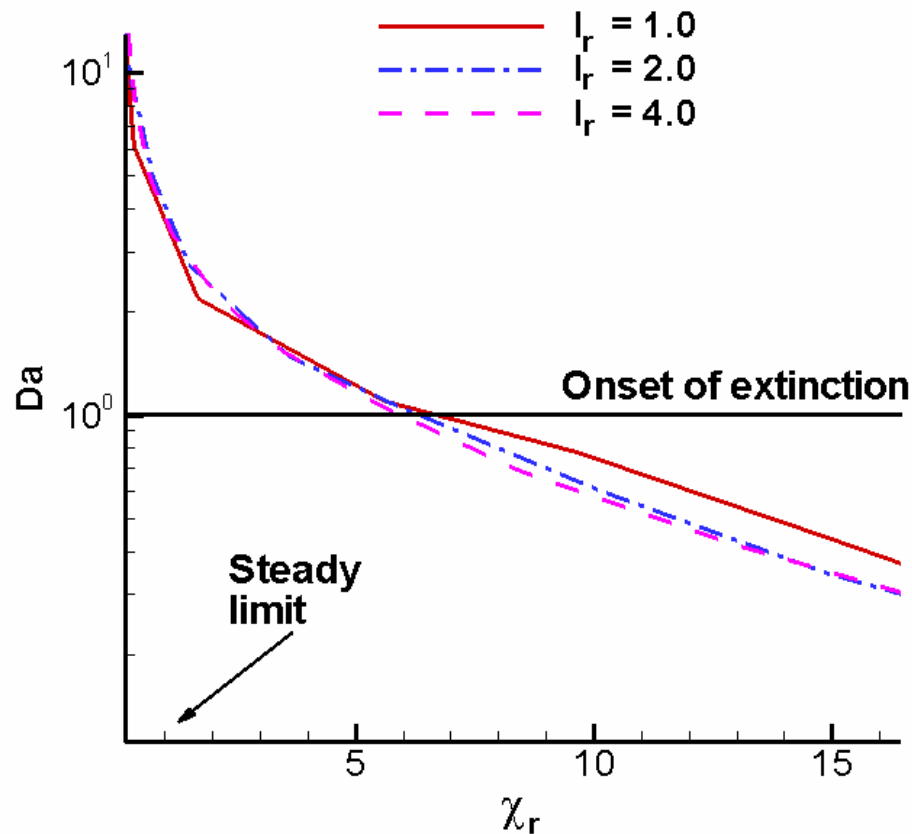
Figure 7.9. Da as a function of χ_r for higher values of Re_v and u_{fv} (~200) during the extinction phase (Venugopal and Abraham, 2008a).

It is possible that as the vortex size decreases, the relative importance of the lateral diffusion term $DELHX$ (see Eq. (6.2)) in comparison to the convective heat loss $CNVHY$ may increase. $DELHX$ contributes to heat loss from the thin flame zone near the vortex-tip and this may in turn contribute to shorter extinction time-scales. Consider Fig. 7.10, in which the various heat flux terms are compared with the heat release rate $CHRR$ (see Eq. (6.3)) along the vertical centerline at t* = 2.8 for $l_r = 0.75$. This time-instant is close to the onset of extinction ($Da = 1$) for this case and can be qualitatively compared to the results shown in Fig. 6.6 at t* = 1.4 for $l_r = 1.5$. It is seen that similar to the trends

observed for the $l_r = 1.5$ case, convective heat loss $CNVHY$ (see Eq. (6.2)) is predominant and the contribution of $DELHX$ (Eq. (6.2)) is negligible in the extinguishing region ($0.00125 < Y < 0.00135$). *Therefore, the dominant effect which leads to shorter extinction time scales with decreasing vortex size is the increase in rate of increase of χ_r and not lateral heat diffusion*. This further illustrates the importance of the time-history of the scalar dissipation rate in unsteady extinction processes. Moreover, in the context of modeling, the implication of this finding is that *unsteady flamelet libraries accounting for the time-history of the scalar dissipation rate is applicable to predict the effects of curvature on extinction, even for relatively small vortices ($l_r = 0.75$). Essentially, for the relatively large values of Re_v (270-1080) and u_{fv} (~6.0) employed here, 2-D effects due to curvature are masked by unsteady effects during the extinction phase*.
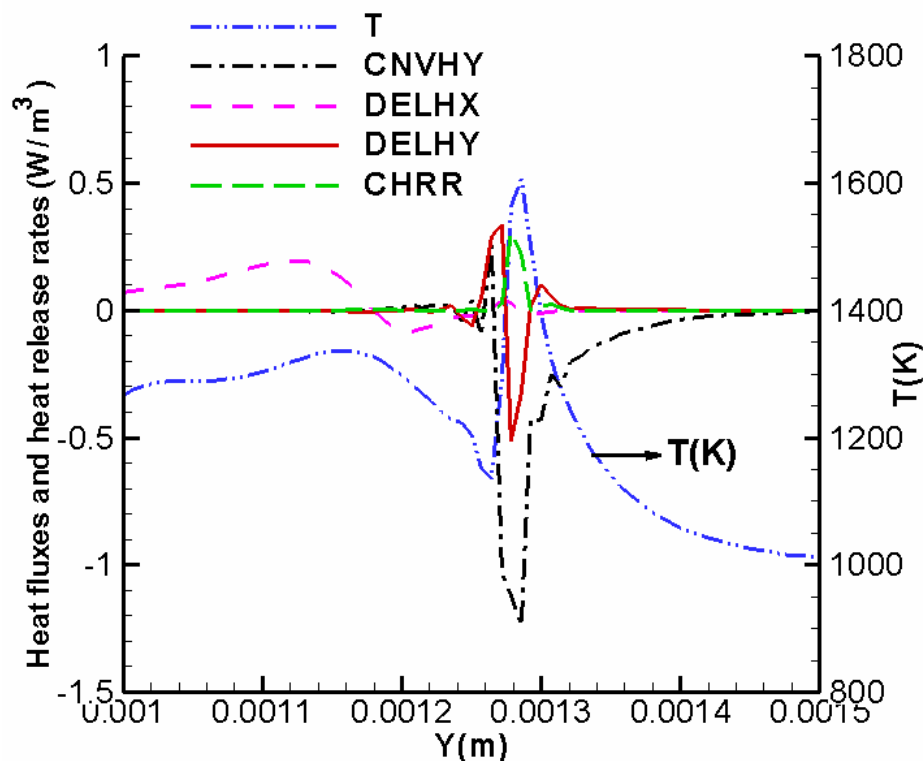
Figure 7.10. Comparison of convective and diffusive heat fluxes and the heat release rate (W/m³) at t* = 2.8 for $l_r = 0.75$. The temperature T is shown on the right axis.

This analysis of the curvature effects on extinction, for the range of Re_v simulated, shows that Re_v by itself is not an indicator of the rate (or time-scale) of extinction. Regardless of whether u_{fv} or l_{fv} is varied, the rate at which extinction occurs directly correlates with the rate of increase of χ_r. Moreover, the trends in χ_r (or χ_{st}) agree with the trends in the ratio, u_v/d_v. This ratio is the inverse of the vortex turnover time-scale and may be interpreted as a global strain rate induced by the vortex. In non-dimensional terms, the rate of increase of χ_r then correlates with $\left((u_v/d_v)\cdot\tau_c\right)^{-1}$, which is a Damkőhler number Da_v based on the vortex turnover time-scale and the chemical time-scale for the flame.

Curvature is expected to have a significant effect on reignition through lateral flame-flame interactions, which were shown to govern edge-flame dynamics leading to reignition for the baseline case discussed in Chapter 6. We will now compare the evolution of the vortex-perturbed flame during the reignition phase for a relatively large vortex with $l_r = 3.0$, and a relatively small vortex with $l_r = 0.75$. Figures 7.11(a)-(c) show the dynamics of edge flames during interactions of a larger vortex ($l_r = 3.0$) with the flame at different times. As before, isocontours of $T = 2000\,\mathrm{K}$ and $Z = 0.05$ are used to define the flame edge location, and representative values of χ_r at the edge locations along with maximum values along the strained stoichiometric contour are shown in the figures. We observe from Fig. 7.11(a) that the edges formed after extinction border a rather large extinguished region, comparable to the size of the vortex (~ 360 μm), and considerably diluted with the oxidizer. During the subsequent evolution of the vortex-perturbed flame (t* = 1.7, 2.625), we observe significant flame rollup into the vortex cores.

(a)

(b)

(c)
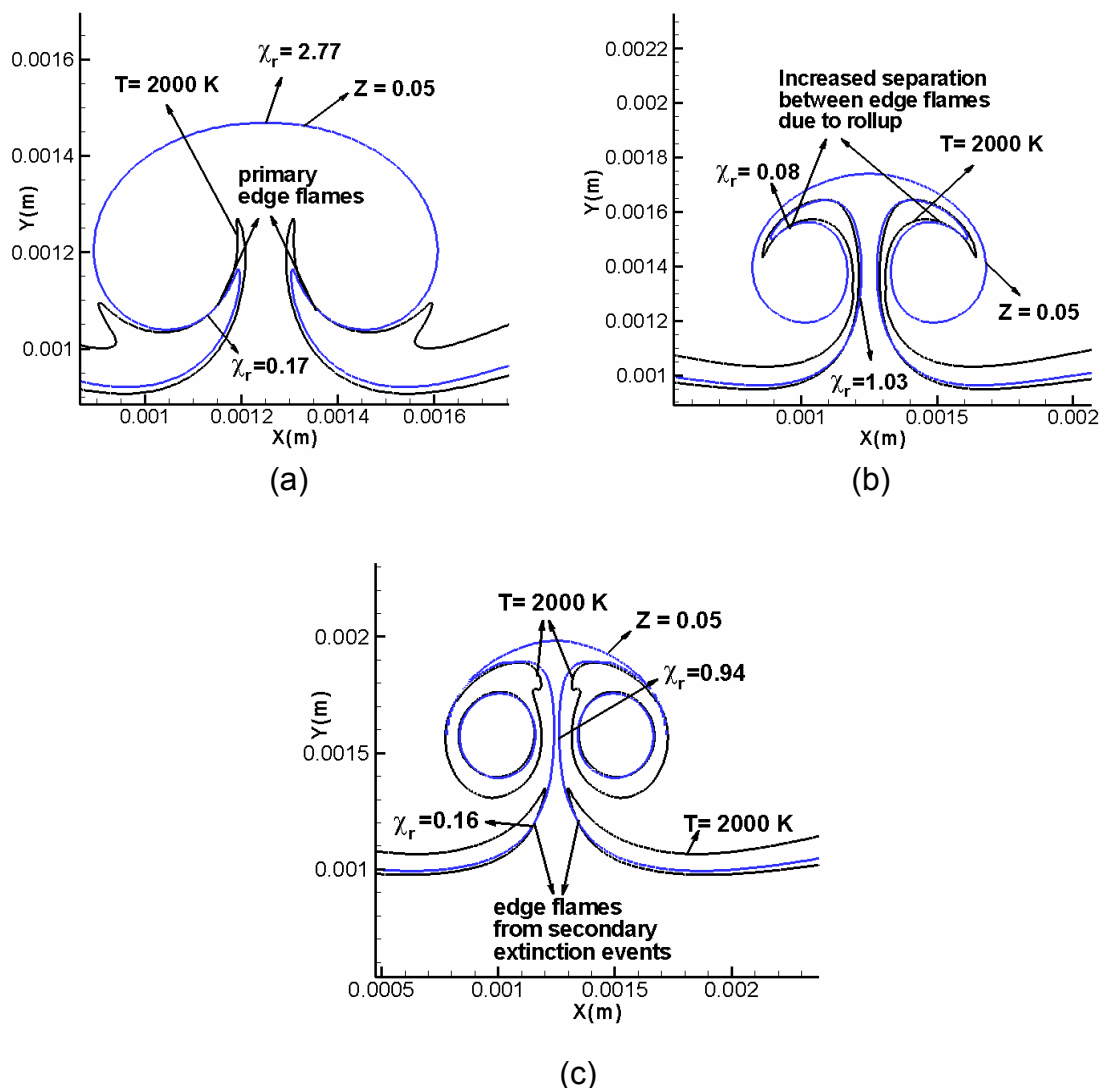
Figure 7.11. Dynamics of edge flames during the interaction of the $l_r = 3.0$ vortex with the flame at (a) t* = 0.8, (b) t* = 1.7, and (c) t* = 2.625.

Notice from Fig. 7.11(b) that flame rollup has a similar effect as negative edge propagation in that it causes the edge flames to recede away from the extinguished region thereby delaying reignition. In addition, Fig. 7.8(b) shows that the rolled-up edge flames are also relatively strained. This leads to secondary extinction events leading to edge flames similar to the primary extinction event, as seen from Fig. 7.11(c). As the scalar dissipation rate relaxes to relatively low

values in the reconnecting region in the wake of the vortex-induced flow (Fig. 7.11(c)), these secondary edge flames would propagate and lead to the eventual reconnection of the diffusion flame. Note that reconnection was not observed in the flame-vortex interaction length simulated here. Essentially, this discussion indicates that dilution due to relatively large extinguished regions, flame rollup, and relatively high straining are factors that decrease the tendencies for reignition as the vortex size increases. In other words, the tendency for reignition through edge flame propagation decreases as the vortex size (or l_r) increases. It is then possible that for relatively large vortices, autoignition could reignite the extinguished regions before vortex-induced premixing creates stoichiometric fractions for the edge flames to propagate into the extinguished regions.

In contrast, let us consider the flame-vortex interaction outcomes when the diffusion flame is perturbed with a relatively small vortex with $l_r = 0.75$. In Figs. 7.12(a)-(c), the non-dimensional times have been chosen to match the physical time elapsed in Figs. 7.11(a)-(c) that show the interaction outcomes with the larger vortex. In Fig. 7.12(a), we observe the edge flames at the onset of reignition, which border a rather small extinguished region. The close proximity of the flame edges leads to strong flame-flame interactions through lateral heat ($DELHX$) and species diffusion, and Fig. 7.12(b) shows that by t* = 6.8, a reconnected diffusion flame begins to form. In addition, we observe in Fig. 7.12(c) that a fuel-rich pocket detached from the reconnected flame propagates on the fuel-side, which would eventually burn out in the vortex cores. Note that in terms of physical time elapsed, reignition occurs approximately four times faster for the smaller vortex, with correlates well with the factor of four increase in the global mixing rate ($\sim u_v / d_v$) with the smaller vortex.

Hence, we can conclude from these qualitative comparisons that while *larger eddies predominantly lead to flame rollup and straining that enhance burning area but decrease the tendency for reignition, smaller eddies lead to rapid reignition following extinction through flame-flame interactions, and formation of fuel-rich pockets (or partially-stirred reactors) surrounding diffusion*

flamelets. Moreover, since the rate of reignition is a measure of flame stability, these studies investigating the effects of unsteadiness (velocity-scale) and curvature (length-scale) on the flame structure show that it is beneficial to have high rates (i.e. higher velocity scales) of fine-scale (i.e. smaller length scales) mixing. In the context of a jet, such small-scale turbulence can be generated by employing smaller orifice diameters and higher injection velocities.
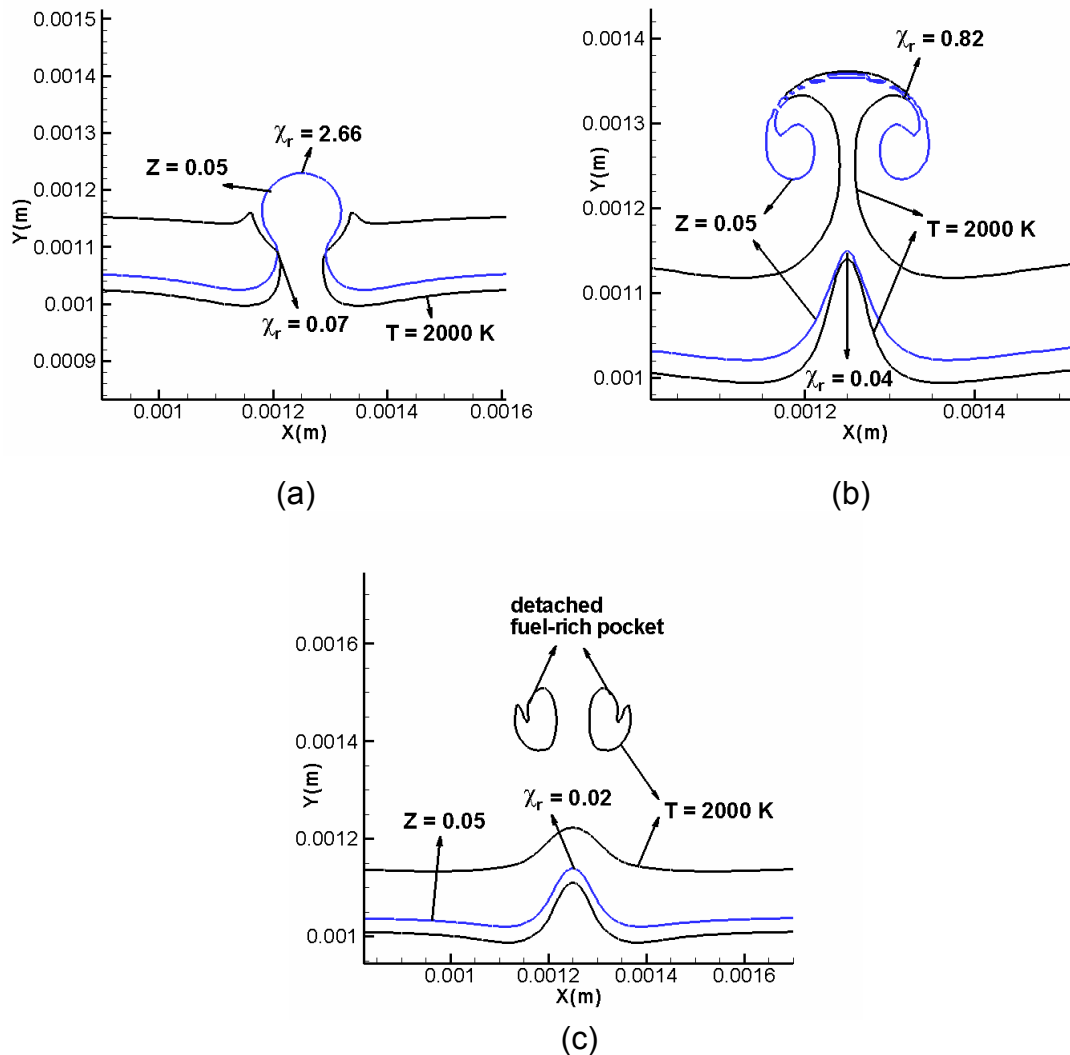
Figure 7.12. Dynamics of edge flames during the interaction of the $l_r = 0.75$ vortex with the flame at (a) t* = 3.2, (b) t* = 6.8, and (c) t* = 10.5.

7.4. <u>Flame-vortex Interactions in the Jet Near-Field</u>

In the results discussed so far, we considered the nature of flame-vortex outcomes relevant to a particular jet location, $x/d = 12$, and explored the effects due to unsteadiness and curvature on the local flame structure. In this section, we will investigate the flame-vortex outcomes at downstream jet locations, $x/d = 16$ and $x/d = 20$, and discuss how unsteady and curvature effects change as we move downstream in the jet. In addition, as we consider conditions varying along the jet axial direction, the effects of the flame-strength parameter Da_i on the flame structure will be clarified. Results from this section will then be used to construct outcome diagrams relevant for local flame dynamics in the jet near field.

Let us compare the flame-response during the extinction phase for conditions relevant to three axial locations, x/d = 12, 16 and 20 close to the jet centerline ($0 \leq r/d \leq 1.5$). The corresponding non-dimensional numbers, estimated from the mean statistics computed using LES, are given by: $l_r = 1.5, u_{fv} = 5.85, Da_i = 30$ at x/d =12, $l_r = 0.98, u_{fv} = 3.86, Da_i = 40$ at x/d =16, and $l_r = 0.67, u_{fv} = 2.27, Da_i = 60$ at x/d =20. The estimated values of the non-dimensional numbers show that while both l_r and u_{fv} decrease as we proceed downstream in the jet, Da_i increases. These trends follow from the LES results discussed in Chapter 5, where it was shown that while the integral length and velocity scales show a gradual (almost linear) increase and decrease, respectively, with axial location in the simulated jet near field (x/d<25), the mean scalar dissipation rate decreases sharply($\sim x^{-4}$). Hence, the flame thickness and the velocity-scale increase sharply along the axial direction, resulting in the decrease in l_r and u_{fv}, and increase in Da_i. In other words, as we proceed downstream in the near field of the jet, we would encounter thicker flames interacting with vortices that are slower, and smaller with respect to the flame (i.e. lower values of l_r).
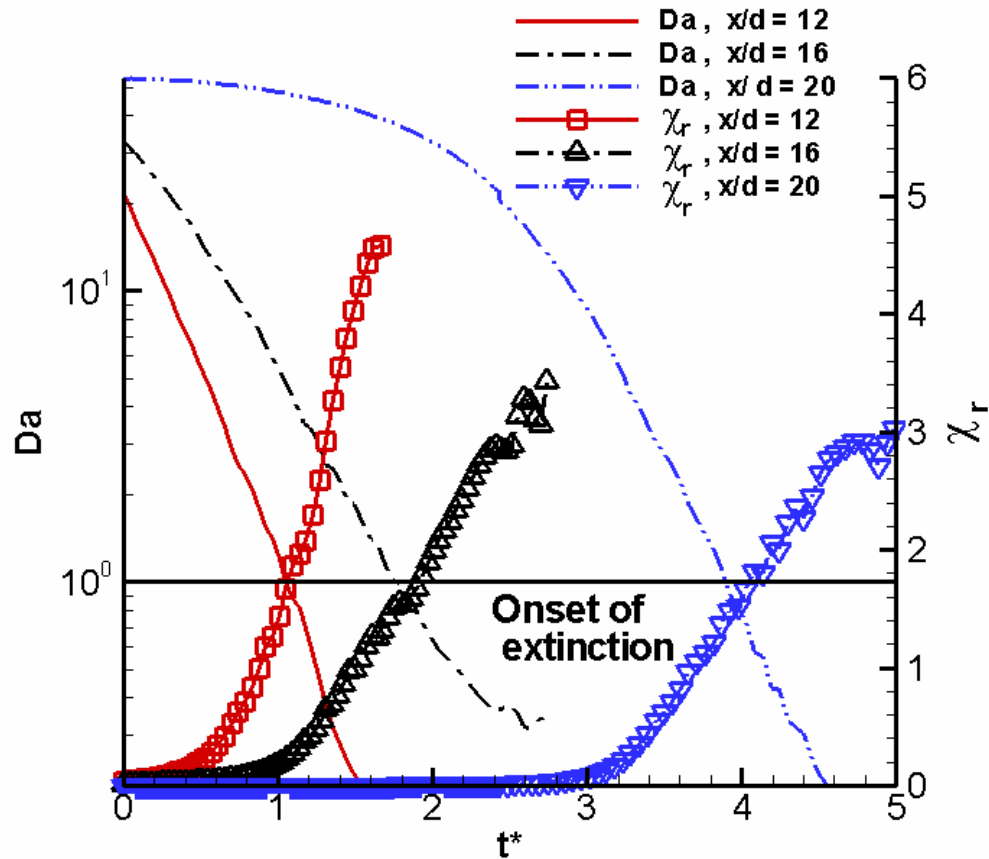
Figure 7.13. Da and χ_r as a function of t* during the extinction phase for conditions corresponding to different axial locations in the jet.

Note that by simulating flame-vortex interactions corresponding to downstream jet locations, we extend the range of non-dimensional numbers, such as l_r and Da_i, beyond that considered so far at x/d = 12. For instance, due to the presence of relatively thicker diffusion layers at x/d = 16 and x/d =20, we encounter higher Da_i values (up to 60), and smaller values of l_r (~ 0.3). As discussed in this section, flame-vortex interactions involving such robust flames (i.e. higher Da_i) with relatively small vortices (i.e. lower l_r) will provide additional insights into the likely nature of localized flame dynamics. Figure 7.13 shows Da and χ_r as a function of t*during the extinction phase of the flame-vortex

interactions relevant to conditions at different axial locations in the jet. We observe that at downstream jet locations, the extinction time scales are longer, implying that the flames are more resistant to extinction. This is consistent with the increase in Da_i with axial location, which is a flame-strength parameter, and with the findings discussed earlier at x/d=12. In addition, Fig. 7.13 shows that the peak magnitude and rate of increase of χ_r decrease at downstream locations, which is consistent with the trends associated with the decrease in u_{fv} (relatively slower vortices) and l_r (relatively smaller vortices) discussed in Sections 7.2 and 7.3.
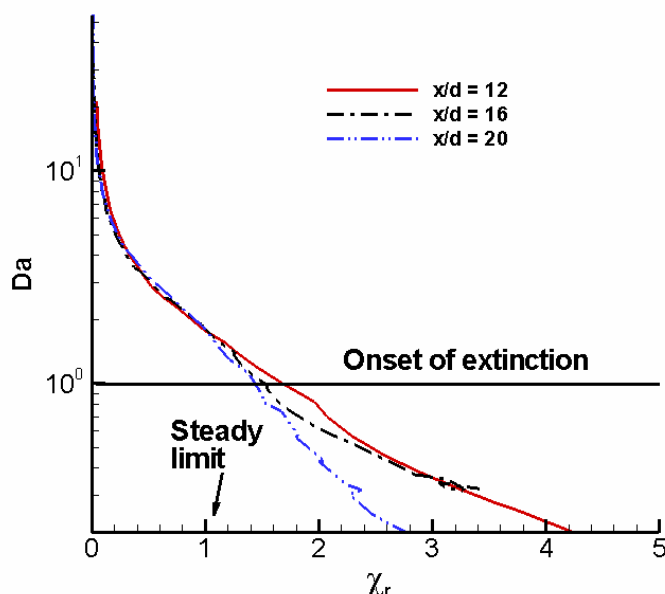
Figure 7.14. Da as a function of χ_r during the extinction phase for conditions corresponding to different axial locations in the jet.

Figure 7.14 shows Da as a function of χ_r for the three cases, and it is observed that the unsteady extinction limit (defined at $Da = 1$) is moderately affected (about 18 % decrease from x/d = 12 to x/d = 20) as we proceed downstream in the jet. This decrease is attributed to the decrease in the velocity-scale ratio u_{fv} (unsteady effects), and increase in the flame-strength

parameter Da_i. Hence, it is expected that at further downstream locations in the jet, unsteady effects on local flame extinction would diminish, and steady extinction limits would be applicable. We will now compare the flame-response during the reignition phase for conditions corresponding to different jet locations.
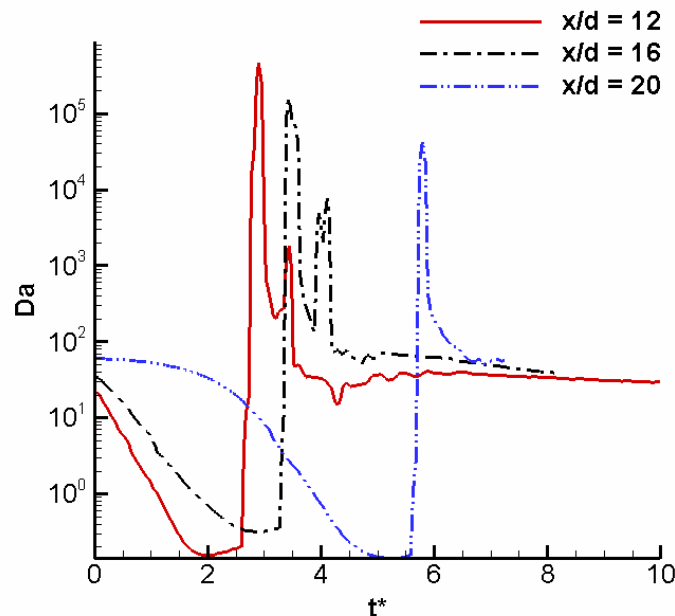
Figure 7.15. Da as a function of t* along the vertical centerline during the flame-vortex interactions corresponding to different jet axial locations.

Figure 7.15 shows the time evolution of the instantaneous flame Damköhler number Da during extinction/reignition of the vortex-perturbed flames under conditions representative of the three jet axial locations. We observe the strong overshoots in Da following extinction in all cases, which marks the onset of reignition under the influence of edge flames bordering the extinguished regions. The presence of significant amounts of diluted fractions (i.e. diluted with oxidizer) in the extinguished regions leads to relatively low mixing rates, and hence relatively large values of Da. With subsequent partial-premixing promoted by lateral heat and species diffusion, Da gradually relaxes to values comparable

to the original diffusion flame, as the reigniting flamelets evolve into a reconnected diffusion flame.

We observe from Fig. 7.15 that even though the time scales for extinction increase from x/d = 12 to x/d =20, as discussed before, the time scales for reignition show the opposite trend. In particular, it is estimated from Fig. 7.14 that the reignition phase occurs over non-dimensional times (t*) of 7.4, 4.9 and 1.7 for conditions corresponding to x/d = 12, 16 and 20, respectively. In terms of physical time, this represents about a 60 % decrease in reignition time-scale from x/d = 12 to x/d =20. This roughly correlates with the 55 % decrease in the length-scale ratio l_r from 1.5 at x/d = 12 to 0.67 at x/d = 20, and indicates the increasing effect of the vortex-induced curvature on reignition dynamics at downstream jet locations. On the other hand, note from Fig. 7.14 that the extinction time-scale roughly increases by about 24 % from x/d = 12 to x/d = 20. Based on the discussion on curvature effects in Section 7.3, even though we expect a decrease in the extinction time-scale due a decrease in l_r from x/d = 12 to x/d =20, the observed increase in extinction time scale indicates compensatory effects due to the increase in the velocity scale ratio u_{fv} and the flame-strength parameter Da_i. Hence, it may be concluded that as we proceed downstream axially in the simulated jet near-field, decreasing unsteady effects lead to longer flame extinction time scales, while increasing curvature effects contribute towards shorter reignition time scales.

Results so far have shown that as l_r decreases, flame-flame interactions manifesting as lateral heat and species diffusion become stronger due to increasing effects of the vortex-induced curvature. These interactions can potentially prevent local extinction, and lead to flame recovery after temporary flame weakening due to the vortex-induced strain. To explore this scenario, let us consider flame-vortex interactions for the set of non-dimensional numbers given by: $l_r = 0.335, u_{fv} = 2.27, Da_i = 60$. These numbers correspond to the interaction of a

relatively small eddy ($d_v = 0.18 L_{11}$) at the jet axial location, x/d = 20, with the flame.
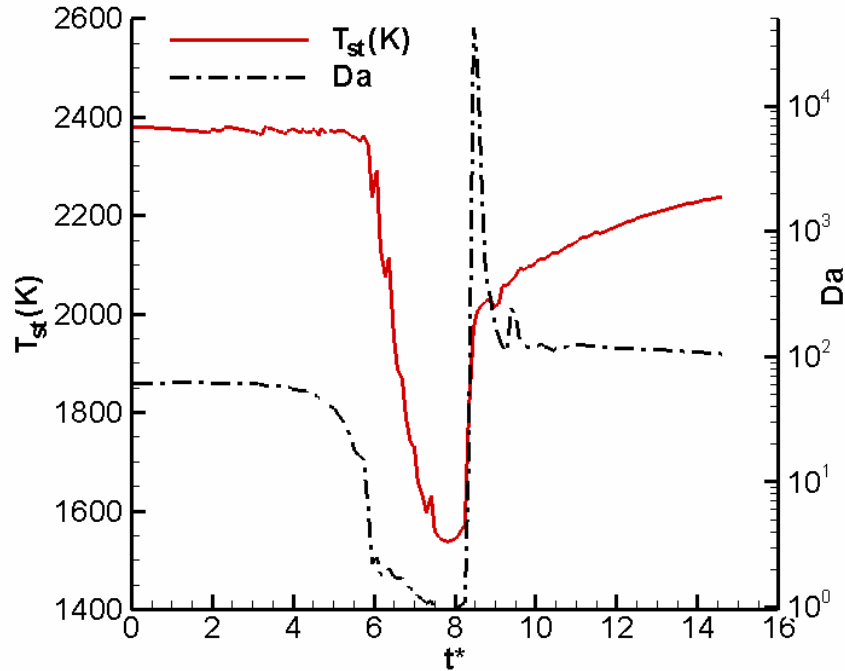
Figure 7.16. T_{st} (K) and Da as a function of t* along the vertical centerline during the flame-vortex interactions with the set of parameters given by
$$l_r = 0.335, u_{fv} = 2.27, Da_i = 60.$$

Figure 7.16 shows the temperature and the flame Damkőhler number Da at the stoichiometric mixture fraction along the vertical centerline as a function of t* during the flame-vortex interaction. We observe that the flame temporarily weakens and momentarily approaches extinction ($Da \sim 1$) due to the vortex-induced strain, but rapidly reignites/recovers within one eddy turnover time (t* =1). This indicates the strengthening effect due to flame-flame interactions resulting from the vortex-induced curvature. Figures 7.17(a) and (b) show the instantaneous snapshots of temperature in the vortex-perturbed flame at t* = 9.1 and 14.6, respectively. We observe the effects due to flame-flame interactions leading to rapid flame recovery following flame weakening in Fig. 7.17(a), and

Fig. 7.17(b) shows that by t* = 14.6, the diffusion flame has reconnected, and a detached fuel-side pocket has formed. Note that for even slower (or weaker) vortices, local extinction may be prevented due to curvature-induced flame-flame interactions, resulting in thickened diffusion flames surrounded by pockets. Hence, the present results indicate that at downstream jet locations, we are likely to encounter regimes characterized by *pocket formation without extinction*. Experiments of Thevenin *et al.* (2000) in vortex-perturbed hydrogen flames have shown evidence of such regimes for relatively small vortex-to-flame length-scale ratios ($0.1 < l_r < 1.0$). Furthermore, as discussed by Thevenin *et al.* (2000), below a certain vortex size ($l_r < 0.1$), the effect of the vortex on the flame structure may be mitigated by viscous effects.
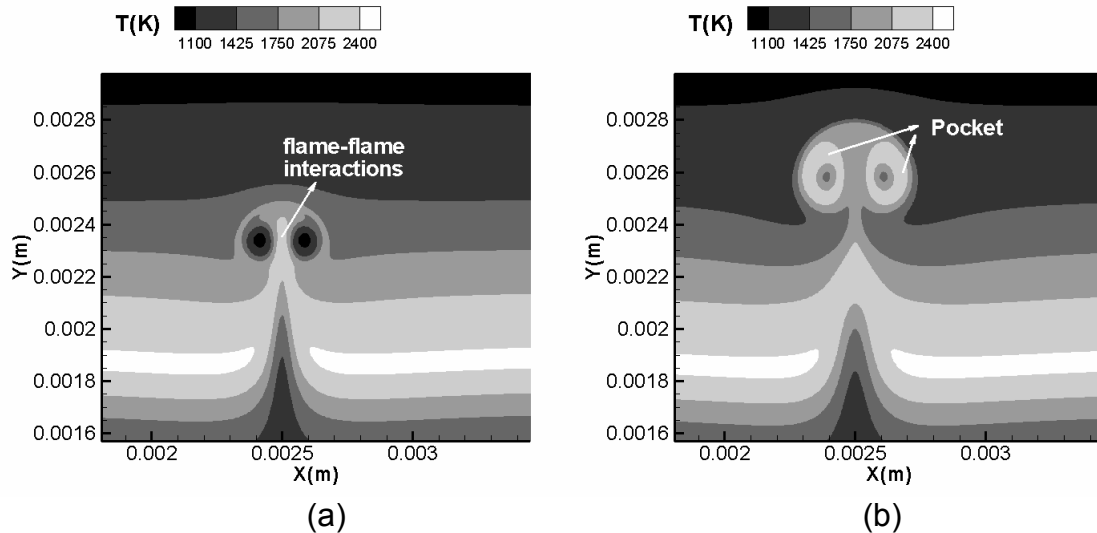
Figure 7.17. Contours of temperature (K) during interaction during the interaction of a relatively small vortex ($l_r = 0.335$) with the flame at (a) t* = 9.1, and (b) t* = 14.6.

7.5. Outcome Diagram and Implications for Turbulent Combustion Modeling

In this section, we will represent the interaction outcomes observed so far through outcome diagrams that are relevant for localized flame dynamics in the simulated near field of the jet. Following prior computational (Cuenot and Poinsot, 1994) and experimental works (Thevenin *et al.*, 2000), we choose l_r and

u_{fv} as axes for the regime diagram. In addition, we will illustrate the effects of other non-dimensional numbers such as Re_{v} through a scaling analysis. Based on the trends discussed in this chapter with respect to unsteady and curvature effects, we have

$$U \sim (\chi_{\text{r}}, \dot{\chi}_{\text{r}}) = f(u_{\text{fv}}, Da_{\text{i}}) \quad , \tag{7.1}$$

$$C \sim (\dot{\chi}_{\text{r}}, DELHX) = g(l_{\text{r}}). \tag{7.2}$$

In Eqs. (7.1) and (7.2) above, U and C represent magnitudes of unsteady and curvature effects, $\dot{\chi}_{\text{r}}$ denotes the rate of change of χ_{r} , and f and g are generic functional relationships. Now, in order to represent U and C on a diagram with u_{fv} and l_{r} as axes, we can derive the following scaling relationships:

$$\frac{l_{\text{r}}}{u_{\text{fv}}} = \frac{d_{\text{v}} \cdot u_{\text{f}}}{\delta \cdot u_{\text{v}}} \sim \frac{d_{\text{v}}}{u_{\text{v}} \cdot \tau_{\text{c}}} = \frac{\tau_{\text{v}}}{\tau_{\text{c}}} = Da_{\text{v}}, \tag{7.3}$$

$$l_{\text{r}} \cdot u_{\text{fv}} = \frac{d_{\text{v}} \cdot u_{\text{v}}}{\delta \cdot u_{\text{f}}} \sim \frac{d_{\text{v}} \cdot u_{\text{v}} \cdot \tau_{\text{c}}}{\delta \cdot \delta} \sim \frac{d_{\text{v}} \cdot u_{\text{v}}}{\nu}(\chi_{\text{st,i}} \cdot \tau_{\text{c}}) = \frac{Re_{\text{v}}}{Da_{\text{i}}}. \tag{7.4}$$

In Eq. (7.3), Da_{v} is a Damköhler number based on the characteristic time scales for the vortex and the flame, and Eq. (7.4) makes use of the approximate dimensional relationship:

$$\chi_{\text{st,i}}^{-1} \sim \frac{\delta^2}{\nu}, \tag{7.5}$$

where ν is the kinematic viscosity and $\chi_{\text{st,i}}$ is the initial stoichiometric scalar dissipation rate. For constructing a log-log diagram, we can recast Eqs. (7.3) and (7.4) as

$$\log(l_{\text{r}}) = \log(u_{\text{fv}}) + \log(Da_{v}), \tag{7.6}$$

$$\log(l_{\text{r}}) = -\log(u_{\text{fv}}) + \log\left(\frac{Re_{\text{v}}}{Da_{\text{i}}}\right). \tag{7.7}$$

The equations above show that at a given jet location ($Da_{\text{i}} \approx \text{constant}$), constant Da_{v} and Re_{v} lines would appear at right angles. Note that since Da_{v} and

Re_v include both the vortex/flame length and velocity scales, they represent the combined effects of unsteadiness and curvature.
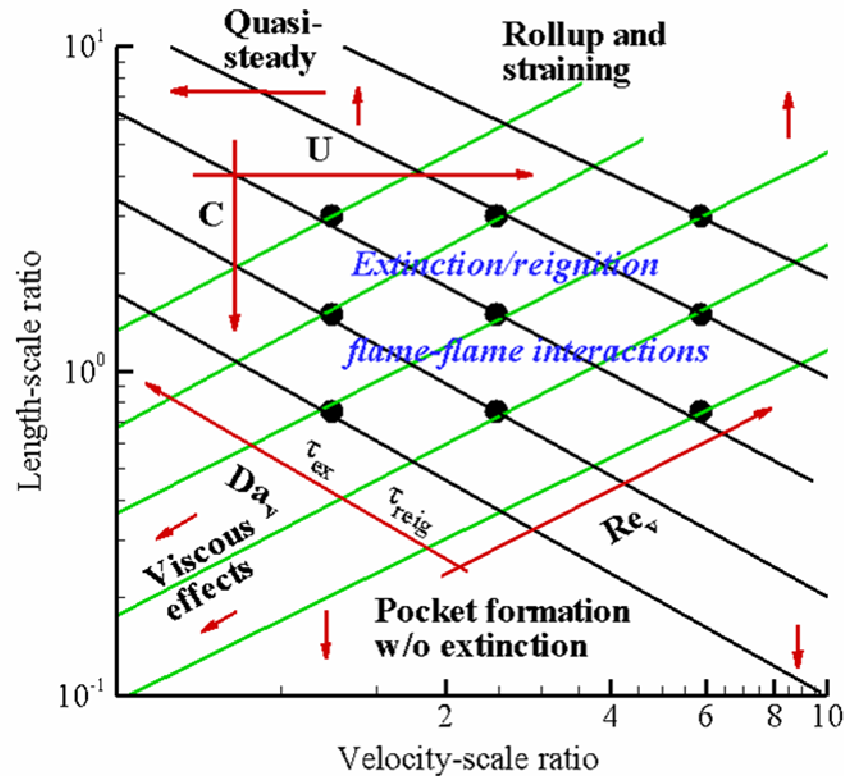
Figure 7.18. Outcome diagram based on flame-vortex simulations corresponding to the jet axial location, x/d = 12.

Figure 7.18 shows the outcome diagram with l_r and u_{fv} as axes for localized flame dynamics at the jet axial location, x/d = 12. In Fig. 7.18, the arrows indicate directions of increasing effects. We observe that while extinction/reignition events are favored for intermediate length and velocity scale ratios, large length scale ratios primarily result in flame rollup and straining. As discussed in Section 7.2, unsteady effects diminish as u_{fv} decreases, and quasi-steady extinction limits may be applicable for relatively small values of u_{fv} (~1.0). Curvature effects increase as l_r decreases, and favor reignition phenomena

through flame-flame interactions. Below a certain length-scale ratio (<0.5), flame-flame interactions render the flame resistant to extinction, and result in pocket formation regimes without local extinction. Since Da_v represents a normalized global strain rate ($\sim u_v / d_v$) imposed by the vortex, it directly correlates with the time scales for extinction and reignition. Moreover, for relatively small values of Re_v, viscous effects would mitigate the effect of the vortex on the flame structure.
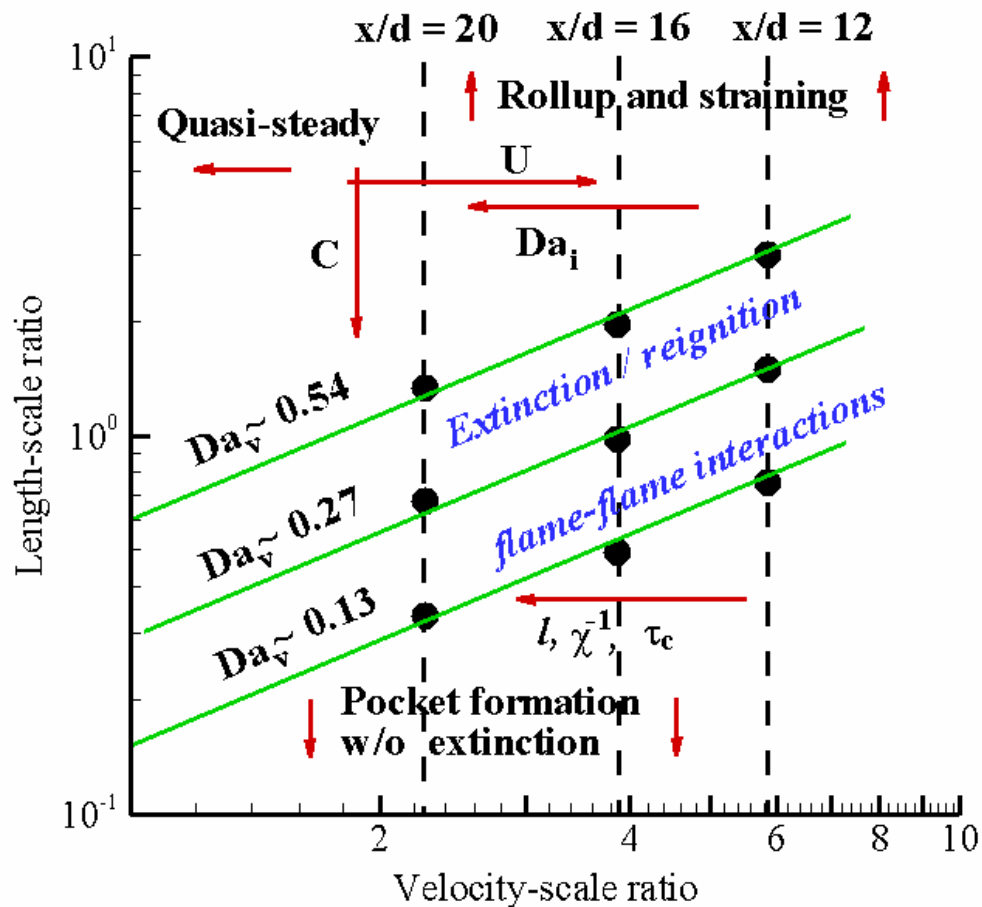
Figure 7.19. Outcome diagram based on flame-vortex simulations corresponding to the jet near field region, $12 \le x/d \le 20$, close to the centerline, $r/d \le 1.5$.

Figure 7.19 shows the outcome diagram relevant for localized flame dynamics for the jet near field region, $12 \le x/d \le 20$, close to the centerline,

r/d≤1.5. The figure shows that unsteady effects diminish due to decreasing velocity scale ratios as we proceed downstream in the jet, whereas curvature effects are enhanced due to decreasing length scale ratios. Note that each of the (approximately) constant Da_v lines represents a constant ratio of the eddy length-scale (d_v) with respect to the local integral length scale (L_{11}), and a constant ratio of the eddy velocity scale (u_v) with respect to the local turbulence intensity (u'). In particular, the constant Da_v lines of 0.54, 0.27 and 0.13 represent eddies with characteristics d_v/L_{11}= 0.72, 0.36 and 0.18, respectively, and u_v/u' = 1.0. This indicates that in the simulated jet near field region, effects due to unsteadiness (u_{fv}) and curvature (l_r) are somewhat compensatory. In addition, Fig. 7.19 shows that due to decreasing length scale and velocity scale ratios, we are likely to encounter pocket formation regimes without local extinction at downstream jet locations. For all the jet axial locations explored, extinction/reignition events were observed for intermediate length and velocity scale ratios.

It is important to note that while the outcome diagram presented in Fig. 7.18 is useful to understand the nature of localized flame dynamics, the observed trends may be specific to the simulated jet near field region (x/d <25). For instance, as we proceed downstream in the jet, while the length and velocity scales would continue to grow, mean scalar dissipation rates may settle down to relatively low values. It is then possible that length scale ratios may begin to increase with axial location. Additional LES-flame/vortex studies exploring a larger jet flowfield domain could provide useful insights into these possibilities.

Even though the flame-vortex interaction studies discussed here correspond to the regions close to the jet centerline, i.e. 0≤r/d≤1.5, where extinction/reignition events are probable, the estimated values of non-dimensional numbers, such as l_r and u_{fv} can be employed to infer interaction regimes at farther radial locations. For instance, at x/d = 12, the mean statistics computed from LES show that for r/d≥ 2, l_r ≥ 4.0, and u_{fv} ≤3.0, implying that

both curvature and unsteady effects diminish as we proceed radially away from the jet centerline at a given axial location. From the outcome diagram shown in Fig. 7.19, it is evident we are more likely to encounter rollup and straining, which may cause temporary flame weakening/recovery, rather than extinction/reignition at farther radial locations. We will confirm this expectation based on the flame-vortex interactions in Chapter 9, where it will be shown that the localized flame dynamics corresponding to the average stoichiometric locations in the jet (r/d > 1.0) predominantly involves temporary flame weakening/recovery. Moreover, due to increasing values of l_r, the 1-D flamelet assumption is expected to be valid at increasing radial locations at a given axial location in the jet.

The flame-vortex interaction outcomes observed here have important implications for turbulent combustion modeling. The flame-vortex simulations show that unsteady extinction/reignition events are likely in the simulated jet near-field region. While steady flamelet libraries were shown to be inadequate, unsteady flamelet models accounting for the time history of the instantaneous scalar dissipation rate are adequate to predict local extinction. However, it was shown that reignition phenomena following extinction are governed by curvature effects, which are not captured in 1-D flamelet models. As discussed in Chapter 6, unsteady flamelet/progress variable models may be more appropriate to predict both local extinction and reignition. Such models account for partial-premixing effects during reignition through a reactive scalar, such as the progress variable. In the context of turbulent combustion modeling, the mean or filtered progress variable can be obtained through a modeled transport equation, similar to the mixture fraction. Note, however, that the progress variable transport equation will not be source-free, and the filtered/mean source terms would have to be modeled. Recent works, such as the LES study by Pierce and Moin (2004) have explored modeling approaches for the progress variable, and suggest the use of tabulated flamelet/progress variable libraries. Such libraries can be built from the unsteady flamelet equations with the scalar dissipation rate and the

progress variable as flamelet parameters. Moreover, edge flame effects can be incorporated into the progress variable source term in order to account for curvature effects. Some of these possibilities are discussed in Chapter 10 focusing on the implications of the present findings for modeling in diesel flames. In addition, the pocket formation regimes that are expected to be dominant at downstream jet locations can be represented through partially-stirred and perfectly-stirred reactor models.

7.6. <u>Summary and Conclusions</u>

In this chapter, effects due to unsteadiness and curvature on flame-vortex interactions were investigated through parametric studies corresponding to different locations in the LES jet flowfield. The variations in the vortex (length and velocity scales) and flame (scalar dissipation rates) characteristics in the jet near-field region were expressed in terms of three non-dimensional numbers: the length-scale ratio l_r, the velocity-scale ratio u_{fv}, and the initial flame Damköhler number Da_i. The effects of these parameters on the flame-vortex interaction outcomes, and unsteady and curvature effects were investigated. For the range of non-dimensional numbers explored, the flame-vortex dynamics was characterized by local extinction, reignition and pocket formation.

Unsteady effects were primarily influenced by u_{fv} and Da_i. During the extinction phase, the unsteady flame exhibited a greater departure from steady behavior as u_{fv} increased. In particular, χ_r values at extinction increased with an increase in u_{fv}, and unsteady extinction limits up to four times the steady limits were observed for the specific conditions employed here. This observation is consistent with prior studies on vortex-induced extinction (Oh *et al.*, 2004). During the reignition phase, increasing u_{fv} resulted in higher rates of partial-premixing which promotes faster reignition. However, the extent of roll-up of the edge flames and burning in the vortex cores decreased due to reduced residence

times for the flame-vortex interaction. Variation of Da_i in the range of 30-60 moderately influenced unsteady extinction limits (by about 18 %), and the unsteady flame showed an increasing tendency towards steady behavior as Da_i increased. In addition, owing to faster flame response, reignition time scales decreased with an increase in Da_i.

Curvature effects were characterized through variations in the length-scale ratio l_r. For l_r values in the range of 0.75-3.0, the predominant effect of curvature on extinction was found to be the modification of the rate of increase of the scalar dissipation rate. Accordingly, as l_r decreased, shorter extinction time scales were observed owing to a higher rate of increase of χ_r. Since lateral diffusion effects were not significant in the extinction phase, 1-D unsteady flamelet models may be employed to predict the effects of curvature on extinction. The vortex-induced curvature had a direct effect on flame-flame interactions during the reignition phase through lateral diffusion of heat and species into the extinguished region from the adjoining edge-flames. As l_r is increased, a larger extinction-hole diluted with oxidizer is created which needs to premix and form flammable fractions before reignition can occur. Even though the extent of roll-up and straining is increased, flame-flame interactions are weakened leading to longer time scales for reignition. For relatively small length-scale ratios ($l_r \sim 0.3$), flame-flame interactions prevent local extinction, and lead to formation of fuel-rich pockets surrounding thickened flames. Such pocket formation regimes were found to be more likely at downstream jet locations.

Based on scaling relationships and the observed flame-vortex interaction outcomes, outcome diagrams relevant for localized flame dynamics in the jet near-field $(12 \leq x/d \leq 20)$ of interest were constructed. These diagrams showed that unsteady effects decrease as we proceed axially downstream in the jet, while curvature effects show an increasing trend. These trends are attributed to the fact that while length and velocity scales show a gradual increase and decrease, respectively, in the jet near-field, scalar dissipation rates decay

strongly with axial location. Hence, at downstream jet locations, we are likely to encounter relatively slower and smaller vortices interacting with thicker flames. Across the jet near field, extinction/reignition regimes were observed for intermediate length scale and velocity scale ratios. However, these trends may be somewhat specific to the simulated jet near field region (x/d < 25). In particular, as we proceed further downstream, it is possible that the length and velocity scales may change more rapidly than the scalar dissipation rates, which may alter the nature of variation of unsteady and curvature effects along the axial direction. Additional LES/flame-vortex studies investigating a larger jet flowfield are required to explore these possibilities. Moreover, owing to increasing values of l_r and decreasing values of u_{fv} with increasing radial locations at a given axial location in the jet, it is expected that curvature and unsteady effects would diminish, resulting in temporary flame weakening/recovery events rather than extinction/reignition. In addition, 1-D flamelets would be applicable at farther radial locations (r/d>2) due to the relatively large values of l_r (> 4.0).

The implications of the observed flame-vortex interaction outcomes for turbulent combustion modeling in the near fields of turbulent jet diffusion flames were discussed. The present results show that unsteady flamelet models satisfactorily predict local extinction, but are not applicable to predict reignition, which is governed by curvature effects and edge flame dynamics. Furthermore, as shown in Chapter 6, reignition may be predicted through modeling approaches, such as unsteady flamelet/progress variable models, which account for partial-premixing effects through the progress variable.

The present work explores likely regimes of flame-vortex interactions relevant to the near-field of a 70,000 Reynolds number jet with a fuel-to-oxidizer density ratio of 3.5, and fuel and oxidizer temperatures of 1000 K. Practical diesel jets may involve an order-of-magnitude higher Reynolds numbers, colder fuel temperatures (~ 400 K), and higher fuel-to-oxidizer density ratios (~ 8). Qualitative comparisons of the present results with our recent flame-vortex interaction studies (Venugopal and Abraham, 2008a, b) under engine conditions

(i.e. higher density ratios, lower fuel temperatures) and relevant to higher Reynolds number (~400,000) jets show that the physical mechanisms of flame-vortex interaction outcomes such as extinction and reignition remain unaffected. In particular, while extinction is associated with unsteady effects and satisfactorily predicted by unsteady flamelet models, curvature effects and edge flame dynamics govern reignition. Hence, the trends reported with respect to extinction/reignition and unsteady/curvature effects reported in this chapter can be extrapolated and expected to be valid in higher Re jets. Moreover, while the present work employs air-side vortices, we discussed the possible implications for extinction/reignition with fuel-side vortices. It is expected that fuel-side vortices would result in different unsteady extinction limits, and different time scales for extinction and reignition. The trends with respect to unsteady and curvature effects on extinction and reignition observed for air-side vortices are expected to be valid for fuel-side vortices as well. Flame-vortex interaction studies employing fuel-side vortices are useful directions for future work.

The flame-vortex simulations discussed so far employed a single-step kinetic model, and focused on interaction regimes. In the next chapter, results from flame-vortex simulations employing a multi-step kinetic model for n-heptane oxidation are discussed for a limited set of conditions. Through these simulations, the influence of multiple chemical time scales on the flame-vortex interaction is assessed. Moreover, the unsteady response of major species and pollutants like nitric oxide (NO) to the vortex perturbation is investigated.

CHAPTER 8. FLAME-VORTEX INTERACTION STUDIES WITH MULTISTEP CHEMISTRY

8.1. <u>Introduction</u>

The dynamics of flame-vortex interactions were discussed in Chapters 6 and 7 by employing a single-step chemical mechanism for n-heptane. In this chapter, we will present studies employing a multi-step reaction mechanism. Through these studies, the response of major species (like CO_2, H_2O, CO) and pollutants (like NO and unburned hydrocarbons (UHC)) to the vortex perturbation will be investigated, and the influence of unsteadiness (related to vortex velocity-scale) and curvature (related to vortex length-scale) on product/pollutant formation and distribution in the vortex-perturbed flame will be assessed. In the discussion, the influence of multi-step kinetics on the conclusions in the previous two chapters will be highlighted. in Section 8.2, results showing the flame temperature and species response for a baseline case are discussed. In Sections 8.3 and 8.4, the effects of unsteadiness and curvature are investigated, respectively. The chapter closes with summary and conclusions in Section 8.5. Some of the results discussed as part of this chapter appear in a recent paper accepted for publication in the AIAA journal (Venugopal and Abraham, 2008b)

8.2. <u>Flame-response</u>

In this section, we discuss the temperature and species response during the flame-vortex interaction for a baseline case employing the 56-step mechanism. The characteristics of the vortex (i.e. $d_v = 90\ \mu m$, $u_v = 9\ m/s$) and the diffusion layer (i.e. $\delta = 120\ \mu m$, $\chi_{st,i} = 18\ s^{-1}$) are identical to those for the baseline

case with the single-step kinetic model (see Chapter 6). In addition, similar to the baseline case with the single-step kinetic model discussed in Chapter 6, these vortex and diffusion layer characteristics correspond to temporal mean statistics from LES at the jet axial location, x/d = 12, computed as averages over the radial region $0 \leq r/d \leq 1.5$. However, note that since the 56-step mechanism is associated with multiple chemical time scales, it may result in Damköhler numbers different from the ones computed with the single-step model. Hence, the focus of this analysis is not to make a direct *quantitative* comparison between the multi-step and single-step models, but to investigate whether the physical mechanisms governing flame-vortex interaction are consistent between the two models. Furthermore, a multi-step kinetic model allows us to characterize the response of both major species and pollutants for different vortex sizes and velocities.

Figures 8.1(a), (c) and (e), and Figs. 8.1(b), (d) and (f) show the contours of temperature and OH mass fraction (scaled up by 1000) at different times during the flame-vortex interaction. From the figures, we observe local extinction (Fig. 8.1(a), (b)) followed by reignition through lateral (i.e. in the X-direction) flame-flame interactions. We observe from Fig. 8.1(a) that the extinction is characterized by unsteady effects, as in the single-step chemistry case, resulting in unsteady limits more than 3 times the steady limit. Recall that with single-step chemistry the unsteady limit was about 4 times the steady limit The OH mass fraction is observed to peak close to stoichiometric (i.e. on the lean side), and the trends in OH spatial distribution correlate well with the temperature. The reconnected flame is surrounded by a fuel-rich pocket. Contours of CO_2 and CO mass fractions at different times are shown in Figs. 8.2(a), (c) and (e), and Figs. 8.2(b), (d) and (f), respectively. As expected, CO_2 essentially peaks close to the stoichiometric mixture (Z = 0.05) (Figs. 8.4(a), (c)) in the reconnected flame (Fig. 8.2(e)) and CO peaks at rich fractions (Z ~ 0.08) (Figs. 8.2 (b), (d), (f)) and in the fuel-rich pocket detached from the reconnected flame (Fig. 8.2(f)). These spatial differences in the distribution of CO_2 and CO can have implications for the

dependence of the formation rates on unsteadiness and curvature. We will discuss these implications in Sections 8.3 and 8.4.
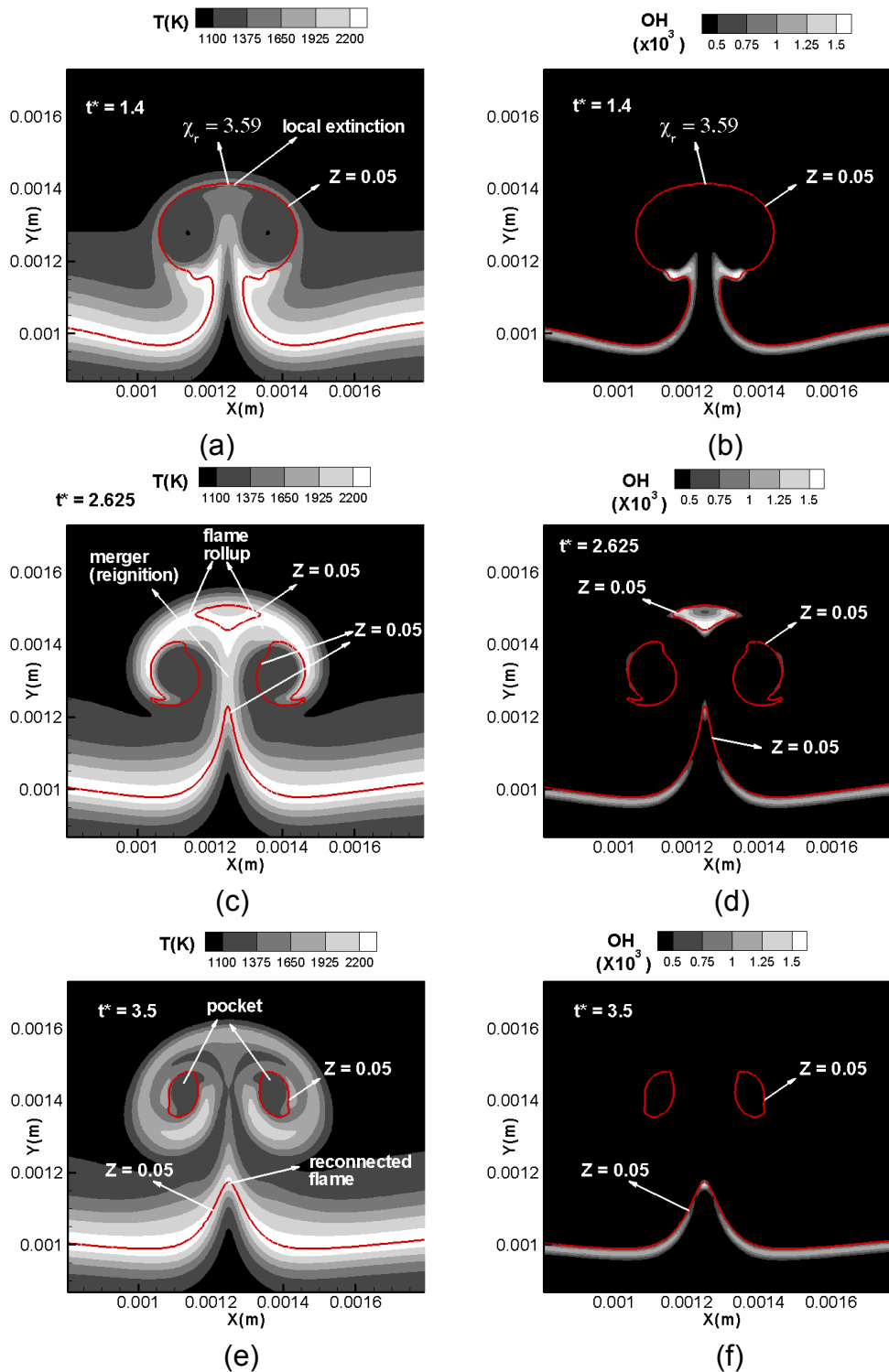
Figure 8.1. Contours of temperature (K) ((a), (c), and (e)) and OH mass fraction ((b), (d) and (f)) at different times during the flame-vortex interaction.
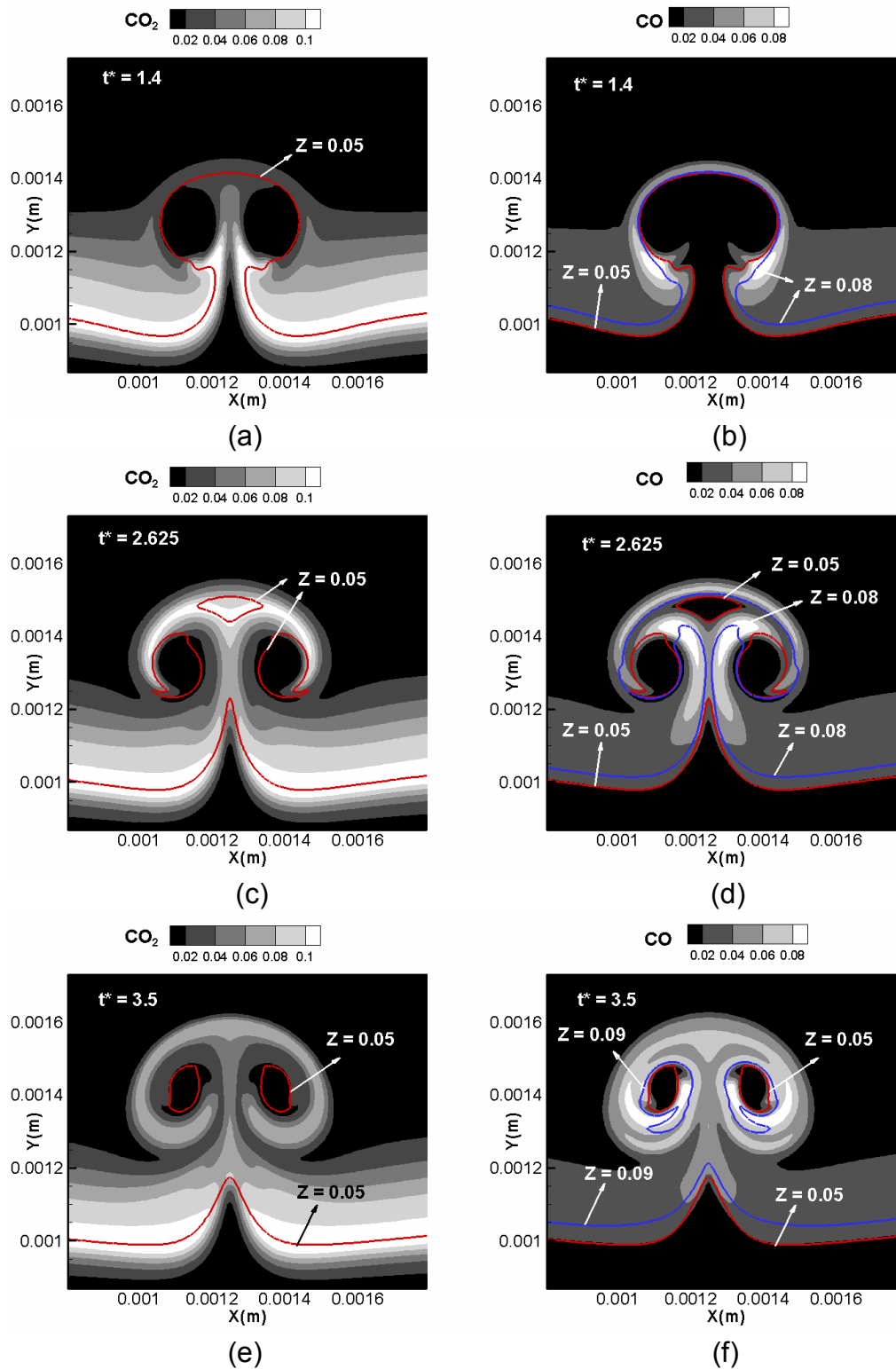
Figure 8.2. Contours of CO_2 ((a), (c), and (e)) and CO mass fractions ((b), (d) and (f)) at different times during the flame-vortex interaction.
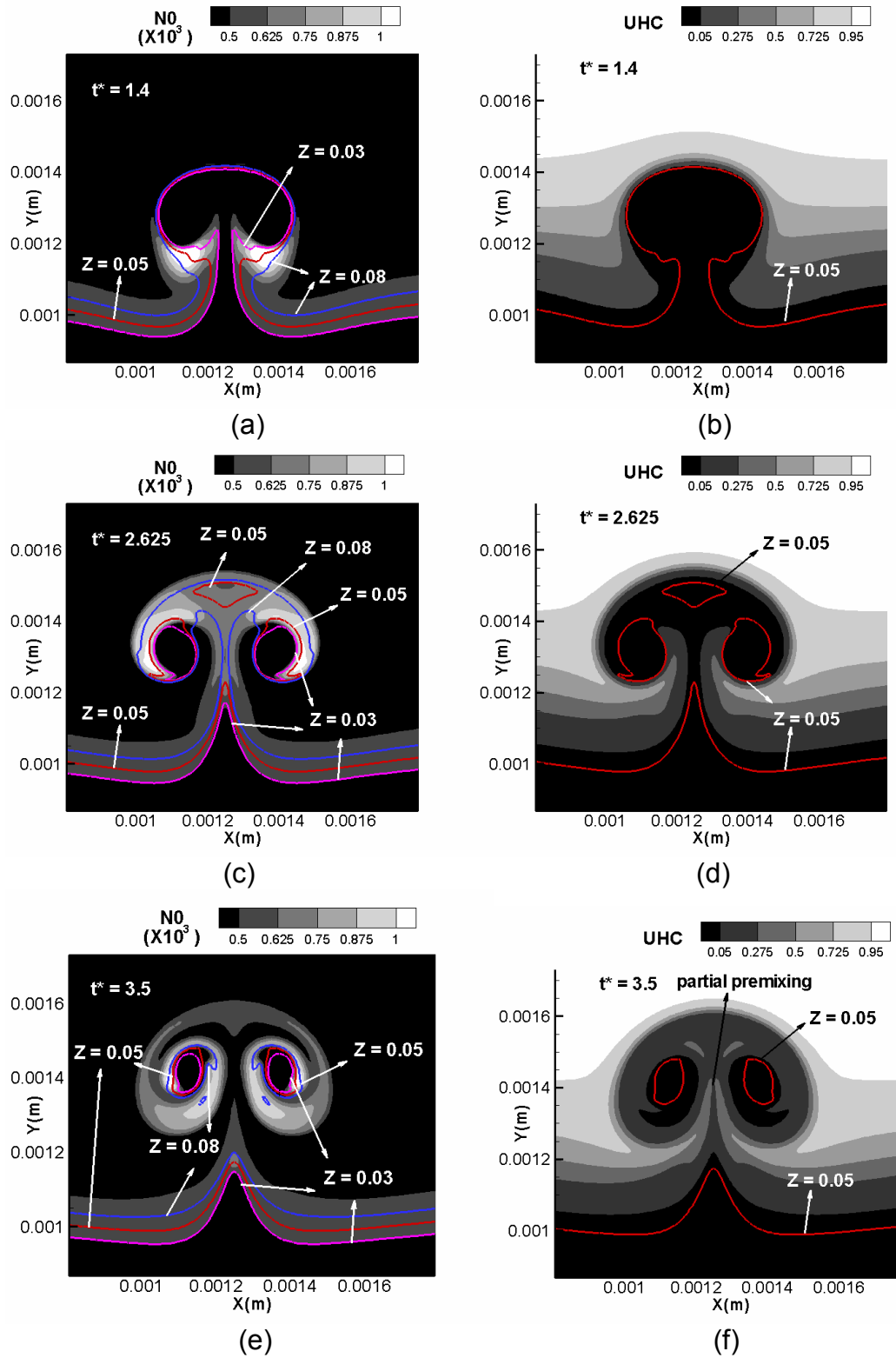
Figure 8.3. Contours of NO ((a), (c), and (e)) and UHC mass fractions ((b), (d) and (f)) at different times during the flame-vortex interaction.

Note that the trends in H_2O distribution were found to be similar to those in CO_2. Figures 8.3(a), (c) and (e), and Figs. 8.3 (b), (d) and (f) show the time evolution of the contours of NO (scaled up by 1000) and UHC mass fractions during the flame-vortex interaction. NO mass fraction peaks in the Z range of 0.03-0.08 centered around stoichiometric. Note that following reconnection of the diffusion flame, it is expected that peak NO mass fractions would occur in the reconnected flame as the pocket becomes fuel-rich. However, in Fig. 8.3(e), we observe relatively high concentrations of NO in the pocket in addition to the reconnected flame. This may be attributed to unsteady effects associated with the relatively slow chemical response times of NO. Essentially, due to rollup of the edge flames during reignition into the vortex cores, NO formation is favored in the high temperature regions around the oxidizer pocket. As time progresses, fuel-rich mixtures are formed in these regions due to partial-premixing, which leads to lower temperatures. However, NO does not respond fast enough due to relatively slow chemical time scales and hence high concentrations of NO are observed even in fuel-rich (Z ~0.08) regions in the vortical pocket (see Fig. 8.3(e)). The trends in UHC mass fraction shown in Figs. 8.3(b), (d) and (f) are similar to those in the mixture fraction. Increasing levels of UHC are seen in the reigniting regions due to partial premixing, and in the fuel-rich regions surrounding the vortical pocket following the reconnection of the diffusion flame.

The discussion so far indicates that reignition processes following extinction result in a trade-off with respect to flame stability and pollutant formation. While reignition is favorable in terms of flame stability, pockets that form following reconnection of the diffusion flame may be sources of formation of pollutants like CO, NO and UHC. Note that typically in steady diffusion flames at relatively low scalar dissipation rates (i.e. far from extinction), NO forms in lean (near-stoichiometric) mixtures, whereas CO forms in relatively rich mixtures (Z ~0.08-0.1). On the other hand, high concentrations of UHC tend to occur in even richer (Z > 0.3) mixtures. However, in the present case with unsteady vortex-perturbed flames, high concentrations of both NO (due to unsteady effects) and

CO are observed in fuel-rich regions in the vortical pocket (see Figs.   8.3(e) and 8.2(f)).   We will investigate how the rate of reignition and product/ pollutant formation depend on unsteadiness (vortex velocity) and curvature (vortex length scale) in Sections 8.3 and 8.4, respectively.

To investigate the transient flame structure during extinction and reignition, it is useful to introduce the cross-scalar dissipation rate L, defined as

$$L = 2D_Z(\nabla Y_F \cdot \nabla Y_O),$$ (8.1)

where Y_F and Y_O represent the mass fractions of the fuel and oxygen, respectively. Also called the flame index (Favier and Versvisch, 2001), L may be used to identify regions with premixed and diffusion modes of combustion. From Eq. (8.1), it is clear that L is positive for the premixed mode while it is negative for the diffusion mode. Hence, L is a useful parameter to identify the mode of combustion during transient extinction/reignition. Note that the analysis in terms of the flame-index L can also be performed with the single-step model. Though not shown in Chapter 6, we observed trends similar to those discussed below with the single-step model as well.
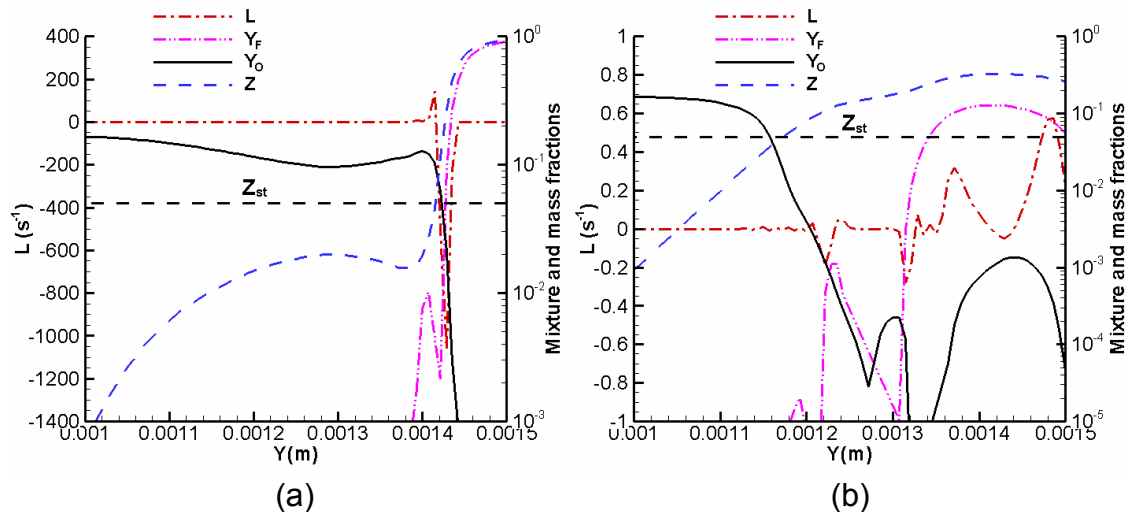
Figure 8.4. Flame-index L (s^{-1}) as a function of the Y coordinate along the vertical centerline during (a) the extinction phase at t* = 1.4, and (b) the reignition phase at t* = 3.5. Mass fractions of fuel (Y_F) and oxygen (Y_O) and the mixture fraction (Z) are shown on the right axis.

Figures 8.4(a) and (b) show the variation of L along the vertical centerline during extinction and reignition, respectively. The mass fractions of fuel (Y_F) and oxygen (Y_O), and the mixture fraction (Z) are shown on the right-hand side axis. In addition, the Z_{st} value (~ 0.05) is indicated by a dashed line in the figures. At t* = 1.4, soon after extinction and at the onset of reignition, we observe strong diffusive mode of combustion, indicated by the relatively large negative values of L. At t* = 3.5 during the reignition phase, we observe from Fig. 8.4(b) that both positive and negative values of L occur in the reigniting region, indicating a mixed or partially-premixed mode of combustion.

Note that along the vertical centerline (symmetry axis) shown in the figures, only the Y derivatives are non-zero in the ∇ operator. It may be deduced from Figs. 8.4(a) and (b) that the positive and negative signs of L are in fact consistent with the signs of ∇Y_F and ∇Y_O. For instance, consider the variation of L in Fig. 8.4(b). We observe that $L < 0$ in the region 0.0013<Y<0.00134 since Y_F increases (i.e. ∇Y_F > 0) and Y_O decreases (∇Y_O <0), whereas $L > 0$ in the region 0.00142<Y<0.00148 since both Y_F and Y_O decrease. Moreover, as seen from Figs. 8.4(b), there exist premixed regions ($L > 0$) that are flammable ($Z \sim Z_{st}$), into which the neighboring edge flames can propagate to promote reignition. Hence, these observations further confirm that transient reignition and reconnection of the diffusion flame evolves through a partially-premixed flame structure, and purely diffusion flamelet libraries are not applicable. This was also pointed out in Chapters 6 and 7 when the single-step mechanism was employed. Moreover, as in the case of the single-step model, it was observed from an inspection of various heat fluxes that the lateral diffusion term $DELHX$ makes a dominant contribution during reignition in the form of heat addition from the neighboring edge flames. Hence, the multi-step chemistry results reveal physical mechanisms similar to those from the single-step kinetic model discussed in Chapter 6.

As in the case of the flame-vortex studies with the single-step model, we have employed $T_{\text{fuel}} = T_{\text{a}} = 1000\,\text{K}$ to match the conditions simulated in the jet computed with LES. As discussed in Chapter 7, with lower fuel temperatures (~400 K) typical of diesel engine chambers, unsteady extinction limits would be greater relative to steady values due to the presence of relatively weaker flames. Moreover, steady autoignition limits would be lower due to two-stage ignition behavior. However, it is expected that similar to the single-step chemistry cases (see Section 7.2), reignition would still occur through edge flame dynamics for the present vortex characteristics (i.e. $u_{\text{v}}, d_{\text{v}}$) due to significant excursions of the unsteady scalar dissipation rates above the steady limits. For instance, consider Figs. 8.5(a)-(d), which show the contours of the lateral (i.e. lateral to the flame along the vertical centerline) diffusion term $DELHX$ during the flame-vortex interaction from simulations (Venugopal and Abraham, 2008b) employing a lower fuel temperature (= 450 K). At the onset of reignition (Fig. 8.5(a)), we observe peak values of χ_{st} as much as 15 times χ_{e}, indicating strong effects due to unsteadiness.

Notice from Fig. 8.5(a) that with stronger flames ($T_{\text{fuel}} = 1000\,\text{K}$), maximum χ_{st} values are only about 3.5 times χ_{e}. Moreover, Figs. 8.5(b)-(d) reveal similar mechanisms for reignition, involving edge flame dynamics, as in the case of simulations employing $T_{\text{fuel}} = 1000\,\text{K}$. When $T_{\text{fuel}} = 450\,\text{K}$, greater effects due to unsteadiness are observed in the dynamics of the edge flames, where the edges withstand χ_{r} values greater than unity without extinction (see Figs. 8.5(c) and (d)). As discussed in our recent publication (Venugopal and Abraham, 2008b), this implies that theoretical formulations for the edge flame speed (Santoro *et al.*, 2000; Herrmanns *et al.*, 2007) that differentiate between positive and negative propagation based on χ_{e} are not applicable. Flow-dependent criteria suitable for unsteady flowfields are required. One such criterion is discussed in Section 10.3 of Chapter 10 focusing on the relevance of the present findings to the modeling of diesel jet flames.
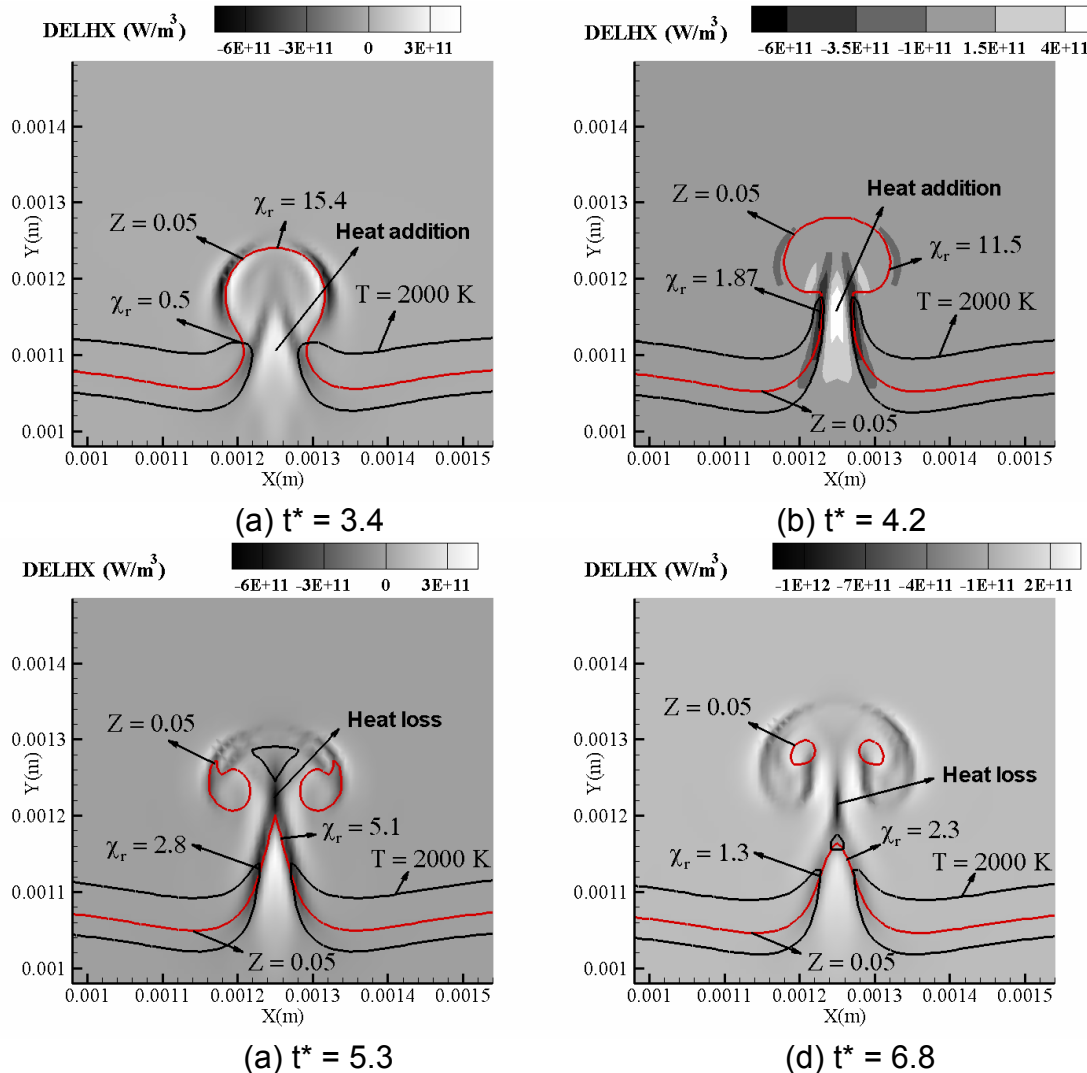
Figure 8.5. Contours of the lateral heat diffusion term $DELHX$ at different times during the flame-vortex interaction with $T_{\text{fuel}} = 450\,\text{K}$ (Venugopal and Abraham, 2008b). Isocontours of $Z = 0.05$ and $T = 2000\,\text{K}$ are shown to indicate the flame-edge location.

Hence, while greater unsteady effects are observed in vortex-perturbed flames with lower fuel temperatures closer to diesel applications, the physical mechanisms for extinction/reignition observed for the present conditions (i.e. $T_{\text{fuel}} = 1000\,\text{K}$) are valid even for localized flame dynamics in diesel chambers. Let us now explore the unsteady response of the flame temperature and different

species to scalar dissipation rates imposed by the vortex along the vertical centerline (diagnostic axis).
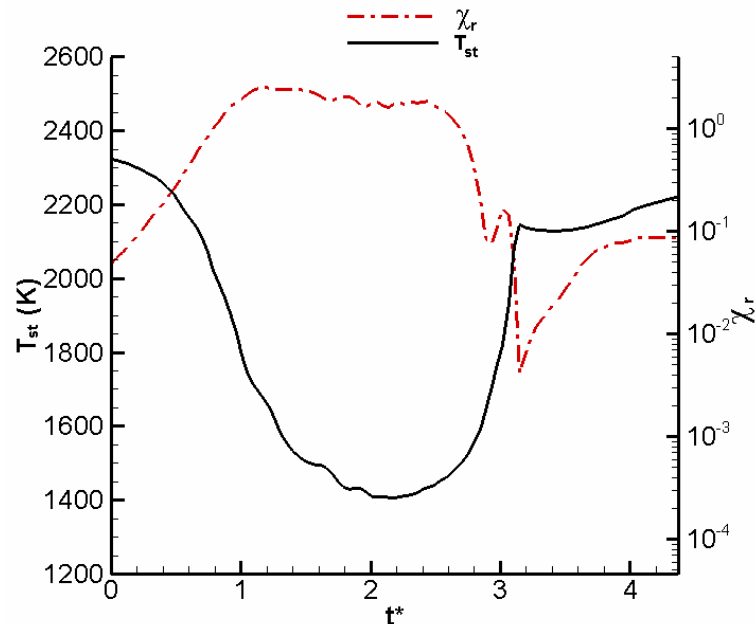
Figure 8.8. T_{st} (K) and χ_r as a function of t* along the vertical centerline during the flame-vortex interaction.

Figure 8.6 shows T_{st} and χ_r as a function of time along the vertical centerline. The vortex-perturbed flame is observed to withstand scalar dissipation rates higher than the steady limit (i.e. $\chi_r > 1$) during the extinction phase. Reignition and subsequent reconnection of the diffusion flame occurs by about four eddy turnover times. The time evolution of the mass fractions of major species, i.e. CO_2, CO and H_2O, and pollutants, i.e. NO and UHC, at the stoichiometric mixture fraction along the vertical centerline is shown in Fig. 8.7. It is interesting that different species show different levels of sensitivity to the imposed scalar dissipation rate. In particular, we observe that NO response is relatively weak, even though the temperature varies significantly during extinction and reignition. On the other hand, OH shows strong sensitivity, and decreases to relatively low values during extinction. Furthermore, while CO_2, H_2O, OH and NO

are observed to decrease during the extinction phase, CO and UHC increase. Since peak temperatures shift to richer regions at relatively high values of scalar dissipation rates, the increase in CO and UHC may be attributed to normal (i.e. in the Y direction) diffusion from richer regions
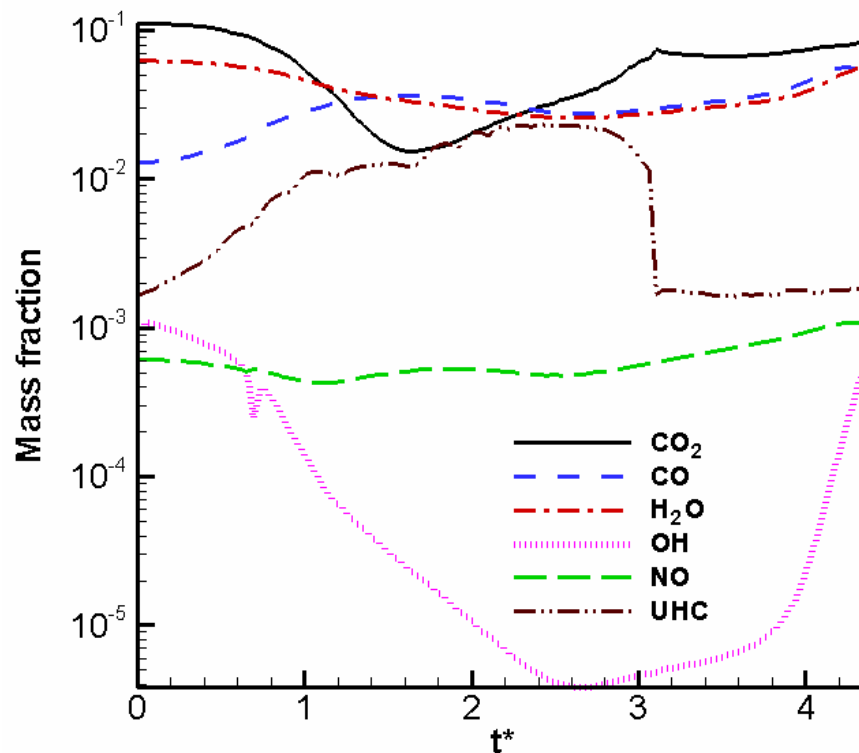
Figure 8.7. Species mass fraction at the stoichiometric mixture fraction as a function of t* along the vertical centerline during the flame-vortex interaction.

Notice in Fig. 8.7 that UHC responds much faster to the vortex perturbation as compared to NO. For instance, Fig. 8.7 shows that while the NO mass fraction falls only by 20 % during the extinction phase due to relatively slow chemical time scales, UHC mass fraction increases by as much as an order of magnitude. Similarly, during reignition, in spite of the significant overshoot during extinction, the UHC mass fraction rapidly decreases to values comparable to those in the unperturbed flame, whereas NO gradually recovers to its initial

value. These disparities in the response time scales can lead to trade offs between NO and UHC, which we will discuss in detail in Chapter 9.

The unsteady response of the species to scalar dissipation can be correlated to the characteristic chemical time scales. Here, the chemical time-scale τ_{ck} of species k is computed as

$$\tau_{ck}^{-1} = \frac{|\dot{w}_{ck}| \cdot MW_{mix}}{\rho},$$ (8.2)

where $\dot{w}_{ck}$ is the net molar chemical production rate of species k, MW_{mix} is the mixture molecular weight, and ρ is the mixture density. Note that the definition in Eq. (8.2) is similar to the chemical time-scale defined in the flame-vortex simulations of Safta and Madnia (2004) with a single-step kinetic model.
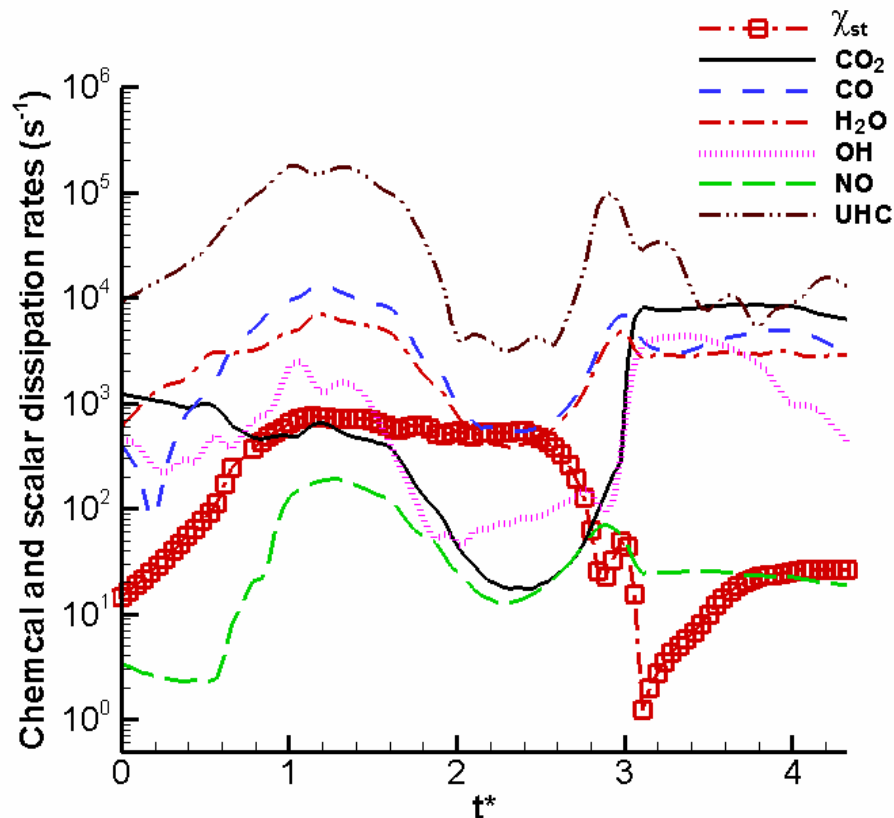
Figure 8.8. Chemical and scalar dissipation rates (s^{-1}) at the stoichiometric mixture fraction along the vertical centerline as a function of t* during the flame-vortex interaction.

Figure 8.8 shows the chemical rates (i.e. τ_{ck}^{-1}) of different species and χ_{st} as a function of t* along the vertical centerline during the flame-vortex interaction. Note that the ratio of τ_{ck}^{-1} to χ_{st} defines a Damköhler number Da_k for species k. The chemical rates initially increase as the mixing rate (i.e. χ_{st}) increases, but decrease thereafter due to the drop in temperature. By t* = 2, the net chemical production rates for the major species, i.e. CO_2, CO and H_2O, become comparable or lower than the scalar dissipation rate, indicating Damköhler numbers $Da_k \leq 1$, and the onset of extinction. During reignition, the chemical rates gradually recover back to values comparable to those in the initial unperturbed flame.

We notice in Fig. 8.8 that the chemical rate of NO is much lower than χ_{st}, indicating chemical time scales much longer than the imposed flow time-scale. Hence, as observed in Fig. 8.7, NO response is relatively weak due to its inability to adjust to rapid changes in the mixing rate. On the other hand, the other species including UHC show much higher chemical rates (or shorter chemical time scales), and hence respond faster to the vortex-induced perturbation. We will explore the chemical response of species to unsteady scalar dissipation rates in detail in Chapter 9. In the sections that follow, effects due to unsteadiness and curvature on the rate of extinction/reignition and product/pollutant formation are assessed.

Table 8.1 shows the simulated cases. In Table 8.1, τ_r is the time-scale ratio, defined as

$$\tau_r = \frac{\tau_c}{\tau_v}, \tag{8.3}$$

where τ_c is the characteristic chemical time-scale, and τ_v is the vortex (or eddy) turnover time ($= d_v / u_v$). Following Versvisch and Poinsot (1998), we choose τ_c as

$$\tau_c = \chi_e^{-1}, \tag{8.4}$$

which corresponds to an extinction Damköhler number of unity. The relatively large values (O (10^2)) of τ_r for the simulated cases indicate interactions of relatively weak (or strained) flames with strong vortices. Note that τ_r is the inverse of the vortex Damköhler number Da_v introduced in Eq. (7.3), and hence represents the normalized global strain rate (=u_v/d_v) induced by the vortex. In Table 8.1, with respect to the baseline case discussed in this section, Case A represents a slower vortex simulation to explore effects due to unsteadiness, while Case B represents a smaller vortex simulation to investigate curvature effects on the flame-vortex interaction.

Table 8.1 Simulated cases

Case	l_r	τ_r	Re_v
Baseline	1.5	167	540
A	1.5	74	240
B	0.75	333	270

8.3. Effects due to Unsteadiness

In this section, we will compare the flame temperature and species response for the baseline case and Case A (see Table 8.1) to explore effects due to unsteadiness on the flame-vortex interaction.

Figure 8.9 compares the temperature T_{st} at stoichiometric mixture fraction as a function of χ_r along the vertical centerline for the baseline case and Case A. We observe that the slower vortex (Case A) induces lower magnitudes and rates of variation of χ_r, which in turn results in longer time scales for extinction and reignition. These trends are qualitatively consistent with those observed with the single-step kinetic model in Chapter 7 (see Section 7.2). Moreover, the lower

values of χ_r and greater residence times for the flame-vortex interaction with the slower vortex (Case A) would result in greater flame rollup and burned area.
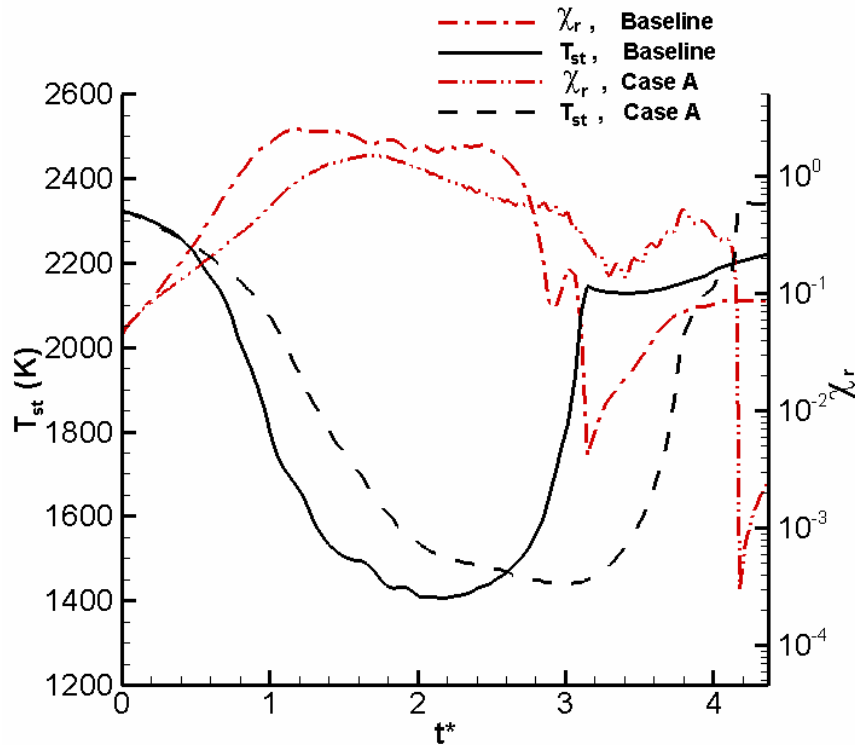
Figure 8.9. T_{st} (K) and χ_r as a function of t* along the vertical centerline during the flame-vortex interaction for the baseline case and Case A.

To confirm this trend, consider Fig. 8.10 that shows the burned and premixed areas for the baseline case and Case A as a function of time. Note that the burned area in Fig. 8.10 is computed as the total computational cell area with temperatures above 1500 K, and the premixed area is the burned area (i.e. area with $T > 1500 \, \text{K}$) with a positive value of the flame-index (i.e. $L > 0$). Though the choice of the temperature cut-off of 1500 K is arbitrary, it is useful to compare trends across the range of simulated conditions. Figure 8.10 shows that the slower vortex (Case A) leads to a larger burned area, and somewhat larger premixed area owing to longer residence times for the flame-vortex interaction.

Hence, the slower vortex results in greater flame roll up and burned area, but lower rates of extinction and reignition.
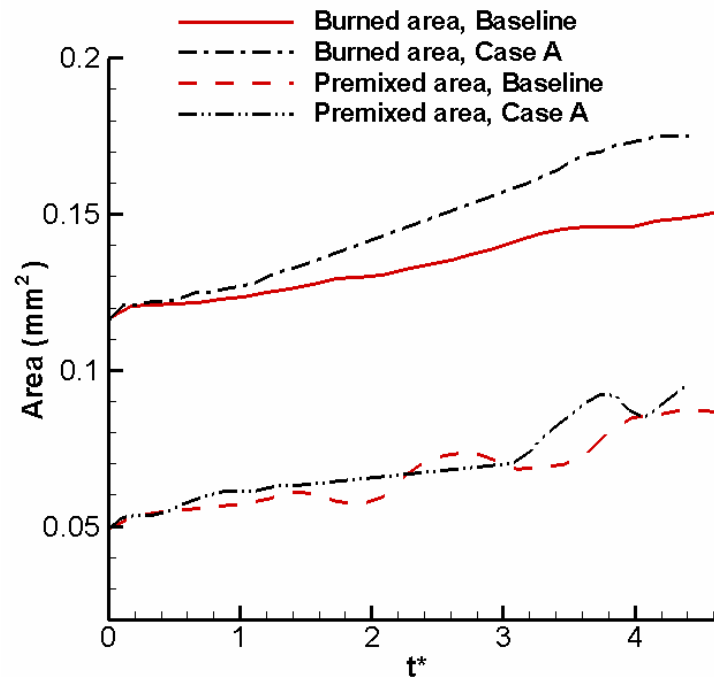
Figure 8.10. Burned and premixed areas as a function of time for the baseline case and Case A.

Figures 8.11(a)-(d) shows the total density (= $\sum \rho Y_k$) of CO_2, CO, NO and UHC, respectively, in the computational domain as a function of time. While the slower vortex results in a higher rate of formation of CO_2 (about 12 %) and NO (about 14%), the formation rates of CO and UHC are about the same for both the cases. Moreover, note that the overall change in total UHC concentration due to the vortex interaction for both cases is relatively small (< 5 %). Essentially, pure fuel, which is relatively dense and occupies about half of the computational domain, contributes towards UHC concentration. Hence, the relatively small vortices employed here do not significantly alter total UHC concentrations. On the other hand, CO_2 and NO are predominantly formed in the near-stoichiometric and high temperature (>2000 K) regions, and hence the increase in the total

concentrations of these species for Case A is attributed to the increase in flame rollup and burning area due to longer residence times (see Fig. 8.10). To clarify the trends with respect to formation of CO and UHC, let us consider the CO and UHC spatial distribution in the vortex-perturbed flame for the two cases at a given time-instant, for instance t* = 4.3.

(a)

(b)

(c)

(d)
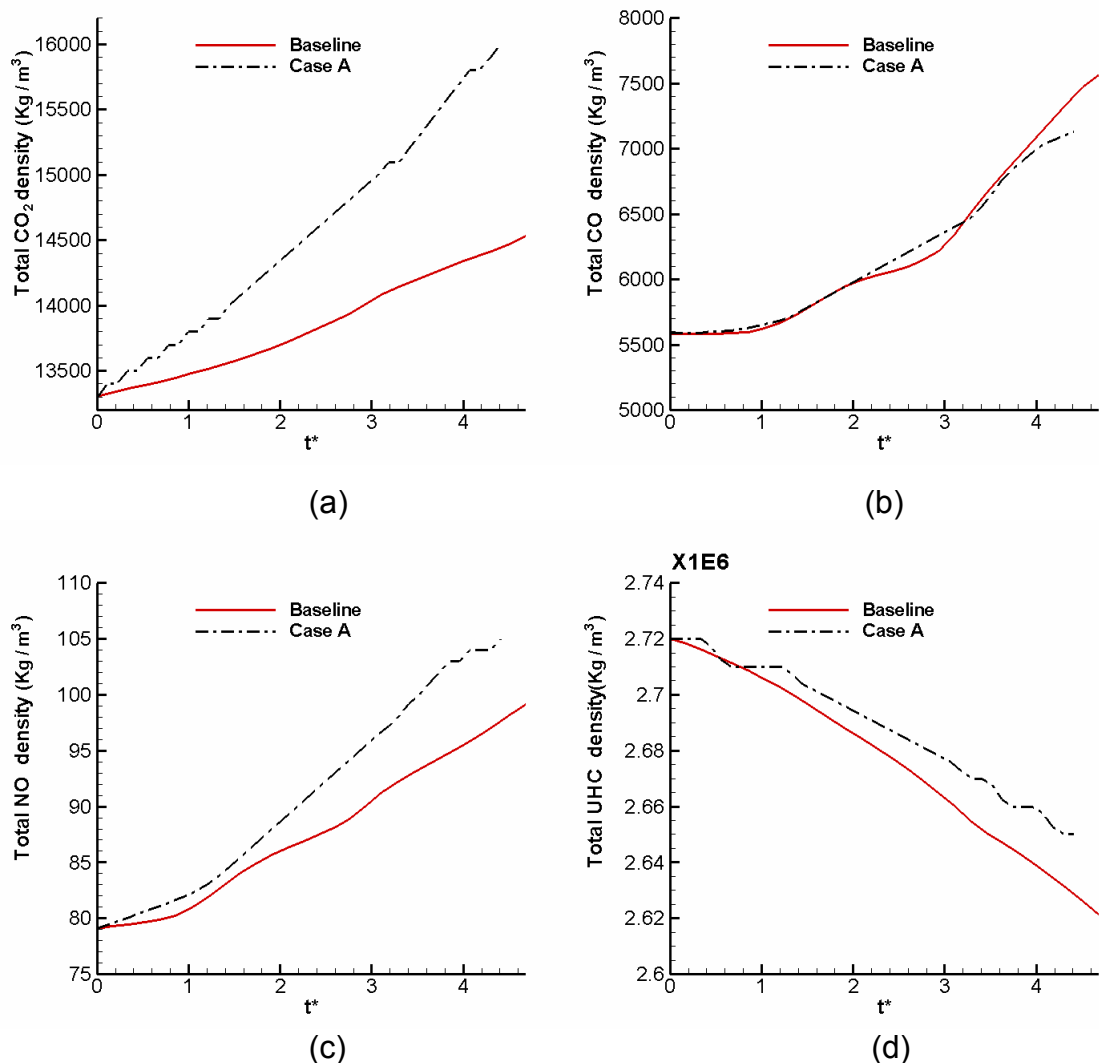
Figure 8.11. Total density (kg/m^3) as a function of time for the baseline case and Case A, (a) CO_2, (b) CO, (c) NO, and (d) UHC.

Instantaneous contours of UHC mass fraction at t*= 4.3 for the two cases are compared in Figs. 8.12 (a) and (b). We observe much lower values of χ_r in

the reconnected flame with the slower vortex, indicating lower mixing rates. This leads to a thicker vortex-perturbed diffusion layer for UHC, which is discernible in the contours shown in Figs 8.12(a) and (b). Note that higher rates of partial-premixing (creating rich fractions) due to the faster vortex (baseline case) leads to higher UHC concentrations along the vertical centerline at t* = 4.3, but this effect is offset by the presence of a relatively thin and strained diffusion layer. Hence, the overall effect is similar UHC concentrations for both the cases.
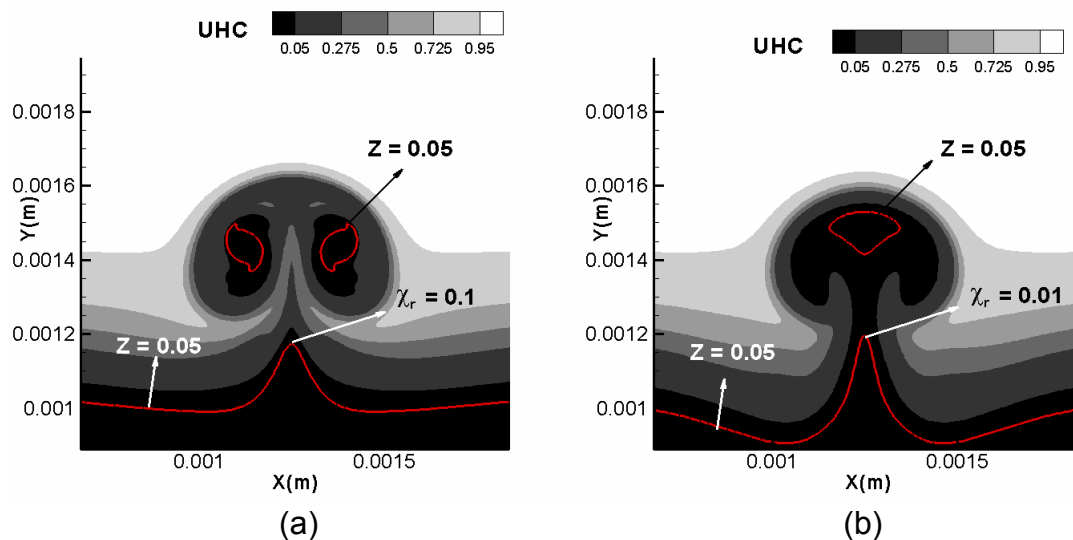
Figure 8.12. Contours of UHC mass fraction at t* = 4.3 during the flame-vortex interaction for (a) the baseline case, and (b) Case A.

The compensatory effects of partial-premixing and straining are also evident in the instantaneous contours of CO mass fraction, shown in Figs. 8.13(a) and (b) for the baseline case and Case A, respectively, at t* = 4.3. We observe that for the baseline case (faster vortex), higher mixing rates create flammable and rich fractions (for e.g. $Z = 0.15$ as shown in the figures) in the vortical pocket where CO can form, but also lead to thinner and relatively strained diffusion layers. On the other hand, the slower vortex (Case A) results in lower rates of partial-premixing but relatively thicker diffusion layers. We will now explore the effects due to curvature (vortex length-scale) on the rates of extinction/reignition and product/pollutant formation.
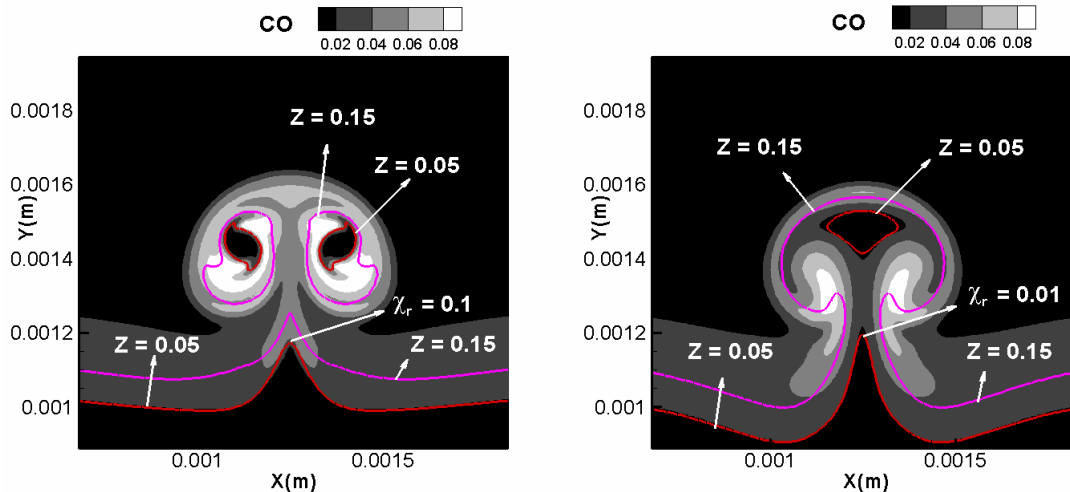
Figure 8.13. Contours of CO mass fraction at t* = 4.3 during the flame-vortex interaction for (a) the baseline case, and (b) Case A.

8.4. Effects due to Curvature

To assess effects due to curvature, let us compare the results for the baseline case ($l_r = 1.5$), and Case B with a smaller vortex ($l_r = 0.75$), while maintaining the velocity-scale constant. These l_r values were chosen to simulate vortices larger (baseline, $l_r > 1.0$) and smaller (Case B, $l_r < 1.0$) than the local diffusion layer thickness. With respect to the local length scales in the jet, the baseline and Case B vortices are sized about 0.36 and 0.18 times the integral length scale (L_{11}) and about 3 and 1.5 times the Taylor length scale (λ), respectively. Hence, the selected vortices represent inertial scales in the turbulent jet. Recall that a wider range of length scales from about $0.72 L_{11}$ down to about 0.75λ was simulated with the single-step model (see Sections 7.3 and 7.4). Based on the correspondence observed here between the single-step and multi-step kinetic models with respect to physical mechanisms, it is expected that the trends reported in Chapter 7 with respect to unsteady and curvature effects for the wider range of length scales would be valid with the multi-step kinetic model as well. We observe from Table 8.1 that when reducing the vortex size for

the same velocity-scale, the time-scale ratio τ_r and the vortex Reynolds number Re_v decrease.
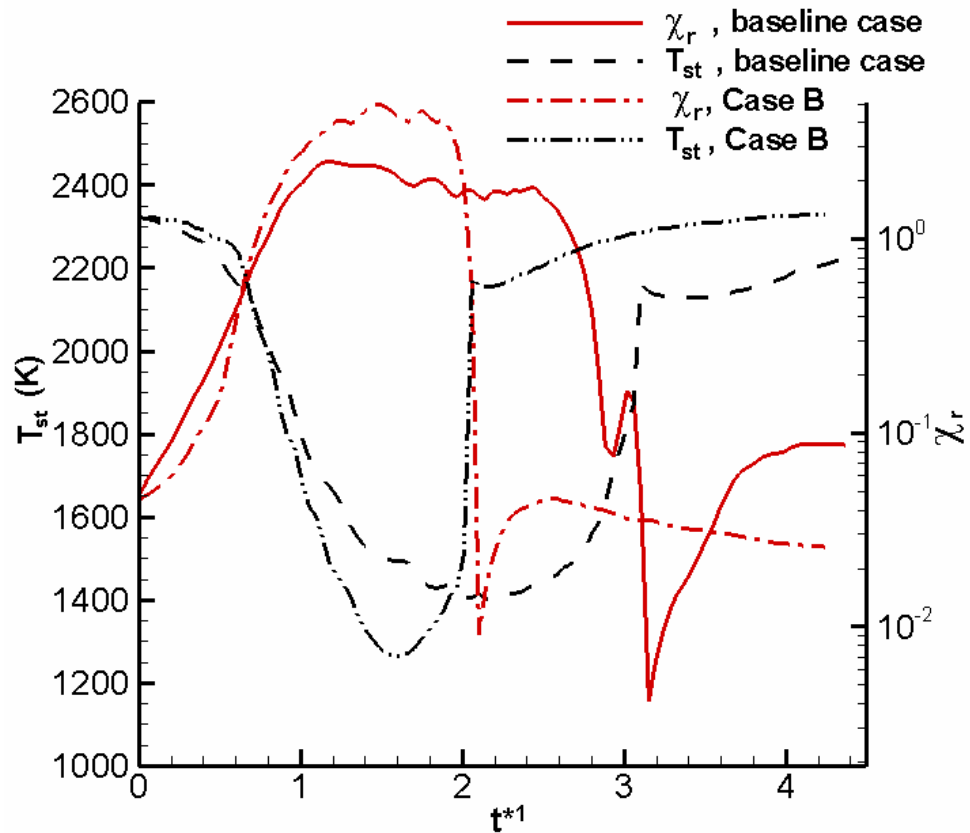
Figure 8.14. T_{st} (K) and χ_r as a function of t*^{1} along the vertical centerline during the flame-vortex interaction for the baseline case and Case B.

Figure 8.14 shows T_{st} and χ_r as a function of time along the vertical centerline during the flame-vortex interaction for the baseline case and Case B. Note that as in Chapter 7 (see Section 7.3), t*^{1} represents the physical time elapsed normalized by the turnover time-scale for the baseline vortex for both cases, and hence essentially equivalent to the actual time. We observe from Fig. 8.16 that the smaller vortex (Case B) results in shorter time scales for extinction and reignition, in qualitative agreement with the single-step model results discussed in Section 7.3. Moreover, as in the single-step chemistry case,

employing a smaller vortex results in a higher rate of increase of χ_r due to hydrodynamic effects (i.e. sharper velocity gradients) during the extinction phase, which leads to faster reignition. Moreover, stronger flame-flame interactions due to the vortex-induced curvature lead to faster reignition following extinction.

To quantify the effect of the vortex length-scale on flame rollup, consider the time-evolution of the burned ($T > 1500\,\mathrm{K}$) and premixed ($T > 1500\,\mathrm{K}$ and $L > 0$) areas for the baseline case and Case B, shown in Fig. 8.15. As expected, the larger vortex (baseline case) causes a greater rollup and burned area, and a greater fraction of this burned area is premixed for the baseline case. Essentially, flame-flame interactions prevent rollup of the edge flames in the case of the smaller vortex (Case B), but lead to faster reignition and reconnection of the diffusion flame.
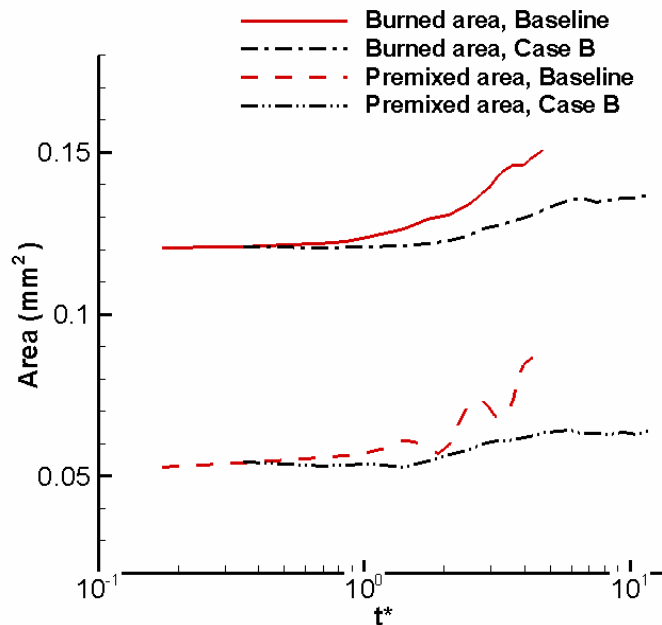
Figure 8.15. Burned and premixed areas (mm^2) as a function of t* for the baseline case and Case B.

The total densities of the major species CO_2 and CO, and pollutants NO and UHC, are shown as a function of time in Figs 8.16(a)-(d). Note that the simulated time of about 0.15 ms represents a much longer non-dimensional time

(t*) for Case B (smaller vortex) since the turnover time-scale t_{eddy} ($= d_v / u_v$) is about half as compared to the baseline case. As indicated before, the total UHC concentration shows a relatively small change due to the vortex interaction for both the baseline case and Case B.
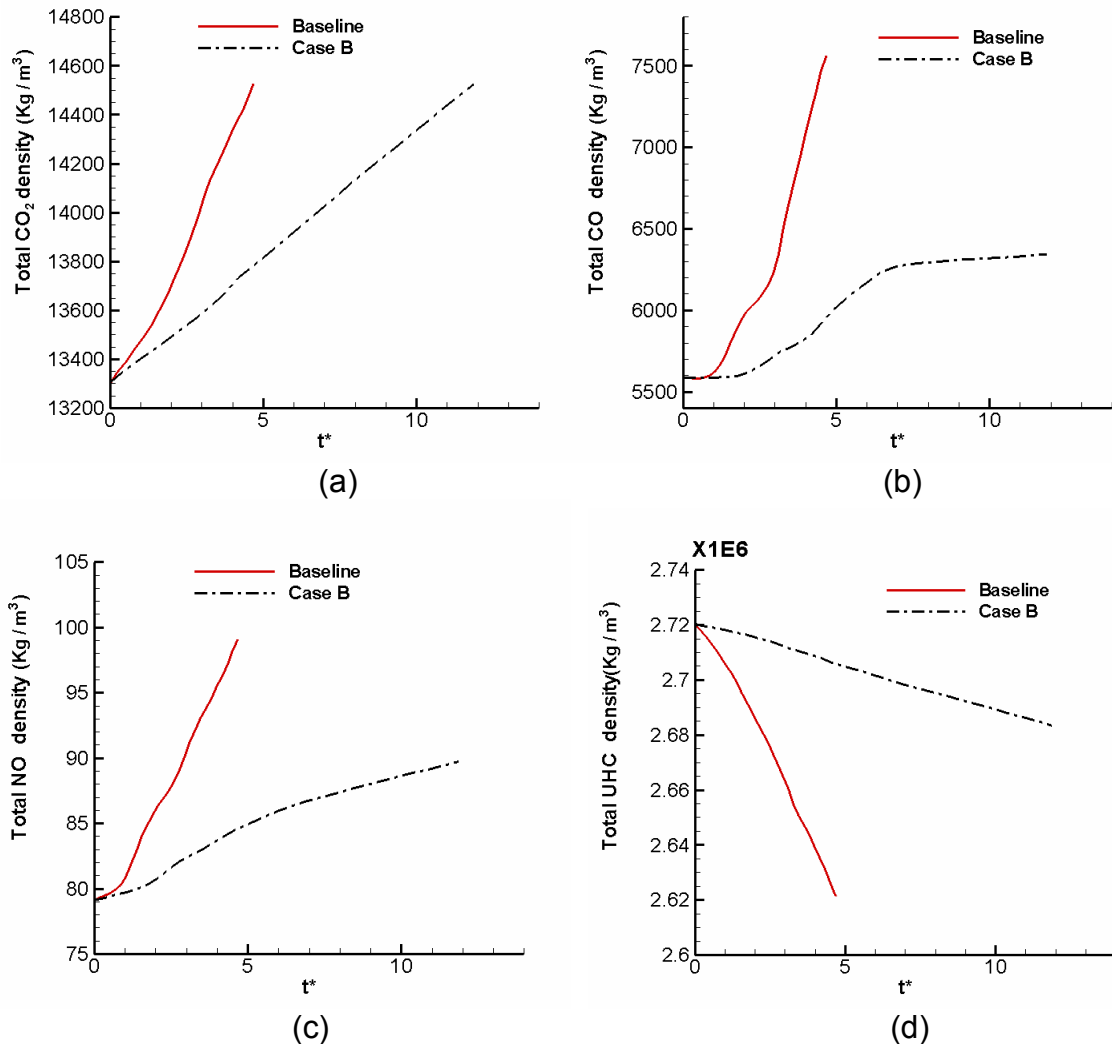
Figure 8.16. Total density (kg/m^3) as a function of time for the baseline case and Case B, (a) CO_2, (b) CO, (c) NO, and (d) UHC.

From Figs. 8.16(a)-(d), we observe a higher rate of formation of CO_2, CO and NO for the baseline case (larger vortex), while the change in UHC concentration in the domain due to the vortex interaction is within 5% for both

cases. The decrease in the total concentrations of CO_2 and NO from the baseline case to Case B is consistent with the decrease in flame rollup and burning area, as shown in Fig. 8.15. To clarify the trends with respect to the formation of CO, let us consider the spatial distribution of CO in the vortex-perturbed flame for the baseline case and Case B at a given time-instant, for instance, t* = 4.68.

(a)   (b)
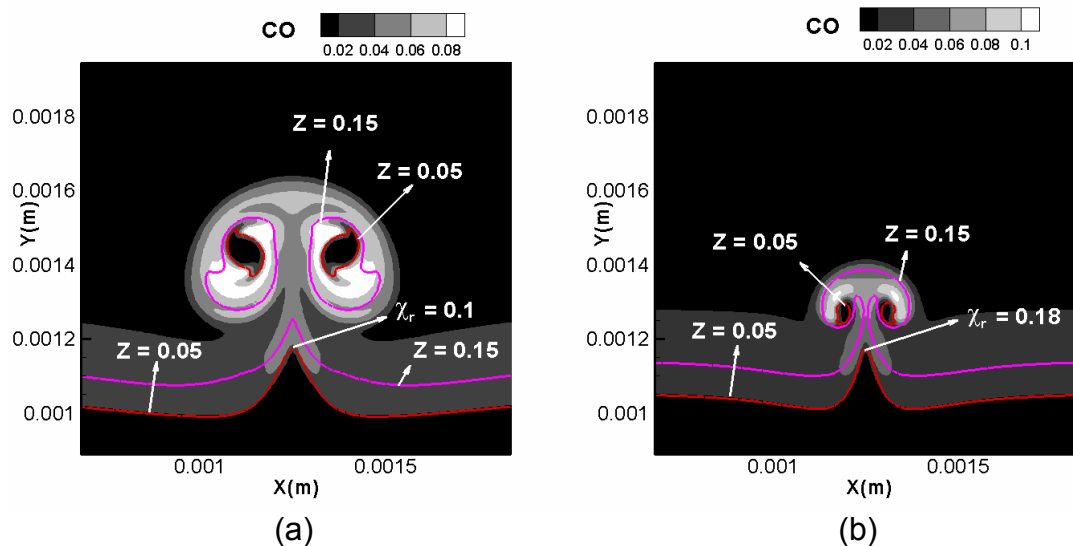
Figure 8.17. Contours of CO mass fraction at t* = 4.68 during the flame-vortex interaction for (a) the baseline case, and (b) Case B.

Figures 8.17(a) and (b) shows the instantaneous contours of CO mass fraction during the flame-vortex interaction at t* = 4.68 for the baseline case and Case B, respectively. Note that since t* = 4.68 represents a longer physical time interval in the case of the larger vortex (baseline case) and both vortices have the same initial velocity-scale, the larger vortex has reached a higher Y position as compared to the smaller vortex. We observe from Figs. 8.17(a) and (b) that CO predominantly forms in the fuel-rich vortical pocket surrounding the reconnected flame. Hence, the larger vortex leads to higher total concentrations of CO. However, higher peak concentrations of CO are seen for Case B (smaller vortex) at t* = 4.68 due to locally richer fractions caused by relatively high partial-premixing rates. Moreover, the reconnected flame is relatively thinner in the case

of the smaller vortex (Case B) due to higher scalar dissipation rates (see Figs. 8.17 (a) and (b)), which also contributes towards lower total concentrations of CO. Furthermore, since CO_2 and NO form predominantly in the reconnected flame, presence of thicker flames in the larger vortex (baseline vortex) results in higher total concentrations of these species relative to Case B.

From the discussions so far on the effects of unsteadiness and curvature, it can be concluded that it is beneficial to have high rates (higher velocity scales) of fine-scale (smaller length scales) mixing with respect to both flame-stability (rate of reignition) and pollutant (NO) formation. Moreover, the results show that the global mixing rate induced by the vortex ($= u_v / d_v$) is a direct measure of the rates of extinction and reignition. For instance, the rate of reignition decreases for case A relative to the baseline case due to a decrease in u_v / d_v, and vice-versa for Case B relative to the baseline case. Note, however, that these trends correspond to localized flame dynamics in a jet flame, and consider the isolated effect of a single length-scale (or a turbulent eddy) on the flame structure. Simultaneous interactions of the flame with a spectrum of vortices of varying length and velocity scales may alter the rates of extinction/reignition and product/pollutant formation. In Chapter 9, we will address this issue in part by investigating the response of diffusion flamelets to turbulent time records of the scalar dissipation rate obtained from LES, which may be viewed as simultaneous effects of a spectrum of length scales. These investigations will provide useful insights into the probability of extinction/reignition events in a turbulent jet flame.

8.5. Summary and Conclusions

In this chapter, results from flame-vortex interaction studies employing a multi-step chemical kinetic model for n-heptane oxidation were discussed. The kinetic model chosen was the skeletal mechanism developed by Peters *et al.* (2002), which comprises 34 species among 56 reaction steps. In Chapter 4, this mechanism was validated for the prediction of non-premixed flame structure,

extinction, and partially-premixed flame structure through comparison with available experimental data at 1 bar. The effects of unsteadiness (vortex velocity-scale) and curvature (vortex length-scale) on the rates of extinction/reignition and product/pollutant formation were investigated. Qualitative comparisons were presented with the results obtained in Chapters 6 and 7 with a single-step mechanism. The characteristics of the simulated vortices and diffusion layers (scalar dissipation rates) were chosen to correspond to mean statistics computed with LES at the jet axial location, x/d = 12, in the radial region $0 \leq$ r/d ≤ 1.5.

Results showed that the physical mechanisms of extinction and reignition were qualitatively similar to the single-step kinetic model results discussed in Chapter 6. In particular, extinction was characterized by unsteady effects, and unsteady extinction limits as much as three times the steady values were observed due to relatively large values of the chemical-to-vortex time scale ratios ($\sim O(10^2)$). Moreover, reignition occurred following extinction due to flame-flame interactions between edge flames aided by the vortex-induced curvature. Examination of the flame-index (L) in the extinguishing/reigniting regions revealed a diffusive mode of combustion during the extinction phase, which transitions to a partially-premixed mode during reignition and subsequent reconnection of the flame. Effects of unsteadiness (vortex velocity-scale) on the rates of extinction/reignition and product/pollutant formation were assessed. Consistent with the single-step model results discussed in Section 7.2, decreasing the vortex velocity scale resulted in lower unsteady extinction limits, and longer time scales for extinction and reignition. To investigate the effects due to curvature (vortex length-scale) on the rates of extinction/reignition and product/pollutant formation, simulations with $l_r = 1.5$ (baseline) and $l_r = 0.75$ (Case B) were compared. The smaller vortex was found to result in shorter time scales for extinction owing to higher rates of increase of scalar dissipation rates (hydrodynamic effects), and shorter time scales for reignition due to stronger curvature effects and flame-flame interactions. These trends were consistent with the single-step model results discussed in Section 7.3. Since the single-step and

multi-step kinetic models reveal similar mechanisms, the qualitative conclusions drawn in Chapters 6 and 7 regarding the effects of unsteadiness and curvature on the localized flame dynamics at different locations in the LES jet near field are expected to be valid in general for the simulated conditions.

Moreover, in the flame-vortex studies presented here with multi-step chemistry, we considered relatively high fuel temperatures ($T_{\text{fuel}} = 1000\,\text{K}$) that resulted in relatively strong flames. Based on our recent studies employing the 56-step mechanism (Venugopal and Abraham, 2008b), it was shown that with lower fuel temperatures (~ 400 K) typical of diesel engine conditions, greater unsteady effects leading to higher unsteady extinction limits relative to steady values would be observed. Moreover, due to large excursions of the unsteady scalar dissipation rates above the steady values, the physical mechanisms of reignition for conditions closer to diesel chambers are governed by edge flame dynamics as in the case of the studies reported in this chapter with a higher fuel temperature (= 1000 K). Hence, the physical mechanisms of extinction/reignition observed with the present choice of vortex and flame characteristics are valid even under conditions (i.e. lower fuel temperatures) closer to practical diesel engines.

Investigation of the spatio-temporal evolution of major combustion products, such as CO_2 and CO, and pollutants like NO and UHC, showed interesting trends. With respect to major species, while CO_2 spatial distribution closely correlated with that of the temperature, CO was found to predominantly form in rich mixtures, and in the vortical pocket during the later stages of the flame-vortex interaction. The interaction of the flame with a slower vortex resulted in greater roll up of the edge flames due to lower scalar dissipation rates, and larger burned and premixed burned areas due to longer residence times. Consequently, total CO_2 concentration was found to increase as the vortex velocity was decreased. On the other hand, the total CO concentration was predicted to be about the same for the baseline case and the slower vortex (Case A). This similarity was attributed to compensatory effects of partial-

premixing that creates rich fractions in the vortical pocket (thereby increasing total CO), and straining that leads to thinner diffusion layers and reconnected flames (thereby decreasing total CO). With respect to curvature (vortex length scale) effects, mutual interactions between the edge flames prevented flame rollup in the case of the smaller vortex (Case B), thereby decreasing the burned and premixed burned areas. Consequently, the total concentrations of CO_2 were found to decrease as the vortex length-scale was decreased. Furthermore, presence of a smaller fuel-rich pocket (where CO predominantly forms) and relatively thinner reconnected flames (due to higher scalar dissipation rates) resulted in lower total concentrations of CO with the smaller vortex.

With respect to pollutants NO and UHC, the characteristic chemical response times (τ_{ck}) were found to be significantly different. In particular, NO was associated with relatively slow response times, and showed a relatively small decrease (about 20 %) during the extinction phase, and a gradual recovery during reignition. On the other hand, UHC responded much faster to the vortex-induced perturbation, and increased as much as 10 times during extinction and rapid relaxed to the initial values during reignition. Trade-offs between NO and UHC formation will be discussed in detail in the next chapter. Moreover, peak concentrations of NO occurred both in the reconnected flame and the pocket. The occurrence of relatively high concentrations of NO in the pocket (with rich mixtures, $Z \sim 0.08$ and $T \sim 2000 \, \text{K}$) could be associated with unsteady effects due to relatively slow chemical response times. Trends in UHC spatial distribution were similar to those in the mixture fraction, and partial-premixing in the wake of the vortex-induced flow in the reigniting regions resulted in relatively rich mixtures ($Z > 0.1$) and UHC-formation. With respect to effects due to unsteadiness, as in the case of CO_2, the total NO concentration was found to increase with a decrease in the vortex velocity-scale due to increase in burned areas and residence times. In addition, the total concentration of NO was found to decrease as the vortex size was decreased, primarily due to relatively thinner diffusion layers. Due to the relatively small vortices employed in the present studies, the

changes in the total UHC concentrations in the computational domain showed relatively small changes (< 5 %) because of interactions with the vortices.

In summary, the results presented in this chapter complement those observed with the single-step kinetic model in Chapters 6 and 7, and provide additional insights into the effects of unsteadiness and curvature on the response of major species and pollutants. The flame-vortex studies with both single-step and multi-step kinetic models indicate that local extinction, reignition and pocket formation are likely regimes of localized flame dynamics in the LES jet near field. It is important to note that the trends with respect to the rates of extinction/reignition and product/pollutant formation reported in the studies presented in Chapters 7 and 8 correspond to interactions of isolated vortices (or eddies) with flames. Repeated interactions with a spectrum of length scales may alter the rates of extinction/reignition and product/pollutant formation, and probabilities of these scenarios. We will address the simultaneous effects of a spectrum of length scales in part by exploring the response of flamelets to turbulent fluctuations (due to a spectrum of length scales) of the scalar dissipation rate in the next chapter. Moreover, the flame-vortex studies indicate that extinction/reignition phenomena are associated with unsteady effects, which significantly alter the instantaneous temperature and species response relative to a steadily-strained flame. To assess unsteady effects and the validity of steady flamelets in detail, we will investigate the response of diffusion flamelets to unsteady scalar dissipation rates obtained from the LES jet flowfield in the next chapter.

CHAPTER 9. UNSTEADY RESPONSE OF DIFFUSION FLAMELETS

9.1. Introduction

In Chapters 6-8, the dynamics of flames interacting with an isolated vortex was studied for a range of non-dimensional parameters encountered in the near-field of a 70,000-Re jet. Extinction and reignition were shown to be outcomes of such interaction, and their occurrences were controlled by different physics. In reality, the flame is likely to be impacted by a series of vortices. As shown in the previous chapters, the straining effect caused on the flame by the vortex may be characterized by the scalar dissipation rate. To provide insight into the likely series of events when a series of vortices interact a flame, in this chapter, we will investigate the unsteady response of diffusion flamelets to oscillations and fluctuations of the scalar dissipation rate. The perturbations employed are obtained from the analysis of the unsteady LES flowfield at different jet locations. Using a detailed chemical kinetic mechanism for n-heptane oxidation, the unsteady responses of the flame temperature, major species like CO_2, H_2O and CO, and pollutants like NO and UHC are studied. While the oscillatory perturbation is associated with a specific amplitude and frequency, the turbulent time-records of scalar dissipation rates represent the simultaneous effects due to a spectrum of length scales. These studies will provide insights into the nature of extinction and reignition phenomena in turbulent flowfields, and possible implications for associated phenomena such as flame lift-off.

The numerical methodology is discussed in Section 9.2, following which results from studies employing an oscillatory scalar dissipation rate perturbation are presented in Section 9.3. In Section 9.4, the response of flamelets to turbulent time histories of scalar dissipation rates obtained from the LES flowfield

is investigated. In both sets of studies, the applicability of steady flamelet libraries to predict the temperature and species responses is assessed. An outcome diagram representing the observed unsteady response regimes is discussed in Section 9.5. The chapter closes with summary and conclusions in Section 9.6.

9.2. Numerical Methodology

To compute the transient structure of laminar diffusion flamelets, we employ the 1-D flame code discussed in Section 4.3 that solves the unsteady flamelet equations in mixture fraction (Z) space, with the assumption of unity species Lewis numbers (see Eqs. (4.14) and (4.15)). These equations are repeated here for reference:

$$\rho \frac{\partial Y_i}{\partial t} = \rho \frac{\chi}{2} \frac{\partial^2 Y_i}{\partial Z^2} + \dot{w}_i, \tag{9.1}$$

$$\rho \frac{\partial h}{\partial t} = \rho \frac{\chi}{2} \frac{\partial^2 h}{\partial Z^2} + \frac{\partial p}{\partial t} - \sum_{i=1}^{n} h_i^0 \dot{w}_i, \tag{9.2}$$

where h is the mixture sensible enthalpy, ρ is the mixture mass density, Y_i, $\dot{w}_i$ and h_i^0 are the mass fraction, chemical production/destruction rate and standard specific enthalpy of species i, respectively, and n is the total number of species. In Eqs. (9.1) and (9.2), χ is the instantaneous scalar dissipation rate, which is assumed to depend on Z according to the relation (Peters, 1984)

$$\chi = \frac{\chi_{st} \exp\{-2[\text{erfc}^{-1}(2Z)]^2\}}{\exp\{-2[\text{erfc}^{-1}(2Z_{st})]^2\}}, \tag{9.3}$$

where χ_{st} is the instantaneous scalar dissipation rate at the stoichiometric mixture fraction Z_{st}. Note that the functional form assumed in Eq. (9.3) is valid for both steady diffusion flames and unsteady mixing layers (Peters, 2000).

The governing equations are discretized in Z space using 102 grid points. The grid is significantly stretched about Z_{st} to achieve good resolution (about 12 grid points in a 10% thickness about Z_{st}) in the flame zone. We have verified that this grid is adequate to obtain grid-independent results. Spatial discretization is

achieved through 2nd-order central differences while 1st-order backward temporal discretization is employed. Chemical kinetic source terms are computed through an interface with CHEMKIN (Kee *et al.*, 1999) subroutines. The resulting discretized equations are solved using the Thomas algorithm.

We describe n-heptane oxidation chemistry through a kinetic mechanism, developed by Seiser *et al.* (2000), incorporating 159 species among 1540 reaction steps. Seiser *et al.* showed that the 1540-step mechanism predicts autoignition delay times and extinction strain rates in good agreement with the comprehensive mechanism of Curran *et al.* (1998). In addition, we have employed this mechanism in prior studies on autoignition (Gopalakrishnan and Abraham, 2002) and extinction (Venugopal and Abraham, 2007a) in diesel jet flames. The NO sub-mechanism from GRIMECH 3.0 is employed to describe NO formation.

The simulated pressure is 40 bar. We consider pure n-heptane on the fuel-side ($Z = 1$) at 1000 K, and 15 % O_2 + 85 % N_2 in molar composition on the air-side ($Z = 0$) at 1000 K, which match the conditions employed for the LES. We will show in Section 9.3.1 that using $T_f = T_a = 1000\,\text{K}$ leads to a S-curve response without any bifurcation between the steady ignition (χ_{ig}) and the steady extinction limits (χ_e). Hence, we will use χ_e to represent the characteristic chemical time-scale of the flame. Note that with lower fuel temperatures (~ 400 K) typical of diesel applications, χ_{ig} and χ_e may be distinct. We will indicate the implications of this distinction between the ignition and extinction limits for unsteady extinction/reignition in Section 9.3.2. For the studies, discussed in Section 9.3, involving an oscillatory perturbation, χ_{st} serves as an input, and varies temporally according to

$$\chi_{st} = X\left(1 - \cos\left(2\pi f t\right)\right), \tag{9.4}$$

where X is the amplitude, and f is the frequency. Note that the form of the perturbation in Eq. (9.4) ensures a gradual increase from 0 to X in an interval of $T_o / 2$, where T_o is the time-period of oscillation. In addition, we begin with a

steady flame established at the initial value of χ_{st} (i.e. $\chi_{st} = 0$), and then impose the perturbation. The following two non-dimensional numbers are employed to characterize the unsteady flame response:

1. *Amplitude ratio* AR: Based on X and χ_e, we can define an amplitude ratio AR as $AR = X/\chi_e$. We consider values of AR in the range of 1.0-4.0. AR may also be interpreted as the inverse of a mixing time-scale τ_m.

2. *Time-scale ratio* TR: Based on a characteristic chemical time-scale τ_c for the flame, and the frequency of the perturbation f, we can define a time-scale ratio TR as $TR = \tau_c f$. We employ two definitions: $\tau_{c1} = \chi_e^{-1}$ (Versvisch and Poinsot, 1998), and $\tau_{c2} = Z_{st}^2(1-Z_{st})^2/\chi_e$, based on the flame time of a stoichiometric premixed flame, as discussed by Peters (2000). For the conditions employed here, $Z_{st} = 0.046$ and χ_e is about 500 s^{-1} (as discussed in Section 9.3.1). This leads to τ_{c1} and τ_{c2} of about 2 ms and 0.004 ms, respectively. In other words, the frequencies based on these times, f_{c1} and f_{c2}, are about 0.5 KHz and 250 KHz, respectively. Here, we will consider values of f in the range of $f_{c1} - f_{c2}$. In our discussion, we will use values of TR based on $\tau_c = \tau_{c1}$. This gives a range of 1.0-500 for TR. Note that since f is the inverse of the residence time τ_r, TR represents the relative magnitude of τ_c with respect to τ_r. Furthermore, we will show that some of the values of AR and TR simulated here lie in the range expected in the jet near-field.

In Section 9.4, we will discuss the response of flamelets to turbulent fluctuations in the scalar dissipation rate. The turbulent time records are generated by Lagrangian-type tracking of flamelets (i.e. stoichiometric isocontours) in time and space across the LES jet flowfield. To track a flamelet originating from a given axial location, the following algorithm is employed. At a given time instant, the stoichiometric mixture fraction isocontour is computed as

$$r_f^n = f^n(x_f^n), \tag{9.5}$$

where $r_{\mathrm{f}}^{\mathrm{n}}$ and $x_{\mathrm{f}}^{\mathrm{n}}$ represent the radial and axial locations of the flamelet at the nth time-level, respectively. Moreover, the instantaneous scalar dissipation rate $\chi_{\mathrm{st}}^{\mathrm{n}}$ at a given time-level and axial location is estimated as

$$\chi_{\mathrm{st}}^{\mathrm{n}} = \langle \chi \rangle_{\mathrm{st}}, \tag{9.6}$$

where $\langle \chi \rangle_{\mathrm{st}}$ is the conditional mean scalar dissipation rate conditioned on the stoichiometric mixture fraction, computed using Eq. (5.18). As discussed in Chapter 5, $\langle \chi \rangle_{\mathrm{st}}$ accounts for subgrid fluctuations (through a presumed subgrid PDF of the mixture fraction), and hence an appropriate input for the flamelet computations (Peters, 2000). Note that $r_{\mathrm{f}}^{\mathrm{n}}$ is computed as a number average of all radial distances with $\tilde{Z} = Z_{\mathrm{st}} \pm 0.05 Z_{\mathrm{st}}$ at a given axial location $x_{\mathrm{f}}^{\mathrm{n}}$. At the next time-level, the x-displacement of the flamelet is computed as

$$x_{\mathrm{f}}^{\mathrm{n}+1} = x_{\mathrm{f}}^{\mathrm{n}} + \tilde{u}_{\mathrm{f}}^{\mathrm{n}} \cdot \Delta t, \tag{9.7}$$

where $\tilde{u}_{\mathrm{f}}^{\mathrm{n}}$ is the instantaneous axial velocity at the stoichiometric mixture fraction at a given axial location (computed as a number average over $\tilde{Z} = Z_{\mathrm{st}} \pm 0.05 Z_{\mathrm{st}}$ similar to $r_{\mathrm{f}}^{\mathrm{n}}$). Once $x_{\mathrm{f}}^{\mathrm{n}+1}$ is known, $r_{\mathrm{f}}^{\mathrm{n}+1}$ can be computed from the stoichiometric contour at the n+1 time-level as

$$r_{\mathrm{f}}^{\mathrm{n}+1} = f^{\mathrm{n}+1}\left(x_{\mathrm{f}}^{\mathrm{n}+1}\right). \tag{9.8}$$

In addition, $\chi_{\mathrm{st}}^{\mathrm{n}+1}$ can be estimated using Eq. (9.6) for the n+1 time-level.

Note that flamelets that originate at different axial locations in the jet (i.e. with different x_{f}^{0}) will be subjected to different scalar dissipation rate histories as they traverse through the jet. In the present case, we generate 10 representative flamelet histories spanning a time-interval of 3.5 ms (about 6 flow times in the jet, where one flow time $= L_{\mathrm{domain}} / U_{\mathrm{inj}}$) and the region $6 < x/d < 20$. For instance, consider Fig. 9.1, which shows the computed paths of three flamelets originating at x/d = 6 (flamelet 1), 7.25 (flamelet 5) and 11 (flamelet 10). Furthermore, the flamelets are tracked in time at intervals of 0.01 ms for a period of about 3.5 ms.
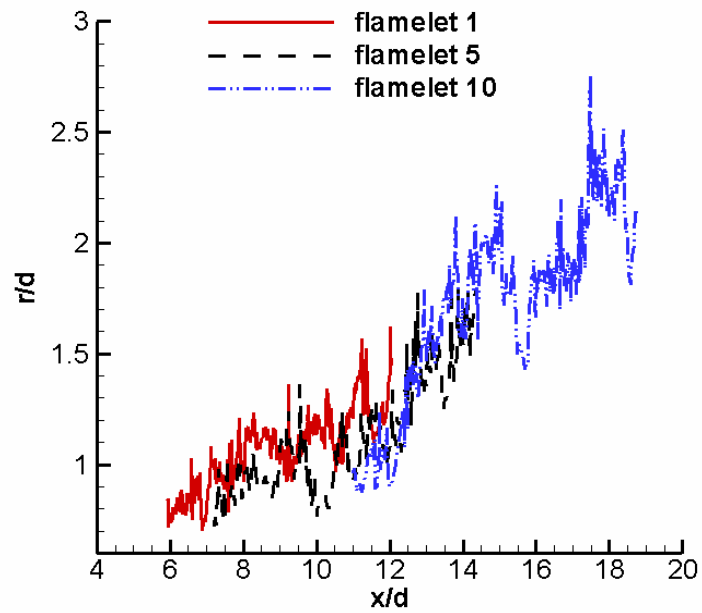
Figure 9.1. Paths of three flamelets originating at different axial locations in the LES jet flowfield.
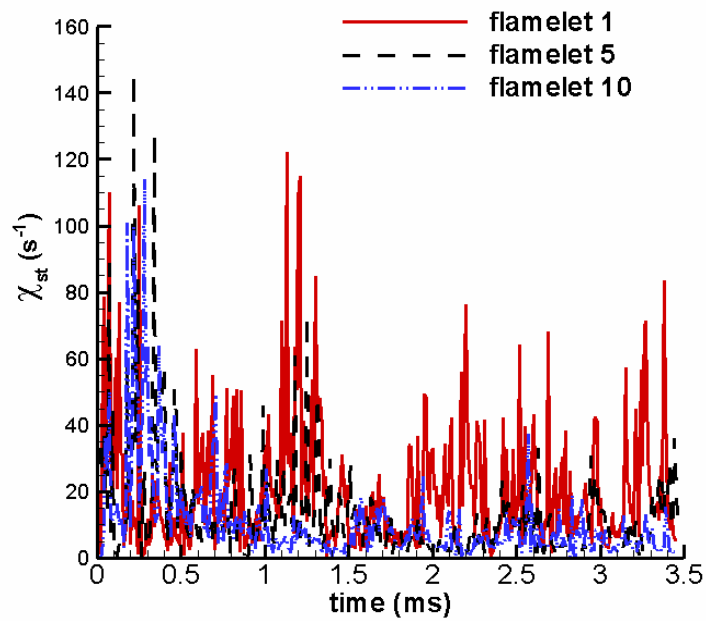
Figure 9.2. χ_{st} (s^{-1}) time histories of three flamelets originating at different axial locations in the LES jet flowfield.

Figure 9.2 shows the time histories of the conditional stoichiometric scalar dissipation rate χ_{st} (see Eq. (5.18)) corresponding to the three flamelets. The differences in the time histories illustrate the unsteady and intermittent nature of the turbulent jet. We observe that while the flamelet originating at an upstream jet location (i.e. flamelet 1) is subjected to a relatively large number of peaks in χ_{st}, the downstream flamelets predominantly encounter relatively low values. Recall from Chapter 5 (Section 5.3.2) that we observed similar trends in the mean filtered ($\overline{\chi}$) and conditional ($\overline{\chi}_Z$) scalar dissipation rates in the jet near-field, which were found to decrease with axial location in the jet. The response of diffusion flamelets to 10 representative flamelet histories generated from the jet flowfield will be discussed in Section 9.4.

In Fig. 9.1, we observe that the stoichiometric contours traverse radial locations, which are relatively far from the jet centerline (i.e. r/d > 1.0). However, as indicated before, we are tracking only an average stoichiometric location (i.e. averaged over all the radial locations with $\tilde{Z} = Z_{st} \pm 0.05 Z_{st}$) at each axial position in the jet. There would be stoichiometric regions close to the jet centerline in the unsteady LES flowfield, which may be associated with stronger χ_{st} fluctuations than those observed in Fig. 9.2. These stronger fluctuations may result in unsteady extinction/reignition close to the jet centerline. Note that in order to track all the individual instantaneous stoichiometric contours in the jet near-field, we would require higher spatial and temporal resolution than that employed here. Recall from Chapters 6 and 7 that the flame-vortex interaction studies indicated that local extinction/reignition events are probable in the 70,000-Re jet near-field in regions close to the jet centerline (i.e. r/d < 1.5). Hence, though the unsteady flame-response to turbulent fluctuations of χ_{st} in stoichiometric regions close to the jet centerline is not simulated here, these flame-response regimes are likely to involve unsteady extinction/reignition, as shown in the flame-vortex simulations. Moreover, employing the 1-D flamelet formulation in the average stoichiometric locations (i.e. r/d > 1.0) is consistent with the expected trends from

flame-vortex interactions, which indicated decreasing curvature effects at farther radial locations due to relatively large values of l_r (> 4.0).

In the section that follows, we present results from studies employing an oscillatory flow perturbation that represents a specific amplitude and frequency.

9.3. Oscillatory Perturbation Studies

As a first step towards understanding unsteady flame response, we consider a simpler and well-defined form of perturbation given by Eq. (9.4). Before we proceed to the discussion of the effects of oscillation frequency and amplitude on the temperature and species response, let us first consider the steady response of the flame, and quantify the steady extinction characteristics.

9.3.1. Steady Flame-response

Figure 9.3 shows the temperature T_{st} and chemical heat release rate Q_{st} at Z_{st} as a function of χ_{st}. As expected, T_{st} decreases as χ_{st} increases due to the diffusive loss of heat and radicals to richer and leaner fractions. Notice that Q_{st} increases initially, up to about $\chi_{st} = 75 \, s^{-1}$, as a result of enhanced mixing, but decreases thereafter due to the opposing effect of decreasing flame temperatures. These trends are in agreement with asymptotic theory predictions (Williams, 2000). Notice that due to relatively shallow temperature gradients close to extinction, the flame becomes increasingly insensitive to large values of χ_{st} (> 300 s^{-1}).

In this work, we define the extinction point as the value of χ_{st} at which the frozen solution ($T_{st} = T_a = 1000 \, K$) is reached. From Fig. 9.3, T_{st} is within 3 % of 1000 K at $\chi_{st} = 500 \, s^{-1}$, and the maximum temperature (at $Z \sim 0.3$) was found to be within 8 % of T_a. Here, we will assume this condition to be close enough to the frozen solution, and hence choose $\chi_e = 500 \, s^{-1}$. It is realized that this is

somewhat arbitrary, and one may choose even higher values to reach closer to frozen flow. Furthermore, alternative criteria for the determination of χ_e can also be employed, for instance, the turning point of Q_{st} (Oh *et al*., 2004), which corresponds to $\chi_{st} = 75$ s^{-1} in Fig. 9.2. In the present case with $T_{fuel} = T_a = 1000\,\text{K}$, these two criteria yield significantly different values. This will change the range of non-dimensional numbers AR and TR discussed before, but not the underlying physical mechanisms for unsteady extinction/reignition. Note that the single-step kinetic model employed for the flame-vortex studies discussed in chapters 6 and 7 also yields $\chi_e = 500$ s^{-1}. Now, we will investigate the unsteady flame response as a function of imposed oscillation frequency and amplitude.
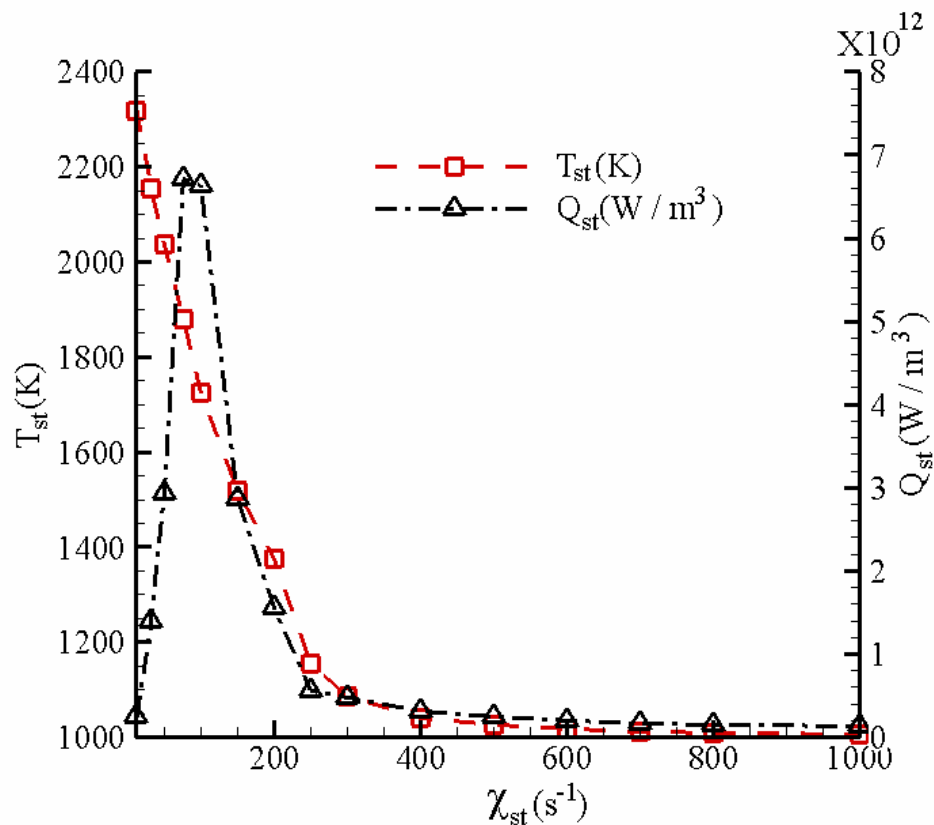
Figure 9.3. T_{st} (K) and Q_{st} (W/m^3) as a function of χ_{st} (s^{-1}) from steady flamelet solutions.

9.3.2. Unsteady Flame-response: Influence of Frequency

As mentioned before, we begin with the steady flamelet solution corresponding to $\chi_{st}=0$, which matches the initial value of χ_{st} imposed by the perturbation (see Eq. (9.4)). This avoids any sudden or step changes in the flame response. The stoichiometric Z location (=0.046) is chosen as the diagnostic point.

Figure 9.4 shows T_{st} and the scalar dissipation ratio $\chi_r (=\chi_{st}/\chi_e)$ as a function of time normalized by the time-period T_o of the oscillation for a range of TR at $AR=2.0$. Note that in each case, the simulation was carried out to $t=3T_o$ to allow sufficient time for the oscillatory limit cycle to be established. From Fig. 9.4, we observe three distinct regimes of unsteady flame response. For relatively small values of TR (or frequency) ($TR=1-10$), the flame undergoes extinction followed by reignition through autoignition, whereas for intermediate values ($TR=10$), the flame extinguishes but fails to reignite. Moreover, for relatively large values of TR ($TR=20-500$), only temporary flame weakening (without extinction) followed by flame recovery is observed. In addition, the decreasing amplitudes of T_{st} oscillation with increasing values of TR suggest that for frequencies even higher than those considered, the flame would be relatively insensitive to the imposed perturbation. These trends indicate that the unsteady flame responds with a phase lag to the imposed perturbation. In other words, the delay in flame response would render it more resistant to extinction, which is confirmed for cases with TR greater than 20, where extinction is not observed even though the peak magnitudes of χ_{st} are well above χ_e (since $AR=2.0$ and $X=2\chi_e$). Recall that these trends agree well with those observed with respect to vortex-induced extinction in chapters 6 and 7, which involved unsteady extinction limits much higher than steady limits. Essentially, the vortices employed in chapters 6 and 7 may be thought of as perturbations with relatively large values of TR, so that the vortex-perturbed flame responds with a phase lag.
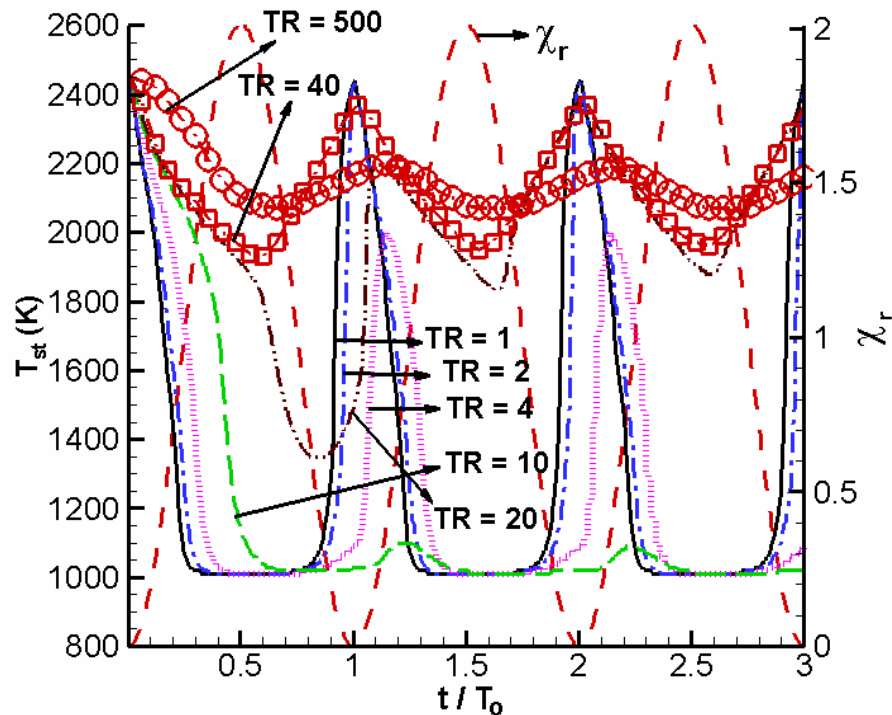
Figure 9.4. T_{st} (K) and χ_r as a function of t/T_o for different values of TR for $AR = 2.0$. The symbols shown for cases with $TR = 40$ and 500 are plotted only every 15th time step for clarity.

The above discussion indicates sufficient residence times are required for both extinction and reignition to occur for a given imposed oscillation amplitude. For instance, while cases with $TR = 20, 40$ and 500 fail to extinguish, the case with $TR = 10$ fails to reignite due to insufficient residence times. To compare the unsteady flame response with that of a steady flame, consider Fig. 9.5 which shows T_{st} (K) as a function of χ_r during the limit cycle for different values of TR along with the steady flamelet solutions. We observe large discrepancies between the unsteady and steady results for relatively large values of χ_{st} ($> 0.2\chi_e$), even for relatively small frequencies ($TR = 1.0$). Moreover, as expected, the deviation of the unsteady flame response from the steady solutions increases as TR (or the frequency) increases. Furthermore, note that the

reignition phase of the limit cycle involves transient partially burned states. At a given value of χ_{st}, these states can be distinguished from those during the extinction phase through a reaction progress variable, c_{st}, which may be computed as the sum of major species mass fractions (Pierce and Moin, 2004). From a turbulent combustion modeling viewpoint, the transient extinction/reignition phenomena observed here can be captured by the use of unsteady flamelet/progress variable (UFPV) libraries, where the temperature (and species mass fractions) are parameterized as $T = fn(Z, \chi, c)$.
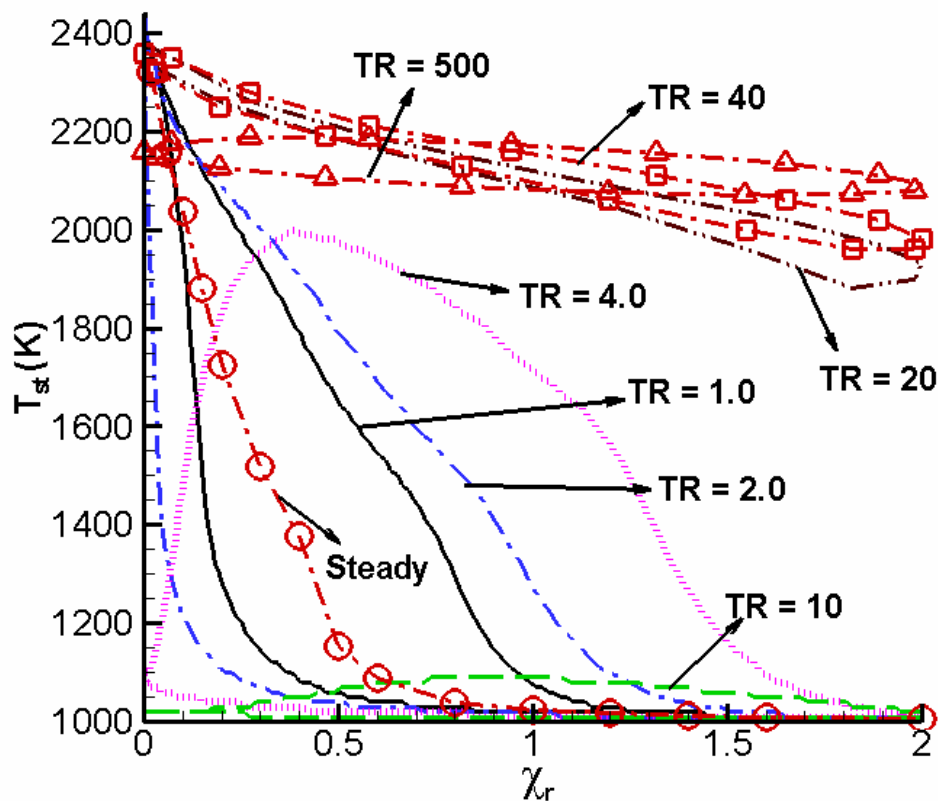
Figure 9.5. T_{st} (K) as a function of χ_r during the limit cycle for different values of TR for $AR = 2.0$. The symbols shown for cases with $TR = 40$ and 500 are plotted only every 15th time step for clarity.

Note that the reignition process observed here can occur only through autoignition (i.e. diffusion normal to the flame surface) due to the 1-D nature of the flamelet formulation. Hence, in a RANS/LES UFPV sub-model accounting for extinction, and reignition via autoignition, the progress variable source term in the mean/filtered progress variable transport equation can be directly tabulated using flamelet calculations. Pierce and Moin (2004) employed this approach in their LES studies of a coaxial gas turbine combustor, where it was shown that the UFPV model provides a more accurate description of the lifted flame in comparison to steady flamelet and infinitely fast chemistry models. However, recall that the flame-vortex studies discussed in Chapters 6 and 7 showed that reignition may occur through edge-flame interactions that involve curvature effects (i.e. diffusion lateral to the flame surface). In the context of modeling, edge flame effects can be incorporated into a reactive scalar like the progress variable, and we showed in Chapter 6 that an UFPV library with the same scalar dissipation rate and progress variable time history as the flame-vortex simulations could accurately describe vortex-induced extinction/reignition. In the context of a RANS/LES combustion sub-model, the mean/filtered progress variable source term would have to be related to the edge flame speed. One possible approach is discussed in Chapter 11.

the simulated pressure in the present case is 40 bar. It is expected that reducing the pressure will decrease the tendency for autoignition. For instance, the experiments of Santoro *et al.* (2000) on vortex-perturbed gaseous methanol/air opposed-flow flames at atmospheric pressure indicate that reignition occurs by edge flame propagation even for relatively weak vortices. In addition, at lower pressures, we would encounter weaker flames with lower values of χ_e, and hence, in the present analysis, the effects of pressure would influence AR and TR values through χ_e. However, it would be interesting to explore whether the values of AR and TR that demarcate different unsteady flame response regimes such as extinction and extinction/reignition would remain the same at different pressures, i.e. the unsteady flame response would show scaling

behavior with respect to pressure. Based on recent studies of Pons *et al.* (2008) on the effects of pressure on non-premixed methane/air flames, this appears unlikely. The work of Pons *et al.* (2008) show that the flame structure in both steady and unsteady strained non-premixed flames may be described by a similarity variable that scales as the square-root of the product of pressure and the strain rate, only for conditions far from extinction. Close to extinction, finite-rate chemistry effects were shown to become important leading to sensitivity to the choice of the chemical kinetic mechanism. Hence, in the present work that involves unsteady extinction/reignition, strong finite-rate chemistry effects on the extinction/reignition behavior may be observed with respect to changes In pressure. Nevertheless, since pressures higher than 40 bar are commonly encountered in heavy-duty diesel engines, it may be worthwhile to investigate and quantify the effects of pressure for both non-extinguishing and extinguishing/reigniting n-heptane flames using available kinetic models.
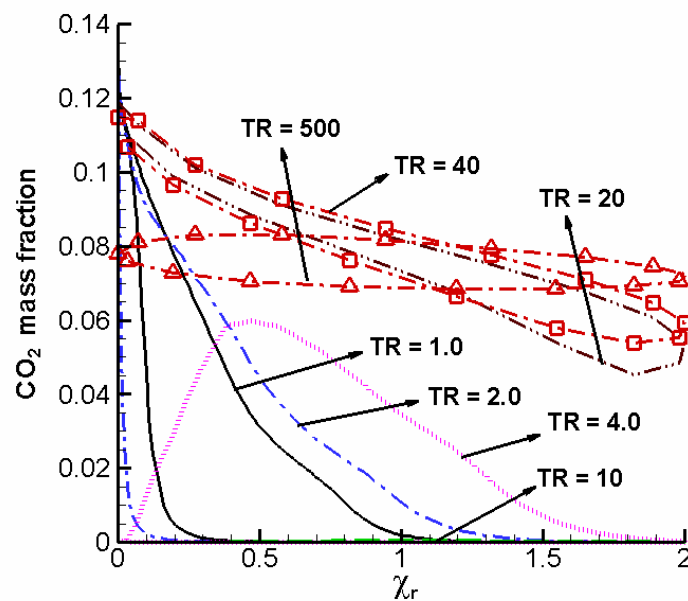
Figure 9.6. CO_2 mass fraction as a function of χ_r for different values of *TR* at $AR = 2.0$.

Figures 9.6 and 9.7 show the mass fractions of CO_2 and H_2O (at Z_{st}) as a function of χ_r during the limit cycle for various values of TR. We observe trends similar to the temperature response. Comparing Figs. 9.6 and 9.7, it is apparent that CO_2 is relatively more sensitive to the imposed frequency (or TR) in comparison to H_2O. For instance, as TR increases from 1.0 to 4.0, the peak CO_2 mass fraction during the limit cycle drops by about 60 %, while that of H_2O drops only by 21 %. However, both species show good recovery to their initial values for cases with relatively small values of TR (< 4.0) involving extinction followed by reignition.
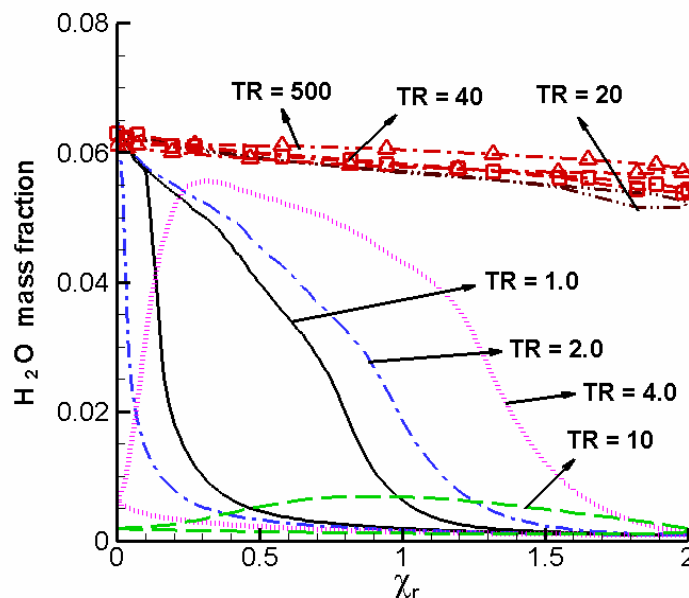
Figure 9.7. H_2O mass fraction as a function of χ_r for different values of TR at $AR = 2.0$.

This difference in the nature of response of CO_2 and H_2O can be correlated with their characteristic chemical time scales τ_{ck} (see Eq. 8.2). For instance, at $\chi_{st} = 0.1\chi_e$, $\tau_{ck,CO2} = 0.16\,\text{ms}$, whereas $\tau_{ck,H2O} = 0.02\,\text{ms}$. Hence, consistent with the ordering of the chemical time scales, H_2O shows a faster response and recovery during reignition in comparison to CO_2. Also, note that

$\tau_{\text{ck, NO}} = 6.41\,\text{ms}$ and $\tau_{\text{ck, UHC}} = 0.19\,\text{ms}$, implying that UHC is expected to respond much faster to the vortex perturbation relative to NO. Recall from Chapter 8 (see Fig. 8.9) that we observed similar trends with respect to the chemical time scales of species in the flame-vortex studies.
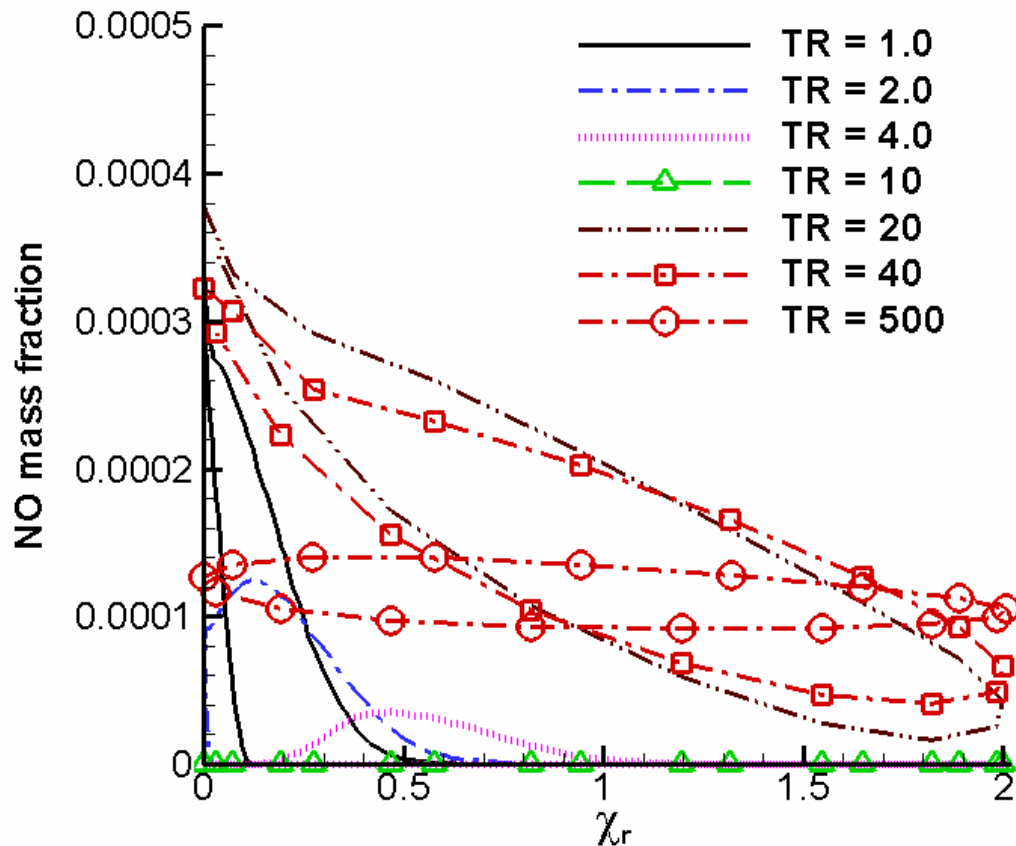
Figure 9.8. NO mass fraction as a function of χ_r for different values of TR at $AR = 2.0$.

Consider the limit cycle curve for NO mass fraction shown above in Fig. 9.8 across the simulated range of TR values. We observe significant reduction in the peak NO mass fraction values for cases involving extinction (i.e. TR values of 1-10), indicating a relatively large sensitivity to the oscillation frequency in the extinction/reignition regime. For instance, as TR increases from 1.0 to 4.0, the

peak NO mass fraction drops by as much as 89 %. However, it is interesting that the corresponding drop in peak T_{st} values, at the same location of scalar dissipation rate, during the limit cycle is only about 18 % as can be inferred from Fig. 9.5. This indicates a relatively significant phase lag of NO to T_{st} and the imposed χ_{st} oscillation, and relatively slow chemical response times. Note that phase lag effects on NO formation due to slow chemical time scales have been reported in engines as well, and the residence time is known to have a significant influence on NO formation rates (Heywood, 1988). However, the occurrence of extinction modifies the phase lag dependence of NO on the residence time (or frequency) in the present case. For instance, for the cases without extinction (TR values of 20, 40 and 500), the peak NO mass fraction is relatively high due to the associated high (> 2000 K) temperatures. In addition, for the case with $TR = 20$, the peak NO mass fraction during the limit cycle is about 17 % higher than the case with $TR = 1.0$, whereas the peak magnitudes are about the same with $TR = 40$. These comparisons indicate that the phase lag dependence of NO mass fraction to the imposed oscillation is non-monotonic.
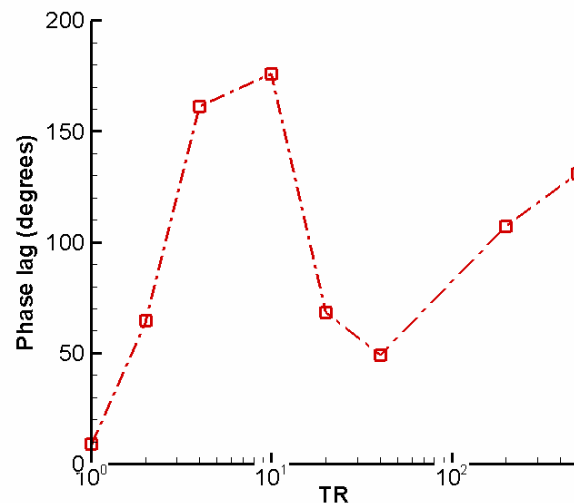
Figure 9.9. Phase lag (degrees) of NO to the imposed oscillation vs. TR.

To confirm this observation, consider Fig. 9.9, which shows the computed phase lag of NO to the imposed perturbation as a function of TR. The phase lag shown in Fig. 9.9 is computed as the time-difference between the points of maximum χ_r and minimum NO mass fraction during the limit cycle. This time-difference is expressed in degrees using the fact that the time-period T_o corresponds to a phase angle of 2π radians or 360 degrees. For all the cases involving extinction ($TR = 1-10$), we observe the expected increase in the phase lag with increase in the frequency. This indicates that as long as extinction occurs and the frozen flow ($T \sim 1000K$) is reached, the phase lag behavior is dictated by the trends in the residence time, which decreases as the frequency (or TR) increases. However, in the TR range of 10-40 during which the unsteady flame response transitions from an extinction regime to a temporary flame weakening regime (see Fig. 9.5), the non-monotonic behavior is evident. Essentially, as TR decreases from 40 to 10, the occurrence of extinction and the associated lower temperatures result in relatively long response times of NO and an additional phase lag that compensate for the increase in residence time. Beyond $TR = 40$, the effect of the extinction-induced lag is absent, and we once again recover the monotonic increase in the phase lag with respect to frequency. Note that prior studies on oscillatory flame response (Im *et al.*, 1999) with flames far from extinction have also reported a monotonic dependence of the phase lag on oscillation frequency. Note that this non-monotonicity in the phase lag was observed for the temperature and major species as well, but is particularly significant for NO due to its relatively long chemical response times.

This discussion indicates that extinction/reignition events that are favored for relatively low values of TR (1-4) are beneficial in terms of both flame stability and NO formation-control. In particular, while the temperature and major species show fast recovery during reignition, NO formation is slower. However, it is important to consider the influence of extinction/reignition events on unburned hydrocarbons (UHCs) as well.
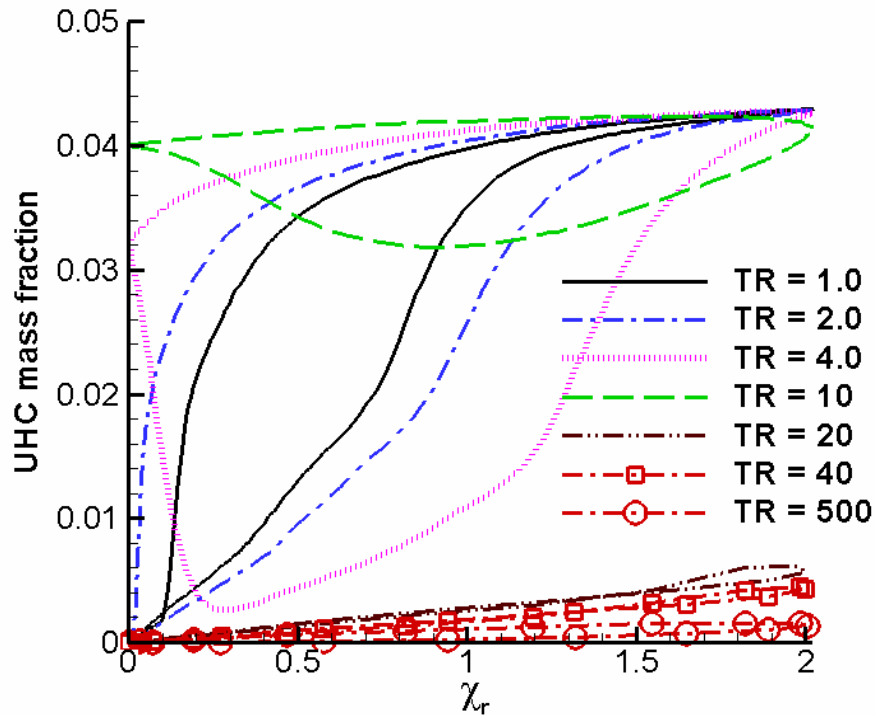
Figure 9.10. UHC mass fraction as a function of χ_r for different values of TR at $AR = 2.0$.

Figure 9.10 shows the limit cycle response of UHC mass fraction for various values of TR. It is interesting to note that the trends in UHC are opposite to those in NO. In particular, while UHC mass fractions are relatively low during reignition, we observe relatively large values during extinction. Moreover, UHC shows good recovery during extinction for all the cases with extinction/reignition (i.e. $TR = 1-4$), indicating faster response times and weaker temperature dependencies relative to NO. Hence, these trends indicate that benefits in flame stability and NO formation-control with extinction/reignition events may be offset by an associated increase in UHC levels.

Figure 9.11 shows the computed mean mass fractions of NO and UHC at Z_{st} during the limit cycle. The mean chemical heat release rate HRR (similar definition as Eq. (6.1)) is also shown in the figure on the right hand side axis. The

trade-off between NO and UHC is evident. Moreover, it is seen that the mean NO mass fraction is much more sensitive to TR in the extinction/reignition regime ($TR = 1-4$) in comparison to UHC. NO is completely suppressed in the extinction regime ($TR = 10$), beyond which we observe relatively large values in the absence of extinction.
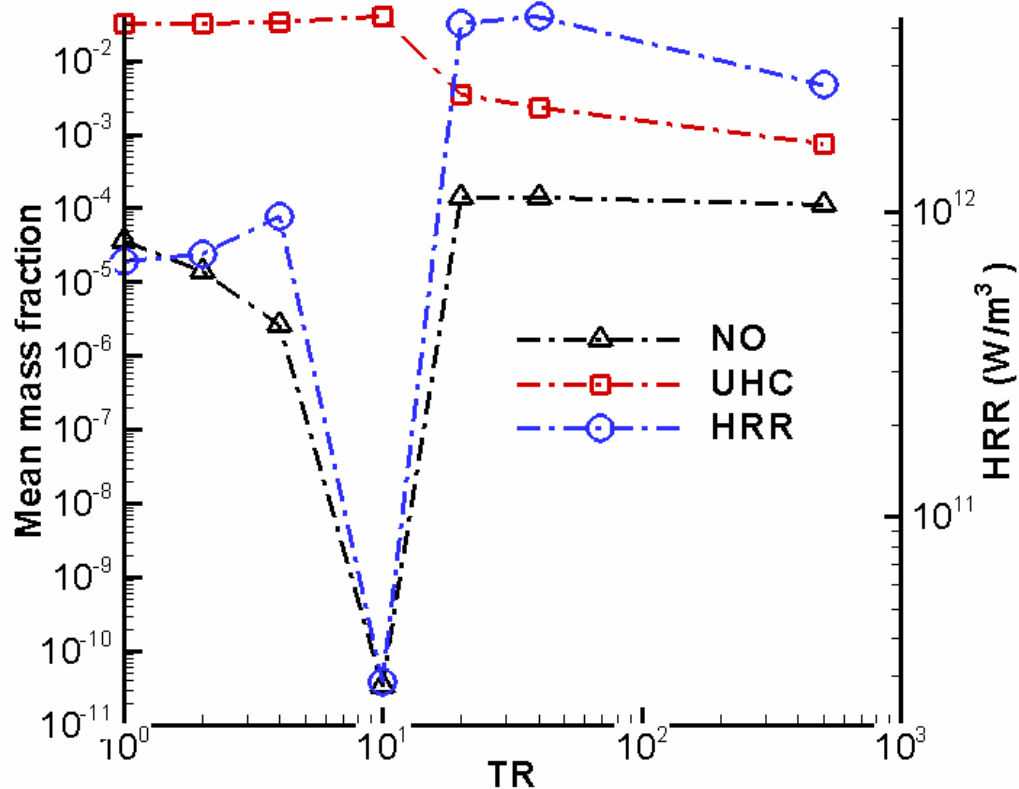
Figure 9.11. Mean mass fractions of NO and UHC, and the mean heat release rate HRR as a function of TR.

Notice in Fig. 9.11 that HRR shows a non-monotonic behavior, and it is interesting that the mean NO mass fraction decreases in the TR range of 1-4 in spite of an increase in HRR. This illustrates the role of slow chemical response times of NO, which are beneficial in the extinction/reignition regime. We can infer from Fig. 9.11 that temporary flame weakening events in the TR range of 10-20

may be beneficial in terms of both NO and UHC. Essentially, in this TR range, while the absence of extinction can control UHC, the peak temperatures during the limit cycle may be low enough (< 2000 K) to control NO formation.

While the observed trade-off between NO and UHC in the unsteady flames simulated here is an interesting result, it is useful to consider the practical relevance of these findings. Note that the unsteady flame response regimes being studied here are relevant to the near-field of the jet, where extinction/reignition phenomena may be prevalent. The UHC that result due to these extinction/reignition or extinction regimes are likely to burn out in downstream regions of the jet where relatively low scalar dissipation rates will be encountered. Likewise, relatively large amounts of NO may form in the high temperature regions at downstream jet locations. Moreover, as shown in Chapter 7, unsteady effects on the flame response are expected to diminish at downstream jet locations due to stronger flames and weaker turbulent eddies. Hence, we may encounter temporary flame weakening events due to lower values of TR (i.e. longer residence times) and AR (i.e. longer mixing times or lower mixing rates) at downstream regions in the jet. In these regions, we may observe similar trade-offs between NO and UHC, though the effects (such as the relative change in NO mass fraction with TR) may not be as significant as in the near-field. Note, however, that they may be applications, such as multiple or split injection strategies in direct-injection (DI) diesel combustion, where unsteady extinction/reignition events may be promoted even in downstream regions of the jet. For example, in multiple injection strategies, the residual burned gases from an earlier injection may interact (due to turbulent entrainment) with the reacting/non-reacting flamelets from the subsequent injection. Extinction may occur due to charge dilution and reduction in oxygen concentration, whereas reignition may be favored due to the high temperatures of the burned gases. In such scenarios, the response of pollutants to unsteady scalar dissipation rate time histories introduced by multiple injections may be of interest. Oscillatory perturbation studies similar to those considered here in the presence of residual

gases may provide useful insights. The recent work of Anders *et al.* (2008) explores the effects of residual gases on the extinction characteristics of vortex-perturbed flames, which is relevant for multiple injection scenarios.

In the section that follows, we will consider the influence of the imposed oscillation amplitude on the unsteady flame response.

9.3.3. Unsteady Flame-response: Influence of Amplitude
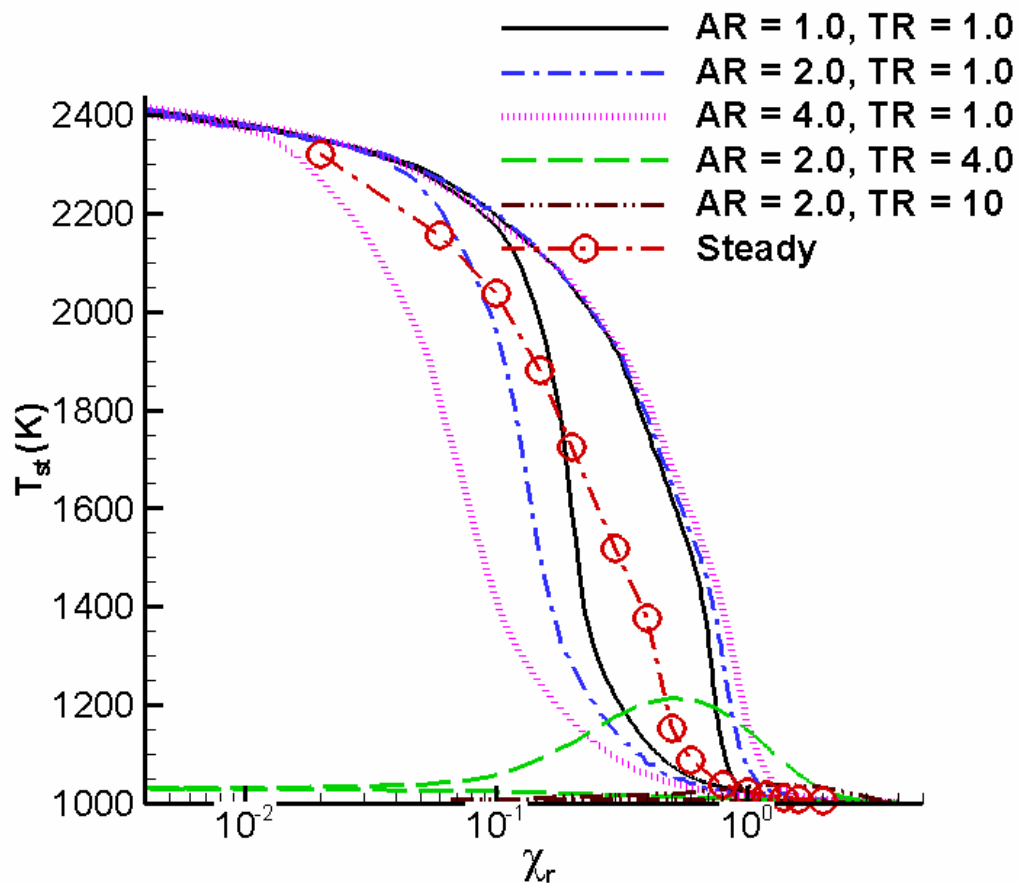
Figure 9.12. T_{st} (K) as a function of χ_r during the limit cycle for different values of AR and TR.

To investigate the influence of the oscillation amplitude, the amplitude ratio AR is varied in the range of 1.0-4.0. Figure 9.12 shows the limit cycle

response of T_{st} as a function of χ_r for different values of AR and TR. It is observed that for $TR = 1.0$, the phase lag to the imposed perturbation increases as AR increases from 1.0 to 4.0, which is indicated by the increasing roundness of the limit cycle curve. This phase lag arises from decreasing mixing times with increasing AR. Figure 9.12 shows that the deviations from steady behavior increase as AR increases. Moreover, at relatively large values of χ_r (~1), the unsteady flames for $AR = 2.0$ and 4.0 show higher temperatures in comparison to the flame for $AR = 1.0$. This indicates that flames subjected to higher amplitudes of oscillation are more resistant to extinction due to the increased response times (or unsteady effects).

Recall that we encountered similar trends in the flame-vortex studies discussed in Chapter 7, where the unsteady extinction limits were found to increase with increase in the vortex velocity-scale. Essentially, increasing the vortex velocity leads to higher scalar dissipation amplitudes, and is equivalent to increasing AR in the oscillatory flame studies. Furthermore, it is observed from Fig. 9.12 that for higher values of TR (= 4.0, 10), the extinguished flame fails to reignite for higher values of AR (=2.0). Hence, these trends indicate that the tendency for reignition via autoignition decreases with increasing AR (or amplitude) for a given value of TR (or frequency). Note, however, that based on the flame-vortex studies discussed in chapters 6 and 7, reignition may occur through edge flame interactions. As discussed before, this finding is also supported by the DNS studies of Sripakagorn *et al.* (2004) in reacting isotropic turbulence, where it was shown that reignition cannot occur without lateral interactions between extinguished and burning regions when the excursions of χ_{st} over χ_e are relatively large (i.e. $\chi_r \gg 1$ and $AR \gg 1$). Let us now consider the unsteady response of NO and UHC for different values of AR. The limit cycles for CO_2 and H_2O show trends similar to the temperature as in the case of TR-variation, and hence will not be shown here for brevity.
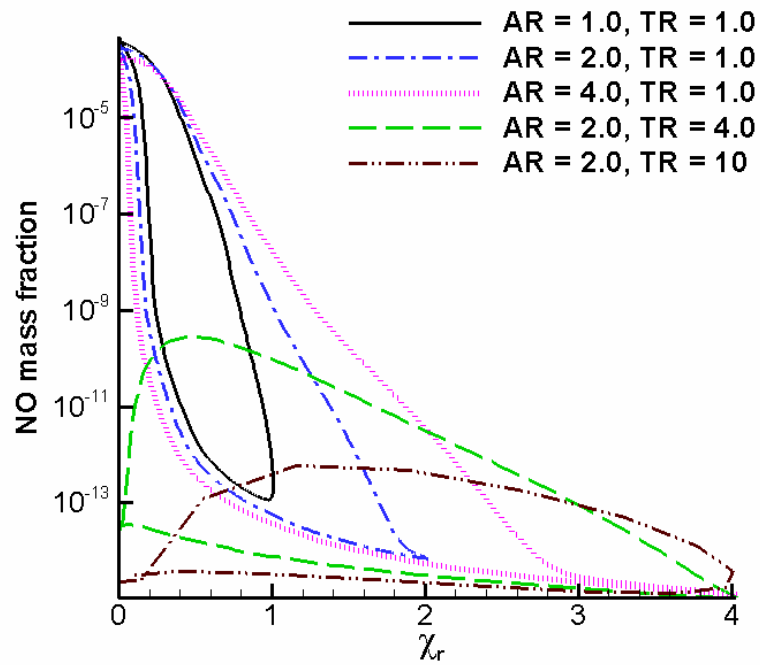
Figure 9.13. Limit cycle response of NO mass fraction for different values of AR and TR.
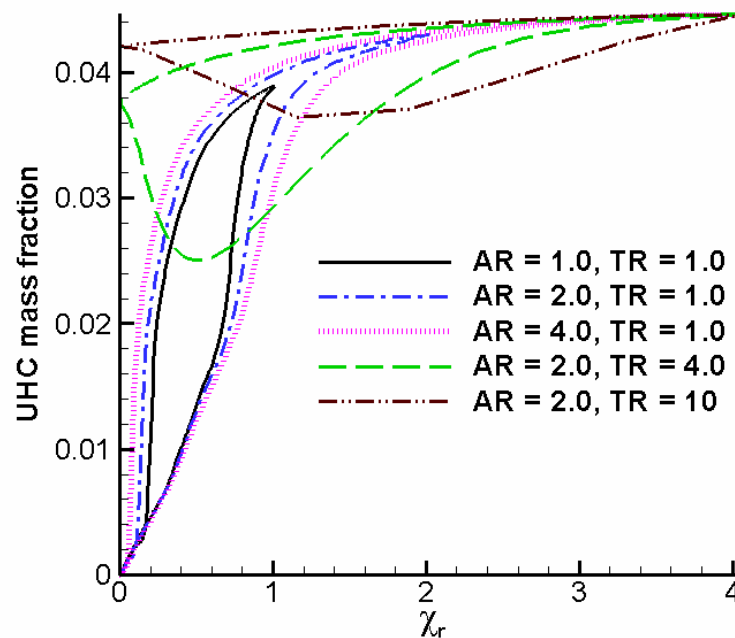
Figure 9.14. Limit cycle response of UHC mass fraction for different values of AR and TR.

Figures 9.13 and 9.14 show the limit cycle responses of NO and UHC mass fractions, respectively. A trade-off similar to that observed for variation in TR is observed here as well. In particular, while the peak NO mass fraction decreases with an increase in AR due to increased phase lag and lower peak temperatures, UHC mass fraction shows an increase due to decreasing tendencies for reignition. However, note that NO is much more sensitive than UHC due to slower response times. For instance, the peak NO mass fractions during the limit cycle decrease by about 25 % and 55 % as AR increases from 1.0 and 4.0, respectively, whereas the corresponding increase in peak UHC mass fraction is 10 % and 15 %. Hence, these numbers suggest that, as in the case of TR-variation, temporary flame weakening scenarios with lower values of AR (< 1.0) may be beneficial in terms of controlling both NO and UHC formation.
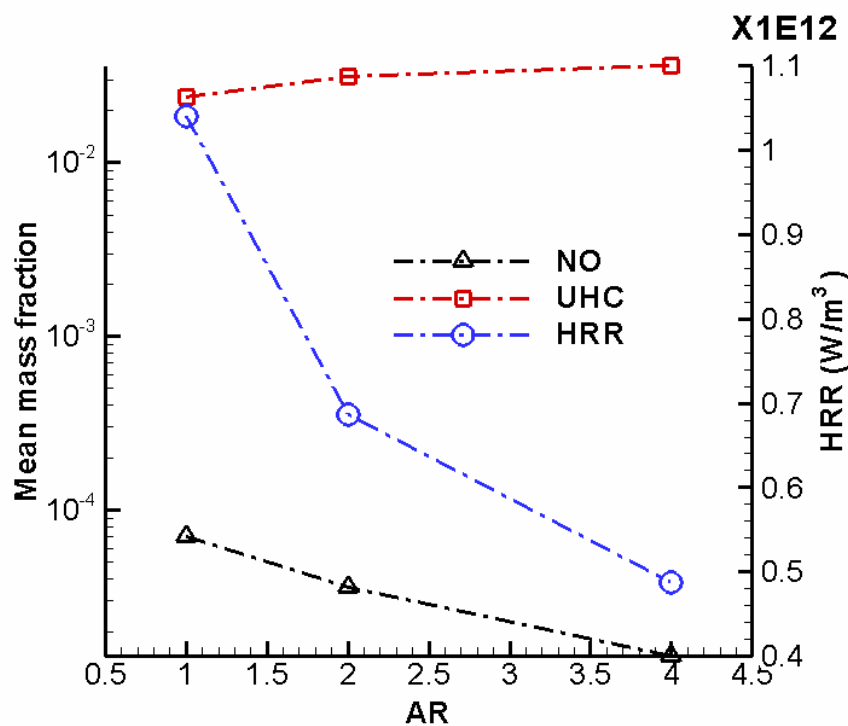
Figure 9.15. Mean mass fractions of NO and UHC, and the mean heat release rate HRR during the limit cycle as a function of AR for $TR = 1.0$.

Figure 9.15 confirms the trade-off between NO and UHC mass fractions for different values of AR for $TR = 1.0$. Note that the mean heat release rate HRR shows a monotonic decrease with increase in AR, due to increasing time scales for the extinction phase at the higher AR values. However, it is interesting that while HRR decreases by about 53 % from $AR = 1.0$ to $AR = 4.0$, the corresponding decrease in mean NO mass fraction is about 80 %, while UHC increases by about 50 %.

Before we proceed to the discussion of studies involving turbulent fluctuations of the scalar dissipation rate, it is useful to comment on other likely regimes of unsteady flame response than those discussed so far. In the oscillatory flame studies presented in this section, we considered a steady burning flamelet to begin with, which is then subjected to an oscillatory perturbation. However, another likely and relevant scenario in the near-field of the jet is that of a non-reacting diffusion layer (i.e. a non-reacting flamelet), which is subjected to unsteady scalar dissipation rates. Here, we will comment on the unsteady response of a flamelet that autoignites and extinguishes/reignites in the presence of an oscillatory flow perturbation.

Figure 9.16 shows the limit cycle response of T_{st} as a function of χ_r for various values of TR for $AR = 2.0$. For the cases shown in Fig. 9.16, we begin with a non-reacting flamelet under the influence of the oscillatory perturbation. We observe from the figure that for relatively low values of TR (1-4), the flamelet successfully autoignites, and then undergoes an extinction/reignition limit cycle. The increasing ignition delay times with increase in TR are indicative of the increased phase lag of T_{st} with respect to the imposed oscillation. For values greater than $TR = 10$, the flamelet fails to autoignite, and for relatively large frequencies ($TR = 40, 500$), the flamelet barely responds to the imposed perturbation. It is interesting to note from Figs. 9.16 (cold flow initial condition) and 9.5 (steady flame initial condition) that the range of TR values (1.0-4.0) in which extinction/reignition events are observed remains the same. This may be

attributed to the fact that in the present case with $T_{\text{fuel}} = T_{\text{a}} = 1000 \text{ K}$, the steady extinction limit (χ_{e}) and the steady ignition limit χ_{ig} are equal (see the S-curve response shown in Fig. 9.4, where there is no demarcation between extinction and ignition). Hence, for the chosen fuel and air temperatures, the autoigniting and the reigniting flamelets have the same characteristic time-scale (i.e. χ_{e}^{-1}), and the definition of TR based on χ_{e} (see Eq. (9.1)) remains valid for both the cold flow and steady flame conditions.
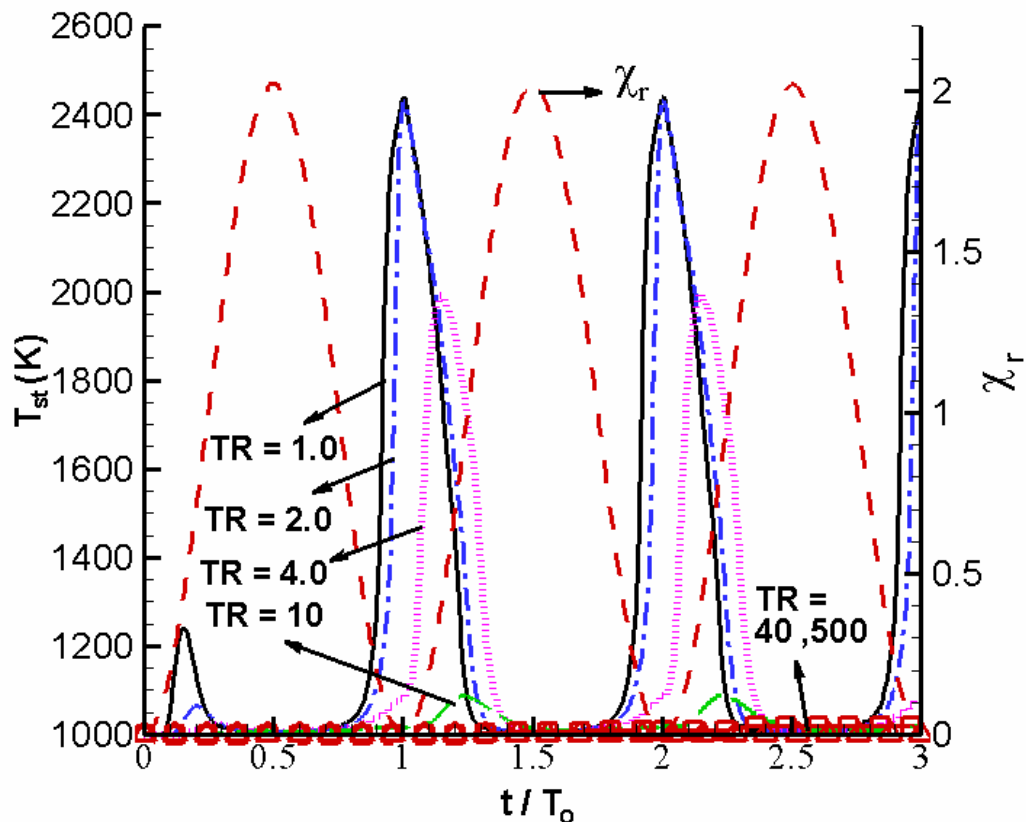
Figure 9.16. T_{st} (K) as a function of χ_{r} during the limit cycle for different values of TR for $AR = 2.0$ with cold flow initial conditions. The symbols shown for cases with $TR = 40$ and 500 are plotted only every 15th time-step for clarity.

Note that for lower fuel temperatures (~400 K) typical of diesel applications, the ignition is two-stage and the S-curve response would show two distinct limits, χ_e and χ_{ig} (Venugopal, 2005). Since $\chi_{ig} < \chi_e$, the autoigniting flamelet (which would respond with a time-scale of χ_{ig}^{-1}) may be associated with longer characteristic times than the reigniting flamelet (which would respond with a time-scale of χ_e^{-1}). This may lower the upper limit of TR (or the maximum frequency) for which extinction/reignition events would occur. Nevertheless, the correspondence between the cold flow and steady flame cases shows that the trends discussed so far with respect to variations in AR and TR are applicable to cold flow initial conditions as well. For instance, our recent studies (Venugopal and Abraham, 2008c) simulating the autoignition-extinction-reignition of an initially non-reacting flamelet subjected to oscillatory perturbations reveal similar trade-offs between NO and UHC response. However, note that for relatively large values of TR, while we observe a relatively insensitive burning flamelet for the steady flame initial condition, a relatively insensitive non-reacting flamelet is recovered for the cold flow initial condition.

It is important to note that while the oscillatory perturbation studies provide useful insights into the unsteady flame response, they only include the effects due to a single amplitude and frequency. In general, flamelets in a turbulent flowfield are subjected to turbulent fluctuations in the scalar dissipation rate, which include effects due to a spectrum of amplitudes and frequencies. In the next section, we will investigate the unsteady response of flamelets to turbulent fluctuations in the scalar dissipation rate generated from the analysis of the LES flowfield. These investigations will provide insights into the nature of unsteady flame-response, and regimes such as extinction and reignition in turbulent flowfields. As in Section 9.3, the validity of steady flamelet models for the prediction of the temperature and species responses will be assessed. In addition, by extrapolating the analysis to higher Reynolds number jets representative of those in diesel applications, we will indicate the implications of

the findings to phenomena such as flame lift-off, which are important for flame stabilization and pollutant formation.

9.4. Flame-response to Turbulent Fluctuations

In Section 9.2, we discussed the generation of Lagrangian time histories of the scalar dissipation rate from the unsteady LES flowfield. Ten representative flamelet histories originating from different axial locations are generated, which are shown in Figs 9.17 and 9.18.
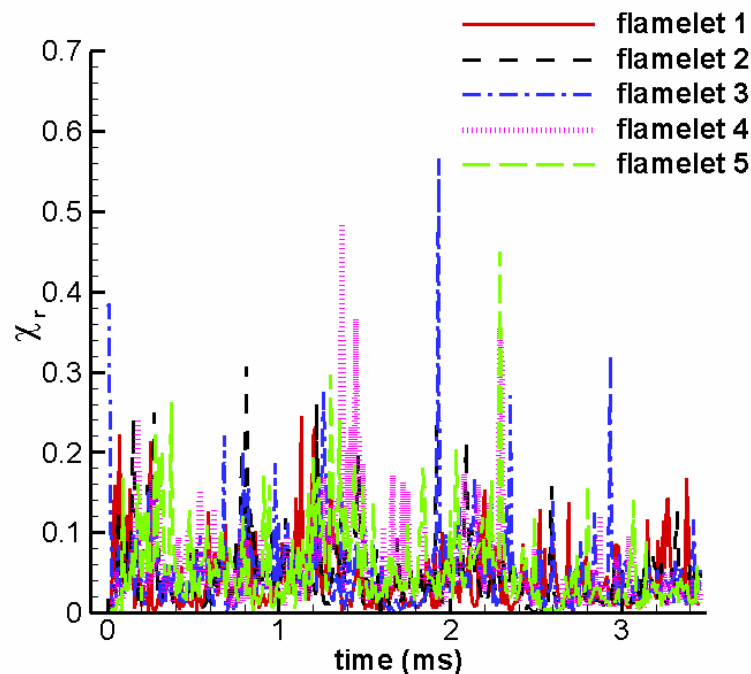
Figure 9.17. Lagrangian-type χ_r time histories of representative flamelets 1-5 from the unsteady LES flowfield.

Note that flamelets 1-10 are tracked across time and space using the stoichiometric isocontours originating from x/d = 6, 6.25, 6.5, 7.0, 7.25, 8.0, 8.5, 9.5, 10.5 and 11.0 in the jet, respectively. As indicated before in Section 9.2, the paths traversed by these flamelets span the region of the jet from x/d = 6 to x/d =20, and a time interval of about 3.5 ms (roughly 6 flow times). The time histories

depicted in Figs. 9.17 and 9.18 show that relatively large values of χ_r (> 0.3) are often followed by relatively small values (< 0.05). It is useful to characterize the generated histories in terms of a mean and RMS value (root-mean-square), which also determine the temporal PDF (probability density function).
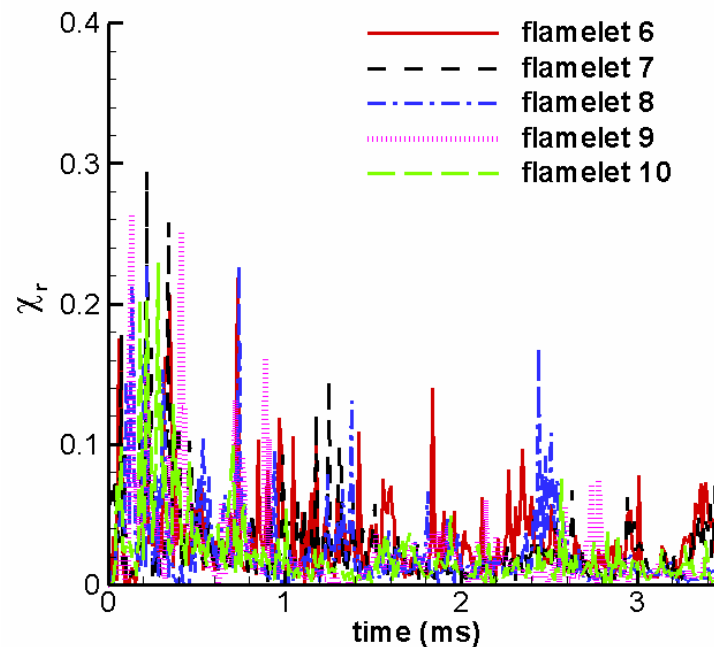
Figure 9.18. Lagrangian-type χ_r time histories of representative flamelets 6-10 from the unsteady LES flowfield.

Figure 9.19 shows the computed mean and RMS of the 10 flamelet histories. It is interesting to note that the mean values are relatively small (< $0.06\,\chi_e$), since the relatively large values of χ_r are short-lived in all the cases. Furthermore, Fig. 9.19 shows that the mean initially increases as we proceed from the flamelet originating at x/d = 6 (flamelet 1) to the one originating at x/d = 7.25 (flamelet 5), but decreases thereafter for the downstream flamelets. The RMS value more or less shows similar trends as the mean. Note that while increasing the mean values would increase the peaks that may lead to flame extinction/flame weakening, increasing the RMS values would decrease the

minimum values of χ_{st} (in addition to increasing the peaks) that may favor reignition/flame recovery. In addition, the time records shown in Figs. 9.17 and 9.18 have been obtained from the unsteady LES data collected every 0.01 ms. Hence, it is possible that some of the additional peaks of χ_r have not been captured in the flamelet histories. However, such peaks would also be short-lived, and may not significantly influence the flame-response. We will now characterize the flame-response to the flamelet histories.
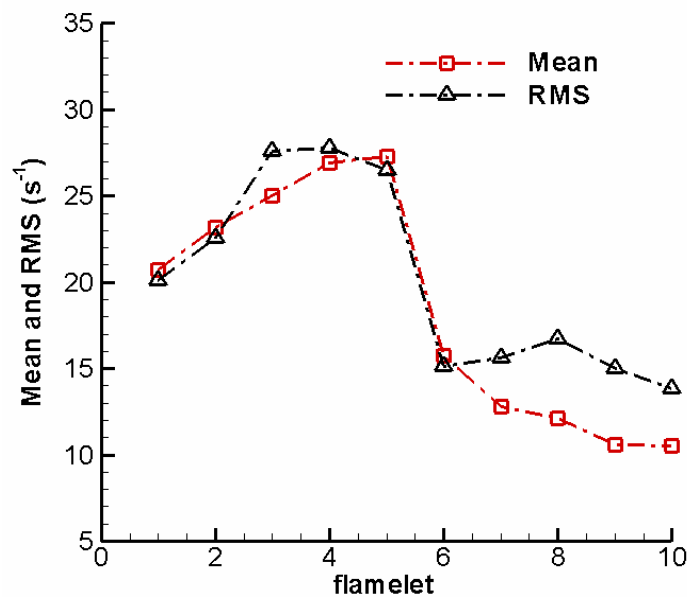
Figure 9.19. Means and RMS values of the generated flamelet histories.

Let us consider the flame-response to flamelet histories 3 and 5. While flamelet 5 has the maximum mean of the 10 flamelet histories considered, flamelet 3 (along with flamelet 4) has the maximum variance of the scalar dissipation rate (see Fig. 9.19). Figures 9.20 and 9.21 show the unsteady temperature (T_{st}) response to flamelet histories 3 and 5, respectively. In both figures, predictions using a steady flamelet library are also shown for comparison. The steady flamelet library was constructed using steady solutions

corresponding to 21 values of χ_{st} in the range of $(0.002 - 4.0)\chi_e$. Interpolation based on χ_{st} from the turbulent time record is then employed to obtain the temperature and species response corresponding to the steady flamelet. Note that for the unsteady cases, the initial condition is the steady flamelet solution corresponding to the initial value of χ_{st} in the time record.
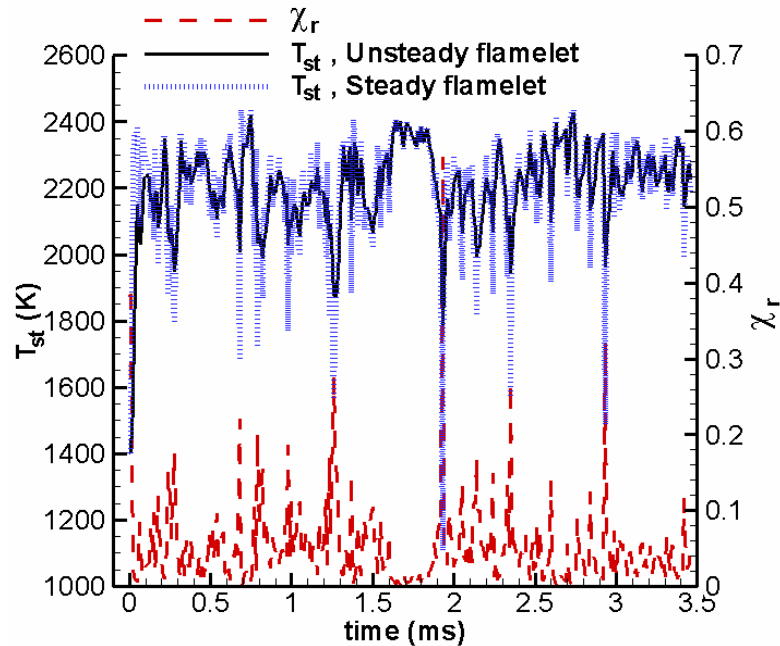
Figure 9.20. T_{st} (K) response to flamelet-history 3 using unsteady and steady flamelet calculations.

The unsteady flame-response to flamelet histories 3 and 5 involves temporary flame weakening events at relatively large values of χ_r (> 0.3) followed by rapid flame recovery at relatively small values of χ_r. We observe from Figs. 9.20 and 9.21 that the peak T_{st} values predicted by both unsteady and steady flamelet calculations agree reasonably well. However, for both flamelet histories, the steady flamelet model does not describe the transient flame weakening and recovery well. For instance, from Fig. 9.20, T_{st} at the maximum value of χ_r (~ 0.6) at about 1.93 ms is underpredicted by about 38 % by the steady flamelet model

in comparison to the unsteady flamelet model. Such discrepancies can have important implications for relatively sensitive species such as NO.
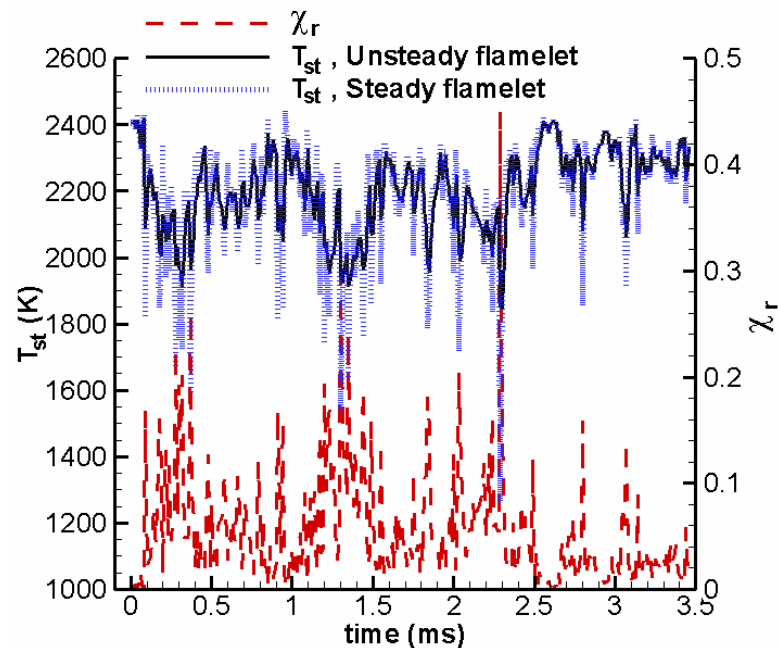
Figure 9.21. T_{st} (K) response to flamelet-history 5 using unsteady and steady flamelet calculations.

To correlate the trends observed here with those in the oscillatory perturbation studies, it is useful to interpret the turbulent time records shown in Figs. 9.17 and 9.18 as superpositions of a set of amplitudes and frequencies, For instance, consider Fig. 9.22, which shows the flamelet histories 3 and 5 on a AR-TR diagram. The AR and TR values are obtained by computing the power-spectral-densities (PSDs) of the turbulent time records, and then appropriately scaling the amplitudes and frequencies with χ_e. We observe from Fig. 9.22 that relatively large values of AR ($\sim 0.3\chi_e$) occur only at relatively low frequencies ($TR < 10$). Hence, in the time interval of about 3.5 ms considered, these relatively large amplitudes do not occur frequently enough to significantly affect the flame structure. As seen from Figs. 9.20 and 9.21, these peaks only cause temporary flame weakening events, following which the flame recovers due to relatively low

scalar dissipation rates. It is interesting to note that based on the estimated values of l_r (> 4.0) and u_{fv} (< 3.0) at farther radial locations (r/d > 2.0) in the jet near-field, the flame-vortex interaction studies indicated rollup and straining as probable regimes of localized flame dynamics, rather than extinction/reignition. In the context of the flamelet formulation, the rollup and straining caused by the turbulent eddies manifest as relatively low values of χ_r (< 1.0), which cause temporary flame weakening/recovery. Moreover, in agreement with trends observed in the oscillatory perturbation studies (see Fig. 9.5 for instance), the steady flamelet model fails to account for phase lag effects at relatively large values of χ_r (> 0.3). In Section 9.5, we will use a AR-TR diagram similar to that shown in Fig. 9.22 to represent different regimes of unsteady flame response, and to infer expected outcomes for flames subjected to turbulent fluctuations. Let us now consider the unsteady response of pollutants like NO and UHC. Responses of major species such as CO_2 and H_2O showed trends similar to those in the temperature.
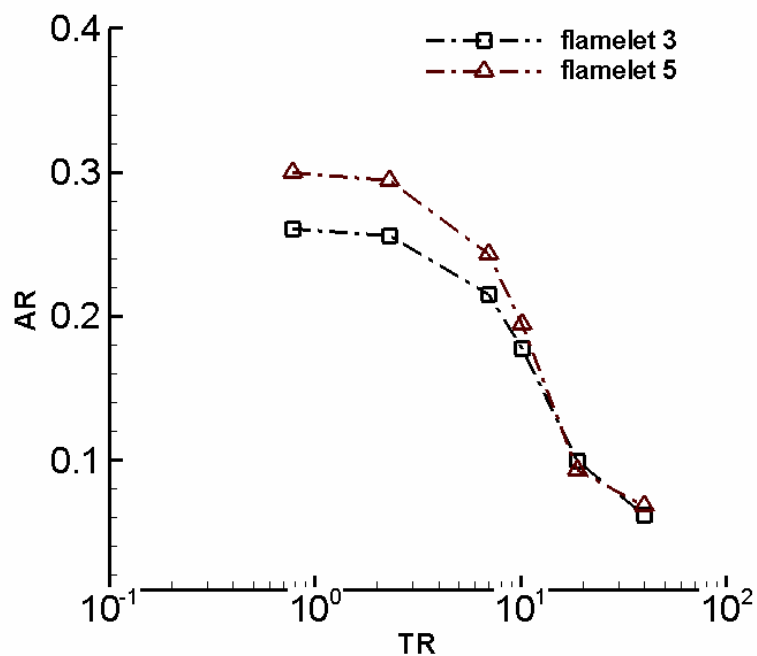
Figure 9.22. AR-TR diagram corresponding to flamelet histories 3 and 5 for the 70,000-Re jet.
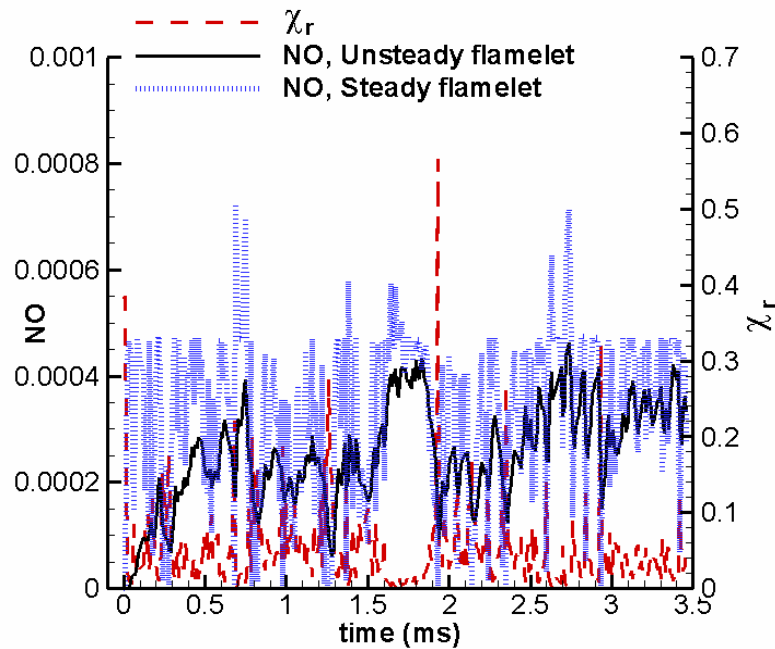
Figure 9.23. Unsteady response of NO to flamelet-history 3 using unsteady and steady flamelet models.

Figures 9.23 and 9.24 show the responses of NO and UHC to flamelet-history 3. NO response shows significant differences between steady and unsteady flamelet predictions. Note that in the case of flamelet-history 3, we begin with a relatively large value of χ_r (~ 0.38), and hence the initial NO mass fraction is negligibly small due to the associated low temperatures (~ 1400 K). Following the rapid decrease in χ_r, the steady flamelet model predicts an immediate increase in NO mass fraction, whereas the unsteady flamelet calculation predicts a delayed response due to the relatively slow response times of NO. Consequently, the steady flamelet overpredicts peak values during the unsteady response by as much as 1.5-2 times in comparison to the unsteady flamelet calculations. Hence, even for the relatively small excursions of χ_{st} above χ_e (i.e. $\chi_r < 1.0$) considered here, steady flamelet models are inadequate to predict NO response. On the other hand, UHC shows much faster response to

χ_{st} fluctuations as seen from Fig. 9.24, in qualitative agreement with the trends reported in the oscillatory perturbation studies. The steady flamelet model significantly overpredicts UHC values at larger values of χ_r (> 0.3), but due to fast response times, the UHC mass fractions relax to values closer to steady values at the lower values of χ_r. Moreover, note that majority of the values of UHC mass fraction are relatively low (< 0.005) due to the absence of extinction and the associated high temperatures.
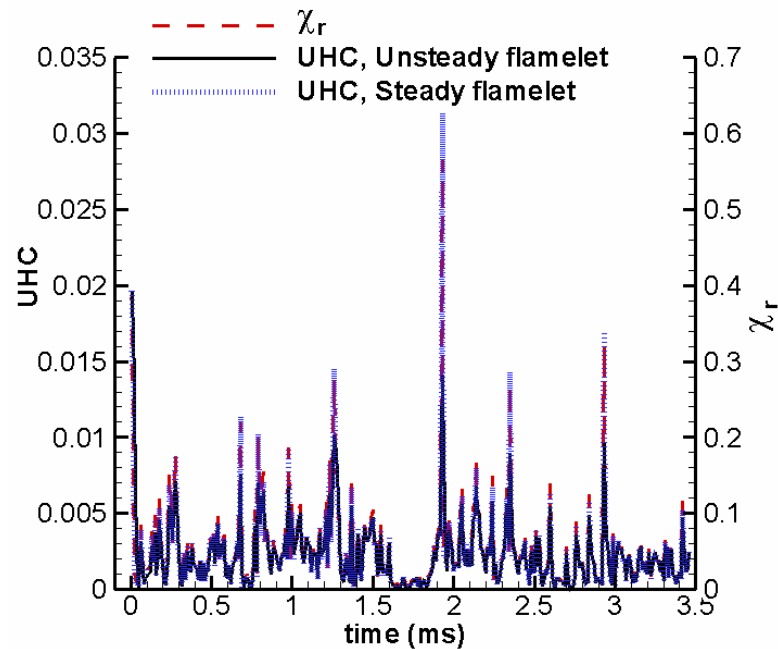
Figure 9.24. Unsteady response of UHC to flamelet-history 3 using unsteady and steady flamelet models.

In engineering applications, it is often useful to estimate mean values, and hence it is of interest to compare the estimated mean values of temperature and species mass fractions from steady and unsteady flamelet models. Based on the trends observed for flamelet-history 3, it is expected that the steady flamelet model would yield means reasonably close to that from the unsteady flamelet, since the relatively large values of χ_r (which lead to discrepancies between the two models) occur with low probability. This is confirmed in Table 9.1, which

shows the computed mean values of temperature, and mass fractions of CO_2, NO and UHC from steady and unsteady flamelet models for flamelet-history 3. We observe that except for NO, the mean values for all the other variables agree within 5 % between the two models.

Table 9.1 Computed mean values from flamelet-history 3

Mean	Unsteady	Steady	% difference(with respect to unsteady)
T_{st} (K)	2.21E+03	2.22E+03	0.8
CO_2	9.62E-02	9.73E-02	1.14
NO	2.53E-04	3.35E-04	32.41
UHC	2.34E-03	2.45E-03	4.7

Recall that in the oscillatory perturbation studies discussed in the previous section, we showed that temperature predictions with steady flamelet models significantly deviate from those with unsteady flamelets even (see Figs. 9.5 and 9.12 for the response of temperature) at relatively large values of χ_r (~ 0.3). However, it is important to note that in the case of the oscillatory perturbation studies, both high and low values of χ_r occur with the same frequency in the simulated time interval of 3 time periods. Hence, the large values of χ_r have a significant effect on the flame structure, and steady flamelet models failed to capture the associated phase lag effects (see Fig. 9.12). In the turbulent cases, as discussed before in the context of Fig. 9.22, the relatively large values of χ_r are immediately followed by relatively low values (see Figs. 9.17 and 9.18), and do not occur frequently enough in the simulated time interval of about 3.5 ms. Hence, deviations between the steady and unsteady flamelet models at these peak values of χ_r do not significantly affect the mean values of temperature and species mass fractions. However, in agreement with the trends reported in the oscillatory perturbation studies, the instantaneous temperatures at large values of χ_r are not predicted well with steady flamelet models.

In addition, we can represent the unsteady flame response to the scalar dissipation rate histories as a temporal distribution across the jet flowfield. Figure 9.24 shows such a distribution, where 5 of the temperature (T_{st}) time histories are plotted as a function of the axial locations traversed by the flamelets in the simulated time interval of about 3.5 ms. Hence, the fluctuations at a given axial location represent temporal fluctuations. We observe temporary flame weakening events predominantly at upstream axial locations (x/d <15). Furthermore, it is useful from a modeling perspective to compute the (temporal) mean temperature at different axial locations from the flamelet histories, and compare the predictions from unsteady and steady flamelet models.
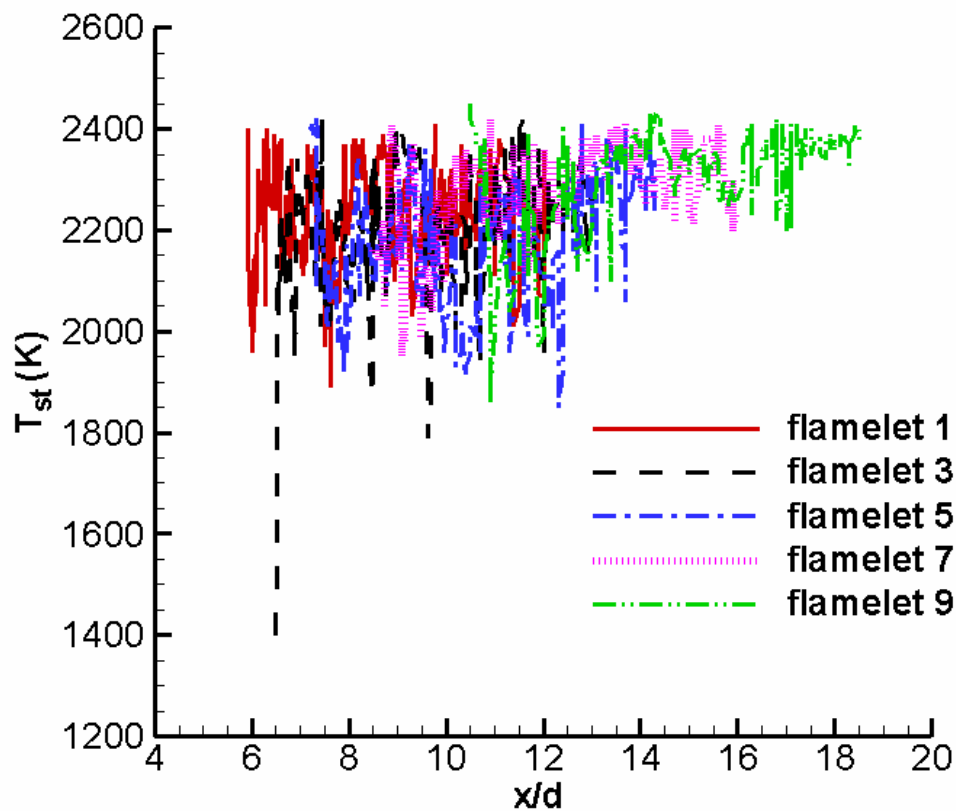
Figure 9.25. Lagrangian-type temperature time histories from unsteady flamelet calculations represented as a function of axial location in the jet. Only 5 flamelets are shown for clarity.

Figures 9.26 and 9.27 show the mean T_{st} and NO mass fraction values computed from the flamelet histories using unsteady and steady flamelet calculations. As in the case of flamelet-history 3, the agreement between the models with respect to mean T_{st} is within 5%. Hence, the relatively small differences between the two models even at upstream jet locations confirm the low probability of events with relatively large values of χ_{st}, which do not significantly affect the mean. Note that since all the tracked flamelets do not penetrate to the downstream jet locations (x/d = 17 and 18 for instance), the number of flamelet histories over which averaging is performed decreases at these locations. However, since we predominantly encounter lower values and lower intensity fluctuations of χ_{st} at downstream regions, the estimates of the mean temperatures and species mass fractions may be reasonable.
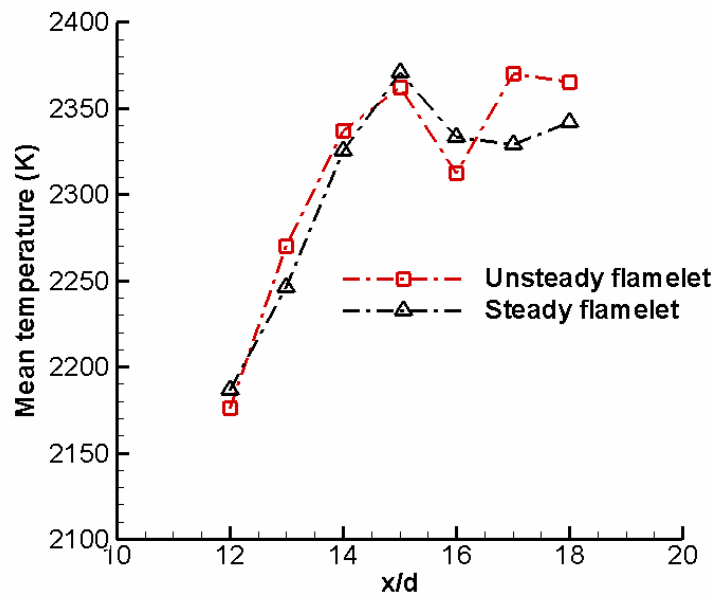
Figure 9.26. Mean T_{st} (K) computed from the flamelet histories as a function of axial location in the jet.

The differences are greater (up to 20 % at x/d = 12) with respect to NO due to relatively high temperature sensitivity and phase lag effects (see Fig. 9.27), but the predictions from both the models agree reasonably well. Hence, in the present case, steady flamelet models are adequate for the prediction of mean temperature and major species, and reasonable for the prediction of the mean concentration of pollutants like NO. This is a useful result from a modeling perspective, since steady flamelets are easier to implement as a reacting LES sub-model compared to unsteady flamelets, and do not require the use of a additional tracking scalar, such as the progress variable, to capture the time coordinate, and therefore computationally more efficient.
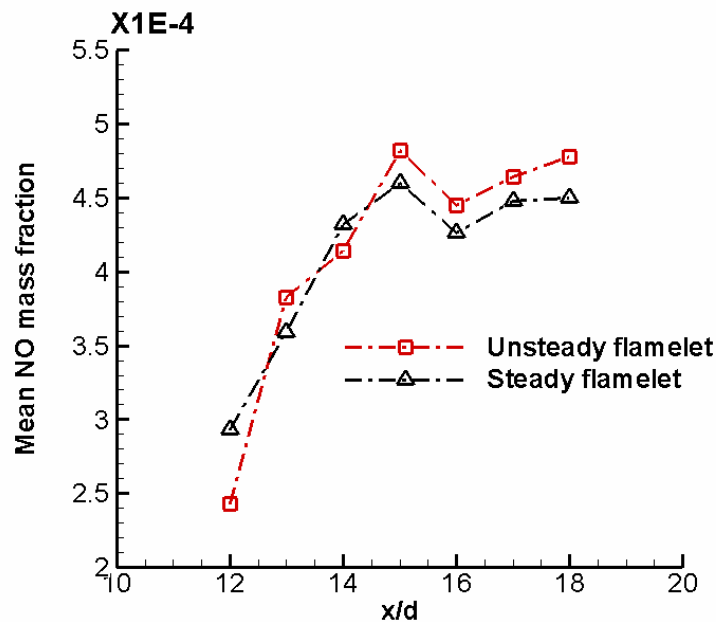
Figure 9.27. Mean NO mass fraction computed from the flamelet histories as a function of axial location in the jet.

It is important to note that while the results discussed so far are useful to understand unsteady flame response in turbulent flowfields, and the applicability of steady flamelet models, the predicted temperatures and spatial distributions (for instance, Figs. 9.25-9.27) may differ in a reacting LES computation. In the present case, the scalar dissipation rate time histories are generated from a non-

reacting jet flowfield, and do not include the feedback effects due to combustion heat-release. In Chapter 11 on the directions for future work, we will identify future work to clarify the effects of heat release on scalar dissipation rates. In addition, the flamelet histories generated here correspond to the unsteady near-field of a 70,000-Re jet. Even though this Re is comparable to that in a diesel jet, the injection velocity (U_{inj}) may be more than an order of magnitude higher, and the orifice diameter (d) may be an order of magnitude smaller. This implies that the global strain rate (=U_{inj}/d), which is an appropriate scaling parameter for the scalar dissipation rate, would be one to two orders of magnitude higher in a diesel jet. In the present case, however, we consider a moderate increase, by a factor of 5, to demonstrate the influence of stronger fluctuations of the scalar dissipation rate on the unsteady flame response.
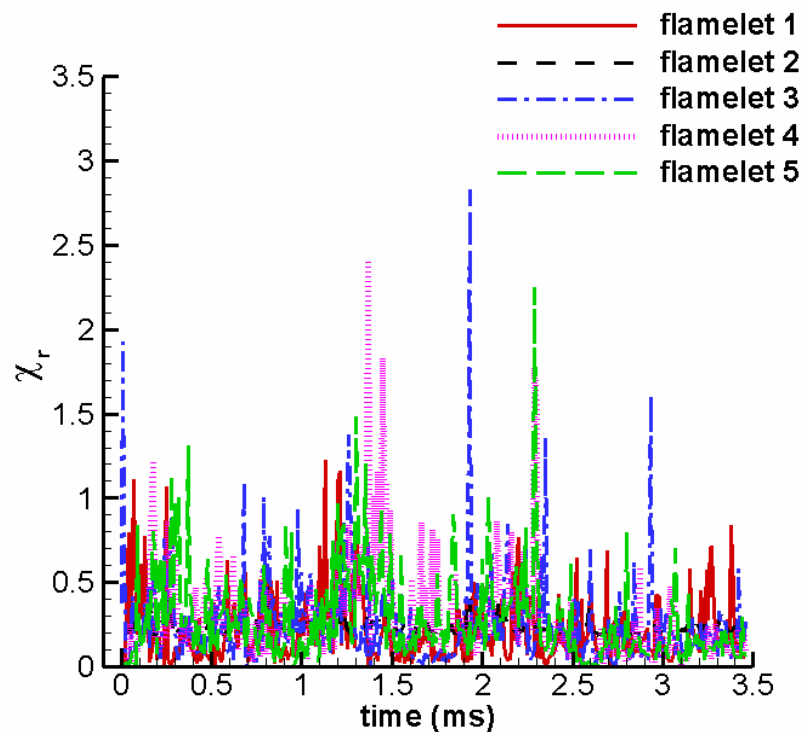
Figure 9.28. Lagrangian-type χ_{r} time histories for 5 representative flamelets corresponding to a higher Reynolds number jet.

For instance, let us consider a jet with $U'_{\text{inj}} = \sqrt{5}U_{\text{inj}}$, and $d' = d/\sqrt{5}$, so that the inlet jet momentum and jet-Re remains constant, but global strain rates increase by a factor of 5. It can be shown from theoretical deductions (Abraham, 1996) that the *mean velocity-field remains unaffected* due to compensatory changes in U_{inj} and d. Here, we will further assume that the instantaneous velocity-field is minimally affected as well. Hence, the flamelet histories obtained using the velocity-field of the present 70,000-Re jet (see Figs. 9.17 and 9.18) can be employed by simply scaling the χ_r values by a factor of 5. However, this scaling assumes that the cumulative-distribution-function (CDF) of the fluctuating time records shown in Figs. 9.17 and 9.18 does not change when U_{inj}/d is increased by a factor of 5. Note that when χ_r values are increased by a factor of 5, both the mean (μ) and the RMS (σ) are increased 5 times. Figure 9.28 shows 5 flamelet time histories with higher means and RMS values. It is observed that for the time records shown, there are repeated excursions of χ_r above unity (i.e. $\chi_{\text{st}} > \chi_e$), which could lead to local extinction in the jet. When χ_r values are increased 5 times, the maximum value of the mean among the 10 flamelet histories considered is about $0.3\chi_e$. Let us now explore the unsteady temperature and species responses for the flamelet histories shown in Fig. 9.28.

Figure 9.29 shows the T_{st} response to flamelet-history 3 when μ and σ are increased 5 times. In this case, the unsteady flame approaches local extinction, indicated by the relatively low temperatures (< 1400 K) at the larger values of χ_r (> 1.0). However, as discussed before in the flame-vortex studies (Section 6.3) and the oscillatory perturbation studies (Section 9.3), the unsteady flame is more resistant to extinction due to phase lag effects, and does not reach frozen flow even at the maximum χ_r value of about 3, as shown in Fig. 9.29. In general, we observe much greater deviations between the steady and unsteady flamelet predictions in this case as compared to the case with a lower mean and

variance (compare Figs. 9.20 and 9.29). It is expected that these deviations will have a significant impact on the NO response.
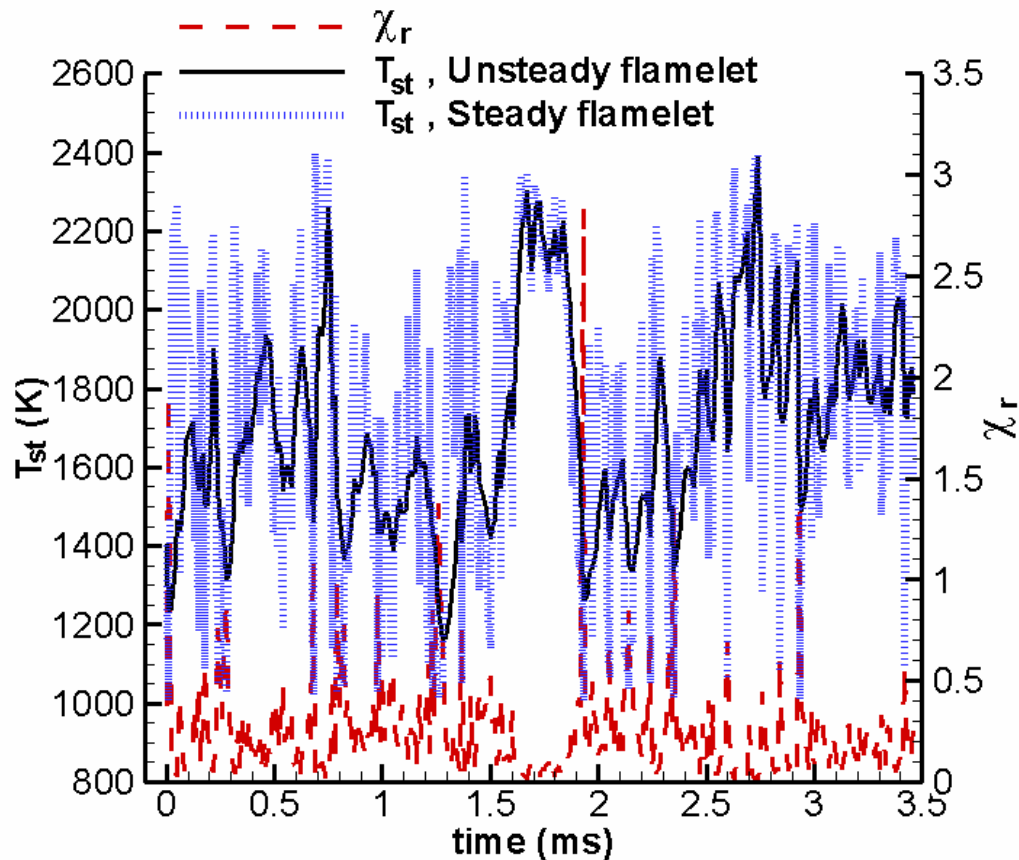
Figure 9.29. T_{st} (K) response to flamelet-history 3 with higher μ and σ using unsteady and steady flamelet calculations.

The unsteady response of NO mass fraction to the higher intensity fluctuations is shown in Fig. 9.30. NO formation is significantly suppressed due to local extinction events, which occur with a higher probability in this case (see Fig. 9.29). Furthermore, due to relatively slow response times, NO fails to recover even during the reignition events, as in the case of oscillatory perturbation studies with relatively large values of AR (see Fig. 9.13 for instance). Hence, unsteady extinction/reignition events are beneficial in terms of flame stability and NO formation-control. Moreover, as expected, the steady flamelet model grossly

overpredicts NO mass fractions at several instants due to its inherent inability to account for transient extinction/reignition and the associated phase lag effects.
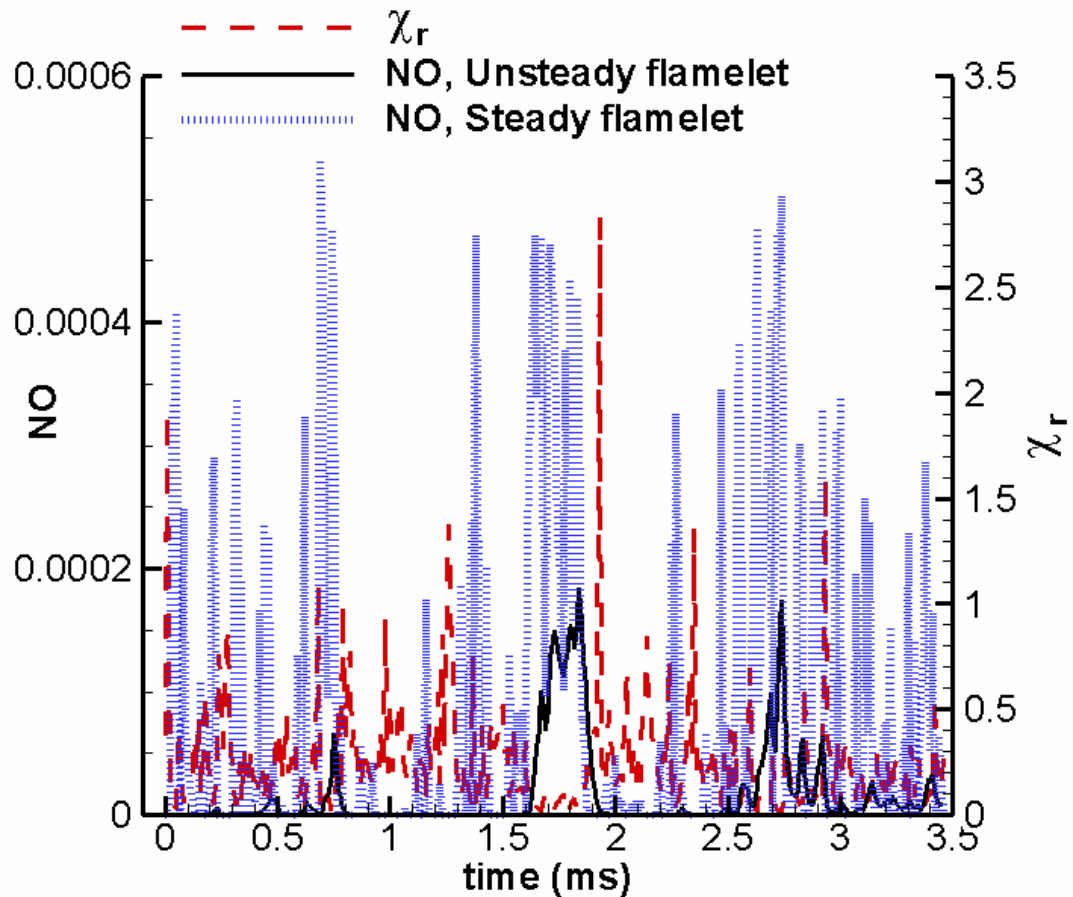
Figure 9.30. NO mass fraction response to flamelet-history 3 with higher μ and σ using unsteady and steady flamelet calculations.

Figure 9.31 shows the UHC mass fraction response to the flamelet-history 3 with a higher mean and RMS value. The trade-off between NO and UHC reported earlier for the oscillatory perturbation studies is evident, with significant levels of UHC forming during extinction events. The steady flamelet model performs relatively better in the case of UHC due to faster chemical response times. However, notice that the peak values during the unsteady response are overestimated by the steady flamelet by as much as 33 %.

Table 9.2 shows the computed mean values of temperature (T_{st}), and mass fractions of CO_2, NO and UHC during the unsteady flame response to flamelet-history 3 with the higher mean and RMS values. We observe good agreement (within 5 %) between the unsteady and steady flamelet models with respect to the temperature, as in the case with lower intensity fluctuations (see Table 9.1). As seen from Fig. 9.29, this is attributed to the fact that while the steady flamelet model significantly underpredicts the minimum temperatures (essentially frozen flow is predicted for values of $\chi_r > 1.0$), it overpredicts the maximum temperatures during reignition as well due to rapid flame recovery (i.e. no phase lag effects). Hence, the effects are compensatory and the mean values are minimally affected.
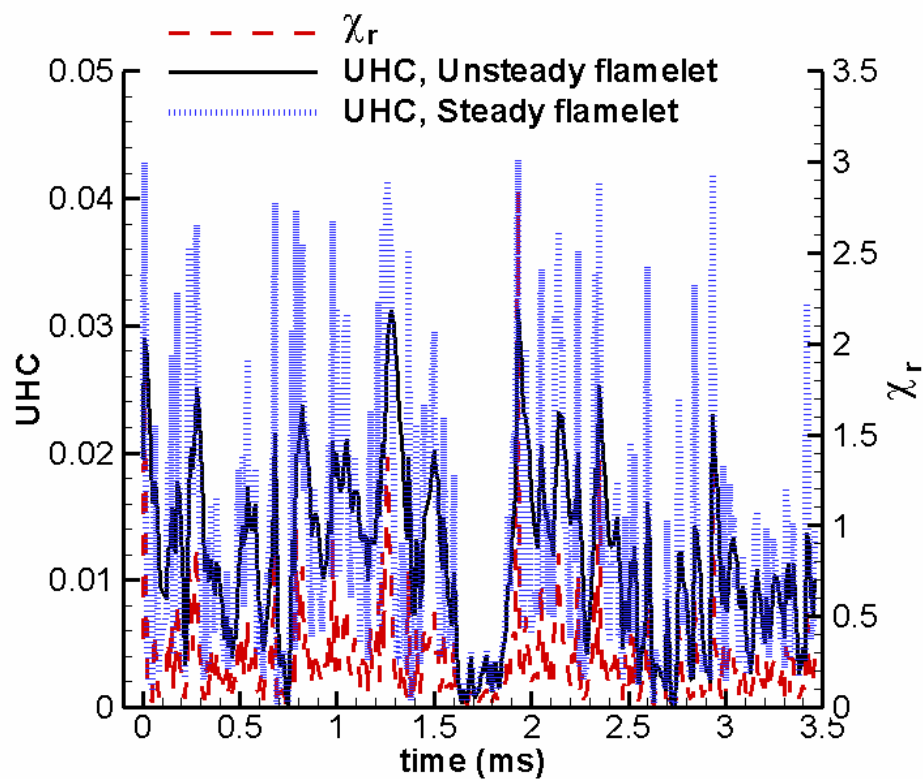
Figure 9.31. UHC mass fraction response to flamelet-history 3 with higher μ and σ using unsteady and steady flamelet calculations.

However, the agreement with respect to the mean temperature does not imply that steady flamelets are adequate, as the instantaneous temperature fluctuations have a strong impact on species like NO, which is evident in the large discrepancy shown in Table 9.2 between the two models. In fact, even mean CO_2 mass fraction is overestimated by about 27 % by the steady flamelet model. It is interesting, however, that the predicted mean UHC mass fractions agree very well between the two models, indicating factors similar to that for the temperature, i.e. strong crests and troughs with the steady flamelet model (this is evident in Fig. 9.31) that result in a mean close to that with the unsteady flamelet model. Now, we will explore the Lagrangian-type temperature time histories across the jet flowfield, and then the mean axial temperature and NO profiles in the jet. We will also discuss implications of the observed results for phenomena such as flame lift-off.

Table 9.2 Computed mean values from flamelet-history 3 with higher μ and σ

Mean	Unsteady	Steady	% difference(wrt unsteady)
T_{st}(K)	1.70E+03	1.75E+03	3.19
CO_2	3.69E-02	4.67E-02	26.60
NO	1.63E-05	8.47E-05	418.69
UHC	1.19E-02	1.20E-02	0.34

Figure 9.32 shows 5 Lagrangian time histories of T_{st} represented as a function of axial location in the jet from unsteady flamelet computations employing higher intensity fluctuations of the scalar dissipation rate. We observe local extinction events at upstream axial locations, and temporary flame weakening events beyond x/d = 14. For the flamelet histories shown, reignition events are also observed at the upstream locations, indicating that the mean temperature would represent the net effects due to extinction and reignition events. We can then think of flame lift-off height as the location where there is

predominantly extinction and very less reignition, so that the mean flame would remain extinguished.
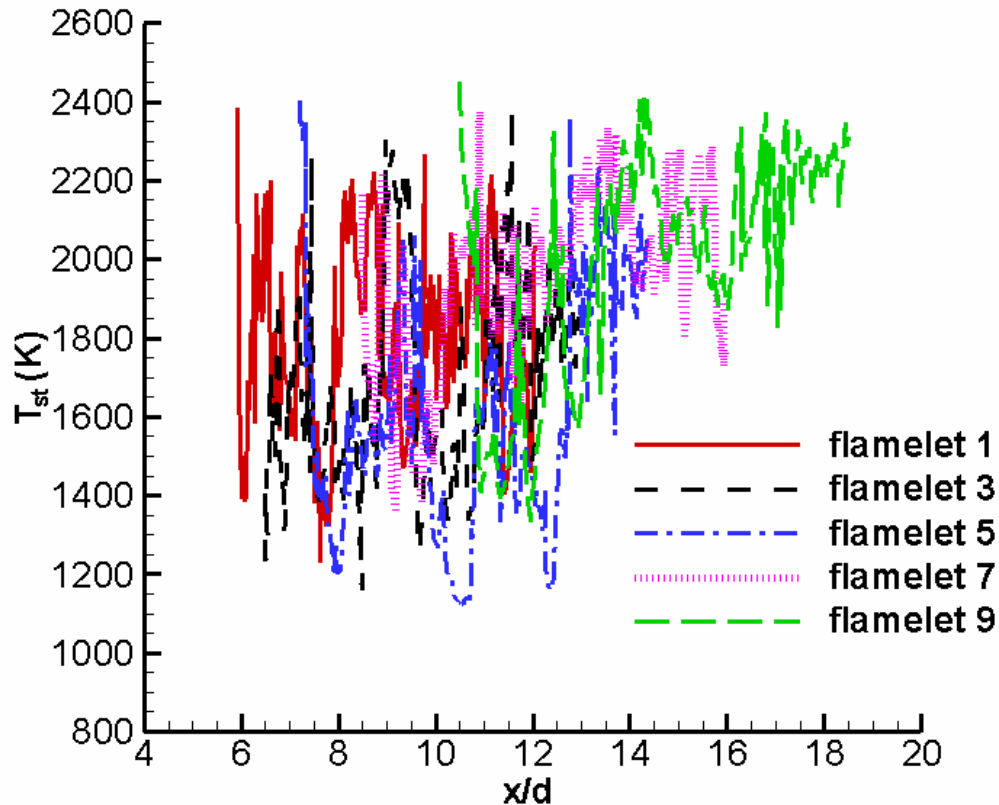
Figure 9.32. Lagrangian-type temperature time histories from unsteady flamelet calculations corresponding to higher intensity fluctuations represented as a function of axial location in the jet. Only 5 flamelets are shown for clarity.

Figure 9.33 shows the computed mean temperature (T_{st}) from the 10 flamelet histories with higher intensity fluctuations as a function of axial location in the jet. Note that in addition to the predictions with unsteady and steady flamelet models, Fig. 9.33 shows the predictions using a *steady-flamelet-steady strain* (SFSS) model. Essentially, the SFSS prediction corresponds to the steady flamelet solution at the mean (or steady) value of the scalar dissipation rate at each axial location. In other words, the SFSS model results are similar to what

one may obtain from a RANS simulation employing a steady flamelet model, where fluctuations are not taken into account. However, note that the (temporal) mean value of χ_{st} at each axial location is estimated using the time histories generated from LES. Hence, in using this analogy between the SFSS model and RANS results, we are making the implicit assumption that the mean value of χ_{st} is the same, regardless of whether it is computed using RANS or LES. Though this is true in principle, the mean values from RANS and LES may differ depending on factors such as the choice of subgrid-scale models, and the selected numerical resolution and filter characteristics in LES. Nevertheless, the analogy between SFSS and RANS is invoked here to merely explore the importance of accounting for fluctuations of χ_{st}.
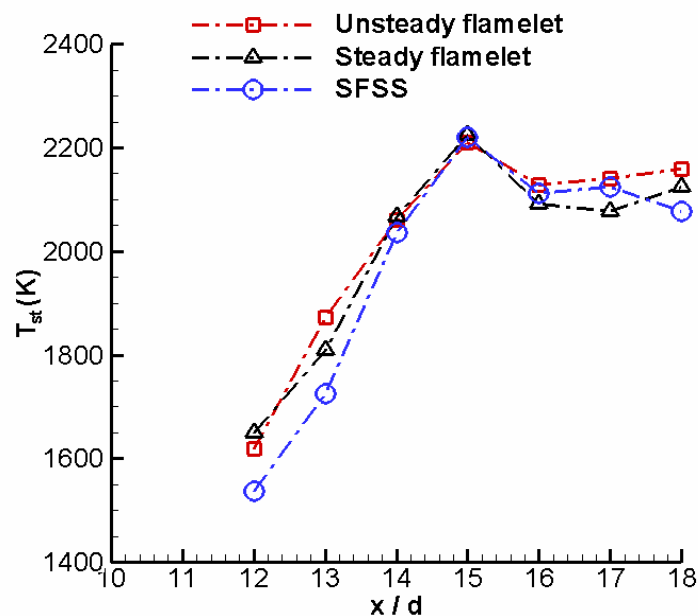
Figure 9.33. Mean T_{st} (K) computed from the flamelet histories with higher intensity fluctuations as a function of axial location in the jet.

We observe from Fig. 9.33 that the predictions from the three models agree within 8 % across the jet near-field region shown, indicating that the mean

values are not significantly affected due to instantaneous excursions of χ_{st} above and below χ_e. In jets with even higher global strain rates, we may observe lower temperatures due to higher probability of extinction events in the near-field region, which may result in a lifted flame.
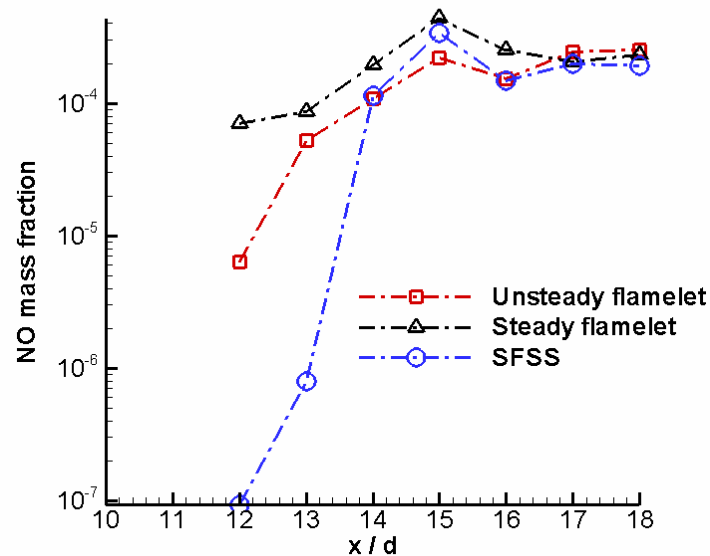
Figure 9.34. Mean NO mass fraction at Z_{st} computed from the flamelet histories with higher intensity fluctuations as a function of axial location in the jet.

Figure 9.34 shows the computed mean values of NO mass fraction at Z_{st} as a function of axial location. We observe that the SFSS model grossly underestimates the mean NO mass fraction at x/d =12, whereas the steady flamelet model overestimates NO by about an order of magnitude. These discrepancies between the models indicate that fluctuations of χ_{st} and transient effects on NO response due to extinction/reignition events are relatively significant at upstream jet locations (x/d < 14). The agreement between the models improves at downstream jet locations, and the SFSS and steady flamelet models yield somewhat similar values of NO. Hence, in the simulated jet near-

field region at higher values of Re, we may expect unsteady effects to significantly affect NO formation.

Finally, Fig. 9.35 shows the mean UHC mass fraction at Z_{st} as a function of axial location in the jet. At x/d = 12, the SFSS model overestimates UHC mass fraction as compared to the unsteady flamelet by about 10 %, but at downstream axial locations, the predictions from all the three models are similar. Therefore, as in the case of the temperature, mean UHC mass fractions are not significantly affected by scalar dissipation rate fluctuations and transient effects.
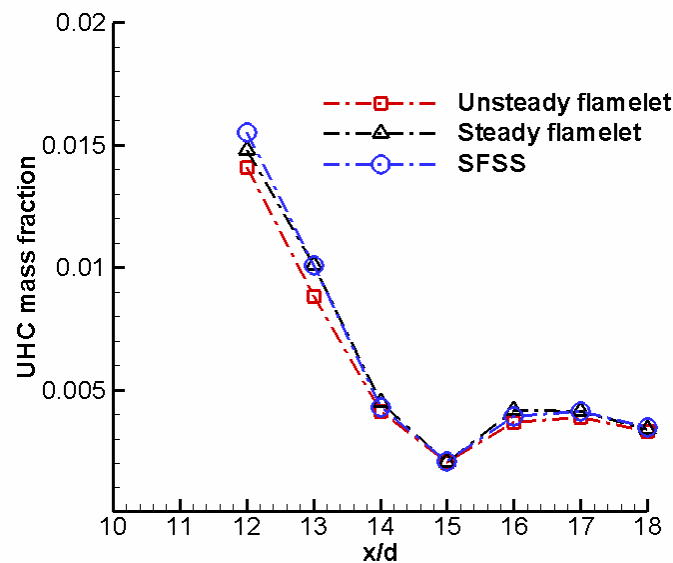
Figure 9.35. Mean UHC mass fraction at Z_{st} computed from the flamelet histories with higher intensity fluctuations as a function of axial location in the jet.

It is important to note that in the present case with $T_{fuel} = T_a = 1000\,\text{K}$, we have considered relatively stronger flames, which respond relatively fast to the imposed scalar dissipation rate fluctuations. Hence, the observed unsteady effects on mean temperatures and species mass fractions (except NO) were not very significant. However, with lower fuel temperatures (~ 400 K) more common in diesel engine applications, the flamelets may respond with longer characteristic time scales, which may in turn result in greater unsteady effects on

the temperature and species responses. In Chapter 10, we will present result from studies employing a lower fuel temperature (= 450 K) closer to diesel applications. Moreover, from the analysis presented in this section, we can conclude that unsteady effects are particularly significant for species like NO with slow response times, and that these effects are expected to increase as the means and RMS values of the scalar dissipation rate fluctuations increase, i.e. as the jet-Re increases.

9.5. Outcome diagram for unsteady flame-response
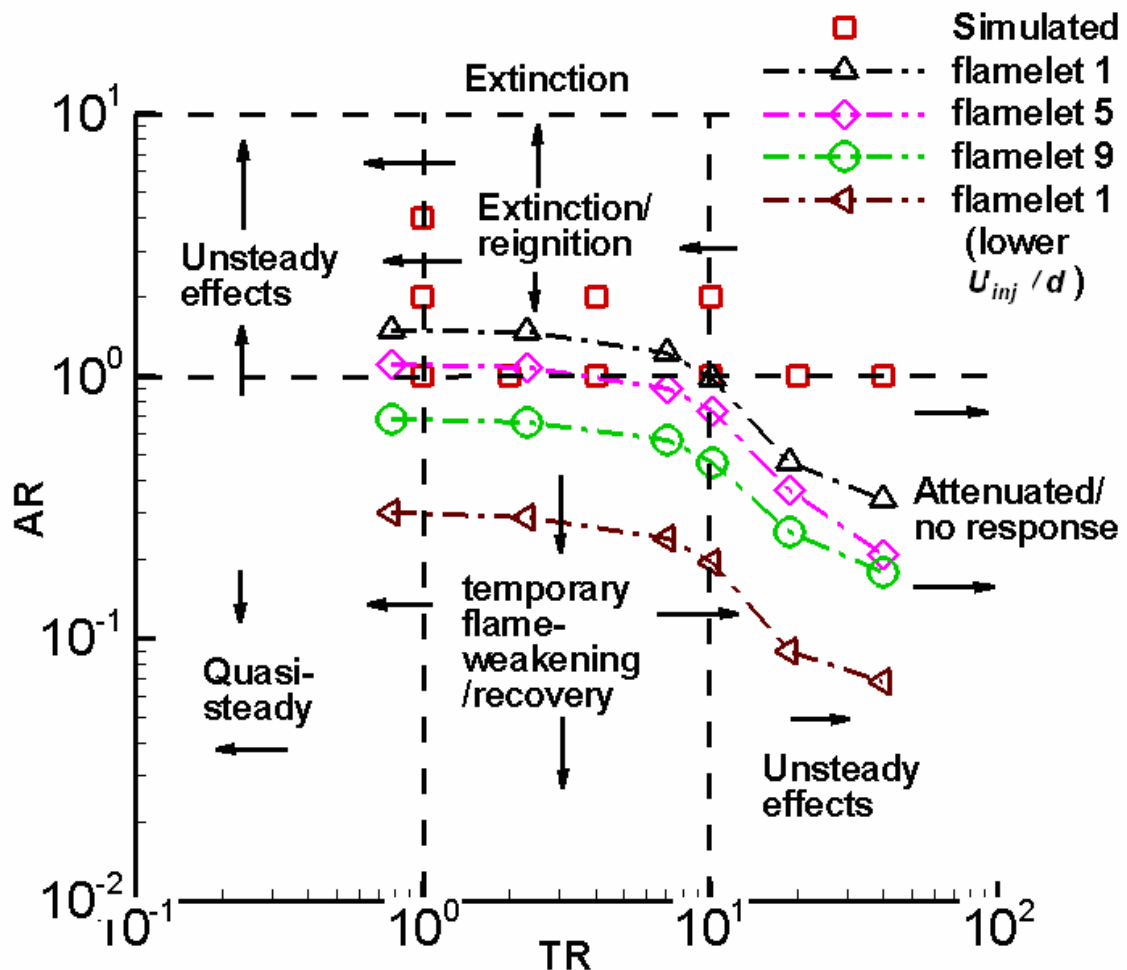
Figure 9.36. AR - TR diagram showing regimes of unsteady flame response in the oscillatory perturbation studies. Values of AR and TR estimated from the Lagrangian flamelet histories generated from LES are also shown.

Before we present the summary and conclusions from the studies reported in this chapter, it is useful to represent the unsteady flame-response regimes observed here in terms of an outcome diagram. Figure 9.36 shows an outcome diagram for unsteady flame-response constructed using AR and TR. In Fig. 9.36, the square symbols represent conditions simulated in the oscillatory flame studies. The different flame-response regimes, such as extinction, extinction/reignition, and attenuated response, discussed in Section 9.3.2 are shown in the figure. In addition, values of AR and TR corresponding to the flamelet histories generated from the LES flowfield are also shown. Note that while flamelets 1, 5 and 9 in the figure represent turbulent time records generated with higher means and RMS values, "flamelet 1(lower U_{inj}/d)" corresponds to the 70,000-Re jet with a lower global strain rate. As discussed before in the context of Fig. 9.22, relatively large values of AR are associated only with lower frequencies ($TR < 10$).

We observe from Fig. 9.36 that the flamelet histories (flamelets 1, 5 and 9) representative of a higher strain rate jet (i.e. with higher means and RMS values of χ) consist of AR and TR values in the range appropriate for extinction/reignition. In Section 9.4, it was confirmed that these flamelet histories indeed result in transient extinction/reignition events. Moreover, as discussed before, flamelet histories corresponding to the 70,000-Re jet (for instance, "flamelet 1 (lower U_{inj}/d)" in Fig. 9.36) are associated with relatively low values of AR (~ 0.3), and hence primarily result in temporary flame weakening/recovery. Therefore, the outcome diagram shown in Fig. 9.36 is useful to understand unsteady flame response regimes in the near field of the jet.

9.6. <u>Summary and Conclusions</u>

In this chapter, we investigated unsteady effects on the response of diffusion flamelets subjected to temporal variations of the scalar dissipation rate. These temporal variations consisted of oscillatory perturbations and turbulent

fluctuations obtained from the analysis of the LES jet near-field. A reduced chemical kinetic mechanism for n-heptane oxidation involving 159 species and 1540 reaction steps was employed. The unsteady response of the flame temperature, and major species and pollutants was investigated, and the applicability of steady flamelet models was assessed.

In the oscillatory perturbation studies, two non-dimensional numbers governing the flame response were the time-scale ratio TR, which measures the relative magnitudes of the residence time (inverse of oscillation frequency) and the chemical time ($\sim \chi_e^{-1}$), and the amplitude ratio AR, which measures the relative magnitudes of the mixing time (inverse of oscillation amplitude) and the chemical time. Extinction/reignition events occur only for intermediate values of AR (< 4.0) and TR (< 10), which result in sufficient mixing and residence times. Unsteady effects increase with increase in both AR and TR. For relatively large values of TR ($\sim 10^2$), the unsteady flame remains relatively insensitive to the imposed perturbation due to increased phase lag. As AR increases for a given value of TR, the tendency for reignition decreases due to insufficient mixing times. Comparison between steady and unsteady flamelet models showed large deviations from steady behavior at relatively large values of χ_{st} (> $0.3\,\chi_e$), and in qualitative agreement with the flame-vortex studies, the unsteady flames were found to be more resistant to extinction than steady flames. The observed unsteady flame response regimes were summarized on an AR-TR outcome diagram.

Investigations of the species response showed similar trends for the major species (like CO_2 and H_2O) as that for the temperature, but the pollutant NO showed significant differences. In particular, while the major species and temperature showed fast recovery during reignition, NO response was relatively slow due to longer chemical response times. Consequently, with increase in AR and TR, the peak and mean NO mass fractions during the oscillatory limit cycles showed significant reductions due to phase lag effects. Hence, extinction/reignition events were found to be beneficial in terms of both flame

stability and NO formation. However, UHC was found to respond much faster than NO, and the decrease in peak and mean NO mass fractions were offset by a corresponding increase in UHC mass fractions. Nevertheless, the much greater sensitivity of NO to temperature and scalar dissipation suggests that temporary flame weakening events with lower values of AR (see Fig. 9.35) may be beneficial in controlling both NO and UHC formation.

In order to gain insights into the unsteady flame response to a spectrum of amplitudes and frequencies, we investigated the response of flamelets to turbulent fluctuations of the scalar dissipation rate estimated from the LES flowfield. These fluctuations were generated as Lagrangian-type time histories of flamelets (i.e. stoichiometric isocontours) tracked through space and time in the jet near-field. These stoichiometric contours were obtained as average radial locations of regions with mixture fraction close to (within 5 %) of the stoichiometric value, and traversed radial locations (r/d > 1.0) relatively far from the centerline at different axial positions in the jet. Ten representative flamelet histories were generated. In the present LES jet with a Re of 70,000, the resulting flamelet histories involved relatively small means (~ $0.06\,\chi_e$), variances and peak values (~ $0.3\,\chi_e$), so that temporary flame weakening events followed by flame recovery were observed in the jet near-field region (6< x/d < 20 and r/d > 1). The unsteady flame response was also compared to predictions from a steady flamelet library corresponding to the instantaneous χ_{st} values from the turbulent time records. The comparisons showed good agreement between the unsteady and steady flamelet models with respect to the mean temperature and mean major species (like CO_2) mass fractions. However, deviations up to 20 % were observed in the mean NO mass fraction due to the inability of steady flamelet models to describe the delayed response of NO (i.e. phase-lag effects) during flame weakening/recovery events.

In order to extrapolate the findings to jets with higher global strain rates closer to practical applications, we considered flamelet histories with higher means and RMS values. On the AR-TR outcome diagram, these flamelet

histories result in values of AR and TR that can lead to local extinction/reignition in the jet. Consequently, transient extinction/reignition events were observed in the unsteady flames when subjected to the higher intensity fluctuations. Steady flamelet models were found to significantly underestimate the temperatures during extinction, and overestimate the temperatures during reignition. Due to these compensatory effects, the mean temperatures with steady and unsteady flamelet models agreed well. However, the failure of steady flamelet models to describe transient extinction/reignition had a drastic effect on instantaneous and mean NO mass fractions leading to deviations more than an order of magnitude at upstream jet locations (e.g. x/d =12). Trade-offs between UHC and NO similar to those observed in the oscillatory perturbation studies were confirmed in the turbulent cases as well. Moreover, due to relatively faster chemical response, the instantaneous and mean UHC mass fractions were relatively well predicted with steady flamelet models.

The analysis of flame response to turbulent time records with higher means and RMS values showed that unsteady extinction/reignition events may be associated with phenomena such as flame lift-off, which have been observed in practical diesel jet flames (Siebers and Higgins, 2001; Pickett and Siebers, 2004). Based on the present results, flame lift-off in the jet can occur at the location where multiple flamelet histories predominantly lead to extinction, and low probabilities for reignition. This would result in the mean flame being extinguished at the lift-off location. Furthermore, recent experimental studies (Pickett *et al.*, 2005) have shown that autoignition phenomena may also be related to diesel flame lift-off. In the next chapter, we will consider the response of initially non-reacting flamelets, which are allowed to autoignite under the influence of fluctuating scalar dissipation rates, and discuss the implications of the findings for lift-off. Finally, while the present simulated conditions show that steady flamelet models may be reasonable to predict mean temperatures and major species mass fractions, it is expected that the unsteady effects would become more important in higher strain rate jets with relatively weaker flames

(with lower fuel temperatures), which may be associated with longer chemical response times.

In the chapter that follows, we discuss the implications of the findings related to the unsteady flame-response for practical phenomena observed in diesel jets. In addition, we will also present results from unsteady flamelet simulations employing a lower fuel temperature (= 450 K) to explore conditions closer to diesel engine applications, and discuss the implications the prediction for steady flame lift-off in diesel jets. Furthermore, the relevance of the findings from the flame-vortex studies discussed in Chapters 6 and 7 to turbulent combustion modeling in the near-field of diesel jets is discussed.

CHAPTER 10. IMPLICATIONS OF THE PRESENT WORK FOR DIESEL JET FLAMES AND TURBULENT COMBUSTION MODELING

10.1. Introduction

In Chapters 6-9, we presented results from studies involving flame-vortex interactions and unsteady response of diffusion flamelets. Both these sets of studies was closely coupled to the results from Chapter 5 involving the LES of a high-Re jet, which provided initial/input conditions for the flame-vortex and unsteady flamelet studies. In this chapter, we will discuss how the fundamental insight gained into the localized flame dynamics in high-Re jets from the studies discussed so far can be related to practical phenomena observed in diesel jet flames. In addition, implications of the findings for turbulent combustion modeling in the near-field of high-Re jets are explored. As stated in Chapter 1, our primary interest lies in phenomena that occur in the near field of diesel jet flames, such as flame lift-off. Accordingly, the simulated range of chamber conditions and non-dimensional numbers are representative of those in diesel combustion chambers. Near-field phenomena not only govern flame stabilization, but also have an influence on pollutant, e.g. soot formation through fuel/air premixing in the near field (Pickett and Siebers, 2004). As discussed in Chapter 2, conventional modeling approaches such as steady diffusion flamelets (Venugopal and Abraham, 2007a) and perfectly-stirred-reactors (Kong *et al.*, 2005) have been employed to predict diesel flame lift-off with only limited success.

Part of this chapter will focus on the recent experimental findings of Pickett *et al.* (2008) related to transient diesel flame lift-off phenomena in the presence of laser-ignition, where we will offer explanations for the measured trends based on unsteady effects on the localized flame dynamics. Conditions closer to diesel

engine applications are considered in additional simulations presented in this chapter, in order to justify the explanations. In particular, we employed a relatively high fuel temperature (= 1000 K) in Chapter 9 focusing on the unsteady response of flamelets, while lower temperatures in the range of 350-450 K are more common in diesel applications. In this chapter, we will discuss results from unsteady flamelet studies employing turbulent fluctuations of the scalar dissipation rate when the fuel temperature is 450 K. Through these studies, we will indicate potential effects due to flow-unsteadiness on flame lift-off in diesel jets. Furthermore, based on the fundamental findings from the flame-vortex interaction studies discussed in Chapters 6 and 7, we will discuss implications for turbulent combustion modeling in the near-field of high-Re jet flames.

We divide this chapter into different sections. In Section 10.2, results from studies of flamelets subjected to temporal variations in the scalar dissipation rate are presented, and implications for transient and steady lift-off phenomena are discussed. Section 10.3 discusses the implications of the results from the flame-vortex studies for flame dynamics and combustion modeling in the near-field of diesel jet flames. The chapter closes with summary and conclusions in Section 10.4.

10.2. <u>Role of Unsteady Effects on Lift-off-related Phenomena in Diesel Jets</u>

In this section, we will explore the role of unsteady effects on the localized flame dynamics related to flame lift-off in diesel jets. First, we will discuss studies related to the recent experimental findings of Pickett *et al.* (2008) on transient lift-off phenomena, and then investigate the potential impact of unsteady effects on predictions of steady diesel flame lift-off.

Recently, Pickett *et al.* (2008) performed experiments in laser-ignited diesel jets. In these experiments, laser-assisted ignition was induced upstream of the natural flame lift-off height L_f, and the subsequent flame dynamics was visualized. These experiments were motivated by the need to elucidate the

nature of physical processes that govern diesel flame lift-off. It was observed that upon laser-ignition, L_f decreases abruptly to the laser position, but gradually relaxes back (i.e. increases) to the natural lift-off height. This relaxation time was found to be of the range of 2.5-9 ms, depending on the laser-position relative to L_f, and the chamber and injection conditions. Note that these times are relatively long compared to injection durations in diesel engines (< 2 ms). Moreover, it was found that the relaxation time decreased as the position of laser-ignition was brought closer to L_f, and as the ambient temperature was increased.
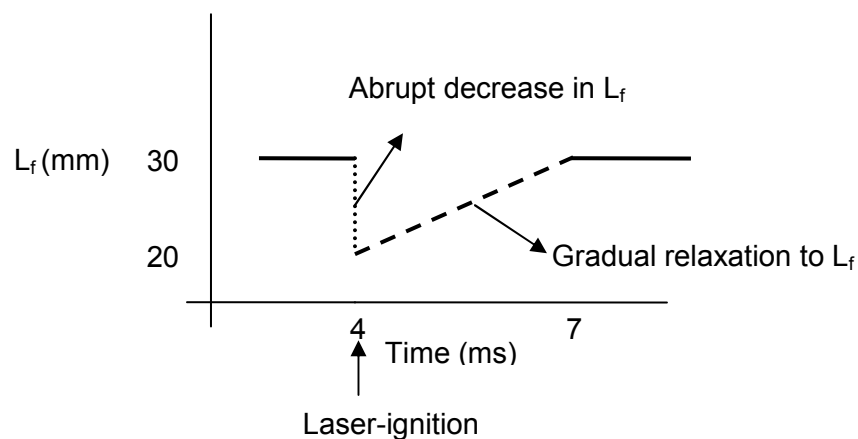
Figure 10.1. Schematic of the experimental observations of Pickett *et al.* (2008) showing the transient variation in the lift-off height of a laser-ignited diesel jet.

Figure 10.1 shows a schematic illustration of the transient lift-off observed by Pickett *et al.* (2008). The numbers indicated for L_f and the time correspond to the following injection and chamber conditions: injection pressure ΔP_{inj} = 150 MPa, chamber temperature T_c = 900 K, chamber density ρ_c = 14.8 kg/m^3, oxygen concentration O$_2$ % = 21, and orifice diameter d_o = 90 μm. In the discussion that follows, we will offer an explanation for the trends observed in the experiments based on the unsteady response of flamelets in the near-field of the jet. Note that in the absence of measured quantitative data on scalar dissipation rates related to the unsteady field and the unsteady flame-response

characteristics, e.g. flame temperature, the analysis below is primarily intended to explain qualitative trends observed in the measurements. In particular, we are interested in explaining the *gradual relaxation* of the lift-off height after laser-ignition to the natural lift-off height.

In order to relate the spatial information, i.e. L_f and the laser-position, in the experimental diesel jet to the gaseous fuel jet simulated in the present work using LES, we invoke the following scaling arguments. Based on the equivalence between gaseous fuel jets and sprays with the same mass and momentum flow rates (Iyer and Abraham, 1997), an equivalent gas jet diameter d_g can be computed as

$$d_g = d_o \left(\rho_l / \rho_g \right)^{1/2},$$

(10.1)

where ρ_l and ρ_g are the liquid and gas densities, respectively. Since the injected-to-chamber gas density ratio for the jet simulated in this work is about 3.5, we get $\rho_g = 3.5\rho_c = 52\,\text{Kg/m}^3$. Also, assuming ρ_l = 712 Kg/m^3 for D2 diesel fuel at 436 K (Siebers and Higgins, 2001), we obtain d_g ~ 0.4 mm from Eq. (10.1). Hence, L_f / d_g ~ (30/0.4) = 75. Note that in the case of the jet simulated in this work, T_c = 1000 K and O$_2$ % = 15, but it can be shown from lift-off height scaling relations, i.e. $L_f \sim \left(T_c \right)^{-3.7} \left(O_2 \right)^{-1}$ (Siebers and Higgins, 2001) that L_f remains about the same (i.e. 30 mm) due to compensatory effects of increase in T_c (from 900 to 1000 K) and decrease in O$_2$ concentration (from 21 % to 15 %). Moreover, since the equivalent gas jet has the same injection velocity V_{inj} as the diesel spray (Iyer and Abraham, 1997), we need to account for the scaling in V_{inj} as well, i.e. $L_f \sim \left(V_{inj} \right)^{1.0}$ (Siebers and Higgins, 2001). It is estimated that V_{inj} ~ 580 m/s for the diesel spray corresponding to ΔP_{inj} = 150 MPa (Pickett *et al.*, 2005). Now, we showed in Chapter 9 that when the mean and RMS values of the scalar dissipation rate time histories generated from LES are increased 5 times, local extinction/reignition events leading to flame lift-off are likely to occur in the

jet. As in the case of studies discussed in Section 9.4, we assume that these higher intensity fluctuations correspond to a jet with $U'_{inj} = \sqrt{5}U_{inj}$, and $d' = d/\sqrt{5}$, so that the global strain rate U_{inj}/d increases, but the velocity-field is not significantly affected. Hence, as in Chapter 9, we will employ the flamelet histories generated from the 70,000-Re jet scaled-up by a factor of 5. For the higher strain rate jet, $U'_{inj} = \sqrt{5}U_{inj} \sim 100\,\text{m/s}$, and $d' = d/\sqrt{5} \sim 0.5\,\text{mm}$, so that using the lift-off scaling $L_f \sim \left(V_{inj}\right)^{1.0}$, $L_f/d' \sim$ 11. Therefore, in the present 70,000-Re jet, we will choose x/d = 11 as the location corresponding to the natural lift-off height (L_f) in the higher strain rate jet.
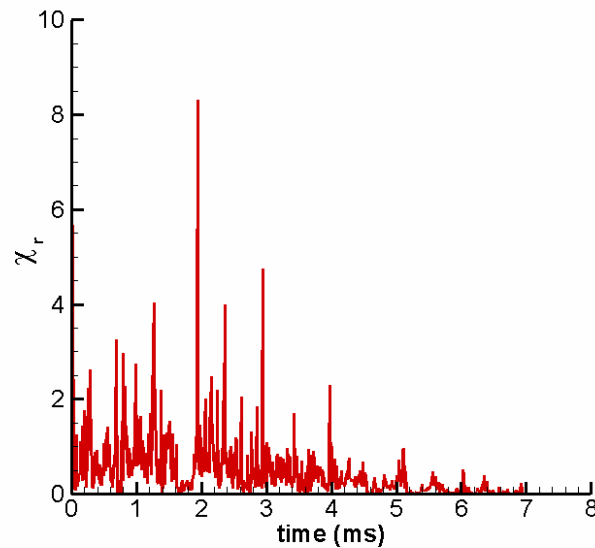
Figure 10.2. Time-record of χ_r for a flamelet-history originating at x/d = 6.5.

In Fig. 10.1, we observe that in the measured diesel spray, the lift-off height relaxation time-scale Δt is about 3 ms. If we assume that this time scales with a global time-scale of the jet given by d_o/U_{inj}, then in the gas jet equivalent to the diesel spray with the same U_{inj}, but $d_g \sim 4d_o$, Δt would be about 12 ms. Now, assuming self-similarity in the jet, we can show that a local characteristic jet

time-scale, defined as $t_{\mathrm{j}} = r_{1/2} / (U_{\mathrm{cl}}/2)$, at the lift-off height (L_{f}) is about 0.06 ms for the equivalent gas jet. Hence, $t_{\mathrm{j}}^{*} = \Delta t / t_{\mathrm{j}} \sim 200$, which indicates that Δt is much longer than the characteristic time scales of the jet in the lift-off region. In the subsequent analysis, we will show that similar order-of-magnitude estimates of t_{j}^{*} can be obtained using a theory based on unsteady flame-response in the higher strain rate jet (henceforth denoted by primed quantities, e.g. U_{inj}', d') considered here.
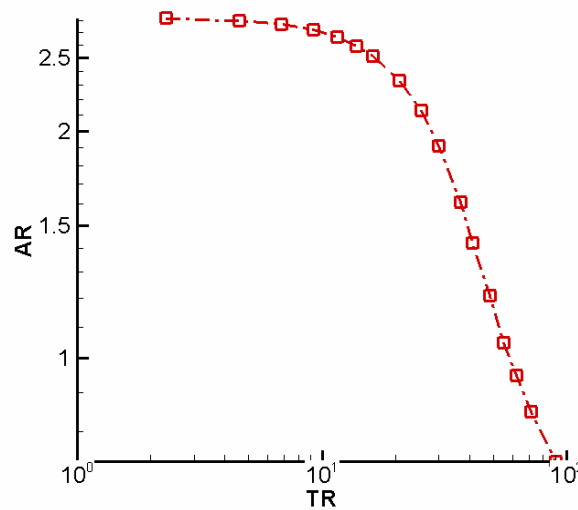
Figure 10.3. AR-TR diagram corresponding to the flamelet-history originating from x/d = 6.5.

To correlate the observed experimental trends to unsteady flame response, consider Figs. 10.2 and 10.3 that show the turbulent time-history and the AR-TR diagram, respectively, for a flamelet that originates from the location, x/d = 6.5, in the jet. Recall from Chapter 9 that the AR-TR for a given flamelet-history is obtained by computing the PSD of the time-record, and then appropriately scaling the amplitude and frequency by the steady extinction limit χ_e to give AR and TR, respectively. Moreover, the fuel temperature in the present case is chosen to be T_{fuel} = 450 K to simulate conditions closer to the diesel jets.

Hence, χ_e at T_{fuel} = 450 K is about 170s^{-1} compared to 500s^{-1} at T_{fuel} = 1000K. In the experiments, the laser is positioned at a distance of 20 mm from the orifice, which using scaling arguments discussed above, corresponds to about x/d = 7.3. Therefore, the chosen flamelet-history originating at x/d = 6.5 may represent a laser-ignited flamelet that traverses from the laser position to the natural lift-off height. We are interested in simulating the dynamics of this flamelet.

Figure 10.2 shows large excursions of χ_{st} above χ_e,i.e. $\chi_r \gg 1$, though as discussed in Chapter 9, these excursions are relatively short-lived. Figure 10.3 shows the spectral representation of this flamelet-history in terms of AR and TR. As before, we will first clarify the underlying physics using an oscillatory perturbation, and then investigate the flame-response to the turbulent time-record. In the results discussed below, we consider an initially non-reacting flamelet that is allowed to autoignite, and then undergo extinction/reignition in the presence of temporal variations in the scalar dissipation rate. The non-reacting flamelets simulated here represent flamelets in the region upstream of the natural lift-off region of the diesel jets, where laser-ignition is induced.
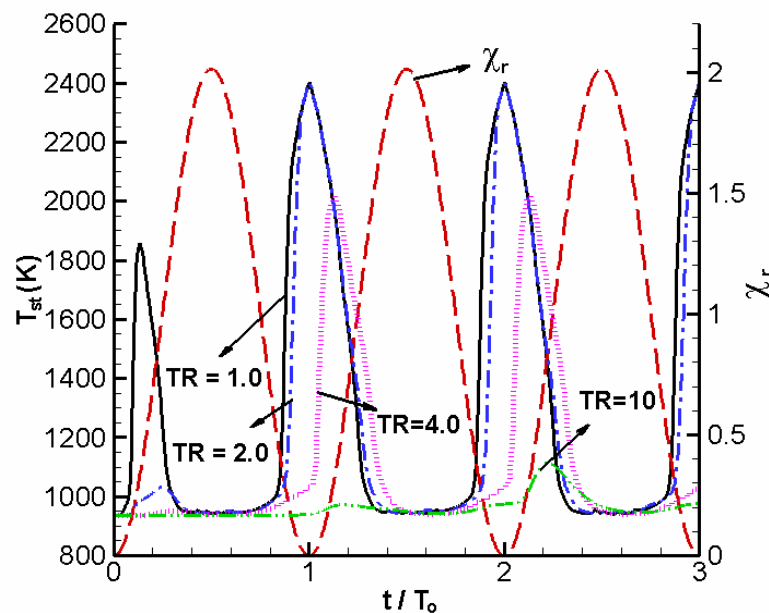
Figure 10.4. T_{st} (K) vs. t /T_o for different TR for an initially non-reacting flamelet.

Figure 10.4 shows the unsteady flame-response to oscillatory perturbations in terms of T_{st} as a function of the normalized time, t / T_o (T_o is the oscillation period). Notice that χ_r is shown on the right-hand-side axis, and the simulations are performed for different values of TR at AR = 2.0. Similar to the trends discussed in Chapter 9, we observe increasing ignition delay times for the flamelets with increasing TR due to decreasing residence times. Accordingly, while oscillatory extinction/reignition limit cycles are observed following autoignition for TR values in the range of 1.0-4.0, the flamelet corresponding to TR = 10 fails to autoignite due to insufficient residence times. Hence, the flamelet subjected to the AR = 2.0, TR = 10 perturbation may correspond to flamelets upstream of the lift-off height prior to laser-ignition. Inspection of the AR - TR diagram corresponding to the flamelet-history shown in Fig. 10.3 reveals that the AR = 2.0, TR = 10 perturbation roughly corresponds to a high-energy mode in the turbulent time-record. In the analysis below, we will use this perturbation as a first-cut representation of the turbulent time-record in the region upstream of the natural lift-off height, and investigate the response of the flamelet in the presence of forced, i.e. laser-assisted, ignition.

Figure 10.5 shows the unsteady flame-response in terms of T_{st} for the baseline case without forced-ignition and with forced-ignition (Case A). Note that the forced-ignition is simulated by initializing the stoichiometric numerical cells with a temperature of 2000 K. We observe that the force-ignited flamelet quenches by one oscillatory period, and then reignites, but the flame is not sustained due to the relatively short mixing and residence times at AR = 2.0 and TR = 10. Accordingly, Fig. 10.5 shows that by 3 time periods, the forced-ignited flamelet temperature relaxes to that of the baseline case, which does not autoignite as discussed before. Note that this observation is contrary to the experimental findings, where the flame was sustained in the laser-ignited region causing a reduction in the lift-off height.
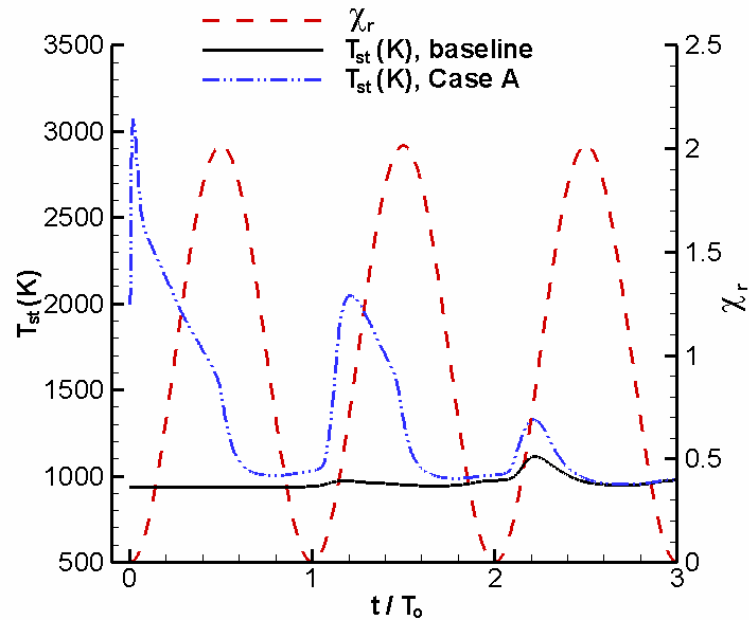
Figure 10.5. T_{st} (K) as a function of t/T$_o$ for the baseline case and Case A with forced-ignition.

As in the case of studies presented in Chapter 9, we have neglected the effects due to combustion heat-release on the scalar dissipation rates in the present case. It is possible that heat-release from the laser-ignited flames in the measured diesel jets modify the scalar dissipation rate field in such a way that the flames are sustained. In other words, one possibility is reduction of the χ_r values due to heat-release from the forced-ignited flames. Note that recent DNS studies of Pantano *et al.* (2003) comparing reacting and isothermal mixing layers show that heat-release tends to decrease scalar variances and dissipation rates, as well as turbulent kinetic energies and dissipation rates. A reduction in χ_r can result from an increase in length scales due to expansion induced by heat release, and greater dissipation of turbulent kinetic energy. On the other hand, experimental and LES studies of Geyer *et al.* (2005) in turbulent opposed-flow isothermal and reactive jets indicate an enhancing effect of heat-release on scalar dissipation rates due to increasing diffusivities. These studies have been

performed at relatively low Reynolds numbers (< 10,000), while we are concerned with relatively high jet Re (~ 100,000) in the present case. Nevertheless, these contrary findings points to the need for clarification of the influence of heat release rate on scalar dissipation rates in high-Re jets. Here, we will hypothesize that χ_r values decrease due to heat-release, and test the hypothesis against experimental observations.
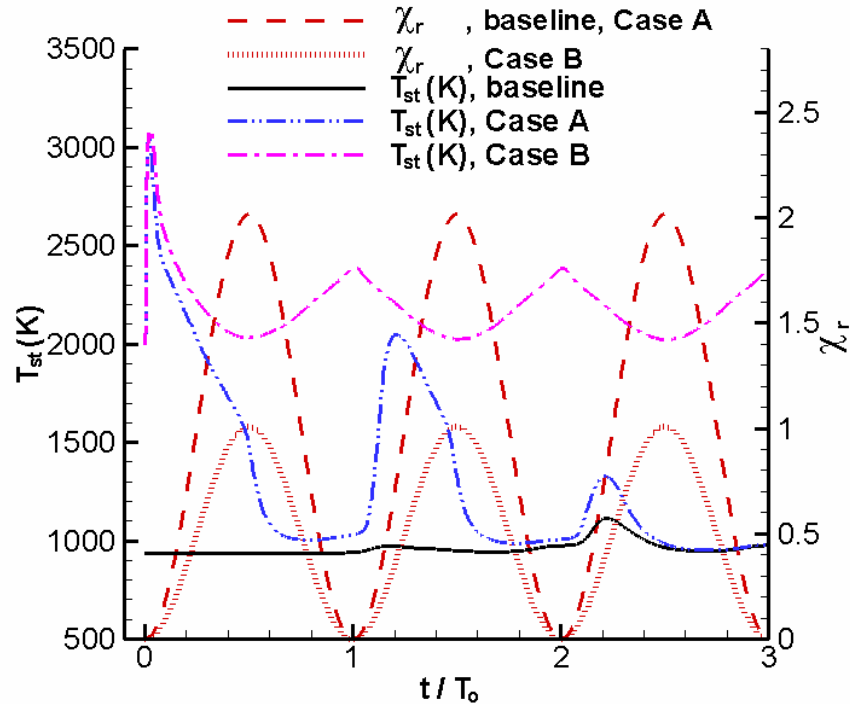
Figure 10.6. T_{st} (K) vs t/T_o for the baseline case, Cases A and B.

Consider Fig. 10.6, which shows the unsteady flame-response in terms of T_{st} for the baseline case, Case A, and Case B. Note that for Case B, the value of AR is decreased from 2.0 (baseline case and Case A) to 1.0 to account for possible effects due to combustion heat-release, while TR is maintained constant at 10. It is interesting to observe that the forced-ignited flame no longer quenches, but rather settles into an oscillatory limit cycle involving temporary flame weakening followed by flame recovery. Essentially, at the reduced value of

AR (= 1.0), the mixing times are long enough to sustain the unsteady flame. This observation is qualitatively similar to that of Pickett *et al.* (2008), where the laser-ignited flame is sustained in the region upstream of the natural lift-off height for a relatively long time.

Pickett *et al.* (2008) offer an explanation for their observations based on the entrainment of hot combustion products downstream in the jet into the laser-ignited regions, which may sustain the flames in these regions. We can interpret this entrainment process as one leading to unsteady perturbations on the forced-ignited flames with amplitudes and frequencies low enough to sustain the flames. This discussion shows that unsteady effects on the localized flame dynamics in the pre-lift-off region of the jet may contribute to the observed transient phenomena. Note that the reduction in AR from 2.0 to 1.0 was merely illustrative, and the quantitative effects of combustion heat-release have to be understood more precisely. Now, we will consider the more realistic case of the force-ignited flamelet subjected to turbulent fluctuations, and relate the observed flame-response to spatial and temporal variations in the jet.
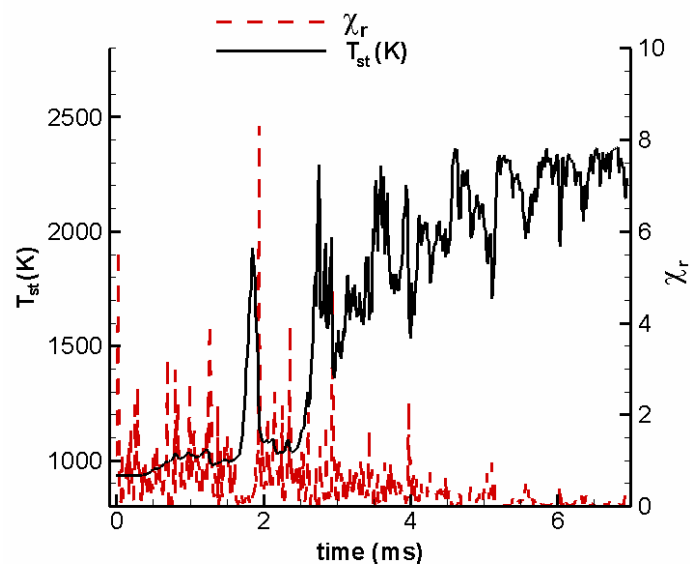
Figure 10.7. Unsteady flame-response in terms of T_{st} (K) as a function of time (ms) for the baseline case without forced-ignition.

Figures 10.7 and 10.8 show the temperature (T_{st}) response as a function of time and axial location (x/d) in the jet, respectively, for the baseline case without forced-ignition. The unsteady flame autoignites after a certain delay time (~ 1.8 ms), and then undergoes transient extinction/reignition in the presence of χ_r fluctuations. As the excursions of χ_{st} above χ_e decrease beyond about x/d = 12, the unsteady flame-response transitions from extinction/reignition to temporary flame weakening followed by recovery. Moreover, notice from Fig. 10.7 that as in the case of the studies discussed in Chapter 9 employing a higher fuel temperature of 1000 K, the unsteady flame (in the region $10 \leq x/d \leq 15$) is more resistant to extinction, since frozen flow is not reached even for relatively large values of χ_r (> 2.0). These trends agree well with the expectation from scaling relations discussed before, which indicated that the natural lift-off height in the present jet is about x/d = 11.
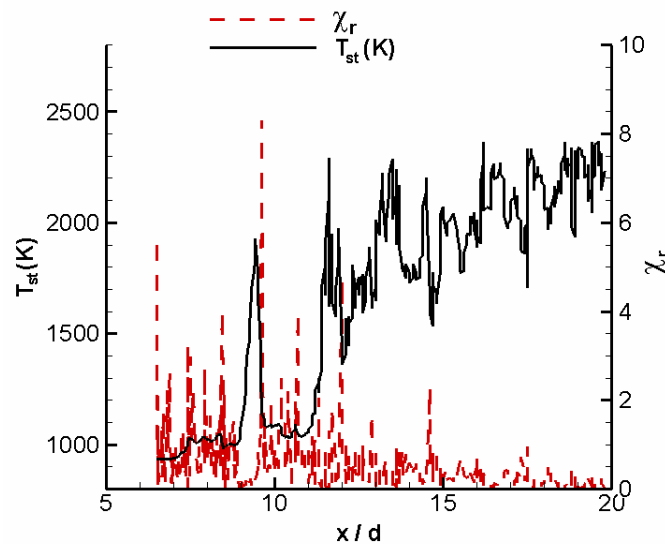
Figure 10.8. Unsteady temperature (T_{st}) response as a function of x/d in the jet for the baseline case without forced-ignition.

It is interesting to observe from Figs. 10.7 and 10.8 that the flamelet traverses the distance from x/d = 6.5 to x/d = 11 in a relatively long time interval

Δt of about 2.5 ms. Now, for the higher strain rate jet with $d' \sim 0.5d$, the flamelet would traverse about half the distance with nearly the same velocity, so that Δt is about 1.25 ms. In addition, it is estimated that the jet characteristic time-scale t_j at x/d' = 11 is about 0.01 ms, so that $t_j^* = \Delta t / t_j \sim 125$. This compares well in terms of order-of-magnitude with the value of 200 estimated for the gas jet equivalent to the measured diesel jet. Hence, the unsteady flame-response occurs over time scales comparable to those reported in the measurements.
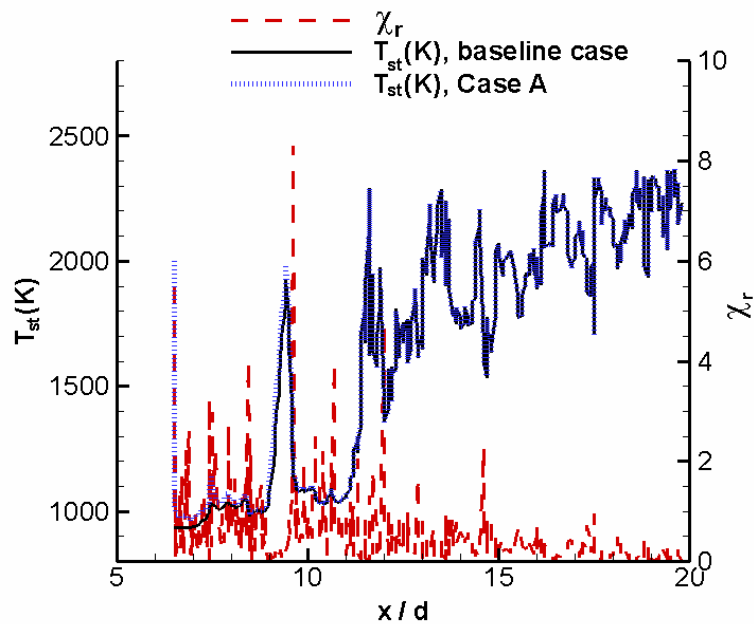
Figure 10.9. Unsteady temperature (T_{st}) response as a function of x/d for the baseline case and Case A.

The unsteady temperature response is shown as a function of x/d for the baseline case and Case A in Fig. 10.9. Note that for Case A, we have not accounted for the effects of combustion heat release on χ_r. We observe from Fig. 10.8 that soon after forced-ignition, the unsteady flame quenches in the presence of relatively strong fluctuations (i.e. $\chi_r > 1$), and the temperature relaxes to that of the baseline case, which autoignites only after a significant delay (> 1.5 ms). These trends agree well with the oscillatory perturbation cases

discussed before, and indicate that if the strain rate field in the pre-lift-off region is assumed to be unaffected due to heat-release, the mixing and flow-residence time scales are insufficient to sustain the forced-ignited flame.
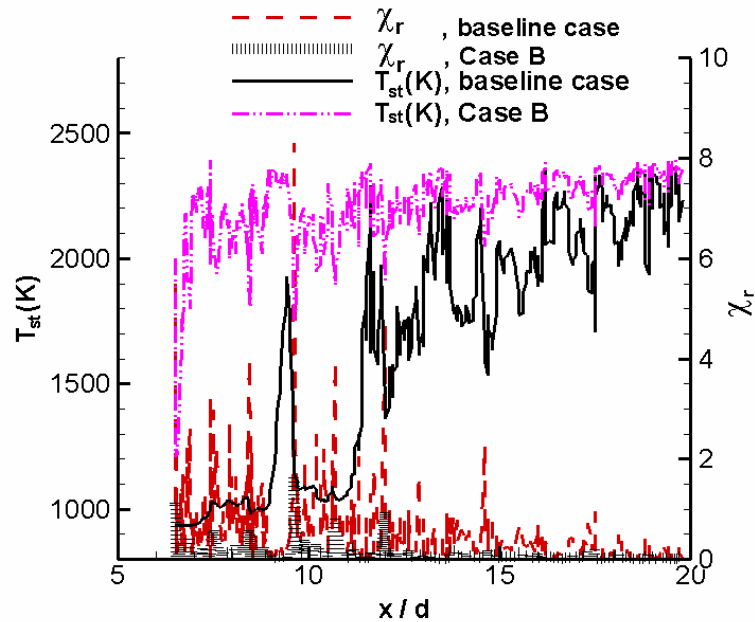
Figure 10.10. Unsteady temperature (T_{st}) response as a function of x/d for the baseline case and Case B.

On the other hand, consider Fig. 10.10 that compares the unsteady flame-response for the baseline case and Case B. As evident from the figure, the amplitudes of χ_r are reduced for Case B to account for possible effects due to combustion heat-release. In particular, the mean and RMS values of the time-record have been reduced by half. Figure 10.10 shows that the forced-ignited flame for Case B quenches soon after forced-ignition, but rapidly reignites due to sufficiently long mixing and residence times. Moreover, in qualitative agreement with the measured trends, the forced-ignited flame is sustained and the temperatures relax to values comparable to those for the baseline case at downstream jet locations.

Hence, the analysis presented here indicates that unsteady effects on the localized flame dynamics can contribute to physical processes that govern transient variations in diesel flame lift-off. As discussed by Pickett *et al.* (2008), processes that affect transient lift-off dynamics are expected to play a role in the establishment of steady lift-off as well, following autoignition in the jet. Now, we will extrapolate the analysis in Chapter 9 under conditions closer to diesel applications to explore the potential impact of unsteady effects on predictions of *steady* lift-off. In particular, we choose T_{fuel} = 450 K, compared to 1000 K in Chapter 9, to simulate conditions closer to diesel chambers, and investigate the unsteady flame response to scalar dissipation rate fluctuations similar to what we did above, but with the focus now on steady lift-off.

Recall from Chapter 9 that in investigating the unsteady response of flamelets, the initial condition was that of a steady flamelet. Another likely scenario in the near-field (pre-lift-off) region of the jet is that of an initially non-reacting flamelet that autoignites in the presence of fluctuating strain, and then undergoes extinction/reignition. Hence, the unsteady responses of initially non-reacting flamelets to ten turbulent time histories were simulated in addition to the scenarios beginning with a steady flame in Chapter 9.

Consider Figs. 10.11 and 10.12, which show the unsteady temperature (T_{st}) as a function of x/d for five flamelet histories with initially non-reacting flamelets and initially steady flames, respectively. As before, the factor of 5 scaling has been employed for the flamelet histories considered in Figs. 10.11 and 10.12. Figure 10.11 shows that at upstream jet locations (x/d < 14), either autoignition does not occur, or it is followed by local extinction/reignition events. At downstream jet locations, the flamelets autoignite, and experience temporary flame weakening/recovery due to reduced fluctuations of χ_{r}. Based on autoignition alone as the governing mechanism, the pre-lift-off region may be viewed as the region where multiple flamelet histories result in a relatively small probability for autoignition due to insufficient mixing and residence times. For

instance, at x/d = 11, only two (i.e. flamelets 1 and 3) of the five flamelets shown autoignite.
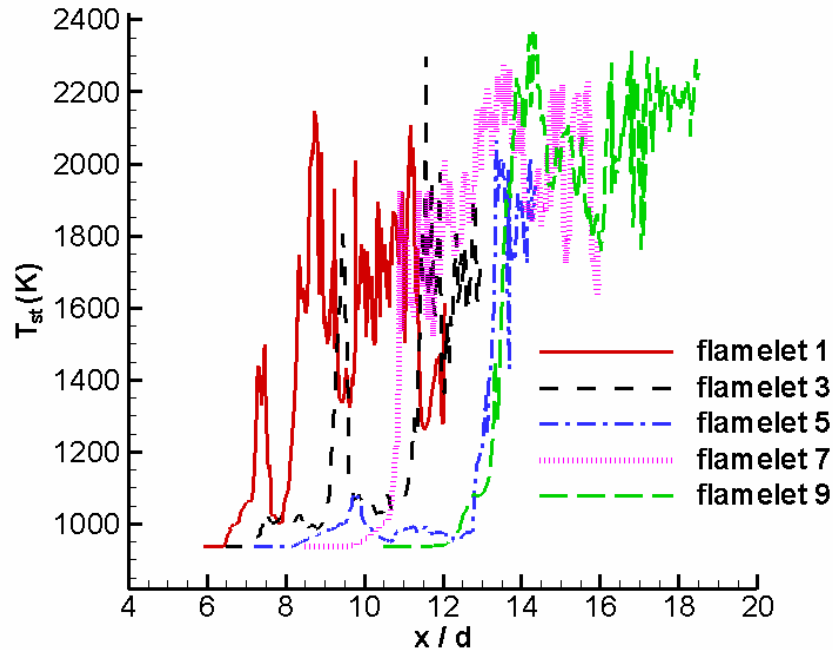
Figure 10.11. Unsteady temperature (T_{st}) response as a function of x/d in the jet for initially non-reacting flamelets.

Note that the evaluation above does not account for flame propagation from autoignited spots upstream into the jet. However, experimental (Pickett *et al.*, 2005) and modeling (Kong *et al.*, 2005) studies do not support upstream flame propagation as a likely mechanism for diesel flame stabilization (Venugopal and Abraham, 2007b). As opposed to flamelets that autoignite, Fig. 10.12 shows that the T_{st} response as a function of x/d in the jet for cases initialized with steady flamelets. As for the cases with T_{fuel} = 1000 K discussed in Chapter 9, we observe a relatively high probability of extinction/reignition events at upstream jet locations. Note that the choice of a lower fuel temperature (= 450 K) decreases the steady extinction limit χ_e from about 500 s^{-1} at T_{fuel} = 1000 K to

about 170 s^{-1} at T_{fuel} = 170 s^{-1}, as indicated before. In other words, the characteristic chemical response time ($\sim \chi_e^{-1}$) becomes longer with T_{fuel} = 450 K.
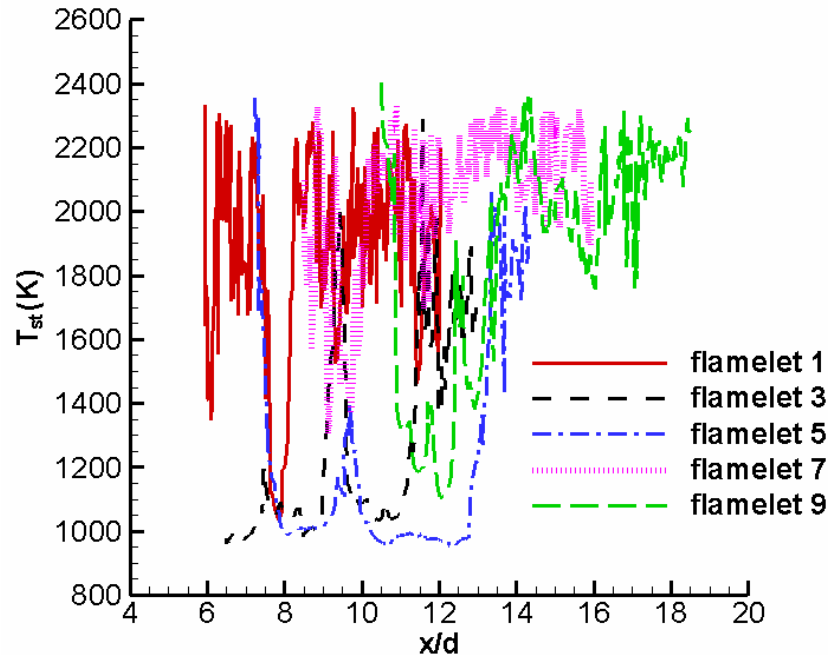
Figure 10.12. Unsteady temperature (T_{st}) response as a function of x/d in the jet for initially steady flames.

A Damköhler number Da, which accounts for effects due to the chemical response time scale may be estimated as

$$Da = \frac{\chi_e}{\langle \chi_{st} \rangle},$$ (10.2)

where $\langle \chi_{st} \rangle$ represents the mean value of χ_{st} experienced by a flamelet as it traverses through time and space in the near-field of the jet. Hence, the range of values for Da represents the range of Damköhler numbers of the flamelets that are likely to be encountered in the jet near-field. Note that $\langle \chi_{st} \rangle$ is different from $\overline{\chi}_{st}$, which represents the temporal mean value of χ_{st} at a given location. For the ten flamelet histories considered here, Da lies in the range of 1.1-3.4 for the

flamelets with T_{fuel} = 450 K and 3.3-10 for the flamelets with T_{fuel} = 1000 K. Hence, with a lower fuel temperature, the flamelets are relatively strained and closer to extinction ($Da \sim 1$), and expected to respond with longer chemical time scales. Accordingly, from a comparison of Figs. 9.32 and 10.12, we observe a higher probability of extinction events (i.e. higher number of extinguishing flamelets) and a lower probability of reignition events at upstream jet locations(x/d < 14) with lower values of Da (i.e. lower fuel temperature).

As discussed before, both the scenarios involving initially non-reacting flamelets and initially steady flames are likely in the jet near-field, and may influence the steady lift-off height. In fact, the initially steady flames can be thought of as flames propagating upstream; such flames then encounter turbulent eddies and are subject to the time records as shown. We can compute the mean T_{st} values across the flamelet histories simulated accounting for both scenarios. In this context, the lift-off height may be viewed as the location up to which multiple flamelet histories result in relatively low probabilities for both autoignition and reignition events, and high probabilities for extinction events.

Consider Fig. 10.13 that shows the mean T_{st} as a function of x/d in the jet. Predictions from the unsteady and steady flamelet models, and the steady-strain-steady-flamelet (SFSS) model, which accounts only for the steady value of T_{st} at the mean (or steady) value of χ_{st} (i.e. $\overline{\chi}_{\text{st}}$) are shown in the figure. It is interesting that the steady flamelet predictions agree well with those from unsteady flamelets at all axial locations. This indicates compensatory effects due to the overestimation of instantaneous temperatures by the steady flamelet model during reignition and the underestimation of temperatures during extinction. Moreover, Fig. 10.13 shows that the SFSS model predictions agree well with the other two models beyond x/d = 12, indicating that accounting for the transient flame-response to χ_{st} fluctuations is not critical beyond this location. However, at x/d = 12, the SFSS model predicts an extinguished flame, whereas the other two models predict temperatures about 40 % higher, indicating the importance of

transient reignition events ignored by the SFSS model, which contribute to higher temperatures with the steady and unsteady flamelet models.
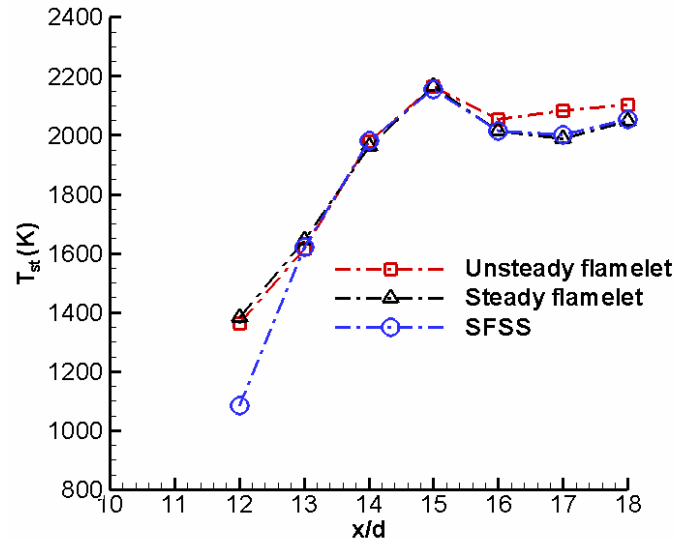
Figure 10.13. Mean values of T_{st} (K) as a function of axial location, x/d, in the jet by accounting for both intially non-reacting and intially steady flamelets.

Hence, it is expected that for jets with higher global strain rates, i.e. with strong χ_{st} fluctuations and relatively strained flamelets (low values of Da), accounting for flow-unsteadiness can potentially influence lift-off predictions. Moreover, as for the cases with T_{fuel} = 1000 K, the mean NO mass fractions predicted using the steady flamelet and SFSS models show significant deviations from unsteady flamelet values at upstream jet locations (x/d < 14), whereas mean UHC mass fractions with all the three models agree well. Hence, the present results indicate that while steady flamelet models in the context of LES, i.e. accounting for χ_{st} fluctuations but not chemical phase-lag effects, may be reasonable for the prediction of mean temperatures, major species and UHCs, unsteady flamelets, i.e. accounting for both χ_{st} fluctuations and chemical phase-lag effects, may be critical for mean NO predictions.

The discussions so far show that it is important to account for unsteady effects on the local flame structure in the near-field of high-Reynolds number jets. Recall that the flame-vortex interaction studies discussed in Chapters 6 and 7 demonstrated the importance of unsteady effects as well. It was shown that unsteady flames extinguish at scalar dissipation rates higher than steady values, implying that the delayed response of the flame, i.e. unsteady effect, renders it more resistant to extinction. This finding was also supported in the results presented in Chapter 9, where the unsteady response of diffusion flamelets to temporal variations in the scalar dissipation rates was investigated. Moreover, while the unsteady flamelet studies (Chapter 9) provided insight into reignition through autoignition, the flame-vortex studies revealed mechanisms involving edge flame dynamics for reignition. In the section that follows, we will indicate the implications of the findings discussed above concerning unsteady extinction/reignition to turbulent combustion modeling, and explore possible approaches to incorporate the observed physics into large-scale simulations of jet flames.

10.3. <u>Flame-Vortex Studies: Relevance for Diesel Jets and Modeling</u>

Chapters 6-8 focused on the results from flame-vortex interaction studies. The simulated range of vortex and flame characteristics were estimated from the mean temporal statistics at different locations in the near field of a 70,000 Reynolds number jet computed with LES. In addition, results from flame-vortex studies relevant for conditions in diesel engines were discussed. These results showed that the likely regimes of flame-vortex interactions in the near-field of high-Reynolds number jets are unsteady flame extinction and reignition. In the case of the flame-vortex interactions, however, reignition occurred through curvature effects and not through autoignition. We will now discuss the relevance of the findings with respect to extinction and reignition to turbulent combustion modeling. The implications for modeling discussed below pertain to diesel jet flames. Since the regimes of flame-vortex interactions are primarily dependent on

non-dimensional numbers, such as the length and velocity scale ratios, the implications may be valid for laboratory-scale flames (such as the Sandia flames (Barlow and Frank, 1998) E and F) as well, which result in similar values of the non-dimensional numbers. However, since the influence of factors, such as the pressure and the fuel-to-oxidizer density ratio, which differ significantly between diesel and laboratory-scale flames, has not been clarified in this work, we will limit our inferences to diesel flames.

10.3.1. Flame Extinction: Implications

An interesting and important observation in the extinction scenarios simulated in this work, in both flame-vortex and unsteady flamelet studies, is the distinction between *unsteady* and *steady* extinction limits. Traditionally, the steady extinction limit χ_e has been used to define characteristic time scales in diffusion flames (Vervisch and Poinsot, 1998) and parameterize flamelet libraries in flamelet models for turbulent non-premixed combustion (Peters, 2000). However, the present work shows that χ_e is *not a relevant parameter* for the highly unsteady flowfields encountered in high-Reynolds jet flames, such as those in diesel chambers. In particular, large values of the local chemical-to-vortex time-scale ratios, i.e. relatively strained flamelets subjected to strong vortices, result in unsteady effects, which in turn lead to a delayed response of the flame, and extinction limits higher than χ_e. Such unsteady extinction regimes have not been experimentally explored in detail. For instance, as discussed in Chapters 6 and 7, experiments of Santoro *et al.* (2000a) in vortex-perturbed gaseous methanol flames report unsteady limits only about 30 % greater than steady values, owing to chemical-to-vortex time-scale ratios smaller than unity, which essentially correspond to flames that can adjust rapidly enough to the imposed strain. However, recent numerical work of Oh *et al.* (2004) on vortex-induced extinction of diluted methane/air opposed-flow flames report unsteady

limits higher than steady limits. As in the current work, Oh *et al.* considered vortices with characteristic time scales shorter than chemical time scales.

While the distinction between unsteady and steady limits is an interesting finding, an important question in this context is: "*What is a relevant criterion for extinction in highly unsteady flowfields, such as diesel chambers?*" This question may also be recast as "*How do we determine the unsteady extinction limit in a turbulent jet flame, e.g. a diesel jet flame, simulation?*" Note that extinction processes are known to be important for flame lift-off (Peters and Williams, 1983; Venugopal and Abraham, 2007a, b). Hence, in a diesel jet simulation, unsteady extinction limits can be employed to identify the lift-off location. In trying to answer the question above, let us consider two important findings with respect to unsteady extinction. One, that χ_e is unsuitable to characterize extinction, as indicated before, and second, that the unsteady extinction limit is *flow-dependent*, i.e. the unsteady limit increases with increasing vortex velocities (or the local turbulence intensities in a jet flame). These findings further indicate that the scalar dissipation rate χ by itself *may not be an appropriate parameter to characterize unsteady extinction*. A similar viewpoint is expressed in the recent numerical work of Katta *et al.* (2004) involving vortex-induced extinction of hydrogen/air opposed-flow flames. The authors reported unsteady limits moderately higher (about 75 % higher) than steady limits. Conceptually, χ represents the local and instantaneous time scale of diffusion/mixing in the unsteady flame, but being the dissipation rate of a passive scalar, i.e. the mixture fraction, cannot account for *chemical phase-lag effects*. Consequently, unsteady extinction limits expressed in terms of χ are flow-dependent, since the chemical phase lag effects would depend on the specific flow perturbation and the time histories to which the flame is subjected.

In this context, the present work employed the $Da = 1$ criterion (see Section 6.3) to identify the onset of unsteady extinction. Since $Da = \left(\chi_{st}\tau_c\right)^{-1}$, it accounts for the instantaneous mixing time-scale (χ_{st}^{-1}) and the instantaneous chemical

time-scale (τ_c). Accordingly, $Da = 1$ represents the onset of extinction, when the instantaneous mixing time-scale becomes just shorter than the chemical time-scale. It is evident that this criterion does not depend on the characteristics of the vortex and the flame. Recall from Section 3.3.2 that τ_c was estimated as the chemical time-scale (see Eq. (3.42)) for the product of combustion (e.g. CO_2). In the context of a RANS/LES sub-model, the source term of a reactive scalar, such as the reaction progress variable c (Pierce and Moin, 2004; Peters, 2000), can be employed to estimate τ_c. Hence, the criterion for unsteady extinction may be expressed as

$$Da = \frac{\left(\dot{w}_c(Z, \chi, c)/\rho\right)}{\chi_{st}} \leq 1,$$ (10.3)

where $\dot{w}_c(Z, \chi, c)$ represents the conditional mean source term of the progress variable. In the context of RANS/LES, c is a modeled tracking scalar, just as the mixture fraction, and closure models are required for $\dot{w}_c(Z, \chi, c)$. As in the recent LES studies of Pierce and Moin(2004) employing a steady flamelet/progress variable (FPV) model, c may be chosen as the sum of the mass fractions of major combustion products, for example, $c = Y_{CO2} + Y_{H2O}$ in the present case with a single-step kinetic model, and $\dot{w}_c(Z, \chi, c)$ may be tabulated in a flamelet library.

To illustrate the application of the criterion to unsteady flames, consider Fig. 10.14, which shows Da as a function of χ_r during the extinction phase for different values of u_{fv} with $l_r = 1.5$ and $Da_i = 30$, where Da is computed using $\dot{w}_c(Z, \chi, c)$ and χ_{st} (see Eq. (10.2)), and $c = Y_{CO2} + Y_{H2O}$. Note that the range of u_{fv} employed fall in the range of $(0.25 - 1.0)q$ at x/d = 12 close to the jet centerline (r/d $\leq$ 1.5). Consistent with prior studies (Oh *et al.*, 2004; Venugopal and Abraham, 2008a) the unsteady limit (defined here at $Da = 1$) decreases as u_{fv} decreases. Moreover, we observe from Fig. 10.14 that the $u_{fv} = 1.24$ vortex is not strong enough to quench the flame as Da remains greater than unity. Hence, the present extinction criterion, i.e. $Da = 1$, accounting for chemical phase-lag effects

through a reactive scalar is more appropriate for unsteady flames in comparison to the $\chi = \chi_{\mathrm{e}}$ criterion, and provides a means to estimate extinction limits in unsteady flowfields encountered in diesel jet flames. Note that since the scalar dissipation rate and the progress variable appear as parameters in the UFPV model discussed in Section 6.5 of Chapter 6, this criterion can be employed in the context of the UFPV model in RANS/LES. Now, we will discuss the implications of the findings related to reignition for turbulent combustion modeling.
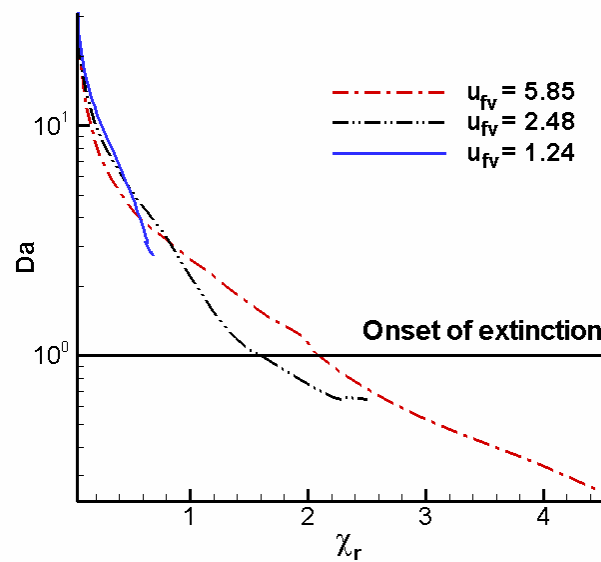
FIG. 10.14. Da as a function of χ_{r} during the extinction phase for different values of u_{fv} for $l_{\mathrm{r}} = 1.5$ and $Da_{\mathrm{i}} = 30$.

10.3.2. Reignition: Implications

The flame-vortex interaction studies discussed in Chapters 6 and 7 showed that reignition phenomena following extinction are governed by edge flame dynamics aided by the vortex-induced curvature. As discussed in Chapter 7 (Section 7.2), reignition through edge flame scenarios are likely for relatively small vortices (or small scales, for e.g. $l_{\mathrm{r}} < 3.0$), when the proximity of the edge flames and relatively less diluted fractions in the quenched regions may promote

reignition through lateral heat and species diffusion before autoignition can occur. However, recall that in the previous section, the reignition scenarios observed occurred only through autoignition due to the choice of the 1-D flamelet formulation. It is expected that as relatively large vortices (e.g. l_r > 3.0) are considered, the influence of the vortex-induced curvature would decrease, and the flamelets would reignite through autoignition following extinction. As discussed in Section 7.5 of Chapter 7, we encounter relatively large values of l_r (> 4.0) and relatively small values of u_{fv} (< 3.0) at radial locations far from the centerline (r/d > 1.0) at a given axial location. In the case of the 70,000-Re jet, this results in temporary flame-weakening/recovery events, as indicated by the trends from flame-vortex interaction studies (see Fig. 7.19), and confirmed in the unsteady flamelet studies presented in Chapter 9. However, for higher-Re jets with higher local values of u_{fv}, the radial locations far from the centerline (r/d > 1.0) may experience extinction, and reignition through autoignition, as shown in Section 9.4.

In addition, the tendency for reignition through autoignition may increase as faster chemical time scales and thinner flames are considered. For instance, in heavy-duty diesel engine applications, higher pressures (60-80 bar) and higher chamber temperatures (1200-1300 K) are encountered, which would result in thinner flames with larger l_r values. It would be interesting to consider higher pressure and temperature flames, and explore the modes of reignition.

In the flame-vortex studies, owing to the relatively large values of u_{fv} (> 1.0) and Re_v (> 100) characteristic of the near-field of diesel jet flames, we observed in Chapter 7 that the vortex-induced flow had a dominating influence on the edge flame dynamics. Note that experiments in vortex-perturbed flames (Santoro *et al.*, 2000a; Santoro and Gomez, 2002) with relatively low-Re vortices (Re_v < 100) reveal complete viscous dissipation of the vortex following extinction, so that reignition occurs solely by edge flame propagation. The dominance of the vortex-induced flow on the reignition mechanisms suggests that relatively simple

kinetic models may be adequate to capture the physics. This observation was confirmed in Chapter 8, where flame-vortex simulation results with multi-step n-heptane chemistry showed good qualitative agreement with that employing single-step chemistry with respect to physical mechanisms for reignition.

In Chapter 6, we showed that the unsteady flamelet/progress variable (UFPV) (Pitsch and Ihme, 2005) with the instantaneous scalar dissipation rate and the instantaneous progress variable as model parameters adequately describes the unsteady extinction/reignition phenomena observed in the flame-vortex simulations. In the context of applying the UFPV model to RANS/LES, the mean/filtered progress variable $\tilde{c}$ (see Eq. (6.8)) has to be solved through a transport equation, and closure approximations are required for the conditional mean source term of the progress variable, $\dot{w}_c$ (see Eq. (6.9)). In the versions of the flamelet/progress variable models developed so far in the literature for reacting-LES (Pierce and Moin, 2004; Pitsch and Ihme, 2005), $\dot{w}_c$ is directly tabulated in a flamelet library for look-up. Due to the 1-D nature of the flamelet formulation, such an approach involving the tabulation of $\dot{w}_c$ using the flamelet equations accounts for reignition through autoignition, but not through edge flame dynamics that involve curvature effects. Hence, in a RANS/LES UFPV model accounting for reignition through edge flame effects, $\dot{w}_c$ has to be related to edge flame characteristics, such as the edge displacement speed (Buckmaster, 2002).

One possible approach is to invoke an analogy with progress variable models for turbulent premixed combustion (Peters, 2000), and estimate $\dot{w}_c$ as

$$\dot{w}_c(Z,\chi,c) = \rho S_{\text{edge}}|\nabla c|, \tag{10.3}$$

where S_{edge} represents the edge displacement speed. To model S_{edge}, theoretical formulations relating S_{edge} to the Damköhler number (Da) at the flame-edge can be employed (Hermanns *et al.*, 2007).

In addition, appropriate forms of the subgrid PDF of the progress variable, $P(c)$, would have to be presumed to estimate the unconditional

mean/filtered source term, $\widetilde{w}_c(Z, \chi, c)$. For instance, the recent modeling studies of Ihme *et al.* (2006) comparing the FPV model predictions to the DNS database of Sripakagorn *et al.* (2004) indicate sensitivity of the model to the choices for $P(c)$. Hence, while the present work shows that the UFPV model is a potential improvement over steady flamelet models for the prediction of extinction/reignition, further studies may be required to obtain closure sub-models involved in its implementation in RANS/LES.

10.4. <u>Summary and Conclusions</u>

In this chapter, we discussed how the findings from the present work can be employed to provide insight into observed near-field phenomena in diesel jets, and the implications of the findings for turbulent combustion modeling in the near-field of high-Reynolds number jets encountered in diesel applications.

Recent experimental observations related to transient variations in diesel flame lift-off in the presence of laser-ignition were discussed. It was shown that the qualitative trends in the measurements can be adequately described based on the effects of unsteadiness on the localized flame dynamics. Specifically, it was proposed that combustion heat-release from the forced-ignited flamelets upstream of the natural lift-off location reduces the scalar dissipation rate magnitudes in the pre-lift-off region. With this assumption, the forced-ignited flamelets are sustained for a relatively long time ($t_j^* \sim O(10^2)$), and gradually convect to the natural lift-off location. These trends agree well with measurements. In addition, the role of transient flame response to scalar dissipation rate fluctuation in the prediction of steady lift-off heights was explored. As an extrapolation of the analysis presented in Chapter 9, flamelets with a lower fuel temperature (= 450 K) more common in diesel engine applications were considered. Results showed that as in the case of flamelets with higher fuel temperatures (= 1000 K) considered in Chapter 9, steady flamelet models predicted mean values of temperature close to those with unsteady flamelets,

due to compensatory effects during extinction and reignition. However, at upstream jet locations (x/d = 12), predictions from a steady-flamelet-steady-strain (SFSS) model, which accounts only for the steady(or mean) temperature at the steady(or mean) scalar dissipation rate, were as much as 40 % lower than those with unsteady and steady flamelets. This indicates that accounting for the transient flame response to scalar dissipation rate fluctuations is important for the prediction of near-field phenomena, such as lift-off, in high-Re jets.

The implications of the findings from the flame-vortex studies, related to unsteady extinction and reignition, for the modeling of diesel jet flames were discussed. With respect to extinction, it was shown that a criterion based on the Damköhler number Da, where Da is computed in terms of the conditional mean scalar dissipation rate (mixing time-scale) and the conditional mean source term of the reaction progress variable (chemical time-scale), is more appropriate for unsteady flames than the $\chi = \chi_e$ criterion. This criterion, $Da = 1$, for the onset of unsteady extinction, was employed to estimate unsteady extinction limits across the range of vortex velocity scales (or u_{fv}) considered in this work. In agreement with prior works, the unsteady limit was found to decrease with decreasing vortex velocity scales. The $Da = 1$ criterion can be employed as an unsteady extinction criterion to identify lift-off heights in RANS/LES of diesel jets with the UFPV model.

With respect to reignition, the flame-vortex studies show that for conditions typical of high-Reynolds number jet flames in diesel chambers, curvature effects and edge flame dynamics are important. In this context, it was shown in Chapter 6 that the unsteady flamelet/progress variable (UFPV) model with the instantaneous scalar dissipation and the instantaneous progress variable as model parameters adequately describes vortex-induced extinction/reignition. However, models for the conditional mean source term of the progress variable and the subgrid PDF of the progress variable are required. In order to account for reignition through edge flame dynamics in the UFPV formulation, it is proposed here that closure approximations similar to those in progress variable models for

turbulent premixed combustion can be employed. In particular, the progress variable source term is related to the edge flame displacement speed, which can be tabulated as a function of the Damköhler number at the edge location.

CHAPTER 11. SUMMARY, CONCLUSIONS AND FUTURE WORK

11.1. Introduction

The present work is focused on the numerical simulations of localized flame dynamics in the near-field of high-Reynolds number jets. Such jets are important in a range of practical applications, e.g. diesel engines, gas turbines. This work is motivated by diesel engine applications, though the findings have broader implications. The near-field of turbulent reacting jets is characterized by complex interactions between turbulence and chemistry, which could influence and/or lead to a variety of processes, such as autoignition, partially-premixed flame propagation, and local extinction/reignition. The interplay of these processes in the near-field of the jet may result in flame lift-off, where the jet stabilizes at a certain distance, i.e. the lift-off height, from the injector.

Recent experiments (Siebers *et al.*, 2002; Pickett and Siebers, 2004) in diesel jet flames have shown that flame lift-off can be correlated with the formation of pollutants, such as soot, in the jets. This correlation arises because the same processes which influence lift-off also influence fuel/air premixing in the near-field. The accurate representation of these physical processes in models is, hence, necessary if such models are employed to optimize diesel engine combustion. The ability of such models to predict lift-off is indicative of their accuracy. To develop models, the understanding of the physical mechanisms governing jet near-field phenomena, such as lift-off, is important. Conventional modeling approaches employing RANS-based closures, such as steady flamelets (Venugopal and Abraham, 2007a) and perfectly-stirred-reactors (Kong *et al.*, 2005a) are successful in predicting lift-off only over a limited range of operating conditions, thereby indicating that they lack accurate representation of

the physics. Moreover, due to the inherent lack of effects due to flow-unsteadiness, RANS-based models cannot predict transient variations in the lift-off height and the near-field flame structure (Pickett *et al.*, 2008). Hence, the present work seeks to provide insight into the near-field jet flame dynamics.

The following are the three primary questions addressed in this work: 1.) What are the likely regimes of localized flame dynamics in the near-field of high-Reynolds number jets? 2.) How do unsteadiness and curvature influence the flame dynamics in the jet near-field? 3.) What modeling approaches are applicable to predict the local flame structure in the near-field?

The approach adopted consists of the LES of a 70,000 Reynolds number isothermal variable-density round jet to compute turbulent statistics, and studies of flame-vortex interactions and unsteady flamelets using the information obtained from LES. In particular, the LES is employed to estimate mean turbulent integral length and velocity scales, and time-averaged values and turbulent time records of conditional-mean scalar dissipation rates in the jet near-field ($x/d <$ 25). The flame-vortex interaction studies provide insight into the detailed effects of a single length-scale (or a turbulent eddy) on the local flame structure, effects due to unsteadiness and curvature, applicability of modeling approaches such as steady-flamelet and flamelet/progress variable models, and directions for the development of improved models. On the other hand, the studies of unsteady flamelets subjected to turbulent time records of the scalar dissipation rates provide insight into the simultaneous effects of a spectrum of turbulent scales on the local flamelet structure, unsteady responses of the flame temperature, major species and pollutants, and the applicability of steady flamelet models in unsteady flowfields. The simulated fuel/oxidizer temperatures and pressure are representative of diesel engine combustion chambers.

In the summary that follows, we will first discuss LES studies, and then studies of flame-vortex interactions and unsteady flamelets. Thereafter, in Section 11.3, we will highlight some of the key assumptions in the present approach, and discuss the implications of the assumptions on the findings from

this work. Directions for future work are discussed in Section 11.4; this future work will include suggestions for relaxing some of the assumptions.

11.2. <u>Summary and Conclusions</u>

11.2.1. LES Studies of Jet Near-field Turbulent Statistics

In this work, we employ LES to estimate the statistics of the velocity and mixture fraction fields in the near-field of a 70,000 Reynolds number isothermal variable-density round gaseous fuel jet. The LES model is validated for the prediction of velocity and mixture fraction statistics through comparisons with available experimental data in self-similar jets. Mean turbulent length (l) and velocity scales (q), and time-averaged conditional mean scalar dissipation rates ($\overline{\chi}_Z$) are estimated at different locations in the jet near-field, which are used to initialize the vortex and flame characteristics in the flame-vortex studies. In addition, turbulent time records of the stoichiometric conditional-mean scalar dissipation rates (χ_{st}) are computed, which are then employed to investigate the unsteady response of diffusion flamelets.

In Chapter 2 of the thesis, prior LES studies (DeBonius and Scott, 2002; Bogey *et al.*, 2003, Ribault *et al.*, 2001) focusing on velocity and passive scalar, i.e. mixture fraction, statistics in high-Reynolds number isothermal jets are reviewed. These studies have focused on constant-density jets, while variable-density jets are typical in diesel engine applications. Hence, in the present work, a variable-density jet with an injected-to-ambient gas density ratio of 3.5 is simulated, and turbulent statistics are computed in the near-field of the jet.

The numerical formulation and computational conditions employed for the LES in the present work are presented in Chapter 3. The LES is performed with a numerical code that solves the filtered governing equations on a 3-D non-uniform Cartesian grid with 6th-order spatial accuracy and 4th-order time integration.

Subsonic inflow and non-reflective outflow characteristic boundary conditions extended to account for multicomponent gaseous mixtures are employed. To trigger transition to turbulence, a vortex-ring perturbation technique is used at the jet-inlet. A 6th-order tridiagonal filter is used for spatial filtering, and the constant-coefficient Smagorinsky model is employed for subgrid scale closure. Gaseous n-heptane is injected at 1000 K into an ambient gas comprising diluted air (15 % O_2 + 85 % N_2 molar) at 1000 K. A relatively high ambient pressure of 40 bar is chosen to simulate conditions in diesel combustion chambers. The inlet jet Reynolds number is 70,000, based on the injection velocity of 42.5 m/s and the inlet jet diameter (d) of 1 mm. This Reynolds number (Re) is representative of those in diesel jets where the injection velocity is higher and the diameter lower by an order-of-magnitude. A 3-D non-uniform grid with about 5.1 million grid points is employed to simulate a computational domain measuring 40dx14dx14d. The physical jet near-field region of interest extends up to 25d, beyond which a numerical sponge layer with exponential grid stretching and artificial damping is employed to prevent spurious pressure reflections from the exit boundary.

Results from the LES studies are discussed In Chapter 5. Turbulent statistics of the velocity-field and the mixture fraction field are computed by temporal and spatial (azimuthal) averaging of the instantaneous flowfield to estimate mean length-scales, velocity-scales and scalar dissipation rates, which are employed in the studies of flame-vortex interactions. To validate the LES model, computed means and variances of the velocity and mixture fraction fields are compared with available experimental data in self-similar jets. In particular, computed mean jet spreading rates and centerline decay rates based on the velocity and mixture fraction agree within 25 % with experimental data in self-similar constant-density and variable-density jets. On the other hand, the computed normalized mean radial profiles of axial velocity and mixture fraction agree within 10 % with measured data, though the profiles at different axial locations lack self-similarity. Greater differences with experimental data up to about 25 % and 20% were found with respect to normalized mean radial profiles

of turbulent kinetic energy and filtered mixture fraction variance, respectively. Apart from the inadequacies of the constant-coefficient Smagorinsky subgrid-scale model, the lack of self-similarity in the simulated near-field region is a likely cause for the discrepancies with measured data, which are available only in the self-similar region (x/d > 50). Nevertheless, the overall reasonable agreement (within 25 %) of the computed 1st and 2nd order statistics with measured data lends credence to the LES model employed here.

Mean integral length-scales (L_{11}) are estimated from the two-point space correlations of fluctuating axial velocities. At axial distances x/d=16 and x/d = 20, far enough from the potential core, the integral length-scales increase as we proceed downstream in the axial direction and radially away from the centerline for a given axial location. The quantitative estimates show good agreement with the experimental values of Wygnanski and Fiedler (1969) in self-similar jets. The range of values of the initial vortex length-scale (d_v) in the flame-vortex studies is chosen from the range of values estimated for L_{11} and Taylor microscales (λ) at different locations in the jet. Similarly, the initial vortex velocity-scale (u_v) is chosen from the range of values of the mean turbulent velocity-scale (q) which, as expected, decreases as we proceed downstream in the jet due to turbulent mixing. In addition, the time-averaged conditional mean scalar dissipation rates ($\overline{\chi}_Z$) are estimated at different axial locations in the jet. In qualitative agreement with the experiments of Namazian *et al.* (1988), $\overline{\chi}_Z$ shows a double-peak radial profile, and decays strongly (~ x^{-4}) as we proceed axially downstream in the jet. Accordingly, the mean diffusion layer thickness (δ) increases sharply at downstream jet locations. In contrast, L_{11} and q, show a gradual (~ x$^{1.0}$) increase and decrease, respectively, with axial location. This leads to decreasing values of the length-scale ratio l_r ($= d_v / \delta$) with increasing axial locations in the jet near-field. The implications of these trends on the localized flame dynamics are explored in the studies of flame-vortex interactions, which are discussed in Chapters 6 and 7.

In addition to temporal mean statistics, turbulent fluctuations of the stoichiometric conditional-mean scalar dissipation rates (χ_{st}) are characterized in the near-field of the jet. At upstream jet locations, e.g. at x/d = 12, close to the jet centerline (r/d $\leq$ 1.5), repeated excursions of χ_{st} above the steady extinction limit χ_e are observed. However, these excursions are relatively short-lived, and followed by relatively low values. The probability-density-function (PDF) of the time records of χ_{st} at the different jet locations x/d = 12, 16 and 20 are computed, and compared with the lognormal distribution. Consistent with trends reported in measurements (Namazian *et al.*, 1988, Effelsberg and Peters, 1988), the lognormal distribution provides a reasonable approximation for the PDF of χ_{st}. The unsteady response of diffusion flamelets to the turbulent fluctuations of χ_{st} in the jet near-field is investigated in Chapter 9.

11.2.2. Flame-Vortex Interaction Studies

Using the turbulent statistics from the LES, flame-vortex interaction studies are carried out to understand the likely regimes of localized flame dynamics in the near-field of the jet. Specifically, the initial characteristics of the vortex (d_v, u_v) and the flame (δ) are obtained from the mean turbulent statistics. In the flame-vortex interaction studies, effects due to unsteadiness and curvature are investigated, and the applicability of modeling approaches, such as flamelet and flamelet/progress variable models, are assessed.

Chapter 2 of the thesis reviews prior works related to non-premixed flame-vortex interactions. Though regimes, such as rollup and straining, have received considerable attention (Renard *et al.*, 2000), studies focusing on vortex-induced extinction and reignition are limited in the literature. Recent studies focusing on unsteady extinction (Santoro *et al.*, 2000; Katta *et al.*, 2004; Oh *et al.*, 2004) show that unsteady extinction scalar dissipation rates in vortex-perturbed flames could differ from steady limits, i.e. χ_e. In particular, when the vortex-to-flame

characteristic time scale ratio (τ_r) is greater than unity, the unsteady flame responds with a phase-lag to the imposed vortex-perturbation, and the delayed response renders the unsteady flame more resistant to extinction. In the present work, τ_r values up to 100 are simulated corresponding to 70,000-400,000 Re jets. Hence, strong unsteady effects on the flame-response are expected for the vortex-perturbed flames simulated here. Moreover, recent studies (Oh *et al.*, 2004) show that unsteady extinction limits are flow-dependent, and increase with increase in the vortex velocity-scale. Results from the present work corroborate the findings of Oh *et al.* (2004), and an extinction criterion more appropriate for unsteady flames than the $\chi = \chi_e$ criterion is proposed. Furthermore, the review of the flame-vortex studies in the literature shows that curvature effects, i.e. effects due to d_v, have received only limited attention. In the present work, curvature effects on extinction are clarified for relatively large vortex Reynolds numbers (> 100).

In addition to vortex-induced extinction, Chapter 2 reviews recent works on reignition phenomena in non-premixed flames. A recent DNS study of diffusion flames evolving in isotropic turbulence (Sripakagorn *et al.*, 2004) shows that following local extinction, reignition may occur either through autoignition, or through interactions with neighboring burning regions, which involve the dynamics of edge flames. Moreover, the DNS results indicate that reignition through autoignition is probable only when the excursions of χ_{st} above χ_e are relatively small, and last for a relatively short period. The importance of edge flame propagation scenarios for reignition phenomena has also been confirmed in recent experimental works on vortex-perturbed flames (Santoro *et al.*, 2000; Santoro and Gomez, 2002; Amantini *et al.*, 2005; Amantini *et al.*, 2007), and DNS studies of jet flames (Pantano, 2004; Hawkes *et al.*, 2007) at relatively low jet Re (< 10000). These studies show that the dynamics of edge flames is strongly influenced by the excursions of χ_{st} above χ_e, and the edges propagate towards the extinguished regions as ignition fronts only for values of χ_{st} smaller

than χ_e. Note, however, that studies above have considered quasi-steady flowfields, where the steady limit χ_e serves as a useful indictor of extinction and edge-flame propagation characteristics. In the present work, it is shown that χ_e is inappropriate for the highly unsteady flowfields encountered in the near-field of high-Re jets, and a criterion based on Da that is applicable to unsteady extinction/reignition is discussed. Moreover, studies so far have not clarified the effects due to curvature in unsteady flowfields with extinction/reignition phenomena, which is the focus of the present work. Moreover, conventional modeling approaches, such as steady flamelets (Peters, 1984), and the more recently developed flamelet/progress variable (FPV) models (Pierce and Moin, 2004; Pitsch and Ihme, 2005) have not been assessed for prediction of extinction/reignition. The present work provides an assessment of these models, and provides directions for the development of improved models.

The numerical formulation for the flame-vortex interaction studies is described in Chapter 4. The numerical schemes for spatial and temporal discretization and the implementation of boundary conditions are similar to those for the LES. A 1-D diffusion flame is initialized in the 2-D domain with pure n-heptane at 1000 K on one side, and 15 % O_2 + 85 % N_2 in molar composition at 1000 K on the other side. A counter-rotating vortex-pair from the air-side is allowed to self-propagate and impinge on the flame. The pressure is 40 bar to simulate conditions in diesel chambers. A single-step kinetic model with n-heptane as the representative fuel is employed. The flame-vortex interaction is characterized by the following set of non-dimensional numbers: the vortex-to-flame length-scale ratio l_r that governs curvature effects, the vortex-to-flame velocity-scale ratio u_{fv} that governs unsteady effects, the initial flame Damköhler number Da_i, which is a flame strength parameter affecting both unsteady and curvature effects through l_r and u_{fv}, the vortex Reynolds number Re_v, which represents the relative importance of viscous effects, and the vortex Damköhler number Da_v, which measures the relative magnitude of the characteristic vortex

time-scale with respect to the chemical time-scale. In addition, a scalar dissipation ratio χ_r is defined which measures the departure of the instantaneous scalar dissipation rate at the stoichiometric mixture fraction χ_{st} from the steady extinction limit χ_e, and hence quantifies unsteady extinction limits.

The results from the flame-vortex interaction studies are discussed in Chapters 6 and 7. These studies explore the regimes of localized flame dynamics in the jet near-field region, $12 \leq x/d \leq 20$, and $0 \leq r/d \leq 1.5$. The region close to the jet centerline is chosen, since the most energetic eddies capable of inducing critical regimes, such as local extinction/reignition, are likely to occur in this region. Moreover, the average values of L_{11}, λ, q and $\overline{\chi}_Z$ in the radial region, $0 \leq r/d \leq 1.5$, are employed at several axial locations to estimate the range of values for d_v, u_v and δ.

In Chapter 6, the flame-vortex interaction outcome for a baseline case, which corresponds to the axial location x/d = 12, is investigated. The non-dimensional parameters of interest have the following values at this axial location: $l_r = 1.5, u_{fv} = 5.85, Da_i = 30$. For these conditions, *local extinction* along the symmetry axis of the vortex-pair followed by *reignition* and *pocket formation* is observed. The extinction phase is characterized by strong unsteady effects due to the relatively large value of u_{fv} (> 1.0). The unsteady extinction limit, defined at $Da = 1$, is about 2 times the steady limit χ_e, clearly invalidating the use of steady flamelet libraries to predict the vortex-induced extinction behavior. In addition, the dominant heat loss mechanisms are convective and diffusive heat fluxes in the flame-normal direction. Heat fluxes in the lateral direction are relatively small. In other words, curvature effects are minimal during the extinction phase and the flame-response resembles that of a 1-D unsteady flamelet. On the other hand, the reignition phase is dominated by curvature effects. Through a series of transient events that involve rollup of the edge flames created after extinction, and flame-flame interactions manifesting as lateral heat and species diffusion from the edge-flames to the quenched region, a

reconnected, i.e. reignited, flame is established. Consistent with prior works (Santoro *et al.*, 2000; Pantano, 2004), the dynamics of the edge-flames is strongly influenced by the instantaneous scalar dissipation rate χ. While the edges initially recede away from the extinction hole due to values of χ higher than χ_e, the edge-flames propagate towards the quenched regions once χ values relax to values lower than χ_e due to the vortex-induced mixing.

In the context of modeling, it is shown in Section 6.5 of Chapter 6 that an unsteady flamelet/progress variable (UFPV) model (Pitsch and Ihme, 2005) accurately describes the unsteady extinction/reignition events observed in the flame-vortex studies. In the UFPV model, the instantaneous scalar dissipation rate (χ) and the instantaneous progress variable (c) are specified as model parameters. Possible ways to implement the UFPV model as a RANS/LES submodel are discussed in Section 6.5. It is emphasized that while the present work validates the UFPV model for the prediction of extinction/reignition from a fundamental, i.e. flame-vortex, viewpoint, accurate closure models for the source term and subgrid PDF of the progress variable would be required in the large-scale RANS/LES of a diesel jet flame.

Chapter 7 builds on the findings in Chapter 6 and explores the effects due to unsteadiness and curvature on the flame-vortex interaction outcomes for a wider range of non-dimensional parameters. In doing so, insight is provided into the range of possible outcomes of flame-turbulence interactions in the jet near-field. The studies show that the velocity-scale ratio u_fv governs unsteady effects. Consistent with the prior work of Oh *et al.* (2004) on vortex-induced extinction, the unsteady effects increase with an increase in u_fv and result in higher values of χ_r at extinction, and decreasing time scales for extinction. With respect to reignition, higher values of u_fv result in higher rates of partial-premixing and faster reignition. On the other hand, curvature effects are governed by the length-scale ratio l_r. Decreasing values of l_r result in faster rate of increase of χ_r, which

leads to shorter extinction time scales. However, due to minimal partial-premixing during the extinction phase, these hydrodynamic effects due to l_r on extinction are captured by 1-D unsteady flamelet models even for relatively small vortices ($l_r \sim 0.75$). The length-scale ratio (l_r) has a significant effect on reignition through flame-flame interactions aided by the vortex-induced curvature. In particular, larger vortices ($l_r = 3.0$) result in large extinguished regions with significant diluted fractions and considerable rollup of the edge flames, thereby decreasing the tendency for reignition. On the other hand, smaller vortices ($l_r = 0.75$) rapidly reignite following extinction due to strong flame-flame interactions and reduced rollup of the edge flames.

To specifically characterize the variation of unsteady and curvature effects in the jet near-field, the flame-vortex interaction outcomes corresponding to the near-centerline region at three axial locations, x/d = 12, 16 and 20, are compared. The comparisons show decreasing tendency for extinction and increasing tendency for reignition and pocket formation at downstream axial locations. It is shown that decreasing values of u_{fv} at downstream axial locations has a predominant influence on extinction, resulting in diminishing effects due to extinction and longer extinction time scales. On the other hand, decrease in values of l_r has a dominant effect on reignition, which leads to stronger flame-flame interactions and faster reignition. For the length scales relatively small compared to the flame ($l_r = 0.3$) that are likely to occur at downstream locations (x/d = 20), flame-flame interactions are strong enough to prevent extinction, so that we encounter *pocket formation regimes without extinction*. The observed interaction regimes are summarized on an outcome diagram constructed with l_r and u_{fv} as axes, which is useful to understand the nature of localized flame dynamics in the near-field of the jet. This outcome diagram represents universal trends based on flame-vortex interaction studies, which would be valid for a wide range of vortex and flame characteristics that result in non-dimensional numbers similar to those employed here. However, certain trends with respect to the jet,

such as increasing curvature effects with axial location, may be specific to the simulated near-field region (x/d < 25).

The studies discussed in Chapters 6 and 7 employ a single-step kinetic model for n-heptane. While the single-step kinetic model results in a well-defined chemical time-scale and non-dimensional numbers, such as $l_{\mathrm{r}}, u_{\mathrm{fv}}$ and Da_{i}, that govern the flame-vortex interactions, it is important to assess whether the physical mechanisms revealed by the single-step model results remain valid with realistic multistep chemistry. Hence, Chapter 8 focuses on flame-vortex interaction studies for a limited set of conditions using a skeletal 56-step kinetic mechanism for n-heptane, developed by Peters *et al.* (2002). The chosen mechanism is validated through comparisons with available experimental data at 1 bar for the prediction of non-premixed flame structure and extinction, as well as partially-premixed flame structure. However, in the absence of experimental data on flame extinction at 40 bar for mechanism-validation, we defer from drawing conclusions about reaction pathways and chemical species contributing to extinction/reignition. Instead, we focus on the physical mechanisms for extinction/reignition, and overall trends in the formation rates of major species such as CO_2 and H_2O, intermediates such as CO, and pollutants such as NO and UHC, for varying vortex length and velocity scales. The vortex and flame characteristics chosen for the multistep chemistry studies correspond to mean temporal statistics from LES at the jet location, x/d = 12, in the radial region, $0 \le r/d \le 1.5$.

The studies presented in Chapter 8 show similar qualitative trends with respect to physical mechanisms for extinction and reignition as those in Chapters 6 and 7. In particular, the vortex-perturbed flame extinguishes at χ_{st} values higher than χ_{e}, and the flame behaves as a 1-D unsteady flamelet until extinction with minimal effects due to partial-premixing. As in the case of the single-step model, lateral diffusion of heat and species from the rolled-up edge flames leads to reignition. Furthermore, consistent with the single-step model results discussed in Chapter 7, extinction/reignition time scales decrease as the vortex velocity

increases, and as the vortex length scale decreases. Hence, the outcome diagram and the conclusions drawn in Chapter 7 about the nature of variation of unsteady and curvature effects in the jet near-field with a single-step chemistry model are expected to hold for more detailed chemistry models.

In addition to the general conclusion drawn on single-step vis-à-vis multistep chemistry models, the studies of Chapter 8 provide useful insight into the spatio-temporal distribution of the major species and pollutants. Major species, such as CO_2 and H_2O, form predominantly in the reconnected flame, and their total concentrations increase with a decrease in the velocity scale due to increased flame rollup and burned areas and longer residence times. Similarly, the total concentrations of CO_2 decreases as the vortex length scale decreases due to reduced flame rollup and burned areas. On the other hand, maximum CO concentrations occur in the fuel-rich vortical pocket that forms during the reignition phase. Consequently, total CO concentrations increase with an increase in the vortex length-scale since larger fuel-rich pockets are formed. However, total CO concentrations show minimal changes with an increase in the velocity scale due to compensatory effects of partial-premixing that creates richer fractions in the vortical pocket (thereby increasing total CO), and straining that leads to thinner diffusion layers and reconnected flames (thereby decreasing total CO). The pollutant NO is observed to respond with a significant phase lag due to the vortex-perturbation, and shows a relatively small decrease (~ 20 %) during the extinction phase. In contrast, UHC responds much faster and increases by as much as 10 times during the extinction phase, before relaxing to values comparable to those in the unperturbed flame. This trade-off between NO and UHC is explored in detail in Chapter 9. Furthermore, peak concentrations of NO occur in the reconnected flame, due to high temperatures, and in the relatively fuel-rich pocket, possibly due to slow response times and unsteady effects. Similar to CO_2, the total NO concentrations increase with a decrease in the vortex velocity scale, and decrease as the length-scale is reduced. On the other hand, total UHC concentrations in the computational domain showed

minimal changes (within 5 %) due to interactions with the relatively small vortices employed here.

Implications of the findings discussed above from the flame-vortex interaction studies for turbulent combustion modeling in diesel jet flames is discussed in Section 10.3 of Chapter 10. Based on the findings, it is expected that unsteady effects would be important in the near-field of diesel jets, where flame lift-off occurs. Since extinction processes are known to contribute towards mechanisms for lift-off (Peters and Williams, 1983; Venugopal and Abraham, 2007), unsteady effects on local extinction need to be included in the modeling of the diesel jet near-field. In this context, an extinction criterion $Da = 1$, where Da is the Damköhler number based on the conditional mean scalar dissipation rate (χ_{st}) and the conditional mean source term of the progress variable ($\dot{w}_c$), is proposed. It is shown through investigations of vortex-induced extinction behavior for different vortex velocities that this criterion is more useful than the commonly employed $\chi_{st} = \chi_e$ criterion to predict trends in unsteady extinction and estimate unsteady extinction limits, regardless of the vortex and flame characteristics. This criterion may be employed in UFPV models, where the scalar dissipation rate and progress variable appear as model parameters.

Section 10.3 also discusses the implications of the findings related to reignition from the flame-vortex simulations for the near-field of diesel jets. The flame-vortex simulations corresponding to the near-field of the 70,000 Re jet show that reignition phenomena through edge flame dynamics are likely for relatively small values of the length-scale ratio l_r (< 3.0) and relatively large values of u_{fv} (> 1.0). In a higher Re (~ 400,000) jet representative of diesel applications, significantly higher values (up to 30 times) of the global strain rate (= U_{inj}/d) will result in thinner diffusion layers and larger values of l_r, which may favor reignition through autoignition. On the other hand, significantly higher injection velocities (about 10 times) will result in higher values of u_{fv}, which may promote edge-flame propagation scenarios. Due to these opposing effects, it is

expected that both autoignition and edge flame propagation scenarios for reignition will be important in diesel jets. In this work, we provide useful fundamental insight into these scenarios for reignition. In Section 10.3, one possible approach to account for edge flame effects in UFPV models is proposed, where $\dot{w}_c$ is related to the edge flame displacement speed, S_{edge}, which can be tabulated as a function of the Damköhler number at the edge location for lookup.

11.2.3. Unsteady Flamelet Studies

In order to gain insight into the simultaneous effects of a spectrum of turbulent scales on the local flame structure in the near-field of high-Reynolds number jets, the unsteady response of diffusion flamelets to turbulent fluctuations of the scalar dissipation rate(χ_{st}) is studied. The fluctuating time records are obtained from the analysis of the LES jet flowfield. As a preliminary step towards the understanding of the unsteady flame response, oscillatory perturbations with specified amplitudes and frequencies are also considered. The unsteady responses of the flame temperature, the major species CO_2 and H_2O, and the pollutants NO and UHC, are investigated, and the applicability of steady flamelet models is assessed. In addition, through an extrapolation of the analysis to higher-Re jets with higher global strain rates ($=U_{inj}/d$) closer to diesel jet flames, the unsteady temperature and species response during extinction/reignition events are studied, and the impact of these events on near-field phenomena, such as flame lift-off, are explored.

Chapter 2 discusses the findings from prior works (Im *et al.*, 1995; Egolfopoulos and Campbell, 1996; Kirsten *et al.*, 1998; Im et al., 1999; Welle *et al.*, 2003) on the unsteady response of diffusion flames. These studies were performed by imposing an oscillatory perturbation on the flame. Two important findings from existing studies are 1.) At high frequencies of the imposed perturbation, the flame responds with a phase-lag. 2.) The phase-lag effects

result in unsteady extinction strain rates higher than steady limits. In addition, the numerical studies of Im *et al.* (1999) on counterflow methane/air flames subjected to oscillatory strain show that the scalar dissipation rate is a more appropriate parameter than the strain rate to characterize unsteady flames. In the present work, we employ the flamelet formulation to investigate the unsteady response of diffusion flames, where the scalar dissipation rate directly appears as a parameter. Furthermore, the studies of Im *et al.* (1999) show that the responses of intermediates, such as CO, and pollutants, such as NO, are weak due to relatively slow chemical response time scales. Prior works so far have not considered unsteady effects on reignition phenomena following extinction, which are addressed in the present work. However, due to the choice of the 1-D flamelet formulation, reignition mechanisms involving edge flame dynamics, which were investigated in the flame-vortex interaction studies, cannot be captured. In the studies of diffusion flamelets subjected to χ_{st} oscillations and fluctuations, reignition occurs only through autoignition. Furthermore, the unsteady response of diffusion flames to *turbulent fluctuations* of χ_{st} has not been studied in the literature so far. In a diesel jet flame, autoignition scenarios for reignition are expected to be important due to the relatively large values of l_r resulting from significantly thin diffusion layers. In the regions close to the jet centerline (e.g. $r/d < 1$) at a given axial location, edge flame propagation scenarios, discussed in Chapters 6 and 7, would contribute as well due to the relatively large values of u_{fv}. However, at farther radial locations, larger values of l_r and lower values of u_{fv} would favor reignition through autoignition. Hence, in Chapter 9, we investigate the unsteady extinction, and reignition through autoignition, in the stoichiometric regions ($r/d > 1$) of the near-field of high-Re jets.

The results from the unsteady flamelet studies are discussed in Chapter 9. Turbulent time records (henceforth referred to as "flamelet histories") of χ_{st} in the near-field of the 70,000-Re jet are generated by Lagrangian-type tracking of stoichiometric contours (flamelets) in time and space across the near-field of the

jet (6< x/d < 20). Ten representative flamelet histories are computed, and the unsteady response of diffusion flamelets to these histories is studied. The unsteady flamelet equations are solved with the assumption of unity species Lewis numbers and n-heptane oxidation is modeled using a reduced mechanism comprising 159 species among 1540 reaction steps.

Results from studies employing oscillatory perturbations show that two non-dimensional numbers govern the unsteady flame response: 1.) the amplitude ratio AR, which represents the relative magnitude of the mixing time (inverse of oscillation amplitude) with respect to the chemical time($\sim \chi_e^{-1}$), and 2.) the time-scale ratio TR, which measures the relative magnitude of the residence time (inverse of oscillation frequency) with respect to the chemical time. It is shown that extinction/reignition events occur only for intermediate values for AR (< 4.0) and TR (< 10), which result in sufficient mixing and residence times, respectively. Examination of T_{st}-χ_{st} state diagrams reveal that the state points during reignition involve partially burned states, which can be distinguished from those during extinction through a reaction progress variable. For relatively large values for TR (~ 100) at a given value of AR, the flame is relatively insensitive to the imposed perturbation due to significant chemical phase-lag, and does not extinguish even for oscillatory amplitudes greater than χ_e (i.e. AR > 1.0). This qualitatively agrees with the trends reported in the flame-vortex studies (Chapters 6 and 7), where the vortex-perturbed flames are more resistant to extinction relative to steady flames. Moreover, predictions of the flame temperature from steady flamelet libraries show large deviations from those with unsteady flamelets at relatively large values of χ_{st} (> 0.3 χ_e), and the deviations increase as AR and TR increase. The observed oscillatory flame-response regimes were summarized on a AR-TR diagram, which is useful to understand unsteady effects on near-field jet flame dynamics.

With respect to species response to oscillatory perturbations, the major species, CO_2 and H_2O, show trends similar to those in the temperature, and

show a fast recovery during reignition following extinction. On the other hand, the pollutant NO responds with a significant phase-lag due to relatively slow chemical response times. Accordingly, the mean NO mass fractions significantly decrease as AR and TR increase in the extinction/reignition regime. This indicates that extinction/reignition events are beneficial in terms of both flame-stability and NO formation-control. However, unburned hydrocarbons (UHCs) respond much faster to the imposed perturbations, and the mean UHC mass fractions increase with AR and TR in the extinction/reignition regime, leading to trade-offs between NO and UHC. However, the much greater sensitivity of NO to the temperature and scalar dissipation relative to UHC indicates that temporary flame weakening events followed flame recovery may be more useful than extinction/reignition events in the simultaneous control of these pollutants.

To gain insight into the simultaneous effects of a spectrum of turbulent scales, the unsteady flame response to the ten representative flamelet histories generated from the LES jet flowfield is studied. The flamelet histories generated from the 70,000 Re jet at relatively farther radial locations (r/d > 2.0) in the jet near-field (6<x/d<20) consists of relatively small means (~ $0.06\chi_e$) and RMS values (~ $0.06\chi_e$), and relatively small amplitudes (AR ~ 0.3). Accordingly, temporary flame weakening followed by flame recovery is observed in the unsteady flame response to the fluctuating time records. Predictions from a steady flamelet library corresponding to the instantaneous values of χ_{st} from the time records are compared with unsteady flamelets. Mean values of temperature, major species and UHCs agree well, but differences up to 20 % are observed with respect to mean NO fractions. Hence, in the 70,000 Re jet simulated with LES, steady flamelet models are adequate at farther radial locations (r/d > 2.0) in the jet near-field (6 < x/d < 20) to predict the mean temperature, and mass fractions of major species and UHCs, and are reasonable for the predictions of mean NO fractions.

The analysis is extrapolated to jets with higher global strain rates ($=U_{\text{inj}}/d$) that are closer to practical applications, such as diesel engines. In particular, the means and RMS values of the flamelet histories are increased by a factor of 5, which leads to local extinction/reignition events. Steady flamelet models are found to significantly underestimate temperatures during extinction, and significantly overestimate temperatures during reignition. This arises from the inherent inability of steady flamelets to account for transient chemical phase-lag effects. However, due to these compensatory effects during extinction and reignition, mean values of temperature agree well (within 5 %) between the unsteady and steady flamelet models. Nevertheless, the lack of phase-lag effects in steady flamelets has a drastic impact on mean mass fractions of NO, where differences up to an order of magnitude are observed at upstream jet locations (x/d < 14). On the other hand, steady flamelet predictions of mean UHC mass fractions agree well with unsteady flamelets due to faster chemical response times. Furthermore, in order to assess the role of the transient flame response to fluctuations of χ_{st}, predictions from a steady-flamelet-steady-strain (SFSS) model, which accounts only for the steady (or mean) value of the temperature (or species mass fraction) at the steady(or mean) value of χ_{st}, are compared with unsteady and steady flamelets. These comparisons reveal discrepancies between the SFSS and steady/unsteady flamelet models at upstream jet locations (e.g. x/d = 12), where the SFSS model predicts somewhat lower (~ 15%) temperatures. At these locations, the steady/unsteady flamelet models predict higher temperatures due to transient reignition events that are ignored by the SFSS model. As expected, the SFSS model performs poorly with respect to NO mass fractions at upstream jet locations (x/d < 14).

The practical implications of the findings discussed above from the unsteady flamelet studies are discussed in Section 10.2 of Chapter 10. In particular, it is shown that the qualitative trends observed in the recent experiments of Pickett *et al.* (2008) on transient flame lift-off behavior in the presence of laser-ignition upstream of the steady lift-off height can be explained

based on effects due to flow-unsteadiness on the local flame response. It is assumed that the scalar dissipation rate amplitudes in the pre-lift-off region decrease due to combustion heat release from the laser-ignited flamelets. With this assumption, the laser-ignited flamelets are sustained for a relatively long time (i.e. much longer than jet characteristic time scales), and gradually convect to the natural lift-off location. These trends agree well with those observed in the measurements. Hence, results presented in Chapter 10 indicate that unsteady effects on the localized flame dynamics in the jet near-field contribute towards mechanisms for diesel flame lift-off.

In addition to transient lift-off behavior, the role of unsteady effects on the predictions of steady lift-off in higher strain rate jets representative of diesel applications are explored. Lower fuel temperatures (= 450 K) more common in diesel engines, which result in lower mean Damköhler numbers of the near-field flamelets, are employed. Scenarios involving extinguishing/reigniting flamelets and autoigniting/extinguishing/reigniting flamelets under fluctuating scalar dissipation rates are simulated. The results indicate that flame lift-off can occur at the axial location where multiple flamelet histories predominantly result in extinction, with low probability of reignition and autoignition of the flamelets. Furthermore, the SFSS model underestimates the temperatures by as much as 30-40 % at upstream jet locations (x/d = 12) relative to steady and unsteady flamelet models, indicating the importance of transient flame response to scalar dissipation rate fluctuations for the predictions of steady lift-off heights. In summary, the present results show that while steady flamelet models in the context of LES, i.e. accounting for flow-unsteadiness but not chemical phase-lag effects, are adequate for the prediction of mean temperatures, and mass fractions of major species and UHCs, unsteady flamelets, i.e. accounting for both flow-unsteadiness and chemical phase-lag effects, are needed for mean NO predictions.

In the next section, we discuss some of the important assumptions invoked in this work, and the possible implications of the assumptions on the

conclusions. The future work discussed in the final section will suggest ways to relax some of these assumptions.

11.3. Key Assumptions and Implications

This work involves some important assumptions, such as *non-reacting* LES, *2-D* flame-vortex interaction studies, *single-vortex*-flame simulations, and *specific choices* for the fuel temperature, injected-to-ambient gas density ratio, and pressure. Below, we discuss these assumptions and their implications on the results.

11.3.1. Heat-Release Effects on Turbulent Statistics Computed with LES

We employed a non-reacting LES computation to estimate turbulent statistics in the jet. We then employed these statistics to derive characteristic length and velocity scales, and scalar dissipation rates, and used these in flame-vortex interaction studies to draw conclusions about flame dynamics in the jet. Moreover, turbulent time records of the scalar dissipation rates were computed from the non-reacting LES flowfield, and then employed in studies investigating the unsteady response of flamelets.

However, heat release in the jet can influence the predicted length and velocity scales, and scalar dissipation rates. DNS studies of reacting shear layers (McMurtry *et al.,* 1989) indicate a reduction in the entrainment and spreading rates due to combustion heat release. This may result from greater viscous dissipation in the flowfield. Similarly, recent DNS studies of Pantano *et al.* (2003) in reacting mixing layers show that turbulent kinetic energies and turbulent dissipation rates, as well as scalar variances and dissipation rates show a moderate sensitivity to heat release. For instance, the authors found that while the peak values of the scalar dissipation rate in reacting mixing layers decrease by up to 30 % relative to non-reacting mixing layers, reacting mixing layers with different levels of heat release show minor differences. On the other hand, recent

LES studies and experiments of Geyer *et al.* (2005) in turbulent opposed-flow jets show that combustion heat release increases scalar dissipation rate magnitudes due to increased diffusivities. Note that these DNS studies are carried out at Re values that are fairly low (< 10000), and the effects of combustion heat release on turbulent statistics in high-Re jets are not known to the best of our knowledge.

In the LES-flame-vortex studies, we are primarily interested in non-dimensional numbers constructed from LES statistics, such as l_r, u_{fv} and Da_i. The presence of heat release may shift the range of the estimated non-dimensional numbers, but the trends observed in the present work with respect to changes in l_r, u_{fv} and Da_i in the near-field of the jet would not be affected. The interesting point, however, is this: from the flame-vortex studies discussed in Chapter 7, we concluded that at x/d=12, extinction predominates followed by reignition aided by curvature effects. How will this behavior change, i.e. at x/d=12, as result of heat release? In other words, will heat release change the parameters in such a way that extinction is no longer favored? We do not have an answer to this question. For the relatively high Reynolds number of 70,000, it is computationally challenging to perform reacting LES with sufficient numerical resolution. In this context, the present LES adequately resolves the mixing characteristics in the jet near-field as evidenced in the reasonable agreement between predicted statistics and measurements in non-reacting jets. We consider our approach to be a reasonable compromise between computational cost and numerical accuracy.

Similarly, with respect to studies investigating the unsteady response of flamelets, it is likely that scalar dissipation rate amplitudes in the generated flamelet histories would be affected by heat release in the jet. However, the DNS of Pantano *et al.* (2003) in reacting shear layers and the LES studies of Pitsch and Steiner (2000b) in reacting jets show that PDFs of conditional mean scalar dissipation rates, i.e. χ_{st}, show lognormality, just as in the case of the non-reacting jet simulated here (see Section 5.3.2). Hence, it is expected that the

nature of fluctuations of χ_{st} computed in the present case for the near-field of a non-reacting jet is fairly representative of the fluctuations in the presence of heat-release and reaction zones, even though magnitudes encountered are likely to differ. In addition, with respect to jet near-field phenomena, such as flame lift-off, it is well-known that theories entirely based on the large-scale mixing behavior of isothermal jets (Broadwell *et al.*, 1985; Pitts, 1989) have met with reasonable success in qualitatively and quantitatively predicting experimental trends (Pitts, 1989). Therefore, in the near-field of high-Re jets, where local extinction/reignition events are expected to predominate, the effects of heat release on the mixing behavior from quenched or partially-burning reaction zones may not be significant.

Nevertheless, the exploration of heat release effects on velocity and scalar statistics in the near-field of high-Re jets is an important and interesting avenue for future studies. Some approaches to address the effects of heat release are discussed in the next chapter.

11.3.2. 2-D Flame-vortex Studies

We neglected 3-D effects, such as vortex stretching, in the flame-vortex studies. The 2-D assumption is typical in flame-vortex simulations (Renard *et al.*, 2000), including recent 2-D flame-vortex studies (Oh *et al.*, 2004; Amantini *et al.*, 2007), which have provided useful insights into unsteady and curvature effects on non-premixed flame structure. Early analytical studies of Karagozian and Marble (1984) employing asymptotic methods compared the vortex-perturbed flame structure with a 2-D planar vortex and a 3-D vortex stretched along its axis. Based on their analysis, the authors concluded that the augmentation of the reactant consumption rate due to the vortex is independent of vortex-stretching. The predominant difference was in the manner in which the combustion products were distributed in the vortex. Nevertheless, based the results discussed in Chapters 6 and 7, it is expected that vortex-induced extinction would be

minimally affected by 3-D effects, since negligible amounts of partial-premixing due to the vortex-induced curvature occur in the extinction phase. However, the reignition phase would be affected, since lateral diffusion from the rolled up edge flames would occur along two directions in the 3-D case. Hence, it is expected that reignition time scales and scalar dissipation rates would be affected. However, our qualitative conclusions regarding the importance of unsteady and curvature effects on extinction/reignition, and the applicability of modeling approaches, such as UFPV models, are likely to be valid in a 3-D flame-vortex simulation as well. Therefore, given the relatively large number of flame-vortex simulations performed here to represent the near-field region of the jet, the 2-D assumption is a reasonable compromise between computational cost and accuracy.

11.3.3. Single-Vortex-Flame Simulations

The present work correlates the observed interaction outcomes in single-vortex-flame simulations to likely regimes of localized flame dynamics in a turbulent jet flame, where the flame may interact with a spectrum of vortices. It is well-known that the single-vortex-flame interaction is a canonical configuration, useful to isolate effects due to unsteadiness and curvature. Moreover, if a modeling framework, such as the UFPV model, has to be valid in a turbulent jet flame, it should be applicable in a simpler configuration, such as a flame-vortex interaction. Hence, the flame-vortex simulation database serves as a useful tool for the validation and development of improved modeling approaches. It is evident, however, that by considering an isolated vortex-perturbed flame, we cannot gain insight into the relative probabilities of local extinction/reignition events in a large-scale jet flame, and the extent to which these events may affect outcomes, such as flame lift-off height. For instance, in terms of jet characteristic times (t_j) introduced in Chapter 10, the vortex-induced extinction/reignition events across the range of conditions employed do not last longer than about $4t_j$, which is of order of 0.2 ms for the 70,000-Re jet considered here. Hence, the unsteady

extinction/reignition events occur over relatively short time scales, and may not have a significant impact on the mean flame structure unless they occur with sufficient probability.

In addition, studies investigating response of flamelets to scalar dissipation rate fluctuations (Chapter 9) showed that relatively large excursions of the scalar dissipation rate locally in the simulated 70,000-Re jet are relatively short lived, implying that local extinction/reignition events may not occur with a high probability. In this context, it is possible that the flame-vortex studies somewhat overestimate the importance of extinction/reignition events, or the failure of steady flamelet models in the jet near-field. However, it was shown in Section 10.2 that as we approach jet flames with relatively high global strain rates and relatively strained near-field flamelets (such as in diesel jet flames), unsteady effects and local extinction/reignition events may occur with sufficient probabilities to influence phenomena such as lift-off.

11.3.4. Choice of the Fuel Temperature, Density Ratio and Pressure

In the present work, we employed a relatively high fuel temperature, i.e. 1000 K, in the LES, and in the flame-vortex and unsteady flamelet studies corresponding to the information obtained from LES. In addition, to assess the influence of the higher fuel temperature, comparisons with simulations employing a lower fuel temperature, i.e. 450 K, were presented in Chapters 6-10. While the choice of the high fuel temperature influences the injected-to-ambient gas density ratio in the LES, which would show scaling behavior in the predicted statistics (Pitts, 1991; Abraham, 1999), chemical time scales are affected in the flame-vortex and unsteady flamelet studies. Lower fuel temperatures (~ 400 K) typical of diesel engine applications will result in weaker (or relatively strained) flames with higher values of u_{fv} and lower values of Da_i for given vortex characteristics (i.e. d_v and u_v). For instance, as shown in Chapter 7 and in our recent publication (Venugopal and Abraham, 2008a), employing a fuel temperature of

450 K and larger values of u_{fv} (> 100) result in greater unsteady effects, leading to higher unsteady extinction limits, than those observed here.

In addition, note that as the temperature of n-heptane is increased from 450 K to 1000 K, the autoignition chemistry transitions from a single-stage to two-stage (Liu *et al.*, 2005). However, based on the DNS studies of Sripakagorn *et al.* (2004) and our flame-vortex studies with multi-step n-heptane chemistry (see Chapter 8), the reignition scenarios are governed by edge flame dynamics and not autoignition for the conditions simulated in this work. Essentially, due to the relatively stronger, i.e. u_{fv} > 1.0, and smaller, i.e. l_{r} < 3.0, vortices employed here, the excursions of the scalar dissipation rate above the steady limit are strong enough, i.e. χ_{r} >> 1, to cause reignition to occur through edge flame interactions before autoignition can occur. Hence, kinetic effects, such as single-stage vs. two-stage autoignition, related to the choice of a relatively high fuel temperature is not of importance for the range of vortex and flame characteristics simulated here. This is consistent with the use of a relatively simple (single-step) kinetic model in the studies reported in Chapters 6 and 7, and the qualitative agreement between the single-step and the multistep chemistry results (Chapter 8) with respect to physical mechanisms.

The present work is focused on the nature of localized flame dynamics in a variable-density jet, with an injected-to-ambient gas density ratio of 3.5. If lower temperatures (~ 400 K), more common in diesel applications, are employed for gaseous n-heptane, the density ratio would be higher (~ 8). In self-similar jets, the density ratio is known to show scaling behavior (Pitts, 1991; Abraham, 1996), but the density ratio effects in the near-field of the jet need assessment. It is likely that the nature of turbulent fluctuations of the scalar dissipation rate would change with density ratio, and certain trends, such as relatively short lived peak values, may be affected. As evident in Chapter 9 and the present chapter (Section 10.2), the validity of steady flamelet models is closely related to the nature of fluctuations of χ_{st}. In the flame-vortex studies discussed in Chapters 7 and 8, we reported simulations (Venugopal and

Abraham, 2008a, b) that employ a lower fuel temperature (= 450 K) that result in a fuel-to-oxidizer density ratio of 8, as against 3.5 with a fuel temperature of 1000 K. These studies show that the density ratio primarily has a hydrodynamic effect, i.e. a higher density ratio leads to shorter residence times for the air-side vortex, thereby decreasing the time scales for extinction and reignition. However, the effects of density ratio on the predicted mean statistics and fluctuations of scalars in the jet near-field needs to be clarified in future investigations.

Furthermore, we simulated relatively high pressures (~ 40 bar) to represent conditions that exist in diesel combustion chambers. Pressure influences the molecular transport properties and chemical time scales. These effects are built into the Reynolds number (Re_v) and the Damköhler number (Da). Moreover, we assumed an ideal gas equation of state (EOS) in the present work, whereas real-gas effects may become significant at high pressures. Our recent studies (Venugopal and Abraham, 2008b) show that even at a fuel temperature of 450 K when the compressibility of n-heptane at 40 bar significantly deviates from unity (Moran and Shapiro, 2000), the temperature and species concentrations in the flame-zone are negligibly affected by the EOS due to the predominant presence of diluents like N_2. Hence, with a fuel temperature of 1000 K, real-gas effects are expected to be negligible in the flame-zone.

11.4. Future Work

It is suggested that future work focus on the following:

1. Evaluate the effects of combustion heat-release on turbulent statistics of the velocity and mixture fraction in the near-field of high-Re jets using reacting-LES with simplified chemistry,

2. Evaluate the density ratio effects on the near-field turbulent statistics through LES of high-Re jets with varying density ratios,

3. Reacting-LES of high-Re jets to predict steady and transient flame lift-off behavior with steady flamelet and UFPV sub-models,

4. RANS simulations of combusting diesel jets with the UFPV sub-
model to predict steady lift-off heights.

The first item is related to the effects of combustion heat release on the turbulent statistics in the near-field of high-Re jets, which were not clarified in the present work. Reacting-LES studies with different levels of heat release can be performed, and effects of heat release can be assessed through comparisons of predicted statistics, such as mean length and velocity scales, and scalar dissipation rates, with the present non-reacting jet results. As a preliminary step, a simplified single-step kinetic model can be employed, where the kinetic rate coefficients can be adjusted to obtain different levels of heat release. Based on the present work, steady flamelet models within the framework of LES may be reasonable for the prediction of mean statistics in the reacting jet, though it would be useful to compare with UFPV models as well, especially to study the effects of heat release on the turbulent fluctuations and PDFs of the scalar dissipation rate. As discussed in Section 6.5.2 of Chapter 6, pre-computed libraries for the filtered reactive scalars, i.e. temperatures and species mass fractions, can be generated for both steady flamelet and UFPV models, and the scalars computed through interpolation in the LES jet flowfield. It would be interesting to investigate the extent to which the outcome diagram for jet near-field flame dynamics presented in Chapter 7 changes with respect to spatial information in the jet, i.e. spatial locations of regimes such as extinction and reignition, due to heat-release. Moreover, since the statistically stationary structure of the jet is of interest here, the present non-reacting LES jet flowfield can be used as an initial condition for the reacting simulations, which would significantly save computational time.

In the case of reacting-LES with the steady flamelet model, a steady flamelet library and a PDF lookup table are pre-computed, so that the filtered reactive scalars (i.e. temperature and mass fractions) in every numerical cell are computed through interpolation based on the mixture fraction and its variance, and the scalar dissipation rate. Hence, the additional computational costs beyond the non-reacting LES arise primarily from interpolation, which would at most

result in a 10 % increase in the CPU time per time-step. Moreover, note that while the present non-reacting LES tracked all the species mass fractions, only the mixture fraction and its variance are tracked in the reacting-LES with the steady flamelet model, which may offset the interpolation costs. The UFPV model would result in greater interpolation costs, possibly up to a 15 % increase in the CPU time per time-step, due to the addition of the progress variable as a tracking scalar. However, the presence of heat-release, and the associated temperature and density gradients, would result in smaller time steps relative to non-reacting simulations, which could increase the simulation time. In addition, the numerical stability of the 6th-order compact scheme (Lele, 1992) employed for the non-reacting LES needs assessment in the presence of higher gradients due to heat release. It is typical in the literature (Pitsch, 2006) to perform reacting-LES with lower-order (~3rd) schemes.

Density ratio effects on turbulent statistics in the near-field of high-Reynolds number jets can be studied using non-reacting LES of higher and lower density ratio jets than that employed here (= 3.5). For instance, two simulations with density ratios of 8 and 1 can be performed, and the present LES database can be employed for comparison. One interesting aspect is the effect of density ratio on the turbulent fluctuations and PDFs of the scalar dissipation rate, which can affect the probabilities of local extinction/reignition events in the jet, and hence the validity of steady flamelet models. Moreover, the effects of density ratio on mean length and velocity scales, and scalar dissipation rates can have important implications for the localized flame dynamics in the jet. For instance, as the injected-to-ambient gas density ratio increases, the decay rates of the velocity field and mixture fraction decrease, thereby decreasing the decay rates of the velocity scales and scalar dissipation rates. Even though these effects are expected to show scaling behavior in the far-field (x/d > 100), it is important to investigate trends in the near-field of the jet. As evident in the present work, the nature of variation of the length and velocity scales, and scalar dissipation rates in the jet near-field influences the nature of variation of the non-dimensional

numbers, such as the length and velocity scale ratios, which govern unsteady and curvature effects on the localized flame dynamics.

In order to simulate higher density ratio (> 3.5) jets, higher numerical resolution would be required in the LES. Based on the scaling behavior of jets with respect to the density ratio (see Eq. (5.4)), the numerical resolution in each direction has to be increased by at least a factor of 1.5 when the density ratio is increased from 3.5 (present case) to 8. While the total number of grid points increases by a factor of 4 (i.e. to about 20 million), the time-step is approximately halved for the higher density ratio simulation. Hence, for the same CPU time per time-step as the lower density ratio case, the number of processors would have to be increased by a factor of 4, i.e. to 512. However, the total simulation time would approximately double due to the reduction in the time-step. On the other hand, based on similar scaling arguments, the unity density ratio LES can be performed with about 0.6 million grid points. Furthermore, based on the reasonable agreement with measured statistics observed in the present work, the compressible form of the constant-coefficient Smagorinsky model is expected to be adequate for the higher density ratio simulation as well.

The third aspect is related to reacting-LES of gaseous-fueled jet flames under diesel engine conditions to study transient and steady flame lift-off behavior. Naturally, this is challenging from both modeling and computational-cost viewpoints, and by no means a straightforward extension of this work. Note that a particularly challenging aspect in the context of simulating diesel jet flames is to account for the relatively large values of the global strain rates ($=U_{\text{inj}}/d$).

For instance, the scaling arguments presented in Section 10.2 of Chapter 10 showed that a gaseous fuel jet equivalent, i.e. having the same mass and momentum flow rates, to the measured diesel jet of Pickett *et al.* (2008) has an injection velocity of 580 m/s and an orifice diameter of 0.4 mm. This represents a global strain rate about 34 times greater than the present jet, implying that the scalar dissipation rates are expected to be much higher, resulting in much thinner diffusion layers. Note that the Re increases only by a factor of 5 from the present

jet to the equivalent diesel jet. Hence, the numerical resolution requirements for adequately resolving scalar statistics are expected to be much more severe than those from Re-based scaling.

It is proposed that as in the case of the analysis presented in Chapter 9, a moderate increase in the global strain rate, by a factor of 5, can be employed. For instance, the injection velocity can be increased 5 times keeping the diameter constant, so that the Re of the jet increases 5 times, i.e. to about 350,000. Since the diffusion layer thicknesses scale inversely as the square-root of the strain rates, a factor of 5 increase in the strain rates would result in diffusion thicknesses roughly half of those in the present 70,000 Re jet. Hence, the numerical resolution in each direction would have to be increased by a factor of 2, resulting in a 8-fold increase in the total number of grid points (i.e. to about 40 million). In addition, the time steps would decrease due to the increased resolution and increased gradients from combustion heat-release. Note that this 8-fold increase in the number of grid points is an upper estimate, since the resolution can be doubled only in the regions of interest, e.g. jet shear layers, and not in farther radial locations at a given axial location. Since the objective here is to quantify lift-off heights, realistic multistep chemistry is required, which would increase the interpolation costs, specifically with the UFPV model, where the pre-computed library is relatively large as discussed in Section 6.5.1. The computational requirements estimated here are for the LES of a 350,000 Re jet with a density ratio of about 3.5. With density ratios closer to diesel applications ($\sim$ 8), the numerical resolution requirements would increase further, as discussed before. Hence, reacting-LES of high-Re jets under diesel conditions with even moderately high global strain rates is challenging from a computational-cost point of view.

The linear scaling of lift-off with injection velocity can be used to estimate the expected lift-off height in the simulated jet. Based on the present findings, the UFPV model, which accounts for unsteady extinction/reignition, is proposed as the combustion sub-model. The model implementation procedure for the UFPV

model was outlined in Section 6.5.2. As a first-step, reignition may be assumed to occur only through autoignition in the jet, so that closure for the progress variable source-term can be obtained directly from the unsteady flamelet equations, as discussed in Chapter 6. Moreover, based on the recent LES studies of Pierce and Moin (2004) employing the steady FPV model, a relatively simple delta function model can be presumed for the subgrid PDF of the progress variable. A skeletal n-heptane mechanism, such as the 56-step mechanism employed in Chapter 8, can be used to generate the UFPV library.

The final aspect is related to RANS simulations of lifted diesel jets with UFPV sub-models. The procedure outlined in Section 6.5.2 is applicable for the implementation of the UFPV model as a RANS sub-model as well. The RANS-based UFPV model would be an improvement over the more commonly employed representative interactive flamelet (RIF) models (Pitsch *et al.*, 1995), since the UFPV model provides a better spatial resolution of the mean scalar dissipation rates ($\overline{\chi}$) in the jet. In particular, RIF models employ a spatially averaged value of $\overline{\chi}$ representative of a certain region of the jet flowfield, thereby resulting in a poor resolution of the spatial variation of $\overline{\chi}$ in the jet near-field. On the other hand, the UFPV approach models each numerical cell as a flamelet, and obtains the mean reactive scalars using a pre-computed UFPV library and interpolation based on the local values of the mean mixture fraction, scalar dissipation rate and the progress variable. For this reason, UFPV models would also be more effective than RIF models in the prediction of localized autoignition spots in the jet, which in turn can affect steady flame lift-off predictions. Detailed kinetic models for n-heptane can be employed to generate the UFPV library. UFPV models accounting for reignition through both autoignition and edge flame propagation scenarios can be employed. However, further studies are required to develop the model closure incorporating edge-flame effects proposed in Section 10.3. For instance, fundamental studies of edge/triple flames propagating in strained diffusion layers can be employed to

develop functional relationships between the edge-flame propagation speed and the Damköhler number.

Based on prior studies (Pitsch and Steiner, 2000b, Pantano *et al.*, 2003) and the present work, the turbulent fluctuations of the scalar dissipation rate χ can be mimicked by presuming the lognormal distribution as the temporal PDF of χ. However, as discussed in Chapter 5, the relatively high and low values of χ that are important for extinction/reignition and form the tails of the temporal PDF may not be captured by the lognormal distribution. Similarly, effects due to unsteadiness that result in unsteady extinction limits higher than steady values, cannot be adequately captured in RANS-based models. Nevertheless, due to the significant savings in computational times with RANS approaches relative to the LES computations discussed before, RANS simulations with improved UFPV models are useful directions for future works focusing on the prediction of jet near-field phenomena, such as lift-off, and their effects on pollutant formation in diesel jet flames.

LIST OF REFERENCES

LIST OF REFERENCES

Abraham, J., Reitz, R.D., and Bracco, F.V. (1985). Comparisons of Computed and Measured Premixed-Charge Engine Combustion. *Combustion and Flame,* 60:309-322.

Abraham, J. (1996). Entrainment Characteristics of Transient Gas Jets. *Numerical Heat Transfer,* 30: 347-364.

Abraham, J. (1997). What is Adequate Resolution in the Numerical Computations of Transient Jets? *SAE Transactions*, 106: 141-155.

Abraham, J. and Magi, V. (1997). Exploring Velocity and Density Ratio Effects in a Mixing Layer Using DNS. *Short Communication, International Journal of Computational Fluid Dynamics*, 8:147-151.

Abraham, J. and Magi, V. (1999). A Virtual-liquid-source (VLS) Model for Vaporizing Diesel Sprays. *SAE Paper 1999-01-0911*.

Amantini, G., Frank, J.H. and Gomez, A. (2005). Experiments on Standing and Traveling Edge Flames around Flame Holes. *Proceedings of the Combustion Institute*, 30: 313-321.

Amantini, G., Frank, J.H., Smooke, M.D. and Gomez, A. (2006). Computational and Experimental Study of Standing Methane Edge Flames in the Two-Dimensional Axisymmetric Counterflow Geometry. *Combustion and Flame*, 147:133-149.

Amsden, A. (1993). KIVA-3: A KIVA program with Block Structured Mesh for Complex Geometries. *Los Alamos Laboratory Report No. LA – 12503- MS.*

Anders, J.W. *Turbulence and Residual Gas Effects in Pulsed Diesel Jets*, PhD Thesis, Purdue University, August 2006.

Anders, J.W., Magi, V., and Abraham, J. (2007). Large-eddy Simulation in the Near-field of a Transient Multicomponent Gas Jet with Density Gradients. *Computers and Fluids,* 36:1609-1620.

Anders, J.W., Venugopal, R., Magi, V., and Abraham, J. (2008). A Study of Flame-Vortex Interactions in the Presence of Residual Gases. *Combustion Science and Technology*, 180: 1395-1420.

Andersson, N., Eriksson, L-E., and Davidson, L. (2005). Effects of Inflow Conditions and Subgrid Model on LES for Turbulent Jets. *AIAA Paper* 20005-2925.

Ashurst, W.T. (1989). Vorticity Generation in a Non-premixed Flame Sheet. *In: Numerical Combustion, Lecture Notes in Physics*, Berlin, Springer, 351, p. 3.

Barlow, R.S., and Frank, J.H. (1998). Effects of Turbulence on Species Mass Fractions in Methane/Air Jet Flames. *Proceedings of the Combustion Institute*, 27:1087-1095.

Birch, A.D., Brown, D.R., Dodson, M.G. and Thomas, J.R. (1978). Turbulent Concentration Field of a Methane Jet. *Journal of Fluid Mechanics*, 88:431-449.

Bird, R.B., Stewart, W.E., Lightfoot, E.N. (1960). *Transport Phenomena*. Wiley, New York, p. 571.

Bogey, C., Bailley, C. and Juve, D. (2003). Noise Investigation in a High Subsonic Moderate Reynolds Number Jet using a Compressible Large Eddy Simulation. *Theoretical & Computational Fluid Dynamics*, 16:273-297.

Bogey, C. and Bailly, C. (2004). A family of low dispersive and low dissipative explicit schemes for flow and noise computations. *Journal of Computational Physics*, 194: 194-214.

Boris, J.P., Grinstein, F.F., Oran, E.S. and Kolbe, R.L. (1992). New Insights into Large-eddy Simulation. *Fluid Dynamics Research*, 10: 199-228.

Bracco, F.V. (1985). Modeling of Engine Sprays. *SAE Transactions,* 94:144-167.

Broadwell, J.E., Dahm, W.J.A., and Mungal, M. (1985). Blowout of Turbulent Diffusion Flames. *Proceedings of the. Combustion Institute*, 20:303-310.

Buckmaster, J.D. (2002). Edge Flames. *Progress in Energy and Combustion Science*, 28:435-475.

Carnahan, B. *Applied Numerical Methods.* John Wiley & Sons Inc., New York (1969), p. 363.

Chomiak, J. and Karlsson, A. (1996). Flame Lift-off in Diesel Sprays. *Proceedings of the Combustion Institute,* 26:2557-2564.

Cuenot, B. and Poinsot, T. (1994). Effects of Unsteadiness and Curvature on Diffusion Flames: Implications for Turbulent Diffusion Combustion. *Proceedings of the Combustion Institute,* 25:1383-1390.

Davies, P.O.A.L., Fisher, M.J. and Barratt, M.J. (1962). The Characteristics of the Turbulence in the Mixing Region of a Round Jet. *Journal of Fluid Mechanics*, 15:337-367.

Daou, J. and Linan, A. (1998). The Role of Unequal Diffusivities in Ignition and Extinction Fronts in Strained Mixing Layers. *Combustion Theory and Modeling*, 2:449-477.

DeBonius, J.R. and Scott, J.R. (2002). Large-eddy Simulation of a Turbulent Compressible Round Jet. *AIAA Journal*, 40:1346-1354.

Dec, J.E. (1997). A Conceptual Model of DI Diesel Combustion Based on Laser Sheet Imaging. *SAE Paper 970873.*

Dold, J. W. (1988). Flame Propagation in a Nonuniform Mixture: The Structure of Anchored Triple Flames. *Progress in Aeronautics and Astronautics*, 113:240-248.

Echekki, T. and Chen, J.H. (1998). Structure and Propagation of Methanol-air Triple Flames. *Combustion and Flame*, 114: 231-245.

Effelsberg, E. and Peters, N. (1988). Scalar Dissipation Rates in Turbulent Jets and Jet Diffusion Flames. *Proceedings of the Combustion Institute*, 22: 693-700.

Egolfopoulos, F.N. and Campbell, C.S. (1996). Unsteady Counterflowing Strained Diffusion Flames:Diffusion-limited Frequency Response. *Journal of Fluid Mechanics*, 318:1-29.

Flynn, P.F., Durret, R.P., Hunter, G.L., zur Loye, A.O., Akinyemi, O.C., Dec, J.E., and Westbrook, C.K. (1999). Diesel Combustion: An Integrated View Combining Laser Diagnostics, Chemical Kinetics, and Empirical Validation. *SAE Paper 1999-01-0509.*

Gago, C.F., Garnier, F. and Utheza, F. (2003). Direct Testing of Subgrid Scale Models in Large-eddy Simulation of a Non-isothermal Jet. *International Journal for Numerical Methods in Fluids*, 42:999-1026.

Germano, M., Piomelli, U., Moin, P. and Cabot, W. (1991). A Dynamic Subgrid-scale Eddy Viscosity Model. *Physics of Fluids*, 3:1760-1765.

Geyer, D., Kempf, A., Dreizler, J., and Janicka, J. (2005). Scalar Dissipation Rates in Isothermal and Reactive Turbulent Opposed-Jets: 1-D Raman/Rayleigh

Experiments Supported by LES. *Proceedings of the Combustion Institute*, 30:681-689.

Ghosal, S., Lund, T.S., Moin, P. and Askelvoll, K. (1995). A Dynamic Localization Model for Large Eddy Simulation of Turbulent Flows. *Journal of Fluid Mechanics*, 286:229-255.

Ghosal, S. and Versvisch, L. (2000). Theoretical and Numerical Study of a Symmetric Triple Flame using a Parabolic Flame Path Approximation. *Journal of Fluid Mechanics*, 415:227-260.

Gill, S. (1951). A Process for the Step-by-Step Integration of Differential Equations in an Automatic Computing Machine. *Proceedings of the Cambridge Philosophical Society*, 47:96-108.

Gopalakrishnan, V. and Abraham, J. (2002). An Investigation of Ignition Behavior in Diesel Sprays. *Proceedings of the Combustion Institute,* 29:641-646.

Gopalakrishnan, V. (2003). *Modeling Combusting Diesel Jets: The Free Jet Regime*. PhD Thesis, Purdue University.

Gopalakrishnan, V. and Abraham, J. (2004). Computed NO and Soot distribution in Turbulent Transient Jets under Diesel Conditions. *Combustion Science and Technology,* 176:603-641.

Hawkes, E.R., Sankaran, R. Sutherland, J.C. and Chen, J.H., (2007). Scalar Mixing in Direct Numerical Simulations of Temporally Evolving Plane Jet Flames with Skeletal CO/H_2 Kinetics. *Proceedings of the Combustion Institute,* 31:1633-1640.

Hewson, J.C. and Kirstein, A.R. (2002). Local Extinction and Reignition in Non-premixed Turbulent $CO/H_2/N_2$ jet flames. *Combustion Science and Technology* 174: 35-66.

Hermanns, M., Vega, M. and Linan, A. (2007). On the Dynamics of Flame-edges in Diffusion-flame/vortex Interactions. *Combustion and Flame*, 149:32-48.

Im, H.G., Law, C.K., Kim, J.S., and Williams, F.A. (1995). Response of Counterflow Diffusion Flames to Oscillating Strain Rates. *Combustion and Flame*, 100:21-30.

Im, H.G., Chen, J.H., and Chen, J-Y. (1999). Chemical Response of Methane/Air Diffusion Flames to Unsteady Strain Rate. *Combustion and Flame*, 118:204-212.

Im, H.G. and Chen. J.H. (1999). Structure and Propagation of Triple Flames in Partially-premixed Hydrogen-air Mixtures. *Combustion and Flame*, 119:436-454.

Iyer, V. and Abraham, J. (1997). Penetration and Dispersion of Transient Gas Jets and Sprays. *Combustion Science and Technology*, 130: 315-335.

Jones, W.P. and Whitelaw, J.H. (1982). Calculation Methods for Reacting Turbulent Flows: A Review. *Combustion and Flame,* 48:1-26.

Karagozian, A.R. and Marble, F.E. (1986). Study of a Diffusion Flame in a Stretched Vortex. *Combustion Science and Technology*, 45:65-84.

Katta, V.R., Meyer, T.R., Brown, M.S., Gord, J.R., and Roquemore, W.M. (2004). Extinction Criterion for Unsteady, Opposing-jet Diffusion Flames. *Combustion and Flame*, 137:198-221.

Kistler, J.S., Sung, C.J., Kreutz, T.G., and Law, C.K. (1998). Extinction of Counterflow Diffusion Flames under Velocity Oscillations. *Proceedings of the Combustion Institute*, 26:113-120.

Ko, Y.S. and Chung, S.H. (1999). Propagation of Unsteady Tribrachial Flames in Laminar Non-premixed Jets. *Combustion and Flame*, 118:151-163.

Kong, S.C., Sun, Y. and Reitz, R.D. (2005a). Numerical Simulation of Flame Lift-off and Soot Formation in Diesel Fuel Jets. *ILASS Americas, 18th Annual Conference on Liquid Atomization and Spray Systems*, Irvine, CA, May 2005.

Kong, S.C., Sun, Y. and Reitz, R.D. (2005b). Modeling Diesel Spray Flame Lift-off, Sooting Tendency and NOx Emissions Using Detailed Chemistry with Phenomenological Soot Models. *ASME-ICES* 2005-1009.

Kortschik, C., Honnet, S. and Peters, N. (2005). Influence of Curvature on the Onset of Autoignition in a Corrugated Counterflow Mixing Field. *Combustion and Flame*, 142:140-152.

Laverdant, A. and Candel, S. (1988). A Numerical Analysis of a Diffusion Flame-vortex Interaction. *Combustion Science and Technology,* 60:79-96.

Lele, S.K. (1992). Finite Difference Schemes with Spectral-like Resolution. *Journal of Computational Physics*, 103:16-42.

Lesieur, M. and Metais, O. (1996). New Trends in Large-eddy Simulations of Turbulence. *Annual Review of Fluid Mechanics*, 28:845-882.

Liu, S., Hewson, J.C., Chen, J.H., and Pitsch, H. (2004). Effects of Strain Rate on High-Pressure Nonpremixed n-Heptane Autoignition in Counterflow. *Combustion and flame*, 137: 320-339.

Madnia, C.K. and Givi, P. (1993). Direct Numerical Simulation and Large-eddy Simulation of Reacting Homogenous Turbulence, in *Large-eddy Simulation of Complex Engineering and Geophysical Flows,* edited by P.Galerpin and S.A. Orszag. Cambridge University Press, Cambridge.

Magi, V. (1987). *REC-87: A New 3-D Code for Flows, Sprays and Combustion in Reciprocating and Rotary Engines.* Mechanical and Aerospace Engineering Report No. 1793, Princeton University, New Jersey.

Magi, V. (2008). *Private Communication*, August 2008.

Marble, F.E. (1985). Growth of a Diffusion Flame in the Field of a Vortex. *In Casci, C. and Bruno, C., editors. Recent Advances in Aerospace Sciences,* New York: Plenum Press, 395-413.

Meneveau, C. and Katz, J. (2000). Scalar-Invariance and Turbulence Models for Large Eddy Simulation, *Annual Review of Fluid Mechanics*, 32:1-32.

Mizobuchi, Y., Shinjo, J., Ogawa, S. and Takeno, T. (2005). A Numerical Study of the Formation of Diffusion Flame Islands in a Turbulent Hydrogen Jet Lifted Flame. *Proceedings of the Combustion Institute,* 30:611-619.

Moin, P., Squires, K, Cabot, W. and Lele, S. (1991). A Dynamic Subgrid-scale Model for Compressible Turbulence and Scalar Transport. *Physics of Fluids*, A 3: 2746-2757.

Moran, M.J. and Shapiro, H.N. (2000). *Fundamentals of Engineering Thermodynamics*, 4th Edition, John Wiley & Sons Inc., New York.

Morris, P. J., Wang, Q., Long, L. N., and Lockhard D. P. (1997). Numerical Predictions of High Speed Jet Noise. *AIAA Paper* 97-1598.

Namazian, M., Schefer, W. and Kelly, J. (1988). Scalar Dissipation Rate Measurements in the Developing Region of a Jet. *Combustion and Flame*, 74:147-160.

Oefelein, J. (2006). Large-eddy Simulation of Turbulent Combustion Processes in Propulsion and Power Systems. *Progress in Aerospace Sciences*, 42:2-37.

Oh, C.B., Lee, C.E. and Park, J. (2004). Numerical Investigation of Extinction in a Counterflow Non-premixed Flame Perturbed by a Vortex. *Combustion and Flame*, 138:225-241.

Panchapakesan, N.R. and Lumley, J.L. (1993a). Turbulence Measurements in Axisymmetric Jets of Air and Helium. Part I. Air Jets. *Journal of Fluid Mechanics*, 246:197-223.

Panchapakesan, N.R. and Lumley, J.L. (1993b). Turbulence Measurements in Axisymmetric Jets of Air and Helium. Part 2. Helium Jets. *Journal of Fluid Mechanics*, 246:225-247.

Pantano, C., Sarkar, S., and Williams, F.A. (2003). Mixing of a Conserved Scalar in a Turbulent Reacting Shear Layer. *Journal of Fluid Mechanics*, 481: 291-328.

Pantano, C. (2004). Direct Simulation of Non-Premixed Flame Extinction in a Methane-air Jet with Reduced Chemistry. *Journal of Fluid Mechanics,* 514: 231-270.

Peters, N. (1984). Laminar Diffusion Flamelet Models in Non-Premixed Turbulent Combustion. *Progress in Energy and Combustion Science,* 10:319-339.

Peters, N. (1985). Numerical and Asymptotic Analysis of Systematically Reduced Reaction Schemes for Hydrocarbon Flames, *Lecture Notes in Physics*, 241:90-109.

Peters, N., Terhoeven, P., Chen, J.H. and Echekki, T. (1998). Statistics of Flame Displacement Speeds from Computations of 2-D Unsteady Methane-Air Flames. *Proceedings of the Combustion Institute*, 27: 833-839.

Peters, N. (2000). *Turbulent Combustion*. Cambridge University Press, pp. 95-119.

Peters, N., Paczko, G., Seiser, R., and Seshadri, K. (2002). Temperature Cross-over and Non-thermal Runaway at Two-stage Ignition of n-heptane. *Combustion and Flame,* 128:38-59.

Phillips, H. (1965). Flame in a Buoyant Methane Layer. *Proceedings of the Combustion Institute*, 10:1277-1283.

Pickett, L.M. and Siebers, D.L (2004). Soot in Diesel Fuel Jets: Effects of Ambient Temperature, Ambient Density, and Injection Pressure. *Combustion and Flame,* 138: 114-135.

Pickett, L.M., Siebers, D.L., and Idicheria, C.A. (2005). Relationship between Ignition Processes and the Flame Lift-off Length in Diesel Fuel Jets. *SAE Paper 2005-01-3843*.

Pickett, L.M., Kook, S., Persson, H., and Andersson, O. (2008). Diesel Fuel Jet Lift-off Stabilization in the Presence of Laser-Induced Plasma Ignition. *Proceedings of the Combustion Institute*, article in press.

Pitts, W.M. (1989). Importance of Isothermal Mixing Processes in the Understanding of Lift-off and Blowout of Turbulent Jet Diffusion Flames. *Combustion and Flame*, 76:197-212.

Pitts, W.M. (1991). Effects of Global Density Ratio on the Centerline Mixing Behavior of Axisymmetric Turbulent Jets. *Experiments in Fluids*, 11:125–134.

Pierce, C.D. and Moin, P. (2004). Progress-variable Approach for Large-eddy Simulation of Non-Premixed Turbulent Combustion. *Journal of Fluid Mechanics*, 504:73-97.

Piomelli, U. (1999). Large-eddy Simulation: Achievements and Challenges. *Progress in Aerospace Sciences*, 35:335-362.

Pitsch, H., Wan, Y.P., and Peters, N. (1995). Numerical Investigation of Soot Formation and Oxidation under Diesel Engine Conditions. *SAE Paper 952357.*

Pitsch, H., Barths, H., and Peters, N. (1996). Three-Dimensional Modeling of NO_x and Soot Formation in DI Diesel Engines Using Detailed Chemistry Based on the Interactive Flamelet Approach. *SAE Paper 962057.*

Pitsch, H. and Steiner, H. (2000a). Large-eddy Simulation of a Turbulent Piloted Methane/ Air Diffusion Flame (Sandia Flame D). *Physics of Fluids*, 12:2541-2554.

Pitsch, H. and Steiner, H. (2000b). Scalar Mixing and Dissipation Rate in Large-eddy Simulations of Non-Premixed Turbulent Combustion. *Proceedings of the Combustion Institute*, 28: 41-49.

Pitsch, H. (2002). Improved Pollutant Predictions in Large-eddy Simulations of Turbulent Non-Premixed Combustion by Considering Scalar Dissipation Rate Fluctuations. *Proceedings of the Combustion Institute,* 29:1971-1978.

Pitsch, H. and Ihme, M. (2005). An Unsteady Flamelet/Progress Variable Method for LES of Non-Premixed Turbulent Combustion. *AIAA Paper 2004-557*, *43rd AIAA Aerospace Sciences Meeting and Exhibit*, January 2005, Reno, NV.

Pitsch, H. (2006). Large-eddy Simulation of Turbulent Combustion. *Annual Review of Fluid Mechanics*, 38:453-483.

Pitts, W.M. and Kashiwagi, T. (1984). The Application of Laser-induced Rayleigh Light Scattering in the Study of Turbulent Mixing. *Journal of Fluid Mechanics*, 141:391-429.

Poinsot, T., Veynante, D. and Candel, S. (1991). Quenching Processes and Premixed Turbulent Combustion Diagrams. *Journal of Fluid Mechanics*, 228:561-606.

Poinsot, T.J. and Lele, S.K. (1992). Boundary Conditions for Direct Simulations of Compressible Viscous Flows. *Journal of Computational Physics*, 101:104-129.

Pons, L., Darabiha, N, and Candel, S. (2008). Pressure Effects on Nonpremixed Strained Flames. *Combustion and Flame*, 152:218-229.

Pope, S.B. (2000). *Turbulent Flows*. Cambridge University Press, pp. 119-122.

Pope, S. B. (2004). Ten Questions Concerning the Large-eddy Simulation of Turbulent Flows. *New Journal of Physics*, 6:35-59.

Renard, P.H., Rolon, J.C., Thevenin, D. and Candel, S. (1999). Investigation of Heat Release, Extinction and Time Evolution of the Flame Surface, for a Non-premixed Flame Interacting with a Vortex. *Combustion and Flame*, 117:189-205.

Renard, P.H., Rolon, J.C., Thevenin, D. and Candel, S. (2000). Dynamics of Flame/Vortex Interactions. *Progress in Energy and Combustion Science*, 26:225-282.

Ribault, C.L., Sarkar, S. and Stanley, S.A. (2001). Large Eddy Simulation of Evolution of Passive Scalar in a Plane Jet. *AIAA Journal*, 39:1509-1516.

Richards, C.D. and Pitts, W.M. (1993). Global Density Effects on the Self-Preservation Behavior of Turbulent Free Jets. *Journal of Fluid Mechanics*, 254:417-435.

Rogallo, R.S. and Moin, P. (1984). Numerical Simulation of Turbulent Flows. *Annual Review of Fluid Mechanics*, 16:99-137.

Ruetsch, G.R., Versvisch, L. and Linan, A. (1995). Effect of Heat Release on Triple Flames. *Physics of Fluids*, 7:1447-1454.

Santoro, V.S., Kyritsis, D.C., Linan, A. and Gomez, A. (2000a). Vortex-induced Extinction Behavior in Methanol Gaseous Flames: A Comparison with Quasi-steady Extinction. *Proceedings of the Combustion Institute*, 28:2109-2116.

Santoro, V.S., Linan, A. and Gomez, A. (2000b). Propagation of Edge Flames in Counterflow Mixing Layers: Experiments and Theory. *Proceedings of the Combustion Institute*, 28:2039-2046.

Santoro, V.S. and Gomez, A. (2002). Extinction and Reignition in Counterflow Spray Diffusion Flames Interacting with Laminar Vortices. *Proceedings of the Combustion Institute*, 29:585-592.

Seiser, R., Pitsch, H., Seshadri, K., Pitz, W.J. and Curran, H.J. (2000). Extinction and Autoignition of n-Heptane in Counterflow Configuration. *Proceedings of the Combustion Institute,* 28:2029-2037.

Senecal, P.K., Pomraning, E. and Richards, K.J. (2003). Multidimensional Modeling of Direct-Injection Diesel Spray Liquid Length and Flame Lift-off Length using CFD and Parallel Detailed Chemistry. *SAE Paper 2003-01-1043.*

Siebers, D.L. and Higgins, B.S. (2001). Flame Lift-off on Direct-Injection Diesel Sprays under Quiescent Conditions. *SAE Paper 2001-01-0530.*

Siebers, D.L., Higgins, B.S., and Pickett, L.M. (2002) Flame Lift-off on Direct-injection Diesel Fuel Jets: Oxygen Concentration Effects. *SAE Paper 2002-01-0890.*

Smagorinsky, J. (1963). General Circulation Experiments with the Primitive Equations. *Monthly Weather Review*, 91:99-164.

Sreedhara, S. and Lakshmisha, K.N. (2000). Direct Numerical Simulation of Autoignition in a Non-premixed Turbulent Medium. *Proceedings of the Combustion Institute*, 28:25-34.

Sripakagorn, P., Mitarai, S., Kosaly, G. and Pitsch, H. (2004). Extinction and Reignition in a Diffusion Flame: A Direct Numerical Simulation Study. *Journal of Fluid Mechanics,* 518:231-259.

Speziale, C. G., Erlebacher, G., Zang, T. A., and Hussaini, M. Y. (1988).The Subgrid-Scale Modeling of Compressible Turbulence. *Physics of Fluids*, 31: 940-942.

Suto, H., Matsubara, K., Kobayashi, M. and Kaneka, Y. (2004). Large Eddy Simulation of Flow and Scalar Transport in a Round Jet. *Heat Transfer-Asian Research*, 33:175-188.

Tap, F.A. and Veynante, D. (2005). Simulation of Flame Lift-off on a Diesel Jet Using a Generalized Flame Surface Density Modeling Approach. *Proceedings of the Combustion Institute,* 30, 919-926.

Thevenin, D. and Candel, S. (1995). Ignition Dynamics of a Diffusion Flame Rolled-up in a Vortex. *Physics of Fluids*, 7(2):434-445.

Thevenin, D., Renard, P.H., Rolon, J.C. and Candel, S. (1998). Extinction Processes during a Non-Premixed Flame/Vortex Interaction. *Proceedings of the Combustion Institute*, 27:2101-2108.

Thevenin, D., Renard, P.H., Fiechetner, C.J., Gord, J.R. and Rolon, J.C. (2000). Regimes of Non-premixed Flame-vortex Interactions. *Proceedings of the Combustion Institute*, 28:719-726.

Uzun, A. (2003). *3-D Large-eddy Simulation for Jet Aeroacoustics*. Ph.D Thesis, Purdue University, December 2003.

Venugopal, R. (2005). *Modeling Flame Lift-off in Diesel Jets*. M.S.M.E. Thesis, Purdue University, December 2005.

Venugopal, R. and Abraham, J. (2006). Effect of Pre-Lift-off Mixing on Pollutant Formation in Diesel Jets. *Proceedings of the Central States Section of the Combustion Institute*, May 2006, Cleveland, Ohio.

Venugopal, R. and Abraham, J. (2007a). A Numerical Investigation of Flame Lift-off in Diesel Jets. *Combustion Science and Technology*, 179:2559-2618.

Venugopal, R. and Abraham, J. (2007b). A Review of Fundamental Studies Relevant to Flame Lift-off in Diesel Jets. *SAE Paper 2007-01-0134. SAE 2007 Transactions Journal of Engines*, 116: 132-151.

Venugopal, R., Magi, V., and Abraham, J. (2007). Extinction and Reignition in Non-premixed Flame-vortex Interactions under Diesel Conditions. *Proceedings of the 5th Joint Meeting of the Combustion Institute*, Paper A19, March 2007, San Diego, California.

Venugopal, R. and Abraham, J. (2008a). A 2-D DNS Investigation of Extinction and Reignition Dynamics in Non-premixed Flame-vortex Interactions. *Combustion and Flame*, 153:442-464.

Venugopal, R. and Abraham, J. (2008b). Numerical Investigations of Reignition in Vortex-Perturbed n-Heptane Non-Premixed Flames. *AIAA Journal*, article in press.

Venugopal, R. and Abraham, J. (2008c). Numerical Investigations of Extinction/Reignition of Laminar Diffusion Flamelets Under Oscillating Scalar Dissipation Rates. *Proceedings of the 2008 Technical Meeting of the Central States Section of the Combustion Institute*, April 2008, Tuscaloosa, Alabama, USA.

Vera, M. and Linan, A. (2004). On the Interaction of Vortices with Mixing Layers. *Physics of Fluids*, 16: 2237-2254.

Vervisch, L. and Poinsot, T. (1998). Direct Numerical Simulation of Non-Premixed Turbulent Flames. *Annual Review of Fluid Mechanics,* 30:655-691.

Viggiano, A. and Magi, V. (2004). A 2-D Investigation of n-Heptane Autoignition by Means of Direct Numerical Simulation. *Combustion and Flame,* 137:432-443.

Visbal, M.R. and Rizzetta, D.P. (2002). Large-eddy Simulation on Curvilinear Grids using Compact Differencing and Filtering Schemes. *Journal of Fluids Engineering*, 124:836-847.

Visbal, M.R., Morgan, P.E. and Rizzetta, D.P (2003). An Implicit LES Approach Based on High-order Compact Differencing and Filtering Schemes (invited). *AIAA Paper* 2003-4098.

Yoo, C.S. and Im, H.G. (2005). Transient Dynamics of Edge Flames in a Laminar Non-premixed Hydrogen-air Counterflow. *Proceedings of the Combustion Institute*, 30:349-356.

Zaman, K.B.M.Q. (1985). Far-field Noise of a Subsonic Jet under Controlled Excitation. *Journal of Fluid Mechanics*, 152:83-111.

Wall, C., Boersma, B. and Moin, P. (2000). An Evaluation of the Assumed Beta Probability Density Function Subgrid-scale Model for Large-eddy Simulation of Non-Premixed Turbulent Combustion with Heat Release. *Physics of Fluids*, 12:2522-2529.

Wan, Y.P., Pitsch, H. and Peters, N. (1997). Simulation of Autoignition Delay and Location of Fuel Sprays under Diesel Engine Relevant Conditions. *SAE Paper 971590, SAE Transactions, Journal of Engines,* 106:1611-1621.

Welle, E.J., Roberts, W.L., Carter, C.D., and Donbar, J.M. (2003). The Response of a Counter-Flow Diffusion Flame Subjected to a Transient Flow Field. *Combustion and Flame*, 135:285-297.

Williams, F.A. (2000). Progress in the Knowledge of Flamelet Structure and Extinction. *Progress in Energy and Combustion Science,* 26:657-682.

Wygnanski, I. and Fiedler, H. (1969). Some Measurements in the Self-preserving Jet. *Journal of Fluid Mechanics*, 38:577-612.

VITA

VITA

Rishikesh Venugopal was born in Kumbakonam, Tamil Nadu, India, in 1981. He graduated with a B.Tech degree in Mechanical Engineering from the Indian Institute of Technology Madras (IIT Madras),Chennai, India, in 2004. Rishikesh was awarded the *Sivasailam Merit Prize* and a gold medal for the best individual project in Mechanical Engineering of the B.Tech Degree Program for the period 2000-2004 by IIT Madras. He joined Purdue University in August 2004 to pursue graduate studies in Professor Abraham's research group in the School of Mechanical Engineering. He received his M.S.M.E degree in December 2005; his Master's research focused on the computational modeling of flame lift-off phenomena and pollutant distribution in diesel jet flames, employing RANS-based flamelet models. This work resulted in two archival journal publications and three papers in conference proceedings. His PhD work has focused on the detailed investigation of flame dynamics related to lift-off in high-Reynolds number jets encountered in diesel engines. This work has employed state-of-the-art simulation techniques, such as LES, and has resulted in two archival journal publications, three journal paper submissions, and three papers in conference proceedings. Rishikesh is a member of the C&SE program at Purdue since August 2006, and received the CSE-OIGP Spring 07 Travel Award to present a paper at the SAE World Congress 2007. He presented an invited seminar on his graduate research at Sandia National Laboratories in May 2008. Upon completing his PhD, Rishikesh would be joining Combustion Research at Cummins Inc., Columbus, IN, in September 2008.

PUBLICATIONS

PUBLICATIONS

Venugopal, R., Pickett, L.M., and Abraham, J., Unsteady Effects on Flamelets in the Near-field of Diesel jets: Implications for Flame Lift-off. *In preparation for Combustion Science and Technology.*

Venugopal, R. and Abraham, J., Numerical Studies of the Unsteady Response of Diffusion Flamelets in the Near-field of High-Reynolds Number Jets. *Submitted to AIAA Journal*, in review.

Venugopal, R. and Abraham, J., Numerical Studies of Flame-Vortex Interactions Relevant to the Near-field of a High-Reynolds Number Jet, *Submitted to Physics of Fluids,* in review.

Venugopal, R. and Abraham, J. (2008). Numerical Investigations of Reignition in Vortex-Perturbed n-Heptane Non-Premixed Flames. *AIAA Journal*, article in press.

Anders, J.W., Venugopal, R., Magi, V., and Abraham, J. (2008). A Study of Flame-Vortex Interactions in the Presence of Residual Gases. *Combustion Science and Technology*, 180: 1395-1420.

Venugopal, R. and Abraham, J. (2008). A 2-D DNS Investigation of Extinction and Reignition Dynamics in Non-premixed Flame-vortex Interactions. *Combustion and Flame*, 153:442-464.

Venugopal, R. and Abraham, J. (2007). A Numerical Investigation of Flame Lift-off in Diesel Jets. *Combustion Science and Technology*, 179:2559-2618.

Venugopal, R. and Abraham, J. (2007). A Review of Fundamental Studies Relevant to Flame Lift-off in Diesel Jets. *SAE Paper 2007-01-0134. SAE 2007 Transactions Journal of Engines*, 116: 132-151.

Venugopal, R., Magi, V., and Abraham, J. (2008). A Coupled LES-DNS Study of Physicochemical Processes in the Near-field of Transient Jets Under Engine Conditions. *To be presented at LES for Internal Combustion Flows (LES4ICE)*, 1-2 December 2008, Rueil-Malmaison, France.

Venugopal, R. and Abraham, J. (2008). Numerical Investigations of Extinction/Reignition of Laminar Diffusion Flamelets Under Oscillating Scalar Dissipation Rates. *Proceedings of the 2008 Technical Meeting of the Central States Section of the Combustion Institute*, April 2008, Tuscaloosa, Alabama, USA.

Venugopal, R., Magi, V., and Abraham, J. (2007). Extinction and Reignition in Non-premixed Flame-vortex Interactions under Diesel Conditions. *Proceedings of the 5th Joint Meeting of the Combustion Institute*, Paper A19, March 2007, San Diego, California.

Venugopal, R. and Abraham, J. (2006). Effect of Pre-Lift-off Mixing on Pollutant Formation in Diesel Jets. *Proceedings of the Central States Section of the Combustion Institute*, May 2006, Cleveland, Ohio.

Venugopal, R. and Abraham, J. (2006). Diesel Flame Extinction at Low Oxygen Concentrations: Importance of Chemical Kinetics Modeling. *Proceedings of the Central States Section of the Combustion Institute*, May 2006, Cleveland, Ohio.

Venugopal, R. and Abraham, J. (2005). Correlating Flame Lift-off Heights in Diesel Jets with Extinction Strain Rates. *Proceedings of the 4th Joint Meeting of the Combustion Institute*, March 2005, Philadelphia, Pennsylvania.